Material Properties of RE- Doped Ln (Ln= Y, La) Oxides and Oxysulfides Phosphors For Red-Emitting Devices

By

Abdub Guyo Ali

(MSc)

A thesis submitted in fulfilment of the requirements for the degree

Doctor of philosophy

in the

Faculty of Natural and Agricultural Sciences

Department of Physics

University of the Free State

Republic of South Africa

Promoter: Prof. F.B. Dejene

Co-Promoter: Prof. H.C. Swart

November 2015

Dedication

This thesis is dedicated to my Son Guyo

Acknowledgements

First and foremost, I express my heartfelt gratitude to **The Almighty God**, for granting me the opportunity to pursue this study. I thank him also for enabling me to complete my studies successfully. ***I bow before Almighty God for giving me the strength and courage to pursue this study.***

I would like to express my heartfelt gratitude to my two advisors Prof. Francis Birhanu Dejene and Prof. Hendrik C. Swart, for giving me the opportunity to work in their research group, and for their guidance, support and encouragement. The two of them have been very valuable in the development of my PhD investigation and they made this interdisciplinary project an exciting adventure. I would like to thank Prof. F.B. Dejene for making me feel from the beginning part of his group and also for introducing me to the field of Material Sciences. I would particularly like to express my indebtedness to my co-supervisor Prof. H. C. Swart for his guidance and encouragement during the entire course of my studies. He has taught me a lot on the writing skills of which he is very good. I would like to acknowledge the moral support from Prof. JJ. Terblans, Prof. W.D. Roos, Prof. P.J. Meintjes, Prof. M.J.H Hoffman, Prof. T. Kroon and Mr. D.P. van Jaarsveldt.

I would like to thank members of staff of the Department of Physics, University of the Free State for the positive interactions and support: Dr. Koao L.F, Dr. Tshabalala K.G, Dr. Motloug S.V, Mr. Ocaya R.O, Mr. Motloung S.J, Mrs Cronje, K.The late Dr. Dolo, J.J. Ms Lebeko, K.M. Prof. Mothudi, B.M, to mention but a few. Fellow researchers: Mr Wako, A.H, Dr Coetsee, E. Prof. Dlamini, M.S. Dr. Duvenhage, M.M, Miss Foka, K.E, Miss Lephoto, M.A, Mr Ungula J, Mrs Jattani (Sharon), Miss Tebele A, Miss Mulwa W.M, Dr Roro, R. (DST), Mr Malevu T.D, Miss Tshabalala, M.A. among others. Prof Van Wyk, P.W.J. and Janecke, B. of the Centre of Microscopy for their support and advice during SEM measurements. My stay at University of the Free State and in particular Qwaqwa was an enjoyable journey due to many of my friends. I am greatly indebted to the African Laser Center (ALC), National Research Foundation (NRF) and University of the Free State for their financial support. I would like to extend my special gratitude to the staff of the National Laser Center (NLC) for their valuable support during my visits to the NLC for my experimental work.

Abstract

Structural and optical properties of Eu^{3+}-doped Ln (Ln=Y, La) oxide and oxysulfide nano crystals synthesized by sol-combustion method were analysed as a function of host to fuel ratio. Structural characterization shows crystallite nanosized particles and the hexagonal phase as the dominant structure. The red emission of Eu^{3+} doped Y_2O_2S, La_2O_2S and Y_2O_3 nanocrystals appearing near 624 nm was assigned to the $^5D_0$-$^7F_2$ transition of Eu^{3+}. Due to insufficient quantities of thiourea at the higher Ln/S mole ratio, the bright red emission has been quenched. Fourier-transform infrared spectrometry analysis showed that there was a negligible difference in the absorbed impurities with various molar ratios. The Ln/S concentration also affects the decay time of the red emission of the Eu^{3+} ions from 140 μs for Ln/S=1 to 76 μs for the higher concentrations. Structural and optical properties of $La_2O_2S:Eu^{3+}$micro crystals synthesized by sol-combustion method were analyzed as a function of La/S concentration. Structural characterization shows a crystallite size of about 178 nm and the hexagonal phase as the dominant crystalline structure. The red emission of Eu^{3+} doped La_2O_2S microcrystals appearing near 624 nm was assigned to the $^5D_0$-$^7F_2$ transition of Eu^{3+}. Due to insufficient quantities of thiourea at the higher La/S mole ratio, the bright red emission has been quenched. Fourier-transform infrared spectrometry analysis showed that there was a negligible difference in the absorbed impurities with various molar ratios. The La/S concentration also affects the decay time of the red emission of the Eu^{3+} ions from 140 μs for La/S=1 to 76 μs for the higher concentrations.

To investigate the effect of co-doping a series of red-emitting phosphors $Y_2O_3:Eu^{3+}:Ho^{3+}$ were prepared by the solution combustion method. X-ray diffraction (XRD) patterns indicate that the Eu^{3+} and Ho^{3+} doping do not show obvious effect on the cubic Y_2O_3 crystal. Their crystallite size estimated by x-ray diffractometry and scanning electron microscopy was about 8 nm. Under UV 325 nm excitation, emission wavelengths at 626 nm was quenched at higher mole percent of Ho^{3+} and energy was transferred from Eu^{3+} to Ho^{3+}. $Y_2O_3:Eu^{3+}$: Ho^{3+} phosphor shows a red-emitting afterglow phenomenon, and the Eu^{3+} ions are the luminescent center during the decay process. The bright red emission near 626 nm has been noticeable due to the $^5D_0$-$^7F_2$ transition of Eu^{3+}. The intensity of the luminescence has decreased with an increase of concentration of Ho^{3+}. In sufficient quantities of Eu^{3+} to Ho^{3+}, the bright red emission near 626 nm has been predominant due to $^5D_0$-$^7F_2$ transition of Eu^{3+}. The decay

characteristic of Y_2O_3:Eu^{3+}: Ho^{3+} phosphor is according with the double exponential equation.

The as-prepared powder Y_2O_2S:Eu^{3+} was deposited on Si (100) substrates by using a pulsed laser deposition technique. The thin films grown under different oxygen deposition pressure conditions have been characterized using structural and luminescent measurements. The X-ray diffraction patterns showed mixed phases of cubic and hexagonal crystal structures. As the oxygen partial pressure increased, the crystallinity of the films improved. Further increase of the O_2 pressure to 140 mtorr reduced the crystallinity of the film. Similarly, both scanning electron microscopy and atomic force microscopy confirmed that an increase in O_2 pressure affected the morphology of the films. The average band gap of the films calculated from diffuse reflectance spectra using the Kubelka-Munk function was about 4.75 eV. The photoluminescence measurements indicated red emission of Y_2O_2S:Eu^{3+} thin films with the most intense peak appearing at 619 nm, which is assigned to the $^5D_0$-$^7F_2$ transition of Eu^{3+}. This most intense peak was totally quenched at higher O_2 pressures. X-ray photoelectron (XPS) indicated that Y_2O_3 thin films are formed on the surfaces of the Y_2O_2S: Eu^{3+} thin films during prolonged electron bombardment. The films grown in a lower O_2 ambient consist of smaller but more densely packet particles relative to the films grown at a higher O_2 ambient. In order to study the effect of annealing temperature on the films, four samples were annealed at various temperatures while one was kept unannealed. X-ray diffraction measurements show that the un-annealed thin film was amorphous, while those annealed were crystalline. At lower annealing temperature of 600 ^{0}C to 700 ^{0}C cubic bixbyite Y_2O_3:Eu^{3+} was formed. As the annealing temperatures were increased to 800 ^{0}C, hexagonal phase emerged. The average crystallite size of the film was 64 nm. Photoluminescence (PL) measurement indicates intense red emission around 612 nm due to the $^5D_0 \rightarrow {}^7F_2$ transition. Scanning electron microscopy (SEM) indicated that agglomerates of non-crystalline particles with spherical shapes were present for the un-annealed films. After annealing at high temperature, finer morphology was revealed. Atomic force microscopy (AFM) further confirmed the formation of new morphology at the higher annealing temperatures. UV-vis measurement indicated a band gap in the range of 4.6 to 4.8 eV. It was concluded that the annealing temperature played an important role in the luminescence intensity and crystallinity of these films.

To investigate the effect of different species of gases Y_2O_2S:Eu^{3+} thin films have been grown on Si (100) substrates by using a pulsed laser deposition technique. The thin films grown

under different species of gases have been characterized using structural and luminescent measurements. The X-ray diffraction patterns showed mixed phases of cubic and hexagonal crystal structures. The crystallinity of the film deposited in vacuum is poor, but improved significantly in argon and oxygen atmosphere. Similarly, both scanning electron microscopy and atomic force microscopy confirmed that different species of gases affected the morphology of the films. The average band gap of the films calculated from diffuse reflectance spectra using the Kubelka-Munk function was about 4.69 eV. The photoluminescence measurements indicated red emission of $Y_2O_2S:Eu^{3+}$ thin films with the most intense peak appearing at 612 nm, which is assigned to the $^5D_0$-$^7F_2$ transition of Eu^{3+}. The intensities of this most intense peak greatly depend on the species of gas with argon having the highest peak. This phosphor has applications in the flat panel displays.

Key words

Y_2O_2S: Eu^{3+}

Y_2O_3: Eu^{3+}

La_2O_2S: Eu^{3+}, La_2O_3: Eu^{3+}

Y_2O_2S: Eu^{3+}:Ho^{3+}

Solution – Combustion Method

Morphology

Excitation

Band gap

Luminescence

Rare Earth Ions

PLD

Laser ablation

decay time

red-emitting

Acronyms and symbols

- PL- Photoluminescence
- XPS -X-ray photoelectron spectroscopy
- XRD -X-ray diffraction
- HRTEM – High resolution Transmission electron microscopy
- SEM- Scanning electron microscopy
- EDS -Energy dispersive spectroscopy
- PLD -Pulsed laser deposition
- AFM- Atomic force microscopy
- FTIR – Fourier-Transform infrared
- He-Cd- Helium Cadmium
- RE- Rare earth
- KrF-Krypton fluoride
- Y- Ylttrium
- La- Lanthanum
- Al- Aluminium
- O2- Oxygen molecule
- O- Oxygen atom
- VB- Valence band
- CB- Conduction band
- VO- Oxygen vacancy
- **CRTs**- Cathode Ray Tubes
- **LPP**-Long Persistent Phosphors,
- **TEM**- Transition Electron Microscopy
- **TL**-Thermoluminescence

List of figures

List of tables

Table of Contents

Chapter 1

Introduction

1.1. Background

Optical materials have a broad range of applications in a variety of aspects of human life. Among those are medicine, military, communications, computing, manufacturing, and various industrial applications. Rapid progress of nanotechnology opens new opportunities in designing optical materials with improved optical properties. Current research in nanotechnology is focused on new materials, novel phenomena, new characterization technique and fabrication of nano devices. $Y_2O_2S:Eu^{3+}$ and $La_2O_2S:Eu^{3+}$ are excellent materials of current interest [1-3] owing to their interesting optical and opto-electronic properties. The crystal structure of M_2O_2S (M = Y, La and including all lanthanides) are discussed in detail [3-5]. The crystal symmetry of the above two systems is hexagonal, with the space group P3m1 (*D33d*), as determined by X-ray diffraction. These systems are grouped under wide band gap (4.6 – 4.8 eV) semiconductors. $Y_2O_2S:Eu^{3+}$, $Y_2O_3:Eu^{3+}$ and $La_2O_2S:Eu^{3+}$ as red- emitting phosphors, with its sharp emission line for good calorimetric definition and high luminescence efficiency, is extensively used in the phosphor screen of display devices, fluorescent lamps used for lighting purposes, television sets used for entertainment and information gathering, X-ray imaging instruments used in hospitals and laser instruments used for experimental purposes and, many other electrical and opto-electronic equipment. They employ luminescent materials for [6, 7] electronic portal imaging devices (EPID), radioisotope distribution and so on [8]. Due to the large size and weight of CRTs, developments of flat-panel displays (FPDs) are of great interest. Among several FPD technologies, liquid-crystal displays (LCDs) dominate the FPD market and plasma display panels (PDPs) are now commercially available in the large area TV market [9-11]. New and enhanced properties are expected due to size confinement in nanoscale dimensions that can revolutionize the display devices market in future. Commercially available bulk oxysulfides are quite expensive and are not easily available. So, for the time being, $Y_2O_2S:Eu^{3+}$ and

$La_2O_2S:Eu^{3+}$ nanostructures are relatively a good choice while compared with the bulk systems. However, for an extensive use in the commercial applications, $Y_2O_2S:Eu^{3+}$, Y_2O_3: Eu^{3+} and $La_2O_2S:Eu^{3+}$ nanocrystals must be prepared at lower temperatures. Therefore, it is necessary to develop a low-temperature synthesis technology for the growth of both oxide and oxysulfide nanophosphors. In this background, this chapter has been devoted to the nanophosphors development using these two systems. The realm of novel devices from this wonderful material is yet to be accomplished in full. To give a quantitative report on the state of art of $Y_2O_2S:Eu^{3+}$ Y_2O_3: Eu^{3+} and $La_2O_2S:Eu^{3+}$ is quite difficult and an attempt has been made to give an account of the synthesis of the nanophosphors in this thesis.

1.2 An overview of past Phosphor research

The scientific research on phosphors has a long history going back more than 100 years. A prototype of the ZnS-type phosphors, an important class of phosphors for television tubes, was first prepared by Théodore Sidot, a young French chemist, in 1866 rather accidentally. It seems that this marked the beginning of scientific research and synthesis of phosphors [12]. From the late 19^{th} century to the early 20^{th} century, Philip E.A. Lenard and coworkers in Germany performed active and extensive research on phosphors, and achieved impressive results. They prepared various kinds of phosphors based on alkaline earth chalcogenides (sulfides and selenides) and zinc sulfide, and investigated their luminescence properties. They established the principle that phosphors of these compounds are synthesized by introducing metallic impurities into the materials by firing. Lenard and co-workers tested not only heavy metal ions but various rare-earth ions as potential activators. P. W. Pohl and co-workers in Germany investigated Tl^+-activated alkali halide phosphors in detail in the late 1920s and 1930s. They grew single-crystal phosphors and performed extensive spectroscopic studies. In co-operation with F. Seitz in the U.S. they introduced the configurational co-ordinate model of luminescence centres and established the basis of present-day luminescence physics. Humbolt Leverenz and co-workers at Radio Corporation of America (U.S.) also investigated many practical phosphors with the purpose of obtaining materials with desirable characteristics to be used in television tubes. Detailed studies were performed on ZnS type phosphors. Since the end of World War II, research on phosphors and solid-state luminescence has evolved dramatically. This has been supported by progress in solidstate physics, especially semiconductor and lattice defect physics. Advances in the understanding

of the optical spectroscopy of solids, especially that of transition metal ions in general and rare-earth ions in particular, have also helped in these developments. The concept of the configurational coordinate model of luminescence centres was established theoretically. Spectral shapes of luminescence bands were explained on the basis of this model. The theory of excitation energy transfer successfully interpreted the phenomenon of sensitized luminescence. Optical spectroscopy of transition metal ions in crystals clarified their energy levels and luminescence transition on the basis of crystal field theory. In the case of trivalent rare-earth ions in crystals, precise optical spectroscopy measurements made possible the assignment of complicated energy levels and various luminescence transitions.

1.3 Statement of the problem

A lot of research has been devoted to luminescence of nano and microsized sulphide phosphors since they are used in many display applications including cathode ray tube and field emission display. A mechanism that shows the relationship between their luminescence and surface chemical reactions has been established. Since these phosphors are not very efficient at low voltages required for field emission displays, micro-sized and nanoparticle oxide phosphors are being investigated to replace them [13]. Several effective red-emitters phosphors, for example $La_2O_2S:Eu^{3+}$, $Y_2O_2S:Eu^{3+}$ and $Gd_2O_2S: Tb^{3+}$, have been investigated for their luminescent properties of both powders and thin films, because of their better emission properties as compared to their counterparts, vanadate. A proper way to evaluate these phosphors for application displays would be to study their luminescent properties. It is important to determine the mechanism that shows the correlation between their PL intensities and changes on the surface chemical composition during electron beam exposure. It is well known that the reduction in particle size of crystalline systems in the nanometer regime gives rise to some important modifications of their properties with respect to their bulk counterparts. Two main reasons for the change of electronic properties of the nanosized particles can be identified as: (1) the 'quantum confinement' effect due to the confinement of delocalized electrons in a small sized particles, which results in an increased electronic band gap and (2) the increase of the surface/volume ratio in nanostructures, which enhances 'surface' and 'interface' effects over the volume effects. In case of rare-earth ions, the electronic f-f transitions involve localized electrons in the atomic orbital of the ions. Therefore, no size dependent quantum confinement effect is found in the electronic transitions of the rare-earth doped nanosized particles. However, the 'surface effect' plays a

vital role in the photoluminescence properties of these ions. Although there has been an explosive growth in the synthesis of nanosized materials, it is still a challenge for material chemists to design a process for the fabrication of highly luminescent nanosized materials with high degree of crystallinity. Somewhat more recently, the focus of interest has shifted to nanosized luminescent materials with tunable morphologies such as nanorods, nanowires, nanotubes etc [14].

1.4 Research objectives

The specific objectives of this study were;

1. Synthesis and characterization of the $Y_2O_2S:Eu^{3+}$ and $La_2O_2S:Eu^{3+}$ phosphor powder.

2. Deposition of the $Y_2O_2S:Eu^{3+}$ and Y_2O_3: Eu^{3+} phosphor thin films onto Si (100) substrates with the use of a KrF excimer laser in pulsed laser deposition.

3. Characterisation of both powder and thin films using Scanning Electron Microscopy (SEM), X-Ray Diffraction (XRD), Photoluminescence Spectroscopy (PL), X-ray Photoelectron spectroscopy (XPS), Uv- vis measurements (UV), Fourier Transform Infrared (FTIR) and Atomic Force Microscopy (AFM).

4. Monitor changes in the material properties, due to ablation of $Y_2O_2S:Eu^{3+}$ thin films in vacuum, oxygen and argon gas ambient, using Pulsed Laser Deposition.

5. Monitor changes in material properties of $Y_2O_2S:Eu^{3+}$ after annealing at several different temperatures.

1.5 Thesis layout

The thesis is organized into ten chapters;

Chapter 1

In this chapter the background information, overview of research contributions on classical phosphors, rationale and aims of the research project are given. The issues, perspectives and general advantages of nanostructured phosphor are briefly discussed. Finally, a summary of the subjects treated in the succeeding chapters of this thesis, is presented.

Chapter 2

This chapter provides background information on the fundamentals of phosphors and types of

luminescence in solids. Detailed information about the phosphorescence mechanism of long persistent phosphors as well as the electronic transition of rare earth ions (Eu^{3+}) is provided. The structural properties of the lanthanides ($Ln_2O_2S:Eu^{3+}$, Ho^{3+}) are briefly discussed.

Chapter 3

A brief description of the experimental techniques used to synthesize and characterize lanthanides phosphors is provided in this chapter. The sol-gel, sol-combustion and solid state reaction methods used to synthesize the phosphors are discussed in detail. Detailed information on the principle and operation of the experimental techniques used to investigate the luminescence and the structure of the phosphors are presented.

Chapter 4

Luminescent and structural properties of Y_2O_3: Eu^{3+} phosphors prepared by a sol-combustion reaction method are discussed in this chapter.

Chapter 5

In this chapter, structural and optical properties of $La_2O_2S:Eu^{3+}$micro crystals synthesized by sol-combustion method were analyzed as a function of La/S molar ratios.

Chapter 6

The influence of oxygen partial pressure on material properties of Eu^{3+}- doped Y_2O_2S thin films phosphor deposited by Pulsed Laser Deposition was studied and analyzed in the chapter.

Chapter 7

In this chapter energy transfer and material properties of Y_2O_3: Eu^{3+}:Ho^{3+} nanophosphors synthesized by sol- combustion method were discussed in detail.

Chapter 8

The chapter presents the temperature dependence of structural and luminescence properties of Eu^{3+} -doped Y_2O_3 red- emitting phosphor thin films by Pulsed Laser Deposition.

Chapter 9.

In this chapter, the influence of different species of gases on the luminescent and structural properties of pulsed laser ablated $Y_2O_2S:Eu^{3+}$ thin films were discussed in detail.

Chapter 10

This chapter gives general concluding remarks on the overall study and suggestions for possible future studies.

References

[1] G. Blasse, B.C. Grabmaier, Luminescence Material, Springer-Verlag, New York, (1994)

[2] S. Shionoya, W.M. Yen, Phosphor Handbook, CRC Press, (1998)

[3] K.F. Braun, Ann. Phys. Chem., 60 (1987) 552

[4] H. Nalwa and L.S. Rohwer, Eds. Handbook of Luminescence, Display, (1999)

[5] Materials and Devices, Vols. 1-3, American Scientific Pub., Stevenson Ranch, CA, (2003)

[6] T. Peng, H Yang, X. Pu, B. Hu, Z. Jiang, C. Yan, Materials Letters 58 (2004) 352 -356

[7] D. Wang, Y. Li, Y. Xiong, Q. Yin, Journal of the Electrochemical Society, 152 (1) (2005) H1-H14

[8] X. Luo, W. Cao, Z. Xiao, Journal of Alloys and Compounds 416 (2006) 250-255

[9] S.K Tokuno, S. Komuro, H. Aizawa, T. Katsumata, T. Morikawa, CISE – ICASE, International Joint Conference, Bexco, Busan, Korea, 18 – 21 Oct, 2006

[10] C. Chang, D. Mao, Thin Solid Films 460 (2004) 48-52

[11] H. Chander, *Mat. Sci. and Eng.*, R49: 113, (2005).

[12] A.M, Srivastava. C.R, Ronda, *Luminescence from Theory to Applications.* Ronda, C. (Ed.), Wiley-VCH, Germany, Chap. 4, (2008).

[13] U, Vater. G, Kunzler. W, Tews. *J. Fluores.*, **4:** 79, (1994).

[14] C.H, Seager. D.R, Tallant. *J. Appl. Physics.*, **87:** 4264, (2000).

Chapter 2

Theory

2.1 An overview of phosphors

Luminescence can be defined as a process by which chemical substances/materials emit photons during an electron transition from the excited to the ground state. The materials can be excited by irradiating them with high energy electrons or photons. Accordingly, the luminescence resulting from excitation by high energy electrons is called cathodoluminescence and that from the excitation by high energy photons is called photoluminescence. The class of materials which emit characteristic luminescence are called phosphors. Phosphors consist of a host material which constitutes the bulk and intentional impurities introduced to the host. The characteristic luminescence properties are obtained either directly from the host or activators/dopants introduced intentionally to the host material. An activator is an impurity ion which when incorporated into the host lattice gives rise to a centre which can be excited to luminesce. If more than one activator is used, they are called co-activators or co-dopants. One activator (sensitizer) tends to absorb energy from the primary excitation and transfer to the other activator to enhance its luminescent intensity [1]. Luminescence in solids, i.e. inorganic insulators and semiconductors, is classified in terms of the nature of the electronic transitions producing it. It can either be intrinsic or extrinsic. In the intrinsic process, the luminescence results from the inherent defects present in the crystal structure [2]. This type of luminescence does not involve impurity atoms. Extrinsic photoluminescence on the other hand, results from the intentionally incorporated impurities in the crystal structure [3]. This type can be divided into two categories; namely localized and delocalized luminescence. In the localized luminescence excitation and emission processes are confined to a localized luminescence center, whereas in the delocalized luminescence the electrons and holes participate in the luminescence process (free electron in the conduction band and free holes in the valence band) [4]. Luminescence processes can be divided into two main categories, namely fluorescence and phosphorescence based on the time the excited electrons takes to return to their ground states after the excitation has been stopped.

2.2 Fluorescence

Fluorescence is the process in which emission of photons stops immediately when excitation is cut off. It is the process in which the excited electrons return to the ground state in a time not greater than 10-6 sec, the resulting emissions is described as fluorescence [5]. In fluorescence there are no traps but many luminescent centres.

2.3 Phosphorescence

Phosphorescence occurs when the recombination of the photo-generated electrons and holes is significantly delayed in a phosphor. If one of the excited states of a luminescent center is a quasistable state (i.e., an excited state with very long life time) a percentage of the centers will be stabilized in that state during excitation. Excited electrons and holes in the conduction and valence bands of a phosphor can often be captured by impurity centers or crystal defects before they reach emitting centers. When the probability for the electron (hole) captured by an impurity or defect center to recombine with a hole (electron) or to be reactivated into the conduction band (valence band) is negligibly small, the center or defect is called a trap [6]. The decay time of phosphorescence due to traps can be as long as several hours and is often accompanied by the photoconductive phenomena [6].

2.4 Properties and Applications of Nanomaterials

2.4.1 Some Properties of Nanomaterials

Nanomaterials are materials with particle sizes less than one micrometer, usually less than 100 nm. These small particle sizes impart different physical and chemical properties compared to the bulk forms. Different phases are also found in some nanocrystalline materials. For example, bulk Er_2O_3 exists in two hexagonal phases, but its nanocrystalline Er_2O_3 exhibits two phases (fcc cubic and monoclinic) that are not found in the bulk.

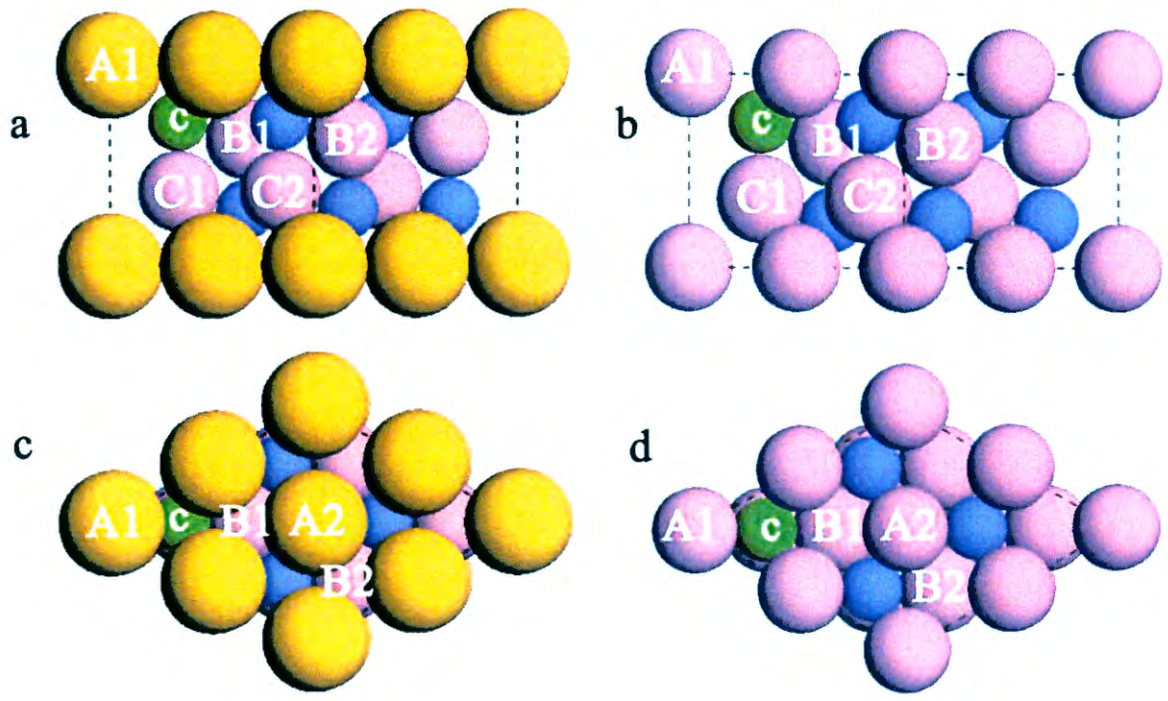

Fig. 2.1. Atomic representations of La_2O_2S along the a) <110> and c) <001> directions. Six possible anion vacancies are noted (i.e. A1, A2, B1, B2, C1, C2, with uppercase letter indicating the corresponding anion layer). Atomic representations of La_2O_3 along the b) <110> and d) <001> directions.

A well-known property of nanomaterials is that their surface areas are tremendously increased. Their surface-to-volume ratios are very high, so that most of the molecules/atoms are on the surface or at the grain boundaries. Since surface molecules/atoms don't have any force above the particle surface to balance the attractive force from inside the particle, they are in high energy states. In addition, molecules/atoms at the grain boundaries are in highly distorted lattice structures, and forces exerted on a molecule/atom from surrounding species are not balanced, so molecules/atoms at the grain boundaries are also in high energy states. Therefore, the surface energy of a nanomaterial is very high. The large surface area and number of grain boundaries of nanomaterials provides a high concentration of low-energy diffusion paths. Therefore, nanomaterials have higher self-diffusivity and solute diffusivity than the bulk forms. Nanoparticles have electrical and optical properties that are not observed in the bulk. These "quantum-size" effects appear when particle sizes are comparable with or smaller than some characteristic lengths, such as a phonon wavelength, an electron de Broglie wavelength, or an effective Bohr radius around impurity centres. The energy states of doped

impurity atoms are strongly modulated in nanocrystallites, whose sizes are smaller than the Bohr radius of the impurity atoms. This phenomenon is called quantum confinement. Quantum confinement effect changes overlaps of the wave functions of the impurity atoms with those of host atoms, leading to more efficient interactions between impurity atoms and the host atoms. For example, luminescent properties of activators in nanocrystalline phosphors are enhanced. In nanocrystalline Y_2O_3: Tb, the luminescent efficiency increases proportionally with square of decreasing particle size (10 nm to 4 nm), which is predicted accurately by a quantum confinement model. Decrease in particle sizes causes localization of exciton wave-functions near the impurities (activators), which results in higher overlaps of the exciton wave-functions with those of the impurities, so energy transfer rate from the excitons to the impurities is higher. Therefore, non-radioactive decay rate is relatively reduced, and luminescent efficiency increases. However, if there are many extinguishing defects at the grain boundaries, the luminescent efficiency of a nanocrystalline phosphor decreases. Controlling grain-boundary defects is an important factor to further improve efficiencies of nanocrystalline phosphors.

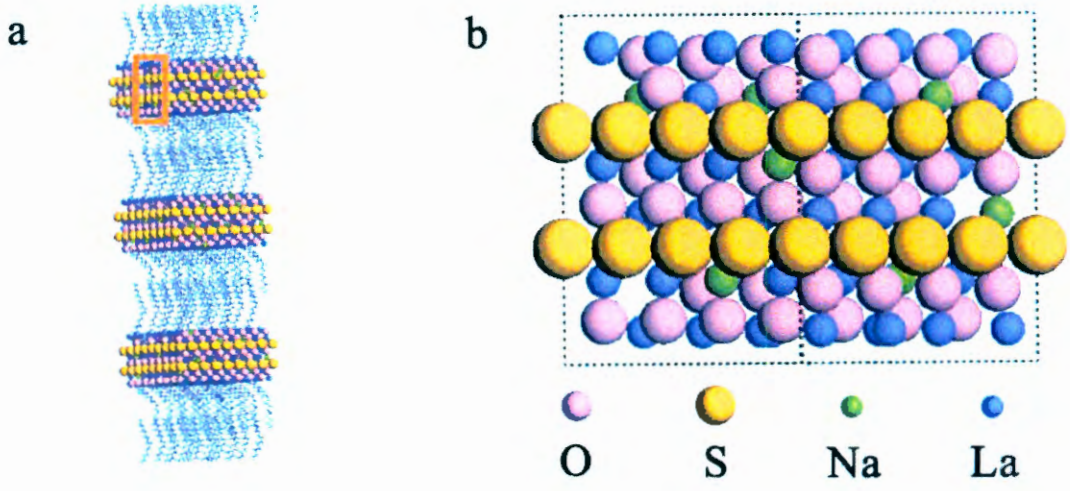

Fig. 2.2. Schematic illustration for self-assembled Na-doped La2O2S nanoplates with OA as capping agents; the orange box highlighted in a) is enlarged in b), which shows the thickness of one nanoplate, indicating the three layers of primitive cells along *c*-axis with La3+ as ending ions on both sides of the nanoplates.

Nanocrystalline monoclinic Y_2O_3: Eu^{3+} prepared by laser ablation method has a longer $^5D_0 \rightarrow {}^7F_2$ transition lifetime than that of the bulk. In addition, line widths in the excitation spectra increase with decreasing particle sizes. This phenomenon has been attributed to

inhomogeneous broadening from lattice distortion. A blue shift in the emission spectra of nanocrystalline $Y_2O_3:Eu^{3+}$ was also observed. Phonons of wavelengths greater than the particle sizes cannot propagate in nanocrystalline materials, so phonon distributions (density-of-states) in nanocrystalline materials change greatly from the bulk materials (the phonon-confinement effect). Due to this effect, as particle sizes become smaller, nanocrystalline Si becomes more emissive. It is suggested that the emission centers in porous Si are actually nanocrystallites of Si. Because of their novel properties due to the quantum-size effects, nanocrystallites of semiconductors are often called quantum dots. The phonon-confinement effect is also observed in Raman spectra of nanocrystalline Y_2O_3 and TiO_2. As the particle size decreases from 40 nm to 7 nm, the characteristic Raman lines of nanocrystalline Y_2O_3 shift to lower frequencies, accompanied by significant broadening. The term super-plasticity is used to describe the ability of a material to exhibit high tensile ductility (elongation) without significant necking. If treated at high homologous testing temperatures, conventionally brittle polycrystalline ceramic materials of average grain sizes smaller than 10 nm, such as Y_2O_3-stabilized ZrO_2, exhibit super-plasticity (elongation > 100%). Decreasing particle sizes further into the nanometer range will not only increase the overall ductility of a material prior to failure, but also decrease the super-plasticity-appearance temperature of the material. Room-temperature super-plasticity is observed in nanocrystalline TiO_2 (rutile). The origin of super-plasticity is grain-boundary sliding with some true sliding contribution accommodated by matter transportation, grain-boundary migration, grain rotation, and diffusion or dislocation motion. Hardness and fracture toughness of a bulk ceramic material increase with increasing sintering temperature. However, same hardness and fracture toughness can be achieved by the nanocrystalline form, such as nanocrystalline TiO_2, sintered at much lower temperatures. This observation indicates that nanocrystalline compacts densify much more rapidly than polycrystalline compacts.

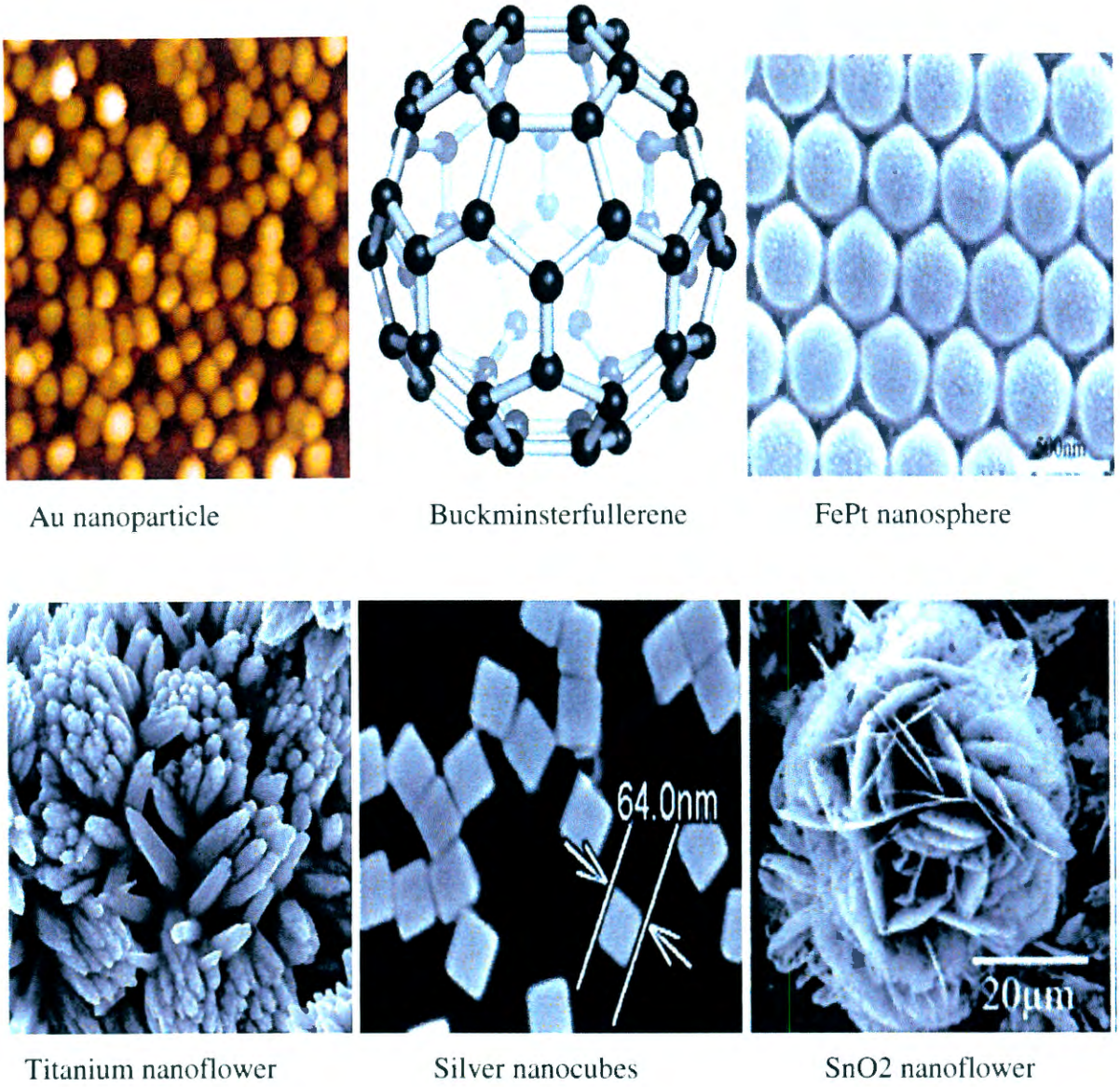

Fig. 2.3. Nanomaterials with a variety of morphologies

2.4.2 Nanomaterial - synthesis and processing

Nanomaterials deal with very fine structures: a nanometer is a billionth of a meter. This indeed allows us to think in both the 'bottom up' or the 'top down' approaches (Fig.2.4) to synthesize nanomaterials, i.e. either to assemble atoms together or to dis-assemble (break, or dissociate) bulk solids into finer pieces until they are constituted of only a few atoms. This domain is a pure example of interdisciplinary work encompassing physics, chemistry, and engineering upto medicine.

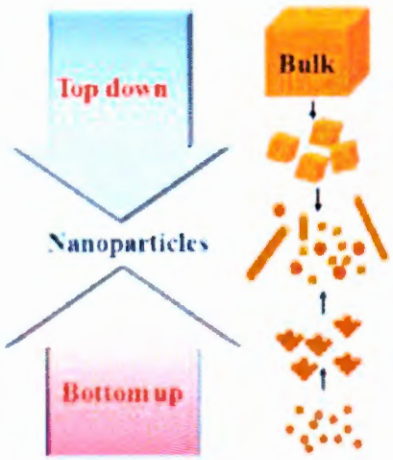

Fig. 2.4. Schematic illustration of the preparative methods of nanoparticles

2.4.3 Applications of Nanomaterials

Because of the novel properties of nanomaterials compared to their bulk forms, they are promising candidates for many advanced technical applications. Nanomaterials inherently have a very high surface-to-volume ratio. Therefore, nanometer-sized catalyst supports, or nanometer-sized catalysts have greatly improved efficiencies. Nanocrystallites of optically active materials (such as Cr: Mg_2SiO_4, Cr: $CaMgSi_2O_6$), whose single crystals are difficult to be grown and are sensitive to their environment, can be embedded in transparent host materials (typically a polymer) to form optical composites. The optical composites have the properties of nanocrystallites and the processability of the polymer hosts. Nanoparticles of magnetic materials exhibit greatly improved magnetic properties and much smaller particle sizes, which find many potential applications in magnetic recording, magnetic refrigeration, and ferrofluids. Nanometer-sized semiconductor clusters are promising materials to prepare devices for efficient conversion of light into electricity (for example, ruthenium polypyridyl sensitizers anchored to porous colloidal TiO_2 films), or electricity into light (for example, nanocrystalline Si). Nanocrystallites of semiconductor materials are considered as quantum dots due to quantum confinement effects, and doped quantum dots are candidates for advanced displays (High Definition TV, Field Emission Display, Plasma Display and Electroluminescent Display), ultra-fast sensors, and lasers. Super-plasticity of nanometer-sized ceramic materials creates a new processing technology for ceramics, the super-plastic forming technology. Superior hardness and fracture toughness of some nanomaterials make them ideal materials for cutting tools. The mechanical properties of nanocrystalline ceramics

lead them to be called "ceramic steel". Commercial realization of ceramic engines also depends on the development of such nanocrystalline ceramics.

2.4.4 Applications of Nanometer-sized Y_2O_3: Eu^{3+}

Y_2O_3 is one of the most important host materials for phosphors, scintillators, lasers, and fiber-optic communications. Eu-doped Y_2O_3 is an important red-emitting phosphor, and Tbdoped Y_2O_3 is a green-emitting phosphor. Because of the quantum-size effects, luminescent properties of nanocrystalline phosphors are different from their bulk forms, which may greatly improve their performance and extend their applications. Due to a maximum field gradient before charge leaking, the maximum voltage (approximately 1 kV) that can be applied on flat panel display devices (FED, EL, and PD) is much smaller than that on normal display devices (approximately 5 kV). As nanocrystalline phosphors generally have higher efficiencies, lower voltages are adequate to achieve a same efficiency. Therefore, nanocrystalline phosphors are ideal candidates for flat panel displays. HDTV requires phosphors of very small particle size, narrow size distribution, uniform shape, and high intensity without light saturation. Nanocrystalline phosphors have very fast luminescent recombination rate, so the saturation can be eliminated, while their nanometer-scale sizes fulfill the other requirements of HDTV. SiO_2 is the gate oxide/dielectric material in metal oxide semiconductors (MOS) in verylarge- scale-integrated (VLSI) circuits. By decreasing the thickness of the SiO_2 layer, increases in charge-storage capacity and trans-conductance are achieved. However, the smallest practical thickness of the SiO_2-gated dielectric layer is being approached in modern silicon devices. Further improvement needs materials of higher dielectric constants as the gate material. Y_2O_3 thin films are excellent substitute gate materials. They can be made very thin (25 nm), and the dielectric constant is approximately four times higher than that of SiO_2. In addition, they have lower leakage current for a given gate voltage, and higher breakdown strength. Y_2O_3 is an important additive in many structural and functional ceramics. ZrO_2 is valued for strength and toughness in industrial ceramic applications. Y_2O_3-stabilized ZrO_2 avoids the destructive phase transformations (volume change during phase transformation causes material cracking) from monoclinic to tetragonal and further to cubic at elevated temperatures. Y_2O_3- stabilized ZrO_2 is used in high-temperature refractory, heating cells in oxidation atmospheres, ceramic engines. Y_2O_3-stabilized ZrO_2 also has high oxygen-ion conductivity at elevated temperatures, which makes it suitable for use in oxygen sensors and oxygen pumps at elevated temperatures. Similarly,

Y_2O_3 is also used to stabilize HfO_2, which is a promising ultrarefractory ceramic material for nuclear applications (control rods and neutron shielding). Y_2O_3- doped ThO_2 is also used in oxygen sensors. Addition of Y_2O_3 nanoparticles influences density and elastic moduli of $Si3N_4$ ceramics, and improves their sinterability. Nanocrystalline Y_2O_3 additives also help to prepare AlN ceramics of higher density and thermal conductivity. Nanocrystalline Y_2O_3 is also used in high-density magnetic recording. To achieve highdensity magnetic recording, the recording medium must have high coercivity (>3000 Oe) with thin or no overcoat. Particle sizes of the medium must be very small (< 10 nm), but magnetically isolated to minimize the transition noise. Y_2O_3-doping effectively reduces particle sizes in thin films of nanocrystalline $BaFe_{12}O_{19}$ magnetic material from several hundreds of nanometer to approximately 50 nm, while keeping the high coercivity of the material. Y_2O_3, Al_2O_3, MgO, and ZrO_2 are novel transparent ceramic materials that can be used in severe environments instead of traditional glasses. Y_2O_3 has a higher melting point and better chemical stability, which makes it suitable for heat-resistant transparent windows and walls for high-pressure sodium electric discharge light bulbs. There are two methods to prepare transparent Y_2O_3 material. One is the traditional sintering method, and the other is the hotpressing of Y_2O_3 nanoparticles in vacuum. Due to the improved sinterability of nanocrystalline Y_2O_3, the hot-pressing method has the advantage of much lower operation temperature (1300 ^{0}C) and much lower operation pressure (44 MPa) than those of the sintering method (2300 ^{0}C and 980 MPa, respectively).

2.4.5. Mechanism of the Persistent Luminescence

Although the overall mechanism of the persistent luminescence of $CAl_2O_4:Eu^{2+}$ is now quite well agreed on [7, 8-10], the details involved are largely unknown. Long persistent luminescence of CAl_2O_4: Eu^{2+} is thought to have originated from alkaline earth vacancies [11]. The formation of both electron and hole trapping and subsequent slow thermal excitation of the traps followed by emission from Eu^{2+} ions (Figure 2.5) are being taken to be the root causes of the persistent luminescence[12-14, 15 ,16]. According to this model the trapped electrons and holes act as pairs and luminescence can take place as a result of indirect centre to centre transitions. In other similar systems (e.g. photo- stimulated materials [17] the main charge carriers were observed to be electrons and ions but the effect of holes has gained more importance in the persistent luminescence materials. However, with the addition

of some trivalent RE^{3+} ions the persistent luminescence lifetime and intensity can be improved further [18]

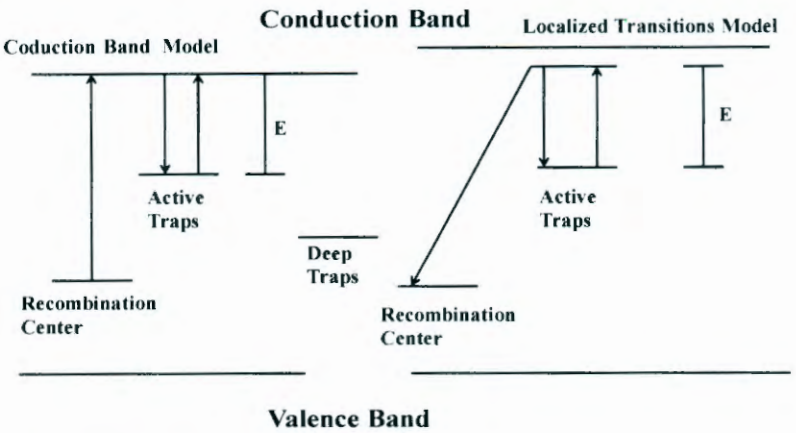

Figure 2.5: Model showing Persistent Luminescence Mechanism.

The knowledge of the underlying mechanism of long persistence is very necessary and would significantly assist in the search for persistent luminescence materials. In the present study, a detailed investigation was carried out on the Eu^{2+} doped alkaline earth aluminates ($CAl_2O_4:Eu^{2+}$). Especially, the role of co-doping with different trivalent rare earth [RE^{3+}] ions (Dy^{3+} and Nd^{3+}) in the enhancement of the afterglow of $CAl_2O_4:Eu^{2+}$, RE^{3+} was studied by several spectroscopic methods viz Photoluminescence (PL) and Thermoluminescence (TL).

2.4.6. The Luminescent Center

Despite the fact that considerable amount of study on the aspects of luminescence could be carried out by taking into account a simple model for the centre it is quite hard to find out what is exactly going on inside the centre. Several theories or approaches have to be put to trial depending on the complexity of the centre. One such famous approach is the configurational coordinate model. This approach assumes that the luminescent centre has some equilibrium position in the crystal lattice and that a change in energy occurs due to some displacement from this position. The interaction of the centre with the crystal lattice in terms of its electronic state and the vibrations of the lattice can be seen to be as a function of the position of the nuclei and the model can be employed to easily explain such effects as the Stokes shift between absorption and emission. But owing to the fact that electronic transitions

of the centre are coupled to the movements of the lattice around the centre the simple model is not generally acceptable.

To differentiate the electronic state from vibrational state of the luminescent centre the Born-Oppenheimer approximation is used but it has been shown by Fowler and Dexter (1962) that the potential energy curves in the configurational coordinate diagram are also a function of the electronic state.

In condensed systems the Einstein relations are not valid as such and the complex relaxations which occur after an excitation do not simplify the scenario because the electronic states in emission are likely not to be the same with those in absorption. Furthermore, because of the Jahn-Teller effect, which tends to remove degeneracy of an excited state by creating asymmetry in the centre, there may be a separation in the excited state. There are also transition probabilities for the absorption and the emission. One of the most important points is that the matrix element for the absorption transition may be different from that for the emission transition. A lot of interest in luminescence now needs to be taken in quantitative studies of phonon-photon interactions (preferably at very low temperatures) [19].

2.4.7. Phase Transformation

In spite of a great deal of research work on Y_2O_2S: Eu^{3+} phosphors, the phase transformations of Eu^{3+} doped lanthanides compounds and their effects on luminescent properties have been rarely reported until now.

2.4.8. Effect of Lattice Defects on Persistent Luminescence

Generally, when the mean particle size of phosphors is smaller than 1-2 μm, there is a drop in their luminescence efficiency. This is due to the fact that surface defects become more important with decreasing particle size and an increase in the surface area. This can often lead to the reduction of the emission intensity [20-24]. The presence of any kind of lattice defect in the host lattice in most cases has been found to greatly reduce the efficiency of luminescence. It also brings about the long afterglow observed in some potentially efficient luminescent materials. These defects are usually considered to be disadvantageous as far as the properties of a phosphor are concerned when the practical applications are considered [25]. Consequently, the luminescence applications based on phosphors with lattice defects are rare.

2.4.9. Energy Transport and Storage in Luminescent solids

The dominant role played in luminescence mechanisms by the transport of energy was pointed out by Broser in an invited paper [26]. In condensed systems the interatomic distance is considerably smaller than in gases and the probability of interaction between a luminescent centre and distant atoms are much greater. Energy transfer may take place by free charge carriers, excitons, quantum mechanical resonance, photons or phonons, and may be studied by direct measurements of such properties as velocity, lifetime and carrier range, or by indirect measurements. Two important parameters are lifetime and diffusion coefficient. Great advances have been made in the study of energy transport by direct mechanisms in phosphors during the last ten years. New experiments have been devised (particularly for excitons) to measure transport parameters and older experiments have been perfected. Nevertheless in the field of energy transport in phosphors there are ample problems remaining to be solved in the next decade.

Storage of energy in phosphors is still being studied extensively by thermal ejection measurements on trapped charge carriers [27-30]. Interpretation of glow curves in terms of traps or metastable states is obviously more difficult in organic compounds than inorganic compounds. Even in inorganic compounds it is not likely that the method gives the true or complete distribution of trapping states in a phosphor.

The conventional method of filling the traps at low temperature is by illuminating the specimen, but if the traps are filled by space-charge injection of charge using a high field across the specimen it is possible to remove any ambiguity as to the sign of the charge carrier responsible for the peak [31]. If a blocking electrode is used as the cathode during the heating-up process it is also possible to distinguish between surface and volume states. The use of high fields causes the carrier transit time to be reduced, the probability of re-trapping to be reduced, and the kinetics to be more like those of the monomolecular theoretical model. For the investigation of trap spectra with a continuous energy distribution the fractionated glow technique is proving to be of value [32].

2.5.1: Emission and Excitation Mechanisms of Phosphors

Basic concepts involved in luminescence will be discussed. We will take a closer look at a number of excitation mechanisms which are involved in generating luminescence and processes which lead to luminescence, taking illustrative examples from luminescent

materials applied in fluorescent lamps and cathode ray tubes. With respect to fluorescent lamps, we will restrict ourselves to discharge lamps based on the low-pressure Hg discharge.

2.5.2: General Considerations – Fluorescent Lamps

On passing a current through an Hg discharge, UV light is generated as a consequence of electronic transitions on the Hg atoms. In low-pressure Hg discharge, the main emission line is located at 254 nm. This light is invisible and harmful; therefore it has to be converted into visible light. This is done by the application of luminescent materials. These materials have to show a strong absorption at 254 nm and have to convert this into visible light very efficiently. In most of the fluorescent lamp phosphors, the optical Luminescence processes leading to luminescence do not involve host lattice states, implying that the energy gap is at least 4.9 eV, this being the energy of a photon with wavelength 254 nm. Therefore, the luminescent materials applied in fluorescent lamps are insulators. The conversion efficiency of luminescent materials is very high: about 90% of the UV photons are absorbed, and also about 90% of the absorbed photons are converted into visible light. This implies that such materials cannot be improved any further in terms of conversion efficiency unless materials can be found that generate more than one visible photon after absorption of a UV photon.
Compact fluorescent lamps have lower light generation efficiency (only 15 %). As the luminescent materials applied are the same or very similar, this must due to the lower discharge efficiency in these devices, which, in turn, is due to the smaller diameter of the lamp envelope and therefore to the increased wall losses: excited Hg atoms reach the ground state on interacting with the lamp wall without generating UV light: energy and momentum can be conserved by interaction of excited species with the wall without generation of light.

2.5.3 General Considerations – Cathode Ray Tubes

Though the importance of cathode ray tubes is rapidly decreasing, we will treat the luminescence mechanism in these materials in view of its historical importance. In addition, the excitation mechanism that comprises excitation with high-energy particles (electrons, X-ray photons, or g-rays) is also operative in phosphors used in scintillators for, e.g., medical applications. Luminescent materials applied in cathode ray tubes in general differ from those applied in fluorescent lamps. Excitation proceeds via the band gap. To achieve high

efficiencies, small values for the band gap are needed, as will be elucidated below. For this reason, quite a few luminescent materials applied in cathode ray tubes are semiconductors.

2.5.4. Emission and Excitation Mechanisms of Phosphors

The luminescence mechanism operating in the blue and green emitting phosphors applied in cathode ray tubes is a beautiful example of luminescence involving defect states in semiconductors. We will therefore also discuss this mechanism in some detail. The maximum energy efficiency of the cathode ray phosphors is relatively low, at most about 25 %, as will be outlined below. Also for these phosphors, the maximum efficiencies have been reached.

2.5.5. Luminescence Mechanisms

Luminescent materials, also called phosphors, are mostly solid inorganic materials consisting of a host lattice, usually intentionally doped with impurities. The impurity concentrations generally are low in view of the fact that at higher concentrations the efficiency of the luminescence process usually decreases (concentration quenching, see below). In addition, most of the phosphors have a white body color. Especially for fluorescent lamps, this is an essential feature to prevent absorption of visible light by the phosphors used. The absorption of energy, which is used to excite the luminescence, takes place by either the host lattice or by intentionally doped impurities. In most cases, the emission takes place on the impurity ions, which, when they also generate the desired emission, are called activator ions. When the activator ions show too weak an absorption, a second kind of impurities can be added (sensitizers), which absorb the energy and subsequently transfer the energy to the activators. This process involves transport of energy through the luminescent materials. Quite frequently, the emission color can be adjusted by choosing the proper impurity ion, without changing the host lattice in which the impurity ions are incorporated. On the other hand, quite a few activator ions show emission spectra with emission at spectral positions which are hardly influenced by their chemical environment. This is especially true for many of the rare-earth ions. Luminescent material containing activator ions (ions showing the desired emission) and sensitizing ions (on which, e.g., UV excitation can take place).

2.5.6. Center Luminescence

In the case of center luminescence, the emission is generated on an optical center, in contradiction to, e.g., emission, which results from optical transitions between host lattice band states or from a transition between two centers. Such an optical center can be an ion or a molecular ion complex. One speaks of characteristic luminescence when, in principle, the emission could also occur on the ion in a vacuum, i.e. when the optical transition involves electronic states of the ion only. Characteristic luminescence can consist of relatively sharp emission bands (spectral width typically a few nm), but also of broad bands, which can have widths exceeding 50 nm in the visible part of the spectrum. Broad emission bands are observed when the character of the chemical bonding in the ground and excited state differs considerably. This goes hand in hand with a change in equilibrium distance between the emitting ion and its immediate chemical environment.

2.5.7. Charge Transfer Luminescence

In the case of charge transfer, the optical transition takes place between different kinds of orbitals or between electronic states of different ions. Such an excitation very strongly changes the charge distribution on the optical center, and consequently the chemical bonding also changes considerably. In these cases, therefore, very broad emission spectra are expected. A very well-known example is $CaWO_4$, used for decades for the detection of X-rays, which shows luminescence originating from the $(WO_4)_2$ groups. A similar compound, also showing blue emission, was used in early generations of fluorescent lamps: $MgWO_4$. The transition involves charge transfer from oxygen ions to empty d-levels of the tungsten ion. In this material no intentional dopant is introduced, and for this reason it is also called self-activated.

2.5.8. Donor Acceptor Pair Luminescence

This luminescence mechanism is found in some semi-conducting materials doped with both donors and acceptors. Emission and Excitation Mechanisms of Phosphors results in luminescence. Electrons that are excited into the conduction band are captured by ionized donors, and the resulting holes in the valence band are captured by ionized acceptors. The emission involves electron transfer between neutral donors and neutral acceptors. The final state (with ionized donors and acceptors) is Coulomb stabilized. Therefore, the spectral

position of the emission generated on a donor-acceptor pair depends on the distance between the donor and the acceptor in a pair: the smaller the distance, the higher the energy of the photon generated.

The energies involved in these processes are:

1. The absorption of energy with the band gap energy.
2. Neutralization of the ionized donor. The Coulomb term originates from the electrostatic interaction between ionized donor and acceptor.
3. Neutralization of the ionized acceptor.
4. The luminescence process.

2.6.1. Mechanisms Underlying Energy Transfer

For energy transfer, the sensitizer ion and the activator ion have to show physical interaction. This energy transfer can find its origin in electrostatic and exchange interaction. In addition, the emission spectrum of the sensitizer ion and the absorption spectrum of the activator ion have to show spectral overlap, for energy conservation reasons.

2.6.2. Cross-relaxation and Energy Transfer

A phenomenon not discussed until now is cross-relaxation. In such a process, which can also be looked upon as energy transfer, the excited ion transfers only part of its energy to another ion. In this case, the energy difference between the $^5D_3$ and $^5D_4$ excited states matches approximately the energy difference between the $^7F_6$ ground state and higher ^7F_J states. As in the energy transfer processes discussed above, the process of cross-relaxation has a low rate. In many host lattices, therefore, at low Eu^{3+} concentration, emission from both the $^5D_0$ and $^5D_2$ excited states is observed (unless the gap between these two states is bridged by phonon emission, for which relatively high-energy phonons are required).

2.6.3. Exchange interaction between sensitizer and activator ion

This mechanism does not require allowed optical transitions. This is the mechanism which is operative in the one-component white fluorescent lamp phosphor $Ca_5(PO_4)_3(F,Cl)$:Sb,Mn, as deduced from an analysis of the decay curve for some Mn^{2+} concentrations [45]. The same study did not reveal evidence for energy transfer between antimony ions, indicating the

necessity of nearest neighbor Sb-Mn interaction, which is a prerequisite for energy transfer via exehange interaction. Please note, in addition, that in view of the large Stokes shift between absorption and emission on the Sb^{3+} ion in this lattice, no energy transfer between the antimony ions is expected. Both for electric dipole – electric quadrupole and exchange interaction, the distance between sensitizer ion and activator ion has to be rather small, not larger than about 1 nm. This requires high activator and/or sensitizer ion concentrations, which is a disadvantage, considering the high costs of these materials.

2.6.4 The Energy does not reach the Luminescent ion

When there is more than one origin of optical absorption at the wavelength at which the excitation takes place, the quantum efficiency can be less than unity, even if the ion showing luminescence has a quantum efficiency of one. This is, e.g., the case if both the luminescent ion and the host lattice show optical absorption at the excitation wavelength, or the energy transfer probability of the host lattice to the luminescent ions is smaller than unity. Comparing the absorption or reflection spectra with the excitation spectra can disentangle the different contributions to the absorption. Degradation of luminescent materials can be due to creation of additional absorption centers in the spectral range where the activators or sensitizers also absorb.

References

[1] J. A. DeLuca, Journal of Chemical Education, **57** (1980) 541.

[2] S. Boggs, D. Krinsley, Application of Cathodoluminescence imaging to the study of sedimentary rocks, Cambridge University Press, England, 2006.

[3] R.D. Blackledge, Forensic analysis on the cutting edge, John Willey & Sons Publications, USA, 2007.

[4] D. R. Vij, Luminescence of Solids , Science, Plenum Press, New York & London, 1998.

[5 J. Ball, A. D. Moore, Essential physics for radiographers, Blackwell Publishing, First edition, Oxford, 1979.

[6] S. Shionoya, W.M. Yen, Phosphors Handbook, CRC Press, USA, 1998.

[7] Z, Li. H, Hahn. R.W, Siegel. Mater. Lett. 6, 342 (1988).

[8] A.W, Adamsom. A.P, Gast. In Physical Chemistry of Surfaces 6th ed., Wiley Interscience, New York, 257 (1997).

[8] H, Gleiter. Progress in Materials Science 33, 223 (1989).

[9] R, Bhargava. Lumin. 72-74, 46 (1997).

[10] E.T, Goldburt. B, Kulkarni. R.N, Bhargava. J, Taylor. M, Libera. *J. Lumin.* 72-74, 190 (1997).

[11] R.N, Bhargava. D, Gallagher. X, Hong. A, Nurmikko. Phys. Rev. Lett. 72, 416 (1994).

[12] T, Hase. T, Kano. E. Nakazawa. H, Yamamoto. Adv. Electronics and Electron Phys. 79, 271 (1990).

[13] D.K, Williams. B, Bihari. B.M, Tissue. J.M, McHale. J. Phys. Chem. *B* 102, 916 (1998).

[9] Q, Li. L, Gao. D.S,Yan. NanoStruct. Mater. 8, 825 (1997).

[14] D, Wolf,; J, Wang,; S. R, Phillpot,: H, Gleiter,: Phys. Rev. Lett. 74, 4686 (1995).

[15] R, Birringer,; U, Herr,; H, Gleiter,: Suppl. Trans. Japan Inst. Metals 27, 43 (1986).

[16] S.M, Prokes, S.: J. Mater. Res. 11, 305 (1996).

[17] C. B, Murray,; C.R, Kagan.; M. G, Bawendi,.: Science 270, 1335 (1995).

[18] C, Bruch,; J. K, Krüger.; H. G, Unruh,; W, Krauss,; B, Zimmermeier,; C, Beck,; R, Hempelmann,: Ber. Bunsenges. Phys. Chem. 101, 1761 (1997).

[19] D, Bersani,; P.P, Lottici, P.; X. Z, Ding,: Appl. Phys. Lett. **72**, 73 (1998).

[20] T. G, Langdon,: Metall. Trans. 13A, 689 (1982).

[21] T. G, Langdon,: Key Eng. Mater. 97-98, 109 (1994).

[22] J, Karch,; R, Birringer,; H, Gleiter,: Nature 330, 556 (1987).

[23] F, Wakai,; N, Kondo,; H, Ogawa,; T, Nagano,; S, Tsurekawa,: Mater. Character. 37, 331 (1996).

[24] R.S, Averback,; H, Hahn,; H.J, Höfler,; J. L,Logas,; T. C, Shen,: Mater. Res. Soc. Symp. 153, 3 (1989).

[25] T, Masui,; K, Fujiwara,; K, Machida,; G, Adachi,; T, Sakata,; H, Mori,: Chem. Mater. 9, 2197 (1997).

[26] D. B, Barber,; C.R, Pollock,; L.L, Beecroft,; C.K, Ober,.: *Opt. Lett.* 22, 1247 (1997).

[27] R, Dagani,: Chem. & Eng. News 70, 18 (1992).

[28] R, Argazzi,; C.A, Bignozzi,: J. Am. Chem. Soc. 117, 11815 (1995).

[29] R.P, Chin,; Y.R, Shen,; V, Petrova-Koch,: Science 270, 776 (1995).

[30] R.N, Bhargava,: J. Lumin. 70, 85 (1996).

[31] J, Wittenauer,: In Plastic Deformation of Ceramics, R. C. Bradt, C. A. Brookes, and J. L. Routbort (eds.), Plenum, New York, 321 (1995).

[32] G, Skandan,; B.H, Kear,: Mater. Sci. Forum 243-245, 217 (1997).

[33] K. H Jack,: High Technology Ceramics, Past, Present, and Future; Ceramics and Civilization 3, W. D. Kingery (ed.), 259 (1986).

[34] R.W, Cahn,: Nature 332, 761 (1988).

[35] E.T, Goldburt,; B, Kulkarni,; R. N, Bhargava,; J, Taylor,; M, Libera,: Mater. Res. Symp. Proc. 424, 441 (1997).

[36] J.M.P.J, Verstegen,; J. L, Sommerdijk, ; J.G. Verriet,; (1973) J. Lumin., 6, 425.

[37] T.F, Soules,; R.L, Bateman,; R. L, Hewes,; E. R, Kreidler: (1973) Phys. Rev. B7, 1657.

[38] D.J, Robbins, (1980) J. Electrochem. Soc., 127, 2694.

[39] R. H, Bartram,; A. Lempicki, (1996) J. Lumin., 69, 225.

[40] A, Meijerink,; J, Nuyten,; G, Blasse. (1989) J. Lum., 44, 19.

[41] G.S, Ofelt. (1962) J. Chem. Phys., 37, 511.

[42] B.R, Judd. (1962) Phys. Rev., 127, 750.

[43] K.J.B.M, Nieuwesteeg. (1989) Philips J. Res., 44, 383.

[44] C.R, Ronda. Frontiers in Optical Spectroscopy, NATO Science Series II Mathematics, Physics, Chemistry, (eds B. DiBartolo and O. Forte), Kluwer Academic Publishers, Dordrecht, Boston, London, 168, 359–392.

[45] C.R, Ronda. Advances in Energy Transfer Processes, World Scientific, the Science and Culture Series (eds. B. DiBartolo and X. Chen), World Scientific, New Jersey, London, Singapore, Hong Kong, 377–408.

Chapter 3

3. Experimental Techniques

3.1. Introduction

This chapter gives a brief account of the experimental techniques used to synthesize and characterize the phosphor. X-ray diffraction (XRD), Scanning electron microscopy (SEM) and X-ray photoelectron spectroscopy (XPS) were used to investigate the crystalline structure, particle morphology and elemental composition of the phosphor respectively. Atomic force microscopy (AFM) was used to analysis the surface roughness of the phosphors. Fourier transform infrared spectroscopy (FTIR) was used to identify and/or verify compounds. A 325 nm He-Cd laser fitted with a SPEX 1870 0.5m spectrometer and a photomultiplier detector was used to collect photoluminescence data in air at room temperature. A Cary Eclipse fluorescence spectrometer fitted with a monochromatic xenon lamp was also used to investigate the photoluminescence (excitation and emission) properties and decay characteristics of the phosphors. The powders investigated in this research were prepared by sol-combustion method, whilst the thin films were deposited by pulsed laser deposition. Theory on the PLD technique, XRD, SEM, PL, AFM, FTIR, TL and XPS can be found in this chapter as well as the experimental procedure.

3.2. Synthesis and deposition technique

The growth of nanoscience and nanotechnology in the last decade has been made possible by the success in the synthesis of nanomaterials. The synthesis of the nanomaterials includes control of size, shape and structure of the materials. Over the past few years, nanoparticles (powders) of ceramic materials have been produced on large scales by employing physical and chemical methods. The considerable scientific progress in preparation of nanomaterials such as ceramics and semiconductors has been made possible by synthesis techniques such as co-precipitation, sol-gel, combustion method, sol-combustion etc [1]. In this study, sol-combustion method was used to synthesize the lanthanides oxides and oxysulfides phosphors doped with rare earth ions.

depending on the desired measurements. The X-ray diffractometer fall broadly into two classes: single crystal and powder. The powder diffractometer is routinely used for phase identification and quantitative phase analysis [7]. X-ray diffractometer consist of three basic elements: an X-ray tube, a sample holder, and an X-ray detector. The X-rays are produced in a cathode ray tube by heating a filament to produce electrons. When the voltage is applied, the electrons will accelerate towards the target material. When electrons have sufficient energy to dislodge the inner shell electrons of the target material, characteristic X-ray spectra will be produced. These X–ray spectra consist of several components and the most common are Kα and Kβ. The target materials that are usually used are Cu, Fe, Mo and Cr. Each of these has specific characteristic wavelengths [8]. In order to generate the required monochromatic X-rays needed for diffraction, a filter such as a foil or crystal monochrometers is usually used. Copper is the most commonly used target material for single-crystal diffraction, with Cu Kα radiation = 1.5418Å. The resulting X-rays are collimated and directed onto the sample. As the sample and detector are rotated, the intensity of the reflected X-rays is recorded. When the geometry of the incident X-rays impinging on the sample satisfies the Bragg Equation, constructive interference occurs and characteristic diffraction peaks of the sample will be observed [9]. The X-ray diffractometer Bruker XRD D8 Advance shown on Figure 3.1, from University of the Free State, Department of Physics, Bloemfontein Campus was used to analyze the samples in this study.

3.3.2. Scanning electron microscopy (SEM)

Scanning electron microscopy is a technique in which a beam of finely focused electrons is used to examine materials on a nanometer to micrometer scale. It is often used as the analytical instrument of choice when the light microscope no longer provides adequate resolution. The SEM consists of an electron optical column mounted on a vacuum chamber with electron gun placed on top of the column, as illustrated in Figure 3.1. The electron gun, which consists of a tungsten or LaB_6 filament or a field emission electron gun is used to generate electrons, when the applied current causes resistance heating which generates the electrons [10]. When a high energy electron beam impinges on the sample, a variety of electrons and/or x-rays will be generated. Depending on the nature of the sample, these can include secondary electrons (electrons from the sample itself), backscattered electrons (beam electrons from the filament that bounce off nuclei of atoms in the sample) and X-rays.

Figure 3.1: Bruker D8 Advance model x-ray diffractometer

This technique can be used to investigate the topography, morphology, and elemental composition of materials (if coupled with an EDS) on the micrometer to nanometer scale. The secondary electrons can be used to investigate the image and the topographic features of solid samples. The SEM coupled with EDS, is used during the analysis of the characteristic x-rays emitted as a result of electronic transitions between the inner core levels to provide a quantitative and qualitative elemental composition of the sample [11].

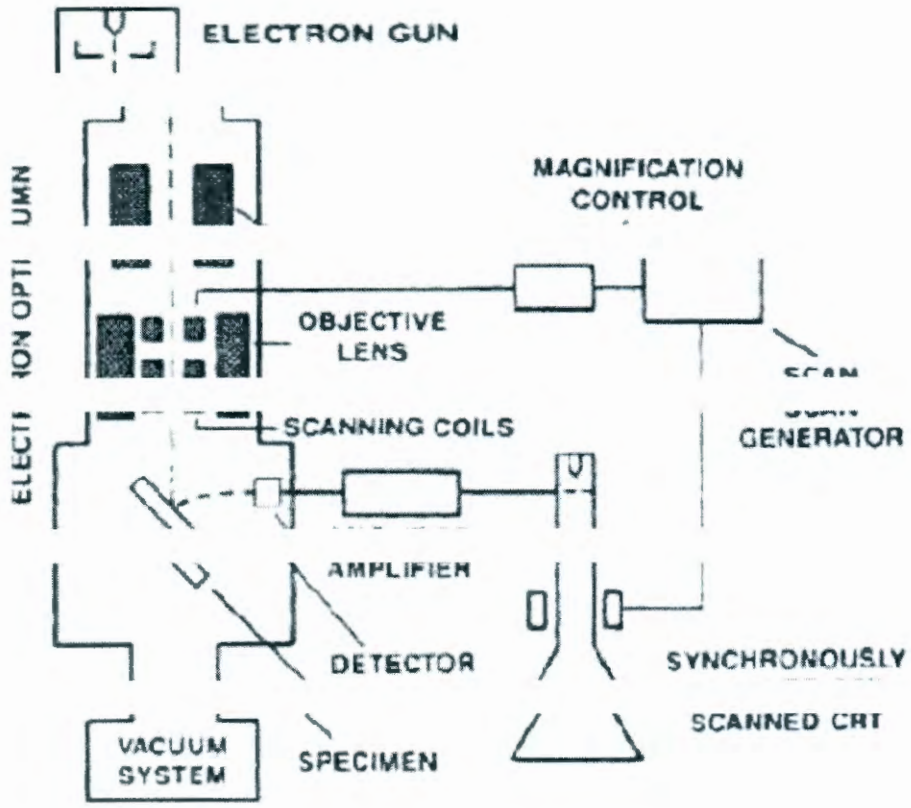

Figure 3.2: Schematic representation of a SEM

The analysis of elemental compositions can be performed by measuring the energy and intensity distribution of the x-ray signals generated by a focused electron beam. Due to a well-defined nature of the various atomic energy levels, it is clear that the energies and associated wavelengths of the set of x-rays will have characteristic values for each of the atomic species present in a sample [12]. The morphologies and elemental compositions of the phosphor powders were obtained by using a Shimadzu Superscan SSX-550 SEM coupled with an EDAX EDS from the Center of Microscopy at the University of the Free State as shown in Figure 3.3.

3.3.3. Photoluminescence spectroscopy (Helium cadmium laser)

Photoluminescence (PL) is a powerful and a relatively simple method, extensively used as characterization technique of semiconductor physics for a number of reasons [13, 14].

- It is non-destructive because it is based on pure optical processes.
- No sample preparation is required.

- Highly sensitive.
- Detailed information on the electronic structure in the semiconductor can be deduced from the experiments.

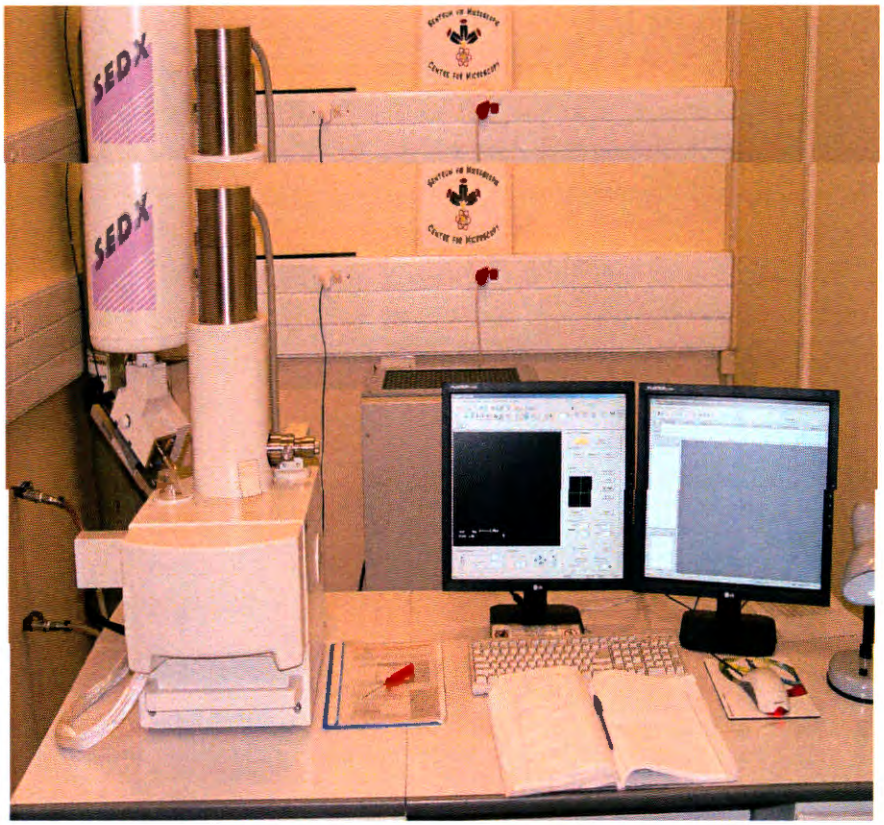

Figure 3.3: Shimadzu Superscan SSX-550 model Scanning Electron Microscope

Information that could be deduced from a PL study includes the size of the band gap, impurity levels, interface, and surface properties as well as density of states and exocitonic states. Basically in PL measurements, a semiconductor sample is optically excited by an excitation source such as a laser which produces photons having energies larger than the band gap of the semiconductor. The incident photons are absorbed under creation of electron-hole pairs in the sample. After a short time the electrons eventually recombine with the holes, to emit photons, and light or luminescence will emerge from the sample. The energy of the emitted photons reflects the energy carrier in the sample. The emitted luminescence is collected, and intensity is recorded as a function of the emitted photon energy, to produce a PL spectrum. In a PL measurement, the excitation energy is kept fixed, while the detection

energy is scanned. The energy of emitted photon is characteristic for radiative recombination process.

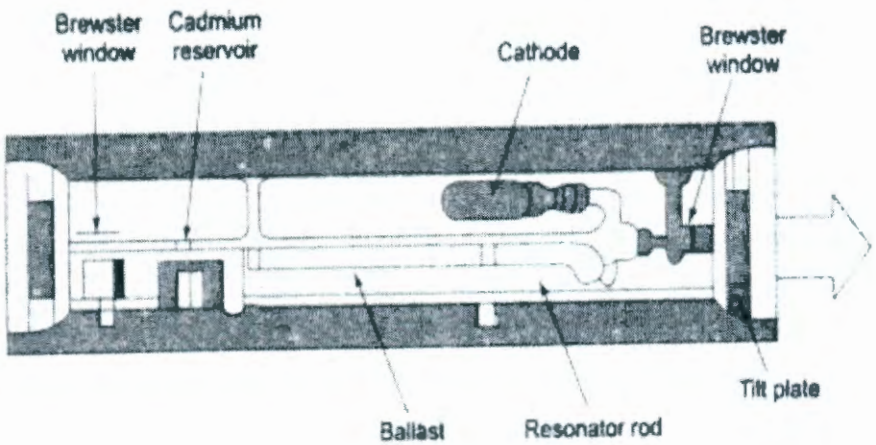

Figure 3.4: The cavity structure of He-Cd Laser

PL technique is particularly helpful in the analysis of discrete defect and impurity states. To gain more knowledge about the electronic structure, magnetic and electric fields can be applied in a controlled manner. Moreover external forces can be used in PL investigations, e.g. the strain by exposing the material to mechanical pressure. Since PL relies on radiative recombination, so it is very difficult for the investigation of non-radiative processes needs indirect methods, and the material having poor quality are hard to characterize through PL.

3.3.4. Radiative recombination mechanisms observed in PL

In semiconductors, the luminescence can be achieved by several radiative transitions between the conduction band and valence band, exciton, donor and acceptor levels, as shown in Figure 3.6. Upon excitation at energy above the bang gap, free electrons are created in the conduction band together with the free holes in the valance bond. These carriers will energetically relax down the band edge. Due to mutual coulomb interaction, electron-hole pair is formed. This electron-hole is usually called a free exciton (FE). Its energy is slightly smaller than the bang gap energy. This energy difference is the binding energy of the free exciton. A neutral donor (acceptor) will give rise to an attractive potential, a free exciton might be captured at the acceptor (donor). A bound exciton (BE) is formed.

Figure 3.5: Cary Eclipse Florescence Spectrophotometer

3.3.4. Radiative recombination mechanisms observed in PL

In semiconductors, the luminescence can be achieved by several radiative transitions between the conduction band and valence band, exciton, donor and acceptor levels, as shown in Figure 3.6. Upon excitation at energy above the bang gap, free electrons are created in the conduction band together with the free holes in the valance bond. These carriers will energetically relax down the band edge. Due to mutual coulomb interaction, electron-hole pair is formed. This electron-hole is usually called a free exciton (FE). Its energy is slightly smaller than the bang gap energy. This energy difference is the binding energy of the free exciton. A neutral donor (acceptor) will give rise to an attractive potential, a free exciton might be captured at the acceptor (donor). A bound exciton (BE) is formed.

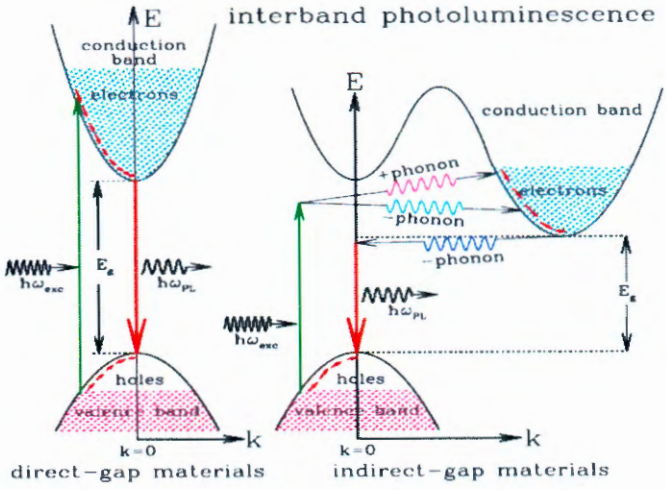

Figure 3.6(a): Schematic illustration of common recombination processes

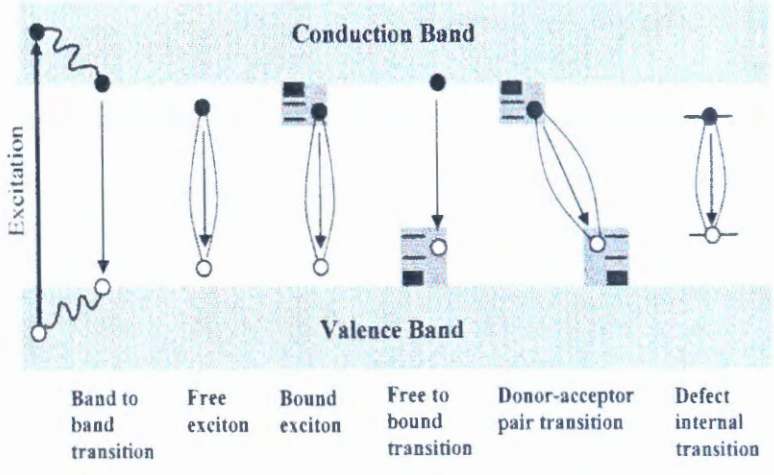

Figure 3.6(b): Schematic illustration of common recombination processes

An electron bound to a donor can recombine directly with a free hole from a valence band. This kind of recombination is called free-to-bound (FB) transition. The recombination energy for such a transition corresponds to the band gap energy reduced with the binding energy of donor. Another possibility is that a hole bound to an acceptor recombines with an electron bound to a donor in donor-acceptor pair (DAP) transition. Both the donor and the acceptor are neutral before the recombination (i.e. the donor positively and the acceptor negatively charged). Thus there is a Coulomb interaction between the donor and acceptor after the transition and extra Coulomb energy is gained in the final state added to the radiative recombination energy. The transition energy E (R) depends on the distance R between the donor and acceptor atoms.

3.3.5 Pulsed laser deposition (PLD)

PLD is the most recent thin film deposition technique compared to MOVPE, MBE and sputtering. Research on the interaction of high power laser beams with solid surfaces have been conducted since the 1960s when the first high power ruby laser became available. However, it was not until 1987 when a more stable Nd:YAG laser was used to deposit ternary HgCdTe layers that research on PLD began to flourish [15]. This method has received considerable attention for its ability to deposit the complex oxides needed to produee superconducting thin films [16- 19]. It also has the ability to operate in high pressure reactive gases, unlike other deposition methods [20]. The advantages of PLD also come from the simple hardware and setup. A deposition system usually consists of an excimer laser and optical elements to maneuver and focus the laser beam. Some of the optieal elements that are used in the set up are focusing lens, apertures, mirrors, beam splitters and laser windows. The substrate and target are housed in a vacuum chamber, while a high-power laser is mounted externally and can be focused via optical lenses to vaporize the target material and deposit thin films on the substrate. A schematic of a basic deposition system that uses oxygen as its reactive gas is shown in Figure 3.8.

Excimer lasers with wavelengths between 200 and 400 nm are most often used for pulsed laser deposition [21]. Excimer lasers below 200 nm are not typically used for PLD due to the possibility of absorption by the Schumann- Runge bands of molecular oxygen. As shown in Figure 3.10, the laser source is located external to the vacuum chamber. The external energy

source allows the film growth process to take place in a reactive environment with any type and amount of gas. The external source gives the added advantage of the laser being available for more than one deposition system.

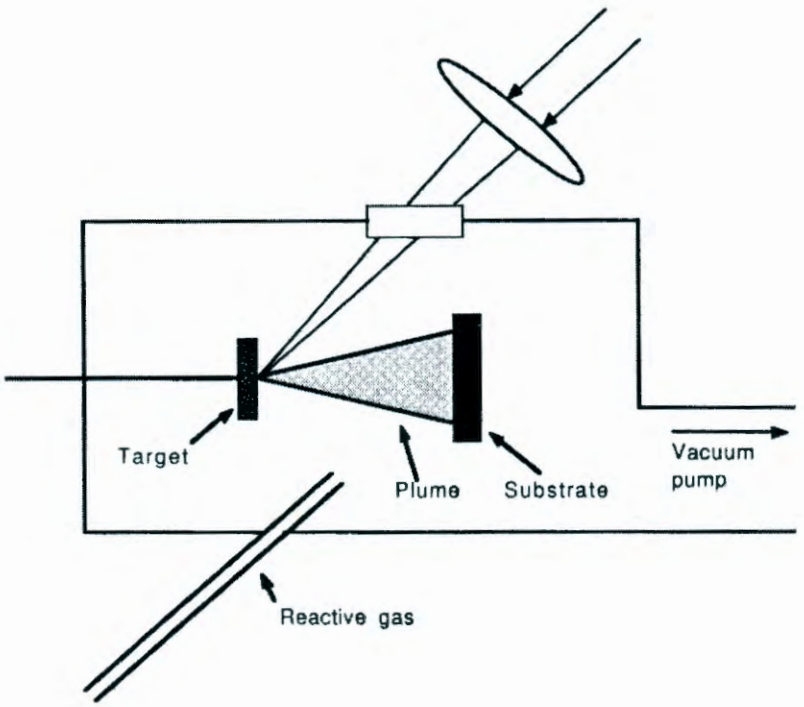

Figure 3.8: Schematic diagram of a pulsed laser deposition chamber setup

Once the laser is focused into the chamber, the target absorbs the energy from the laser. The ultra- violet (UV) radiation is converted to electronic excitation. This is converted into thermal, chemical, and mechanical energy, leading to ablation and evaporation of the target. The evaporants form a mixture of energetic species including atoms, molecules, electrons, ions, and micron sized particulates. This mixture is the often referred to as a plume. An example what a plume looks like during the film growth process is shown in Figure 2.10. The plume quickly expands in the vacuum from the target to form a "nozzle jet" [22]. As the plume reaches the substrate (which may be heated), film nucleation commences. The quality of the thin films produced by pulsed laser deposition is dependent on several variables. Laser power and spot size have a significant effect on particulate size and density. As the laser fluence is increased beyond a threshold, the number of particulates that are formed also increases [23, 24]. Laser fluence is defined as the laser energy per unit area and thus, may be adjusted by varying the laser power or laser spot size. Background gases may change growth

parameters such as the deposition rate and the kinetic energy distribution of the depositing species [25]. For instance, an oxidizing environment can help oxides to form and stabilize the desired crystal phase at the deposition temperature [26]. Substrate temperature has an effect on the stoichiometry of the film as well as the film structure [27]. Film structure has also been influenced by the deposition rate. Wu et al. found that an increase in the deposition rate led to a decrease in the crystallinity of $YBa_2Cu_3O_{7-\delta}$ thin films. At the higher deposition rates, the arrival rate exceeds the diffusion rate. Equilibrium conditions are not maintained and structural defects are formed [28].

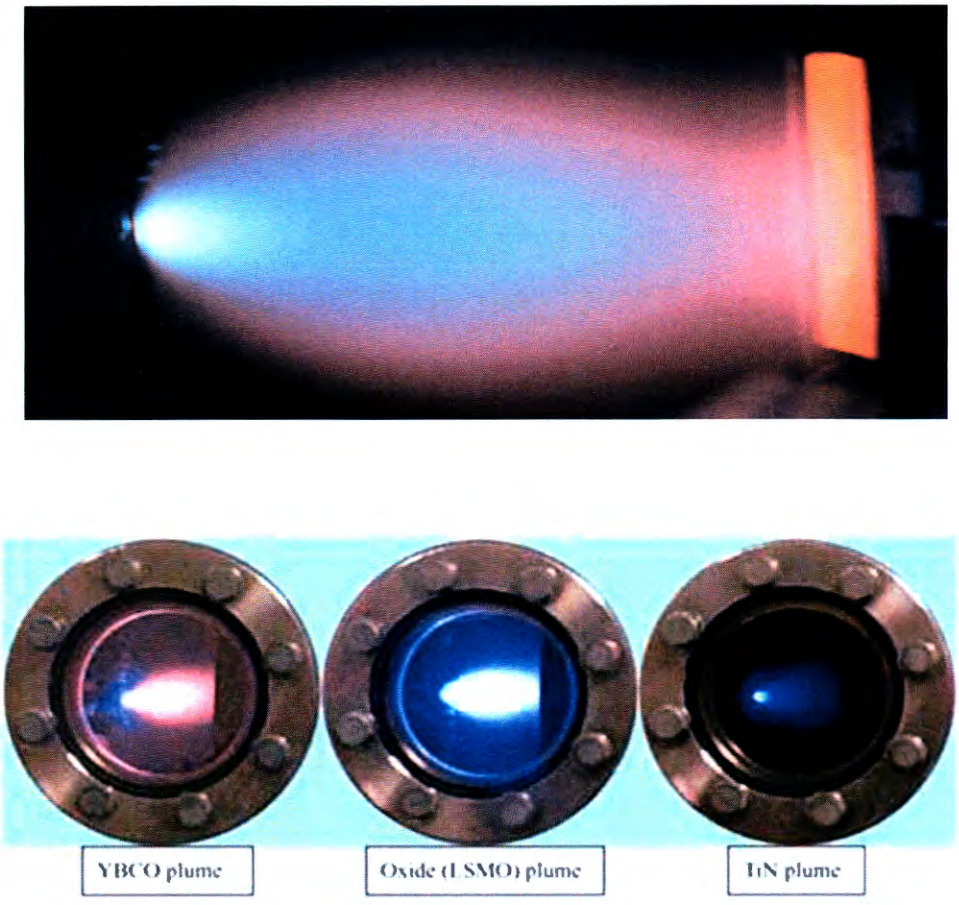

Figure 3.9: Examples of picture of plume developed during PLD

In summary, the advantages of this growth method include [29]:

- Flexibility to use energy source with more than deposition chamber
- Easy process control
- Ability to use high reactive gas pressures

• Decreased contamination from outside sources

• Control of film stoichiometry.

The disadvantages of PLD are:

•The generation of particulates during the deposition process, which is not ideal for the application field.

•The non-uniform layer thickness.

•The ablation plume cross section is generally small and this limits the sample size.

•The deposition of novel materials usually involves a period of optimization of deposition parameters.

The short laser pulses result in congruent evaporants. Congruent evaporation aids in stoichiometry control of the thin films during mass transfer from target to substrate. One obvious disadvantage is the presence of micron sized particulates. Also, scale up to large area deposition is not easily completed. Pulsed laser deposition has been shown as an appropriate method for growing phosphor films, specifically oxide phosphors. Yttria and silicate phosphors are some of the oxide materials that have been grown by this method [30, 33].

While the hardware required in PLD is relatively simple, the laser-target interaction is extremely complex. The mechanism for material ablation depends on properties of the laser as well as the optical, topological, and thermodynamic properties of the target. The electromagnetic energy absorbed by the solid surface is first converted into electronic excitation, and then into thermal, chemical, and mechanical energy that leads to evaporation, plasma formation and exfoliation [34]. There are two main drawbacks of PLD. Due to the angular distribution of the plume, large area deposits are often not uniform. This is usually resolved by rastering the laser or rotating/translating the substrate. The other more intrinsic drawback is known as "splashing," where micron-sized molten globules are deposited onto the substrate from either subsurface boiling, expulsion of the liquid layer, or exfoliation – where solid particulates instead of liquid globules are deposited onto the substrate. In order to

Figure 3.10: 248 nm KrF Lambda Physic excimer laser with PLD setup

In order to reduce or eliminate the effect of splashing from liquid layer expulsion and exfoliation, several approaches have been studied. Using a mechanical particle filter, slow-moving particulates can be screened with a velocity selector placed between the target and the substrate. However, the filters tend to be bulky and have low transmission rate that lowers the deposition rate as well. Other attempts include manipulating laser plumes by using two synchronized laser beams; using a hot screen to re-evaporate lighter particulates; or placing the substrate at an angle from the normal axis [35].

3.3.6 X-Ray Photoelectron Spectroscopy (XPS)

X-ray photoelectron spectroscopy, also known as electron spectroscopy for chemical analysis (ESCA), is a widely used surface technique to obtain chemical information at surfaces of various materials. The XPS process involves the ejection of an electron (photoelectron) in vacuum from the K level of an atom by an energetic incident x-ray photon [36]. Photoelectrons are collected and analyzed to produce a spectrum of emission intensity versus

electron binding energy. In general, the binding energies of the photoelectrons are characteristic of the element from which they are emitted [37]. The schematic of the XPS process is shown in Figure 3.11.

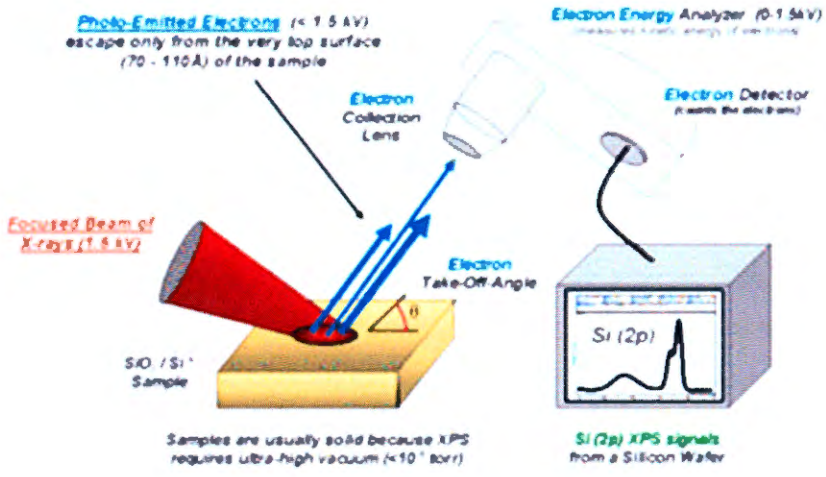

Figure 3.11: Schematic diagram of the XPS process in copper

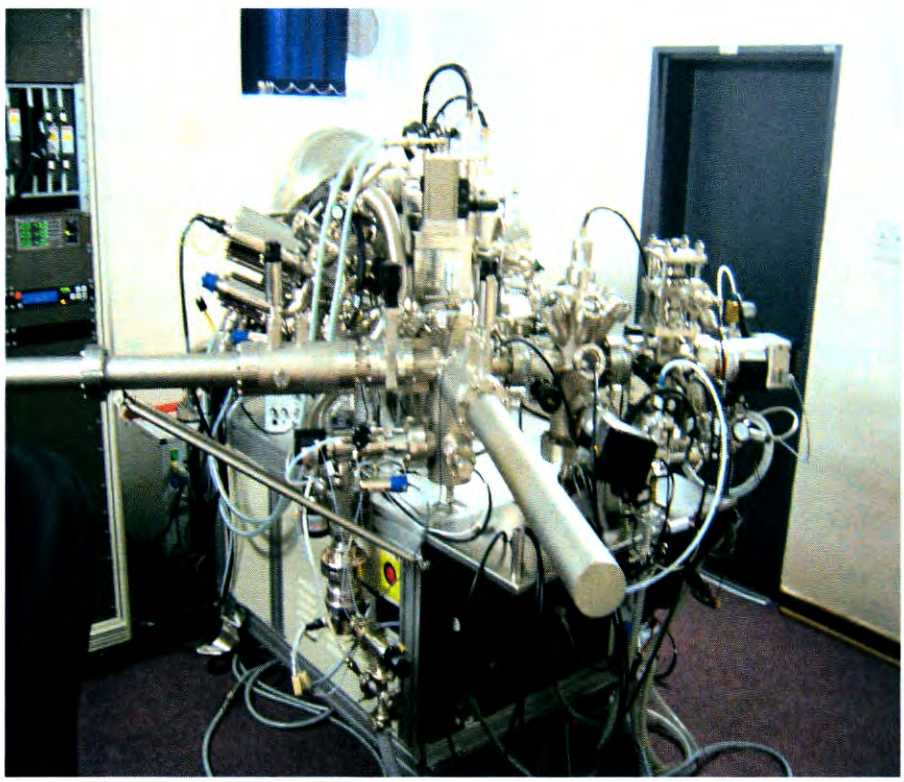

Figure 3.12: PHI 5400 Versaprobe scanning x-ray photoelectron spectrometer

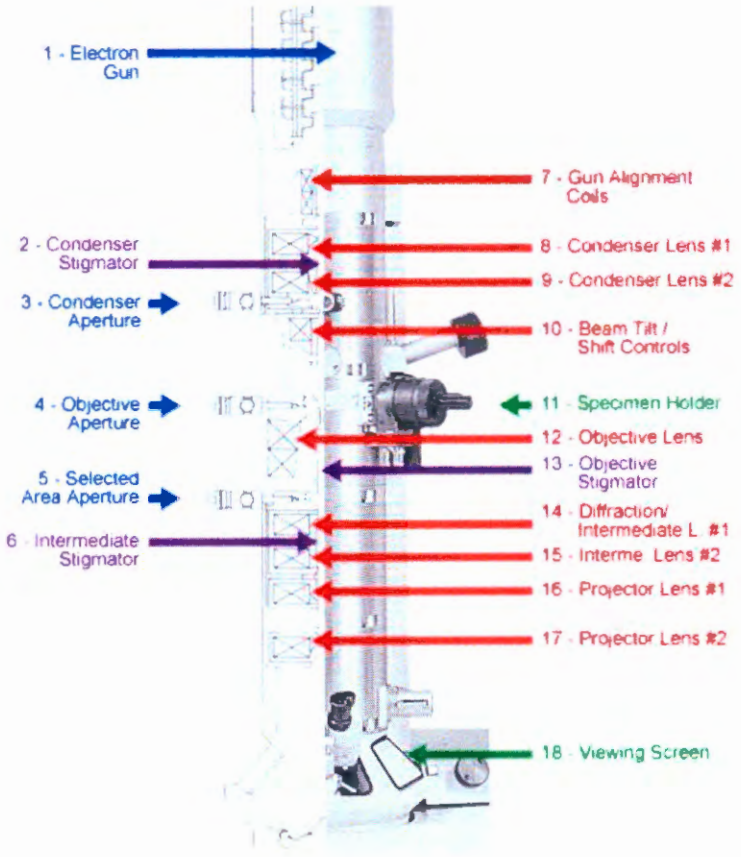

Figure 3.13 (a): Schematic diagram of a transmission electron microscope

electron signal is greatly magnified by a series of electromagnetic lenses. The magnified transmitted signal may be observed in either an electron diffraction mode or direct imaging mode. Data is accumulated from the beam after it passes through the sample. The electron diffraction mode is employed for crystalline structure analysis, while the image mode is used for investigating the microstructure, e.g. the grain size and lattice defects [40]. A modern high-resolution TEM goes down to a resolution <100 pm. While the ability to get atomic-scale resolutions from transmission electron microscopy is of great advantage, TEM is relatively expensive equipment. It requires extensive sample preparation, which makes it a relatively time-consuming technique with a low output of samples.

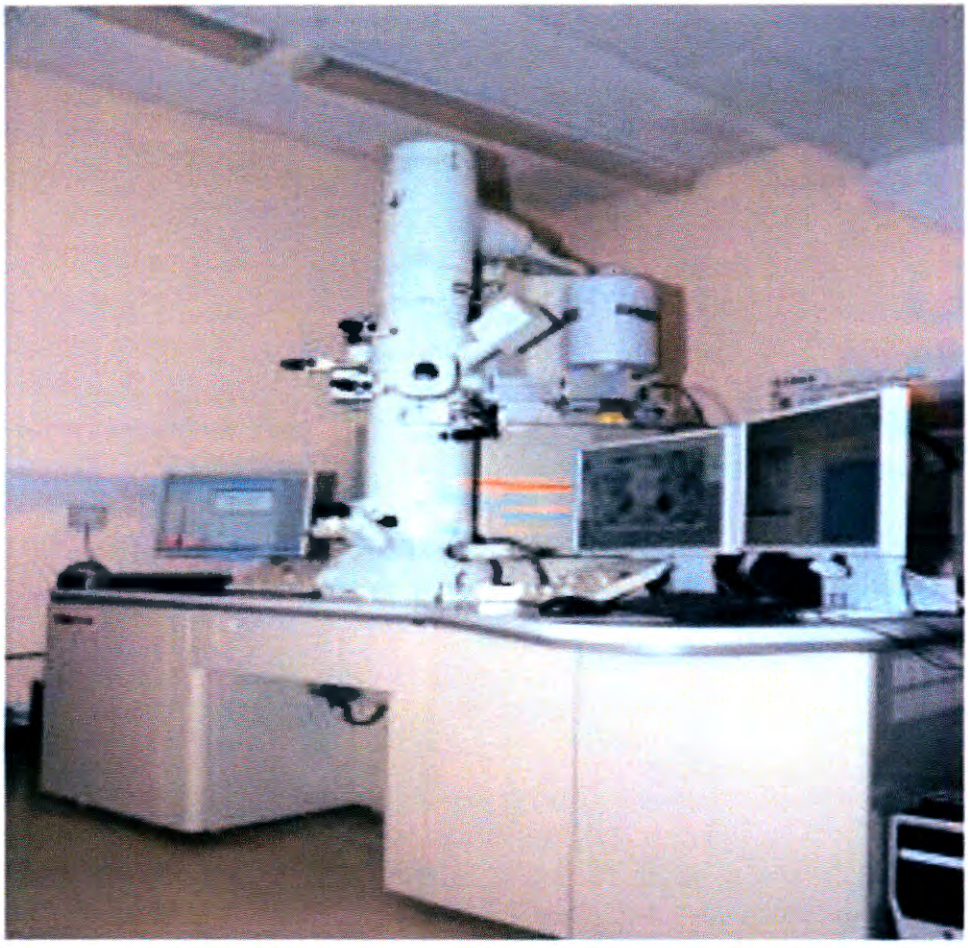

Figure 3.13 (b): JEOL JEM-2100 model transmission electron microscope

3.4 Evaluation of Phosphor

There are several experiments that are completed to evaluate the overall performance of phosphors. This includes chromaticity, spectral distribution, and lifetime of luminescence.

3.4.1 Chromaticity

A quantitative method has been established that relates the color produced on display screens to a standard value. The 1931 Commission Internationale de l'Eclairage (CIE) established a standard that defines chromaticity by x, y, and z coordinates. The chromaticity values are plotted on a two- dimensional graph, shown in Figure 3.16, using the x and y coordinates. The third value, z, is found by knowing $x+y+z=1$. Thus, when mentioning the chromaticity of a phosphor, usually the x and y coordinates are only given. The CIE diagram also shows

how red, green, and blue blend to give all hues needed for image production on a display screen.

In addition to using chromaticity to define color, for incandescent bodies it is also possible to use the *color temperature* to define its color. As seen in Figure 3.17, the *black body curve* is in the sequence of black, red, orange, yellow, white, and blue-white, which corresponds to the increasing temperature of an incandescent object as it radiates thermally. When an object is heated to emit light that correspond to the black body curve, its temperature is defined as the color temperature. Therefore, the color temperature of an incandescent light source is the temperature of a body on the black body curve that has the same color, or chromaticity on the diagram, as the light source. The *correlated color temperature* of a light source, then, is defined as the temperature of the body that is *not* on the black body curve with a color that is *closest* to the light source. Typical color temperatures of the white region in the diagram range between 2500 and 10000 K [41].

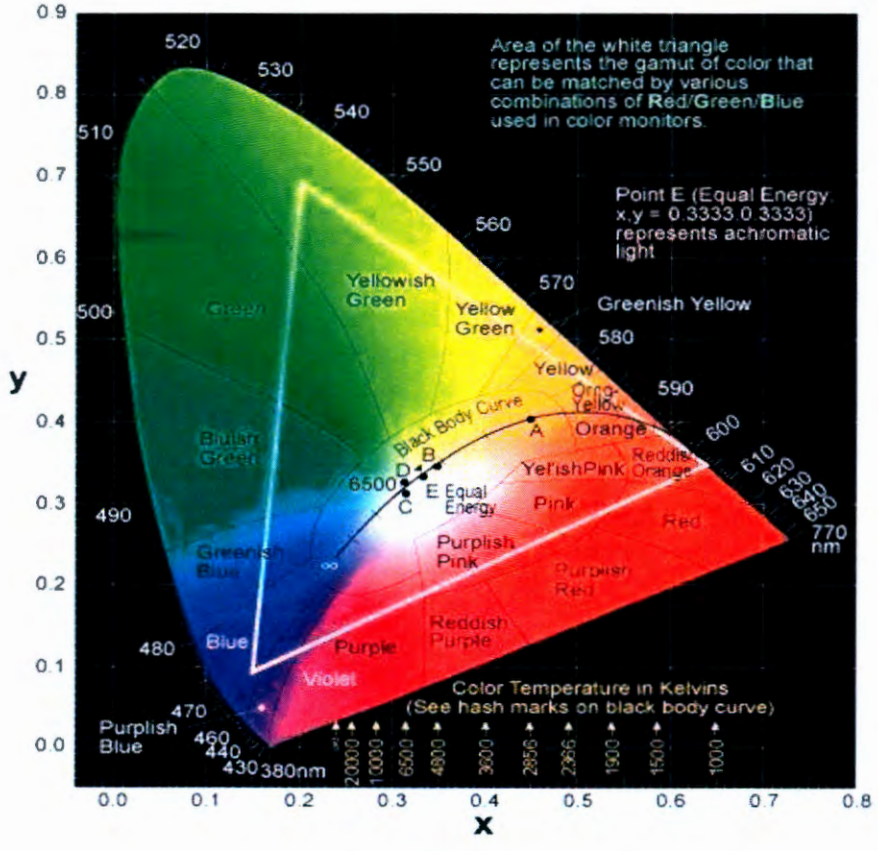

Figure 3.14: CIE chromaticity chart

3.4.2 Spectral Distribution

The spectral distribution gives information about the characteristic emission of a phosphor. The visible light emission of phosphors is within 400- 700 nm. This range of wavelengths is divided into six major divisions for the following colors: red, orange, yellow, green, blue, and violet. An example of this range with its corresponding colors is shown in Figure 3.17. The color that each phosphor emits corresponds to a wavelength within the visible light spectrum.

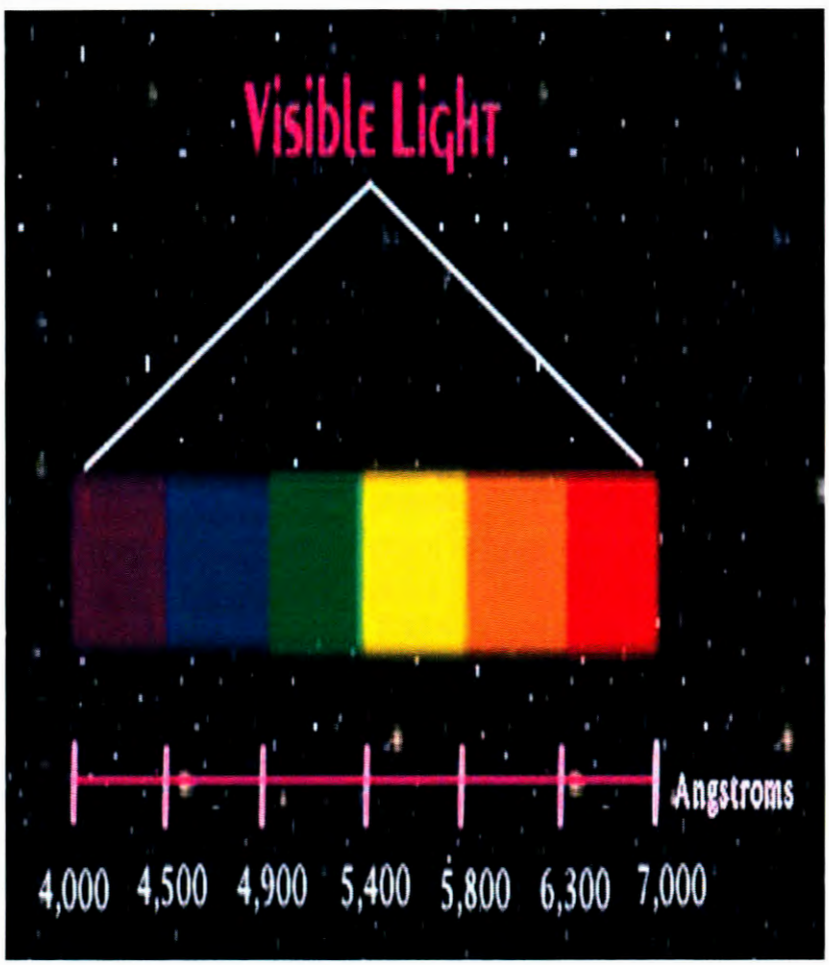

Figure 3.15: Visible light spectrum and corresponding wavelengths

References

1. Y Gogotsi, Nanomaterials Handbook, Materials Science at the Nanoscale, Routledge Publishers, USA, 2006, pp 5

2. K.C. Patil, S.T. Aruna, and T. Mimani, Solid State and Materials Science **6** (2002) 507–512

3. J.J .Kim, J.H. Kang, D.C. Lee and D.Y. Jeon, American Vacuum Society (2003).

4. N Suriyamurthy and B.S. Panigrahi, Journal of Luminescence, (In Press) SCIENCE-53

5. U Schubert, N Hüsing, Synthesis of Inorganic Materials, Second Edition, WILEYVCH, 2005

6. V Darakchieva "Strain-related structural and vibrational properties of group-III nitride layers and super lattices" PhD thesis linköping university Dissertation No.891 (2004)

7. M Ohring "Materials science of thin films, deposition and structure" 2nd edition.5 P.R.Berman, "advanced in atomic, molecular and optical physics", Vol.**45** (Academic press, Amsterdam, 1997)

8. M Larsson "Spectroscopy of semiconductor quantum dots" PhD thesis Linkoping universities Dissertation No.976 (2005)

9. W.M.Yen, S. Shionoya, H.Yamamoto, Practical Applications of Phosphors, CRC Press, Boca Raton, 2006

10. W.M. Yen, M. J. Weber, Inorganic Phosphors, Routledge Publishers, USA, 2004

11. S Elliot, The Physics and Chemistry of Solids, John Willey and Sons, New York, 1998, pp 28

12. R. W. Kelsall, I. W Hamley, M Geoghegan, Nanoscale Science and Technology, Wiley, 2005

13. B. G. Yacobi, D. B. Holt, and L.L. Kazmerski Microanalysis of Solids, New York, Plenum Press, 1994

14. M Kuno, Introduction to Nanosciene and Nanotechnology: A Workbook, Notre Dame, 2005

15. M. Kohler, W. Fritzsche ,Nanotechnology, An Introduction Nanostructuring Techniques, Wiley-VCH, 2003

16. C. Guozhong, Nanostructures & Nanomaterials, Synthesis, Properties & Applications, University of Washington, Imperial College Press, USA, 2004

17. T Allen, Particle Size Measurement, Volume **1**, Fifth Edition, Chapman & Hall, USA, 1968' p50

18.Y. L Mei, M Dechsler and M Ballanff, *Angew. Chem. Int. Ed.*, **45** (2006) 813

19. M Muniz-Miranda and M Innocenti, *Applied Surface Science,* **226** (2004) 125

20. K.S Chou and Y.S Lai, *Materials Chemistry and Physics,* **83** (2004) 82

21. H Chen, Y Wang, S Dong and E Wang, *Spectrochimica Acta Part A,* **64** (2006) 343

22.Z Gryczynski, J Lukomska, JR. Lakowicz, EG. Matveeva, I Gryczynski, *Chemical Physics Letters,* **421** (2006) 189

23. F. A. Settle, Handbook of Instrumental Techniques for Analytical Chemistry, Prentice Hall PTR, USA, pp 339-351

24. http://serc.carleton.edu/research_education/geochemsheets/techniques/XRD.html 15/03/2009

25. J Hecht, The Laser Guidebook, Second Edition, McGraw-Hill Professional Publishing, 1999

26. M Endo, R.F. Walter, Gas Lasers, CRC Press, New York, 2006

27. K.R. Nambiar, Lasers: Principles, Types and Applications, New Age International Publishers, New Delhi, 2004

28. O Svelto, D.C. Hanna Principles of lasers, Fourth Edition, Kluwer Academic/Plenum Publishers, 1998

29. T Katsumata, S Toyomane, R Sakai, S Komuro, and T Morikawa, J. Am. Ceram. Soc., 89 (3) (2006) 932–936

30. The International Pharmacopoeia, Organization Mondiale de la santé, World Health Organization, Fourth Edition, Volume 1, Geneva, 2006

31. B.D.Cullity and S.R.Stock "Element of x-ray diffraction" 3rd edition, Practice-Hall Inc. New Jersy. (2001)

32. M.R.Sardela Jr., "The growth, thermal stability, structural and electrical properties of doped and undoped Si-based epitaxial structures" PhD thesis Linköping university Press, Dissertation No.341 (2000).

33. L.T Lin, Y Hu and TH Hsieh, *Rev.Adv.Mater.Sci*, **5** (2003) 464

34. T Fukuyo and H Imai, *Journal of Crystal Growth,* **241** (2002) 193

35. K.D Kim, D.N Han and H.T Kim, *Chemical Engineering Journal,* **104** (2004) 55

36. M Rong, M Zhang, H Lui and H Zeng *Polymer,* **40** (1999) 6169

37. G Carotenuto, G.P Pepe and L Nicolais, *Eur. Phys.J.,* **16** (2000) 11

38.C Luo, Y Zhang, X Zeng, Y Zeng and Y.J Wang, *Colloid Interface Sci.*, **288** (2005) 444

39. W Songping and M Shuyuan, *Materials Chemistry and Physics,* **89** (2005) 423

40. L Suber, I Sondi E Matijević and D.V Goia, *Journal of Colloidal and Interface Science,* **288** (2005) 489

41. A Sileikaite, I Prosycevas, J Puiso, A Juraitis and A Guobiene, *Materials Science (Medziagotyra),* **12** (2006) 287

Chapter 4

Synthesis and Characterization of $Y_2O_3:Eu^{3+}$ phosphors Using Sol-combustion Method

4.1 Introduction

Global claim for phosphor materials as efficient sources of energy that can supply sustained competence is growing day by day. The phosphors are facing increased global challenges including high production of rare earth materials, environmental and recycling issues, and necessity to supply devices very quickly that may be outdated rapidly due to new technological developments arising in the industry and market. A number of applications have emerged in recent years that will change the future of the industry and new technologies like innovations and specialty phosphors are garnering increased attention. The primary drivers for growth are the expansion of key end-use applications including solid-state lighting and fluorescent lighting. Current research in technology is focused on new materials, novel phenomena, new characterization techniques and fabrication of devices. The manufacturing of the new generation of display equipment in recent years raised a stringent demand on the fluorescent materials [1]. Particular interest is focused on the high-brightness phosphors having sub-micrometer particle sizes. Conventional solid-state synthesis of phosphors followed by milling generally results in a dramatic decline of emission intensities for 1-3μm size particles due to the defects introduced by crushing. Therefore, wet-chemical methods seem to be an attractive alternative to the classical approach. The attempts to prepare fine powders of Y_2O_3: Eu^{3+}, perhaps the simplest oxide among industrially used phosphors, usually lead to broadening of the emission peaks and overall decrease of the luminescence performance.[2-3]Trivalent-europium-doped yttrium oxide ($Y_2O_3:Eu^{3+}$) is an important phosphor system extensively applied in color-television picture tubes owing to higher luminescent efficiency and the saturation degree in color.

Physica B: Physics of Condensed Matter, Volume 439, pp. 181-184. DOI: 10.1016/j.physb.2013.11.051

Y_2O_3, with a band gap of 5.8 eV can be considered as a large band gap semieonductor system [4]. In this paper we investigate how the structure, morphology and the luminescence intensities of these phosphors are affected by varying fuel to host ratios.

4.2. Experimental details

4.2.1 Synthesis procedure

All the chemicals used for the preparation of the powders were of analytical grade. It includes yttrium nitrate (Y $(NO_3)_3.6H_2O$), thiourea (NH_2CSNH_2), europium nitrate ($Eu(NO_3)_3.6H_2O$), ethanol and distilled water. During the preparation of the micro-powders, thiourea was used as a fuel. Y_2O_3: Eu^{3+} micro- powders were prepared as follows;
$Y(NO_3)_3.6H_2O$, NH_2CSNH_2, $Eu(NO_3)_3.6H_2O$, ethanol and distilled water were mixed in required stoichiometric ratios and dissolved by stirring using a magnetic stirrer for 5 -10 minutes.The mixture was heated in an air tube furnace to ignition temperature of 400^0C. A white foamy product was obtained after the combustion reaction.

4.2.2 Characterization

The Photoluminescence (PL) spectrum as well as decay curves for all the samples were investigated by Cary Eclipse fluorescent spectrophotometer equipped with a 150W xenon lamp at an excitation source with the slit of 1.0 nm and scan speed of 240nm min^{-1}. To determine the average particle diameter and the phase of the samples, X-ray powder diffraction(XRD) spectra were measured with a D8 Bruker Advanced AXS GmbH X-ray diffractometer using Cu *Ka* radiation at a wavelength of 0.154056nm, the size and morphology of the as-prepared particles were carried out by using a Scanning electron microscope (SEM), SHIMADZU SSX-550 SUPERSCAN.

4.3. Results and discussion

4.3.1 Crystal structure

The XRD pattern of a representative as-prepared sample is shown in Fig.1. All peaks can be perfectly indexed as the cubic phase with space group D_3d^3 (p^{3m}) and the cell parameter

a_0=10.60Å (a=b=c) is in good agreement with standard Y_2O_3 JCPDS cards (No. 41- 1105). C_3 symmetry operation of Y^{3+} exists in the crystal, and no new crystal phase arose by doping with Eu^{3+}.

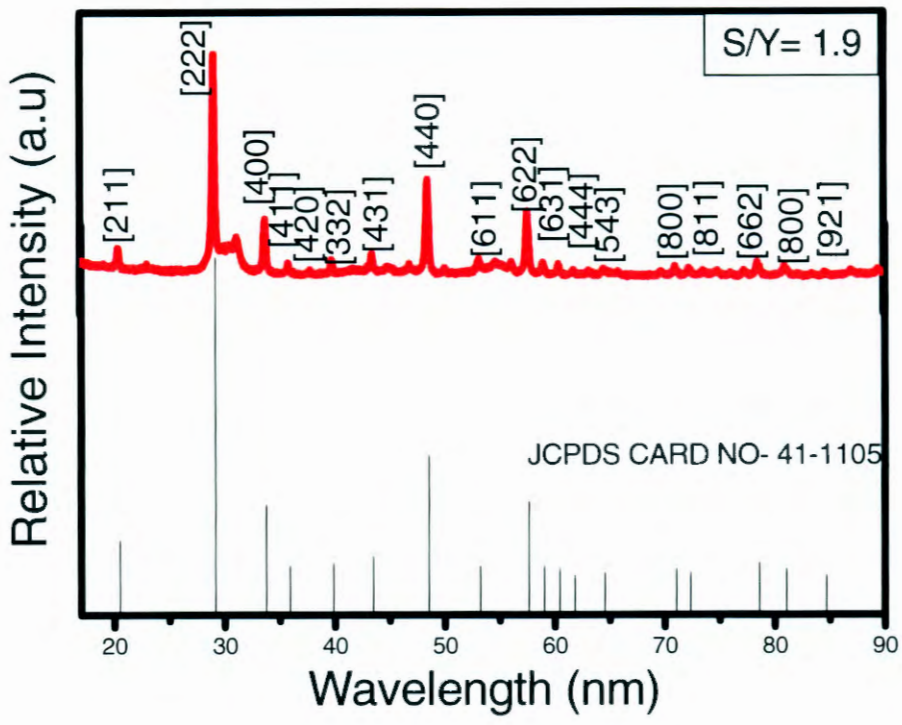

Figure 4.1: Representative XRD pattern of one of the sample with S/Y=1.8 molar ratio obtained by Sol- Combustion method.

The grain sizes ranging between 158 and 180nm were estimated by using Scherrer's equation. In order to investigate marginal decrease, the crystallographic unit cell volume was determined by using the following equation;

$$\frac{1}{d^2} = \frac{h^2 + k^2 + l^2}{a^2}$$

It is observed that for the Y_2O_3 microstructures, there is a marginal decrease (-0.29%) in crystallographic unit-cell that tends to contract due to the increase in surface area of the grains. This may lead to a decrease in the lattice constant. No peaks attributable to other types of oxides are observed in the XRD patterns, indicating the high purity of the phases obtained.

Table 4.1

The average grain size of the synthesized Y_2O_3: Eu^{3+} nanoparticles as a function of S/Y molar ratio.

Average grain sizes as a function of S/Y molar ratios				
S/Y ratio	<222>	<400>	<440>	<622>
1.7	181	178	176	179
1.8	172	172	175	177
1.9	178	178	179	180
2	178	178	179	180
2.5	151	151	158	164
4	150	152	155	154

4.3.2 Morphology

The microstructures of Y_2O_3: Eu^{3+} are studied by SEM patterns and presented in Fig.2. It can be seen from the images that the samples possess a number of micro particles when the S/Y molar ratios are low (1.9 and 2.0). With the increase in the S/Y molar ratio to 2.5, the particles seem to agglomerates to form nanorods-like structures. Further increase in the S/Y molar ratio to 4 reveals agglomeration of the particles. Thus, S/Y molar ratios seem to have an effect on the morphology of the phosphors. This current method also allowed obtaining agglomerates of controlled size since synthesis time can be controlled; this being an important advantage comparing with other methods [1, 10, and 15]. An additional advantage of spherical agglomerates is its excellent fluidity (18), which is beneficial for the elaboration of pressed bodies.

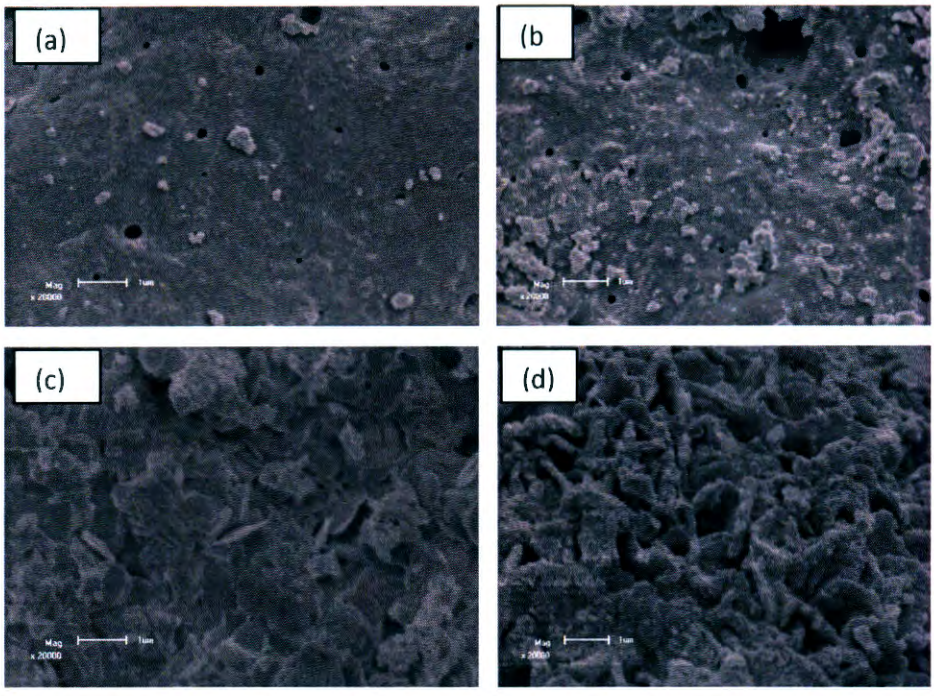

Figure 4.2: The SEM images of the Y_2O_3: Eu^{3+} with (a) 1.9 (b) 2.0 (c) 2.5 (d) 4.0 S/Y molar ratios. 0.5nm field of view.

4.3.3. Photoluminescence

Upon excitation, Eu^{3+} doped systems indicate many Stark energy levels in the visible region. In particular, luminescence transitions corresponding to the $^5D_0 \rightarrow {}^7F_J$ manifold in the orange-red region are of practical significance [16]. Fig.3 shows the emission spectrum of the Eu^{3+} ion doped in aY_2O_3 matrix with different S/Y molar ratios. The figure indicates intense red emission around 626nm due to the $^5D_0 \rightarrow {}^7F_2$ transition, and a line emission around 588 nm.The peak around 618nm is due to electric dipole transition of $^5D_0 \rightarrow {}^7F_1$which is induced by the lack of inversion symmetry at the Eu^{3+} sites and is much stronger than the $^5D_0 \rightarrow {}^7F_1$ transition.

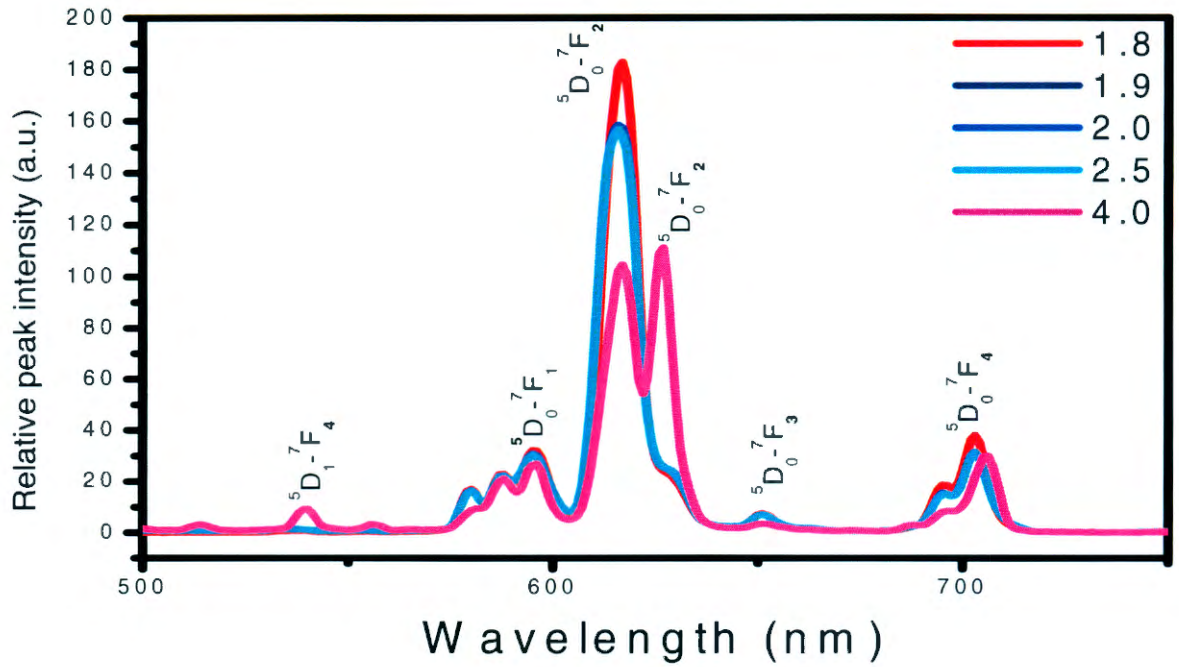

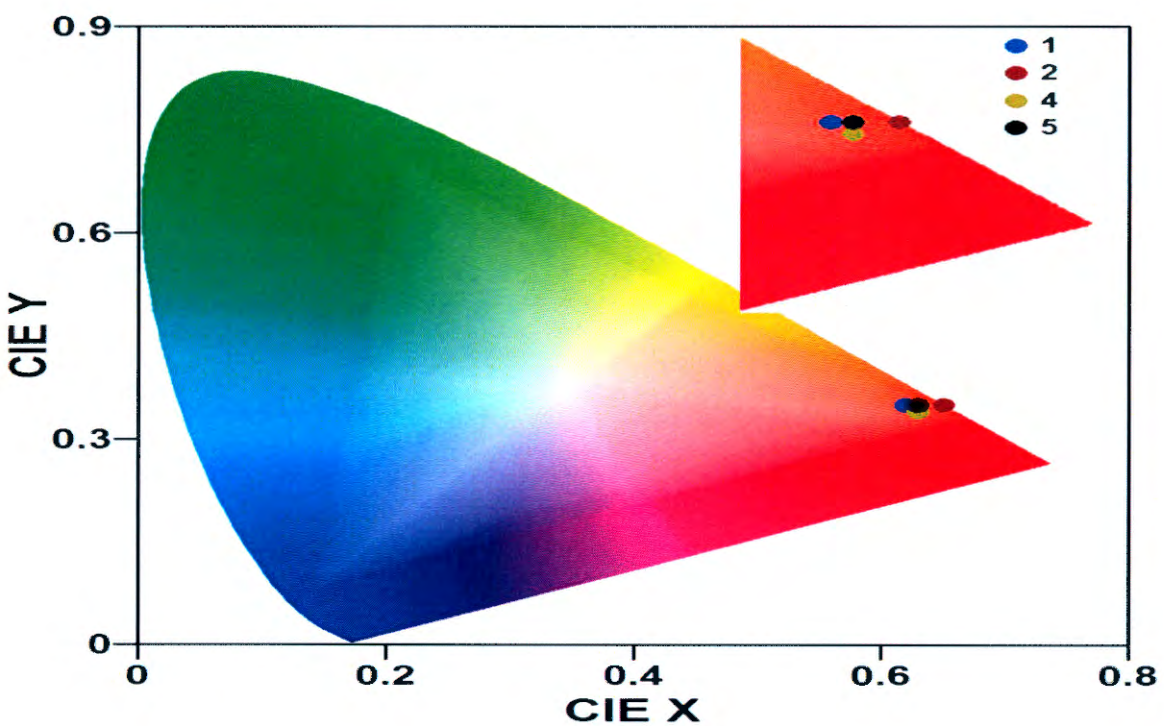

Figure 4.3. (a): Emission spectrum of the different S/Y molar ratio Y_2O_3: Eu^{3+} phosphor excited at 260nm obtained by the Sol-Combustion method. **(b)** CIE coordinate diagram of the different emissions as indicated.

It is well known that the $^5D_0 \rightarrow {}^7F_2/{}^5D_0 \rightarrow {}^7F_1$ intensity ratio is a good measure of the site symmetry of the rare-earth ions in a doped material. This is because the hypersensitive transition $^5D_0 \rightarrow {}^7F_2$ tends to be much more intense at a site with no inversion symmetry, while the magnetic dipole transition $^5D_0 \rightarrow {}^7F_1$ is constant, regardless of the environment [13]. At S/Y=1.8 phosphors have a red emission intensity of transition was the strongest due to the dominance of the $^5D_0 \rightarrow {}^7F_2$ transition. At the S/Y= 4 molar ratio the peak splits due to the magnetic dipole transition. Therefore, to have some insights of various luminescence transitions of Eu^{3+} doped in a matrix, this transition can be used as an internal standard [14, 16, and 17]. Relative intensity of the hypersensitive transition with respect to the magnetic dipole transition as internal standard would give an idea on the transition strength of the hypersensitive transition.

In order to investigate the effect of S/Y molar ratios on the maximum intensity of the phosphors, a graph of maximum peak intensity verse various molar ratios was plotted as shown in figure 5. The plot indicates that the maximum peak intensities are higher at lower S/Y ratios(S/Y=1 to 2.5). It drops drastically for higher molar ratio of S/Y= 4.This is in agreement with the previous discussion that S/Y =1.8 molar ratios give the highest intensity and longer afterglow as pointed out in the next section.

4.3.4. Afterglow decay curves of the red phosphors

The afterglow properties of samples with different S/Y ratios are compared, as shown in Fig.4. It can be seen that afterglow origin of the sample of S/Y= 1.8 and 1.9 has highest afterglow and brightness, while the sample with the ratio of S/Y=4.0 has the lowest afterglow and brightness. Thus, the ratio S/Y= 1.8 was taken as the optimum. The decay times of the phosphor can be estimated by using the following double exponential equation;

$$I = A_1 \exp(-t/\tau_1) + A_2 \exp(-t/\tau_2)$$

where I is the phosphorescence intensity, A_1, and A_2, are constants, t is time, τ_1 and τ_2, are decay times for exponential components, respectively. The fitting results of parameters t_1 and t_2 are listed in Table 2 below.

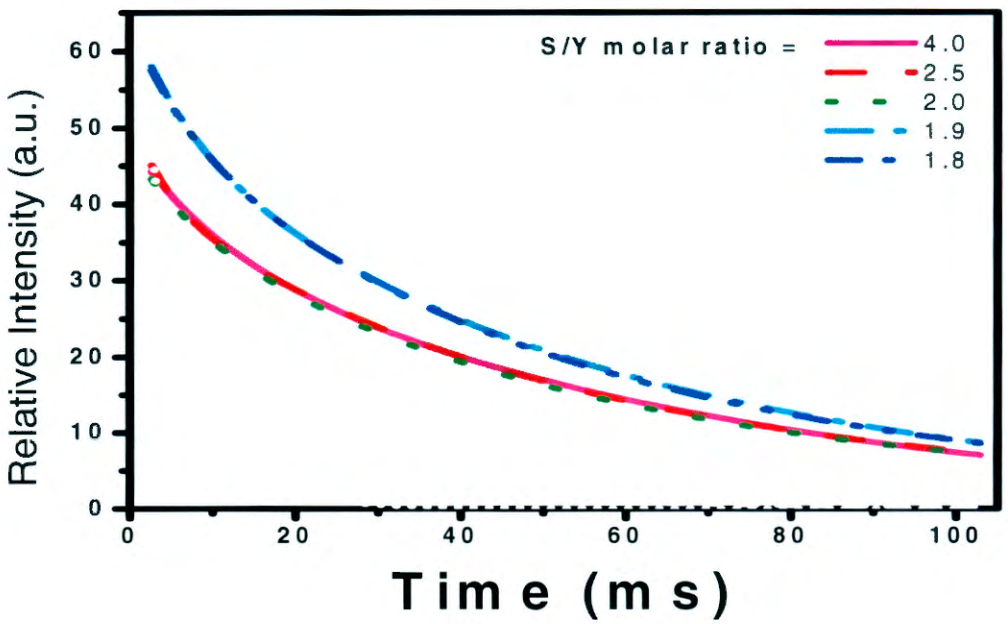

Figure 4.4: The decay curve of Y_2O_3:Eu^{3+} phosphor.

S/Y	1.7	1.8	1.9	2	2.5	4
Components	**Decay constants(τ, s)**					
Fast (τ1)	1.3729	1.3715	1.3656	1.3647	1.3598	1.3579
Medium (τ2)	1.4622	1.4588	1.4571	1.4537	1.4499	1.3989

Table 4.2

Decay constants for the fitted decay curves of the phosphor powders with different S/Y molar ratios.

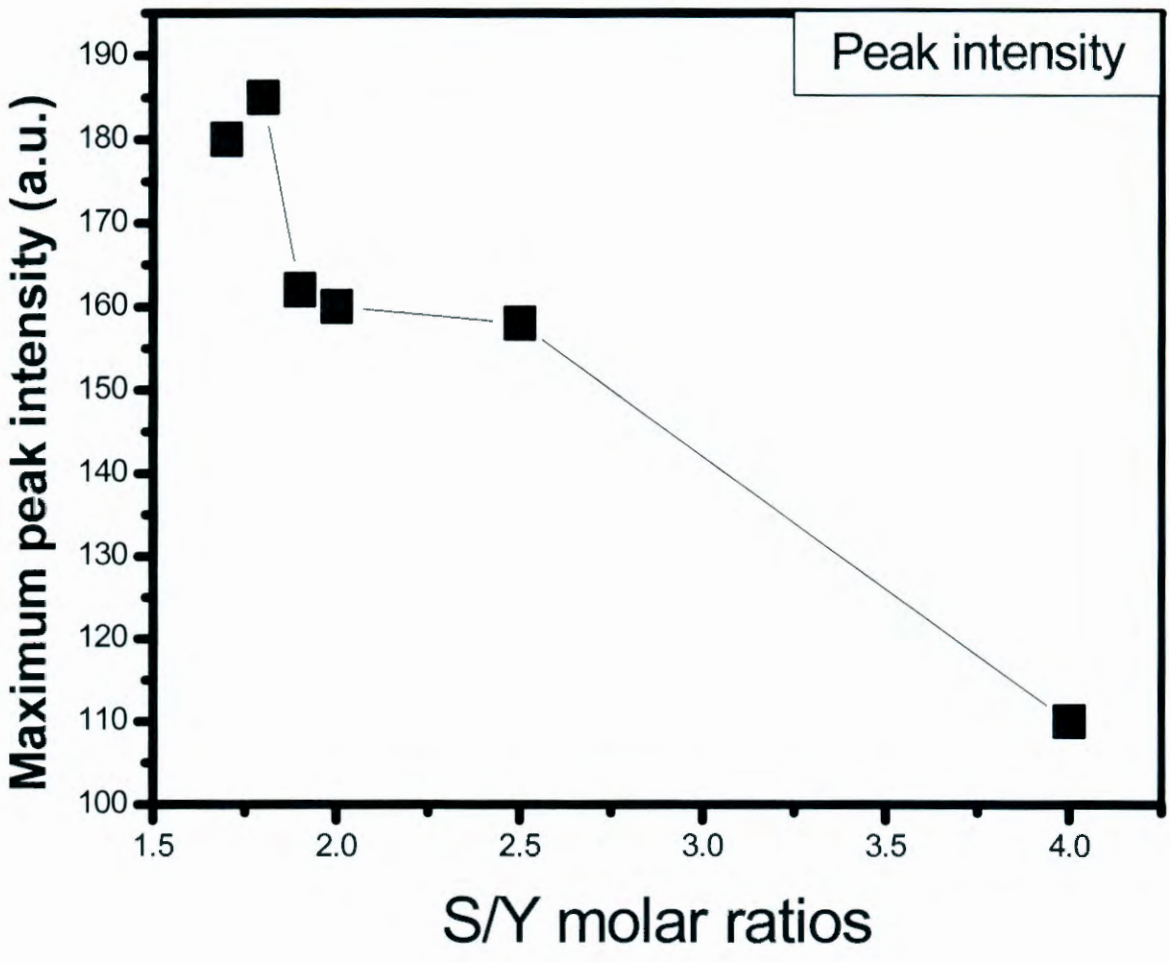

Figure 4.5: Effect of S/Y molar ratios on the intensity of the broad PL peaks and corresponding emission wavelength.

4.4 Conclusion

A very simple and efficient chemical route to prepare a promising afterglow red phosphor by sol- combustion synthesis is presented. Ethanol has the effect of decreasing the water needed, hence simplifying the experimental procedure by dissolving rare earth nitrate and sulfur-contained organic fuel into an even solution. This prompts the formation of rare earth oxide by igniting first during heating that leads to a combustion decomposition reaction. Y_2O_3: Eu^{3+} microcrystalline structures were obtained using thiourea as organic fuel. The increase in the

ratios of fuel to the host decreased the grain size and the maximum PL intensity of the phosphors.

References

[1] K. Narita. Phosphor Handbook; CRC Press LLC: Boca Raton, FL, 1999.

[2] M.R. Royce, US Patent no. 3418, Vol. 246, 1968.

[3] S.H. Cho, Y.S. Yoo and J.D. Lee, J. Electrochem. Soc. 145 (1998) 1017.

[4] M. Mikami and A. Oshiyama, Phys. Rev. B57 (1998) 8939.

[5] Y. Zhiping, F. Jianwei, L. Xu, Journal of Heibei University (Natural Science Edition), 25(3) (2005) 262.

[6] F. C. M. Van de Pol, Ceram. Bull. 69 (1990) 1959.

[7] K. Nashimoto, S. Nakamura, H. Mariyama, Japan. J. Appl. Phys. 43 (1995) 5091.

[8] T. Nagata, T. Shimura, A. Asida, N. Fujimura, T. Ito, J. Cryst. Growth 237 (2002) 537.

[9] A.J. Freeman, K.R. Paeppelmeier, T.O. Mason, R.P.H, Chang, T.J. Marks. Mater. Res. Soc. Bull. 25 (2000 45.

[10] L. Spanhel , M.A. Anderson, J.Am.Chem. Soc., 113 (1991) 2826.

[11] P.P. Hoyer, H. Wetter, Chem. Phys. Lett., 221 (1994) 379.

[12] P. Hoyer, R. Eichberyer, H. Weller, Ber. Bunsen- Ges. Chem. Phys. Chem., 97 (1993) 143.

[13] A. Eric, M. Eulenkamp, J. Phys. Chem *B*, 102 (2002) 5566.

[14] D.C. Reyolds, D.C. Look, B. Jogai, H. Mokoc, Solide State Commum101 (1997) 643.

[15] M. Liu, A.H. Kitai, P. Mascher, J. Lumin. 54 (1992) 35.

[16] Z.W. Jin, Y.Z. Yoo, T. Sekiguchi, T. Chikyow, H. Ofuchi,H. Fujioka, M. Oshima, H. Koinuma, Appl. Phys. Lett. 83 (2003) 39.

[17] X.T. Zhang, Y.C. Liu, J.Y. Zhang, Y.M. Lu, D.Z. Shen, X.W. Fan,X.G. Kong, J. Crystal Growth 80 (2003) 254.

[18] H.J. Lee, S.Y. Jeong, C.R. Cho, C.H. Park, Appl. Phys. Lett. 81 (2002) 4020.

Chapter 5

Characterization of Eu^{3+}activated lanthanum oxysulfide synthesized by sol-combustion method

5. I. Introduction

Lanthanide (La) oxysulfides with high thermal and chemical stability are known as a wide-bandgap (4.6 - 4.8 eV) material suitable for doping ion activation. Compared with the lanthanide oxides, oxysulfide is a more efficient phosphor with a broader excitation band. Therefore, the lanthanide oxysulfides become a very important family of inorganic materials that have high potential for applications in various fields, such as color television picture tubes [1, 2], radiographic imaging [3], field emission displays [4, 5] and long-lasting phosphorescence [6]. Among them, Eu^{3+} activated lanthanide oxysulfide has been extensively investigated due to its excellent efficiency to be used as a red phosphor applied in television picture tubes. Currently, studies on the luminescent properties of micro phosphors are attracting interest; because of its significance not only for applications but also for the essential understanding of micro crystals, such as the quantum confinement and surface effect [7, 8]. Among them, rare earth doped micro phosphors have attracted particular attention [9, 10]. It is expected that in the microsized phosphors, the luminescent quantum yield as well as the resolution of display to be considerably improved. Some rare earth ions, such as Eu^{3+}, may act as common activators to detect local environments [11] due to their supersensitive *f-f* transitions. Until now, a great number of rare earth doped microsized phosphors have been prepared and studied [12-13] especially the role of doping concentrations, crystal sizes and crystal structures on the luminescence in several oxide hosts have been studied extensively [14-15]. The reports on microsized lanthanide oxysulfides are rather scarce. However, in the past few years, there appeared only a few papers regarding the preparation and photoluminescence (PL) properties of rare-earth doped lanthanide oxysulfides microcrystals. It has been shown that the successful synthesis of lanthanide oxysulfide microparticles can be

achieved by a number of processes, including sol-gel [16], gas-phase condensation methods [17] or colloidal chemical methods [18-19]. But efforts to make concentrated colloidal solution of highly uniform size luminescent micro-oxides in the past have met with technical difficulties. To our knowledge, there is no paper reporting the synthesis of $La_2O_2S:Eu^{3+}$ by sol-combustion method which prompted us to attempt it.

In this paper, the original sol-combustion approach for the quantitative synthesis of lanthanum oxysulfide microparticles is described. Preliminary results of some optical and structural investigations as a function of La/S concentrations are reported.

5.2 Experimental

Lanthanum (La) oxysulfides phosphor ($La_2O_2S:Eu^{3+}$) was prepared by a sol-combustion synthesis method. High purity (Aldrich make, 99.99%) raw materials, lanthanum nitrate (La $(NO_3)_3.6H_2O$), europium nitrate (Eu $(NO_3)_3.6H_2O$), ethanol (C_2H_5OH) and thiourea (NH_2CSNH_2), were used for preparation of the phosphor. The materials were weighed in stoichiometric ratios, dissolved in distilled water and mixed by stirring using a magnetic stirrer for 5 -10 minutes. The mixture was heated in an air tube furnace to an ignition temperature of 400^0C. A white foamy product was obtained after the combustion reaction. Several samples with different La/S molar ratios were then prepared via a similar route. During the preparation of La_2O_2S, the doping concentration for all the samples was kept constant at 0.05 mol%.

5.2.1 Characterization

The PL spectra and decay curve of the powders were obtained with a Cary Eclipse fluorescent spectrophotometer equipped with a150 W xenon lamp as an excitation source with the slit of 1.0 nm and scan speed of 240 nm min^{-1}. To determine the average particle diameter and the phase of the samples, X-ray powder diffraction (XRD) spectra were measured with a D8 Bruker Advanced AXS GmbH X-ray diffractometer using Cu *Ka* radiation at a wavelength of 0.154056 nm, the size and morphology of the as-prepared particles were carried out by using a Scanning electron microscope (SEM), SHIMADZU SSX-550 SUPERSCAN. The thermoluminescence (TL) spectra were obtained using a Thermoluminescence Reader (Integral- PC Based). The XPS analysis was carried out with a

PHI 5000 Versa probe-Scanning XPS Microprobe. Fourier Transformed Infra–red (FTIR) spectroscopy was done with a Bruker Tensor 27 FTIR Spectrometer.

5.3 Results and Discussion

5.3.1 Crystal structure

Figure 5.1 shows the XRD patterns of the La_2O_2S powders synthesized by the sol-combustion process at 400 °C. The average crystalline size of the La_2O_2S particles calculated using the most intense reflection at $2\theta = 25.596^{0}$ are tabulated in table 5.1. Estimated aceording to the Scherrer'sequation, the average crystalline size of the powders is determined to be 178 nm.The cell constants a and c were obtained using equation 1 below;

$$Sin^2\theta = \frac{\lambda^2}{4}\left\{\frac{4}{3}\frac{h^2 + hk + k^2}{a^2} + \frac{l^2}{c^2}\right\} \text{---------- (5.1)}$$

The most dominant peaks can be indexed as the hexagonal La_2O_2S phase with space group P3m1 [164] and cell constants (a) 0.4128 nm, (c) 0.6985 nm, which are close to the reported data (JCPDS Cards File: 27-0263). The other peaks marked * are indexed as La_2O_3. It must also be noted that a slight shift in the XRD peaks occurred, as pointed out in table 5.1, with an increase in the La/S ratio. It is well-known that thiourea reacts with water to produce gaseous NH_3, H_2S, and CO_2: The produced gas NH_3 will react with the crystal water. Therefore, a reaction may occur between lanthanum nitrate and the crystal water in the system at elevated temperature to produce La $(OH)_3$:

$$La\{NO_3\}3 + \frac{3}{2}H_2O \rightarrow La\{OH\}3(s) + 3NO_2(g) + \frac{3}{4}O_2(g) \text{---------- (5.2)}$$

Since CO_2 and H_2S are both acidic, reactions between La $(OH)_3$ and them immediately occurred; then the following equilibrium were formed:

$$La\{OH\}3(s) + CO_2(g) \rightarrow La\{OH\}CO_3(s) + H_2O(g) \text{---------- (5.3)}$$
$$2La\{OH\}3(s) + H_2S(g) \rightarrow La_2O_2S(s) + 4H_2O(g) \text{---------- (5.4)}$$

The equilibrium given in eq.5.4 is more likely to move to the right than that expressed in eq.5.3. Therefore, the final product was crystallized La_2O_2S, with small traces of La_2O_3 phase

as detected by XRD. The small traces of La_2O_3 were formed due to the decomposition of La_2O_2S at elevated temperatures according to eq.5.5 below;

$$La_2O_2S(s) + O_2(g) \rightarrow La_2O_3(s) + SO(g) \text{ ---------- } (5.5)$$

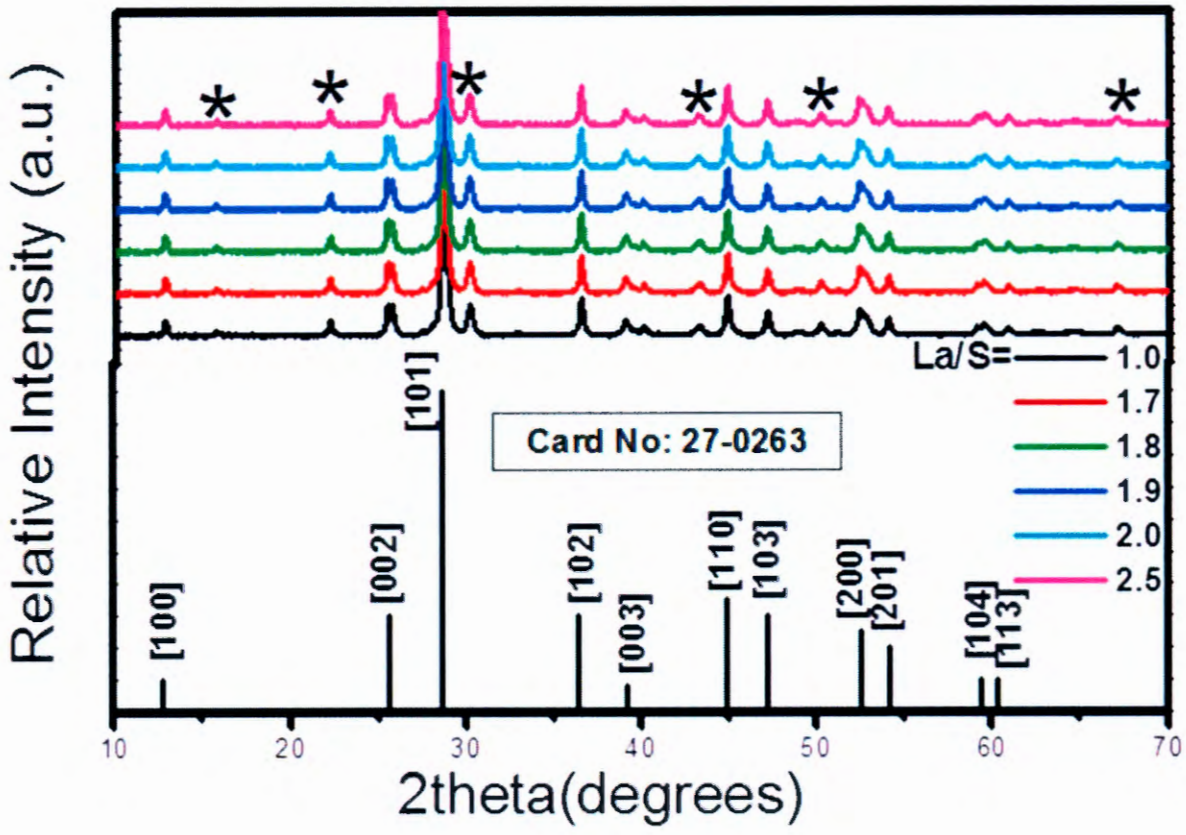

Figure 5.1. X-ray diffraction patterns of La_2O_2S with different La/S ratios as well as the standard XRD pattern

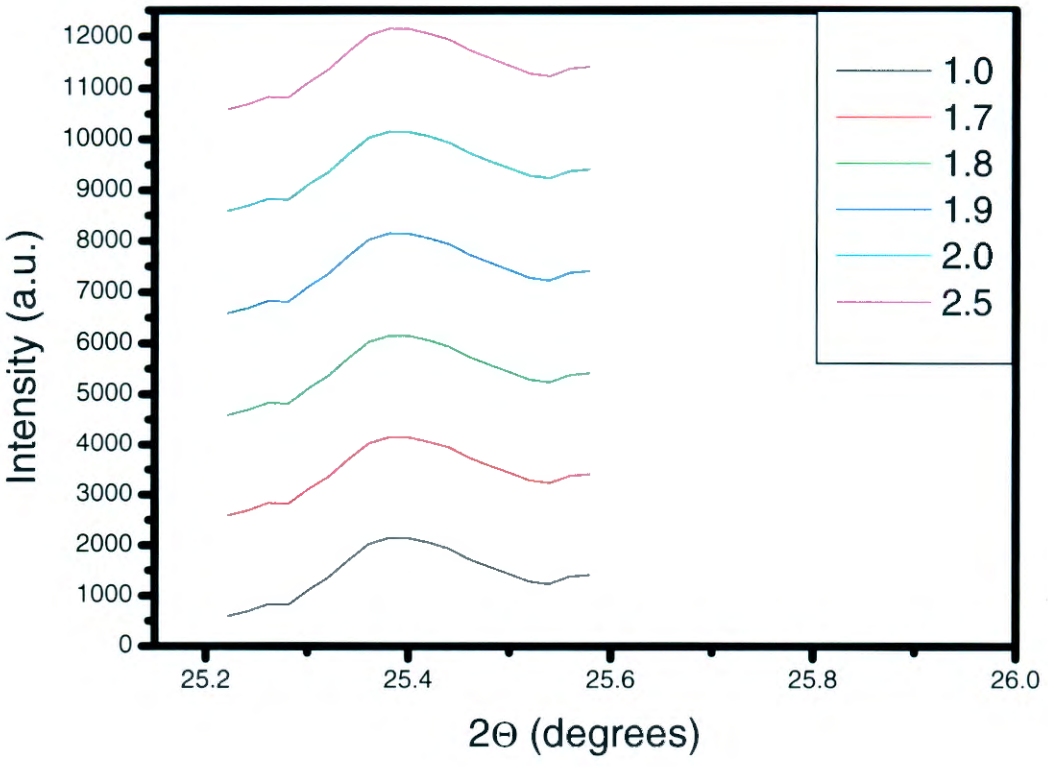

Figure 5.2. X-ray diffraction powder patterns at (*) plane for different La/S mole ratios.

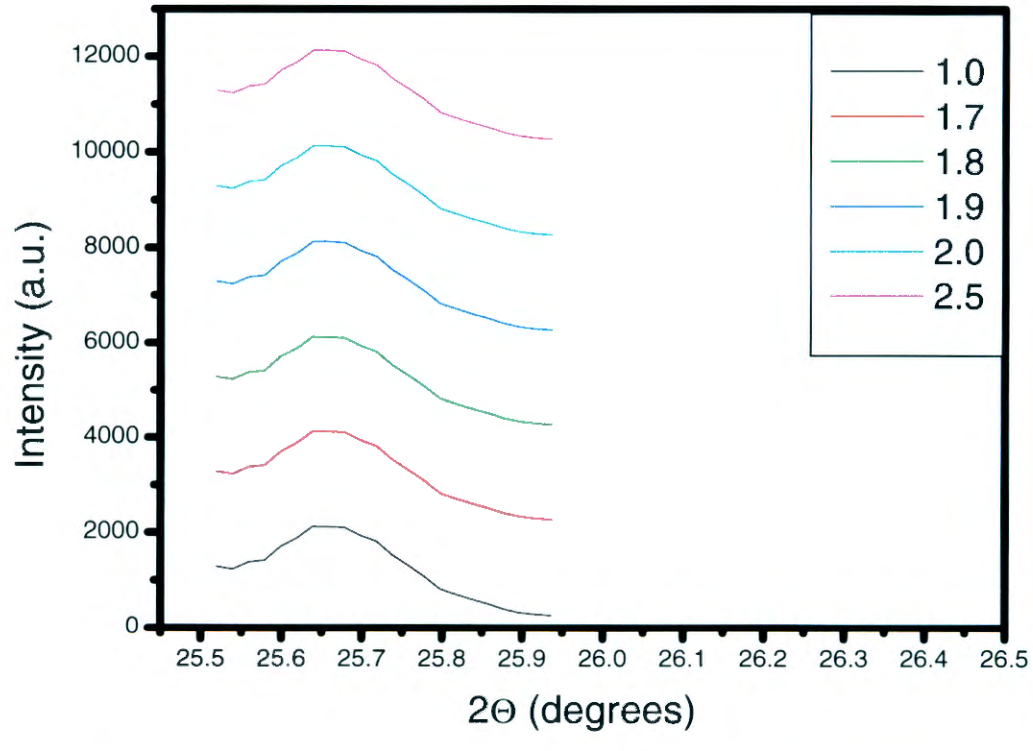

Figure 5.3. X-ray diffraction powder patterns at (101) plane for different La/S mole ratios.

Figure 5.2 shows a graph of X/X+Y versus La/S molar ratios. X denotes the intensity of the most pronounced peak of La_2O_2S which is in the [101] direction, while Y is the intensity of the most pronounced peak of La_2O_3. According to Figure 5.2, the ratio of the two intensities drop gradually between La/S=1 to1.7 and then drastically from La/S =1.7 to 2.5. This shows that at lower ratio of fuel to oxidizer favors the formation of the La_2O_2S rather than La_2O_3 phosphor. The diffraction peaks shift slightly towards lower angles with an increase in La/S mole ratios as shown in Table 5.2, indicating that the lattice parameters are slightly bigger than those of lower mole ratios, which is mainly due to larger radius of La^{3+} 1.18 Å than that of Eu^{3+} (0.95 °A). This indicates that the dopant ions are well incorporated into the lattice sites of La^{3+} at lower ratios and lead to the decrease in inter-atomic distance.

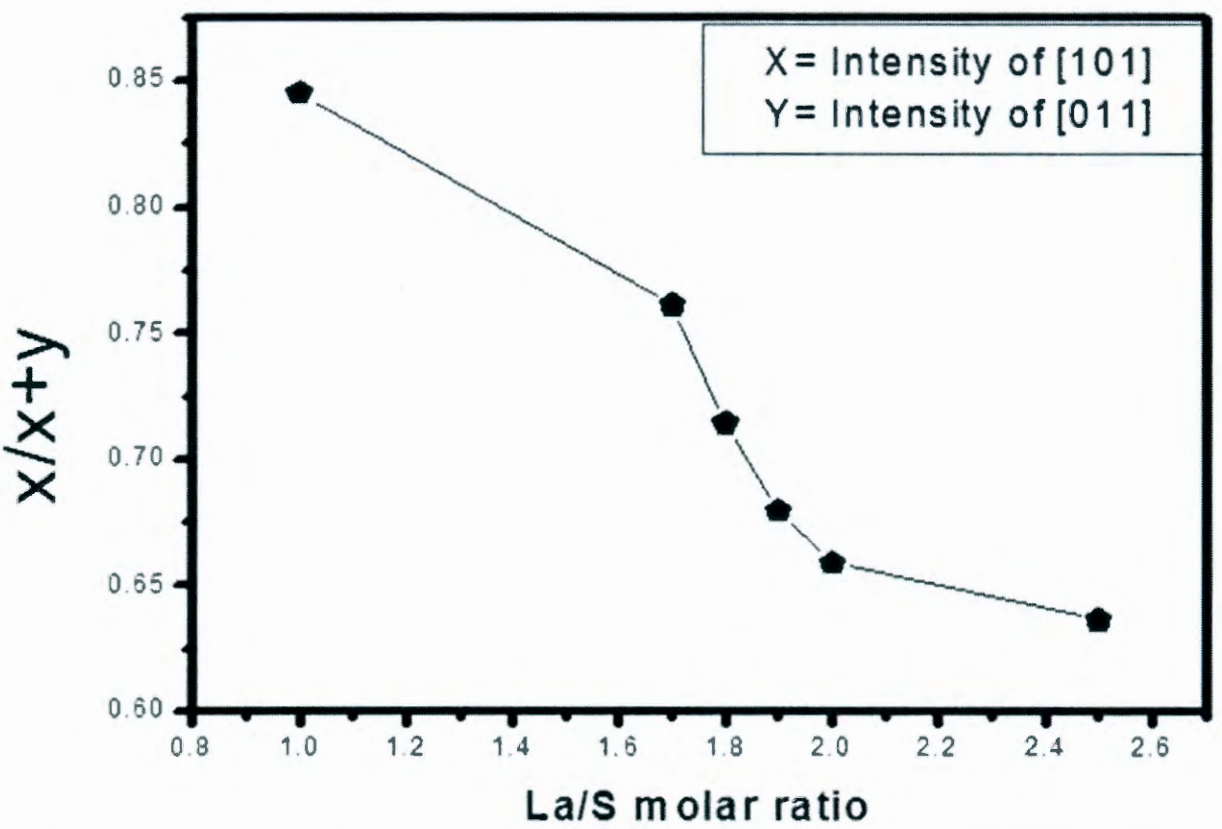

Figure 5.4. The effect of fuel on the formation of La_2O_2S and La_2O_3 prepared by the sol-combustion process.

Table 5.1. The concentration and calculated crystalline size of Eu^{3+} ion doped La_2O_2S microcrystals.

La/S	$2\theta^0$	β	Grain size (nm)
1.0	25.897	0.3786	178
1.7	25.827	0.4273	175
1.8	25.825	0.4519	185
1.9	25.819	0.2411	175
2.0	25.805	0.2256	182
2.5	25.798	0.2045	184

5.3.2. Fourier transforms infrared spectroscopy

The FTIR measurements have been made in the wave number range 400 $cm^{-1}$to 4500 cm^{-1} in order to identify the presence of La_2O_2S. The broad absorption band around 3420 cm^{-1} can be assigned to O–H stretching vibration; the bands around 1500 and 1387 cm^{-1} result from C–O asymmetrical stretching vibration; the peak that appears at 1074 and 1114 cm^{-1} can be assigned to C–O symmetric stretching vibration; the peaks at 856 and 670 cm^{-1} correspond to C–O deformation vibrations [20]. In the spectrum of the samples, the peak around 504 and 620 cm^{-1} associated with the vibration of La-O and La-S [21, 22] is observed, indicating the formation of La_2O_2S. It was observed that an increase in La/ S molar ratios reduce the absorption band at 504 cm^{-1}.

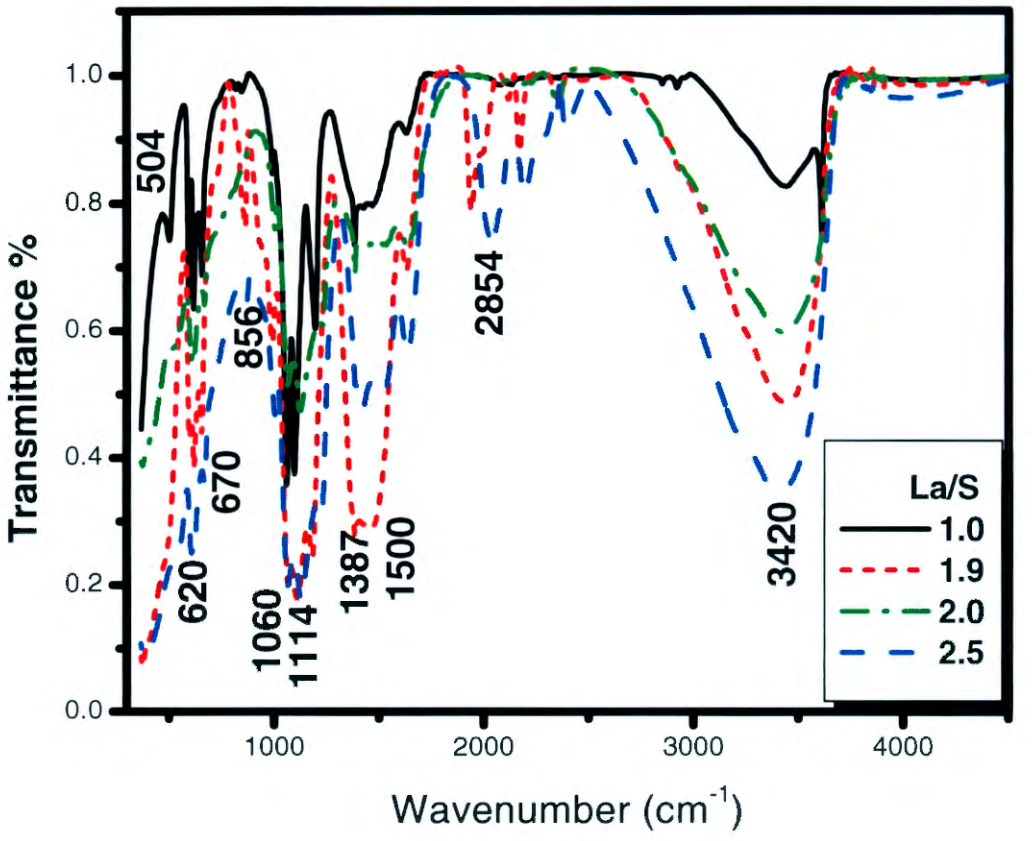

Figure 5.5. Fourier-transform infra-red spectroscopy spectra of the as-prepared La_2O_2S: Eu^{3+}powders for various La/S mole ratios.

5.3.3. X-ray photoelectron spectroscopy

XPS results for the powders of $La_2O_2S:Eu^{3+}$, to identify the presence of elementary states in the oxysulfides, are discussed in this section. Figure 5.6 (a) shows the wide-scan spectra of the hexagonal $La_2O_2S:Eu^{3+}$microstructures for the sample with La/ S mole ratio of 1.0 in the range of 0–1400 eV. All the expected elements can be identified from the survey. Figure 5.6 (b–d) shows the detailed regions of the XPS spectra of the hexagonal $La_2O_2S:Eu^{3+}$microstructures. The binding energy (BE) of the phosphors was determined with reference to the C1s peak at 284.6 eV, the de-convolution not shown. The high resolution XPS spectrum corresponding to the La3d states is characterized by a main doublet composed of six peaks situated at 833.2, 834.6, 837.9, 850, 851.8 and 854.7 eV when fitted by Gaussian

de-convolution. The peaks at 833.2 and 850 eV are related to $3d_{5/2}$ and $3d_{3/2}$ bonds in La_2O_3, respectively. The La 3d peaks show doublets attributed to spin-orbit coupling splitting of the 3d sublevels [23]. These are fitted with La $3d_{5/2}$ peaks (837.9, 850 eV) and $3d_{5/2}$ (851.8, 854.7 eV). The fitting also confirms that La^{3+} ions occupied two different sites. Three distinct components of O1s peak can be consistently fitted by Gaussian de-convolution, centered at 528.9, 530.8 and 532.1 eV, respectively. The first BE 528.9 eV is attributed to the La_2O_3. The other two components at the higher BE of 530.8 and 532.1eV can be attributed to the $La_2O_2S:Eu^{3+}$ [24, 25]. The S2p spectrum presents two components peaked at 168.7 and 169.9 eV. The peaks may be attributed to $2p_{3/2}$ and $2p_{1/2}$ bonds in $La_2O_2S:Eu^{3+}$. The S2p peaks are slightly weak as compared with that of the other major lines. The composition estimated by XPS using the relative sensitivity factors of O and S also revealed excess oxygen in the samples. The XPS results confirm that some impurities are formed (La_2O_3) after combustion synthesis at initial temperature of 400 °C under ambient condition which is consistent with XRD data.

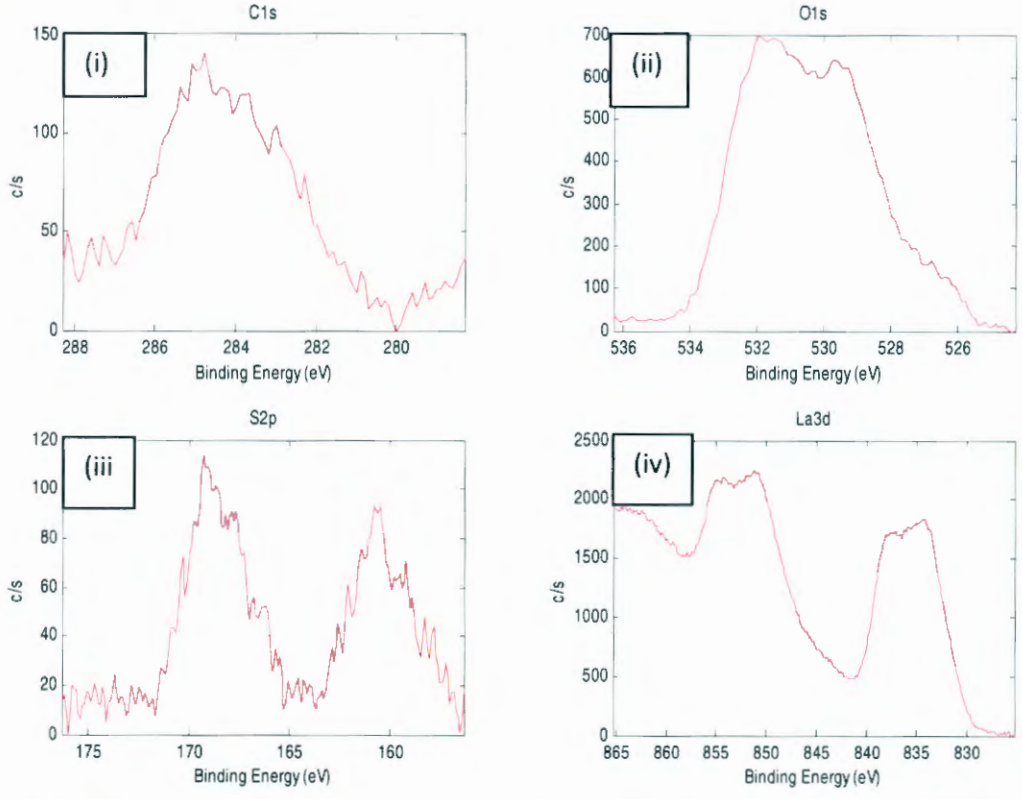

Figure 5.6 (a). Graph of (i) C1s (ii) O1s (iii) S2p and (iv) La3d for La_2O_2S microcrystals prepared with a La/S ratio of 2.5.

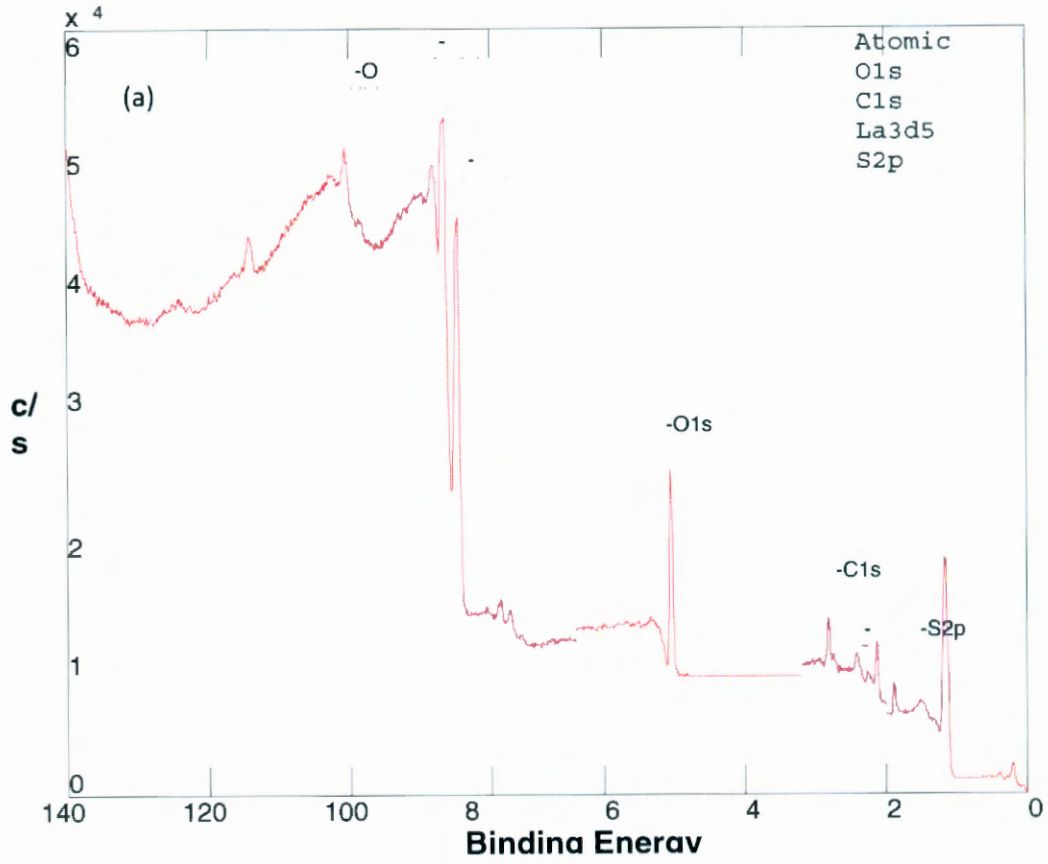

Figure 5.6 (b). XPS survey spectrum of the La_2O_2S microcrystals prepared with a La/S ratio of 1.0.

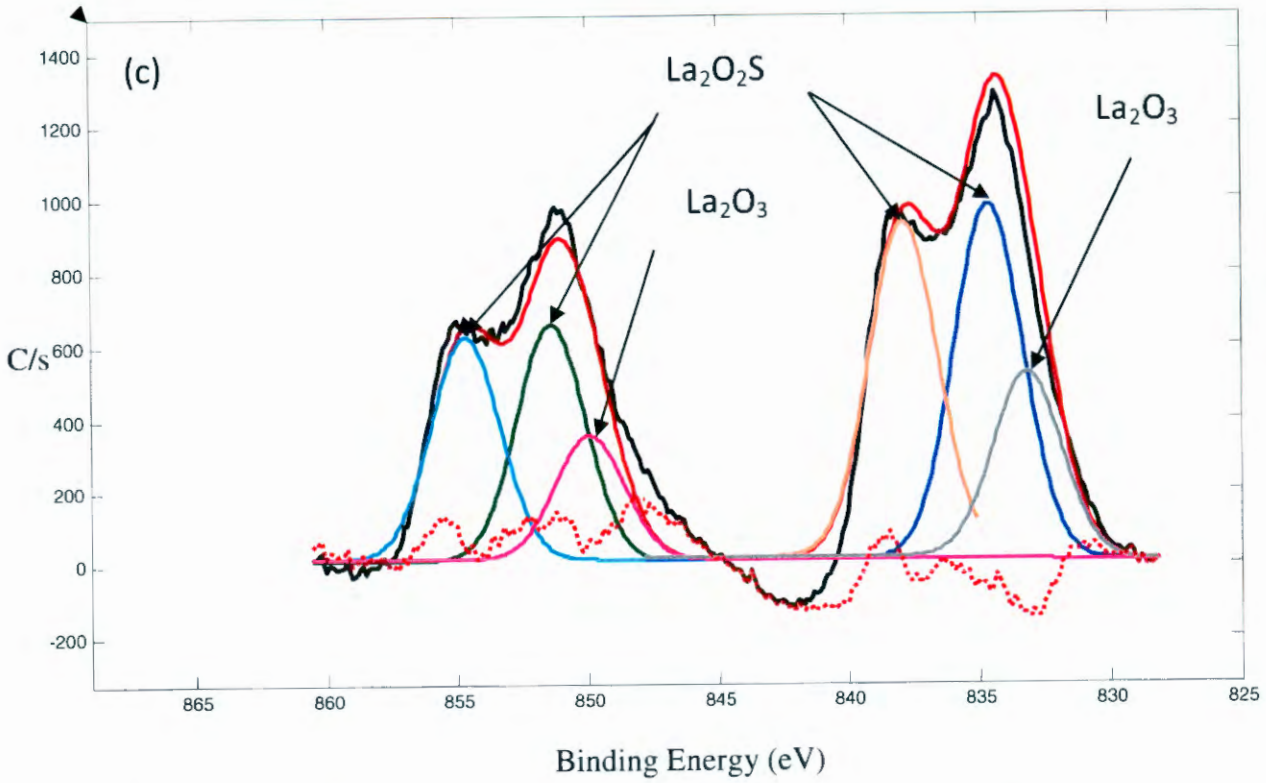

Figure 5.6 (c). La 3d XPS peakfitted with peaks for the La_2O_2S and the La_2O_3.

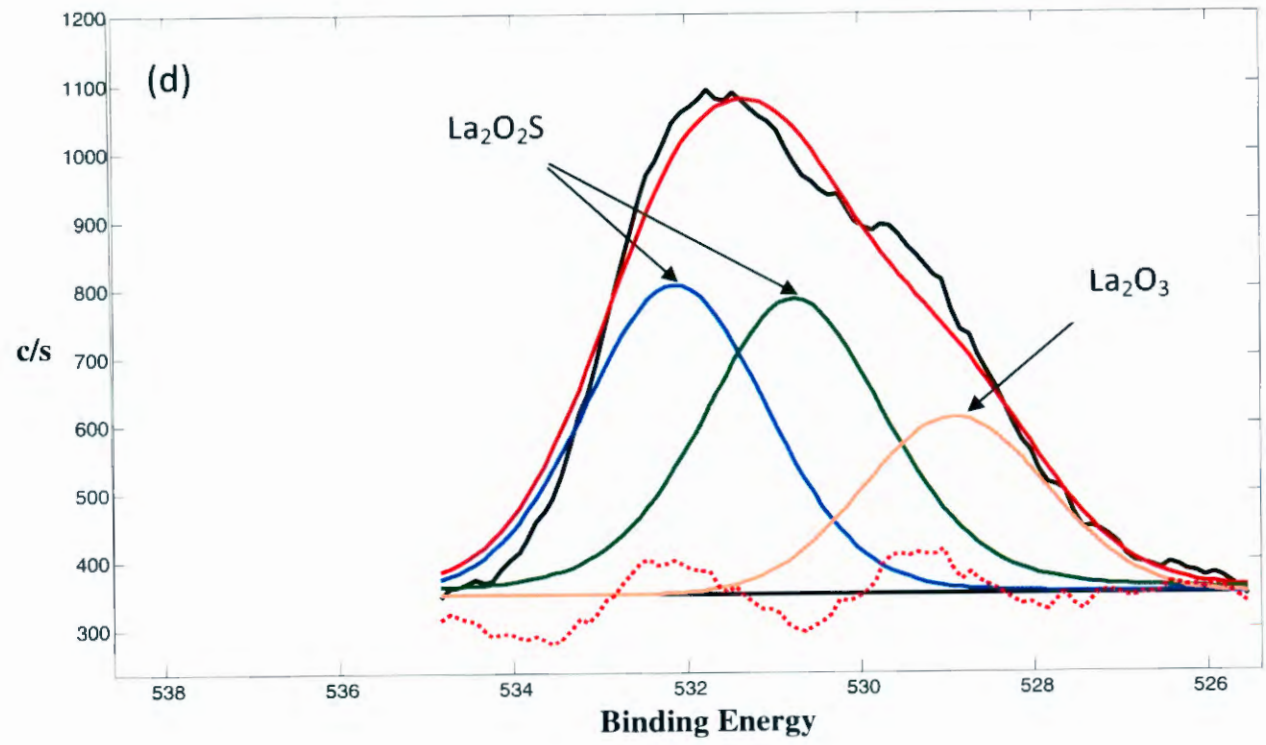

Figure 5.6 (d). XPS spectra of La ($3d_5/_2$) and O (1s) of the as-prepared Eu^{3+}- doped

La_2O_2S microcrystals.La 3d region for La_2O_2S and La_2O_3 with the peak fitting components for the $4p_{5/2}$ peak.

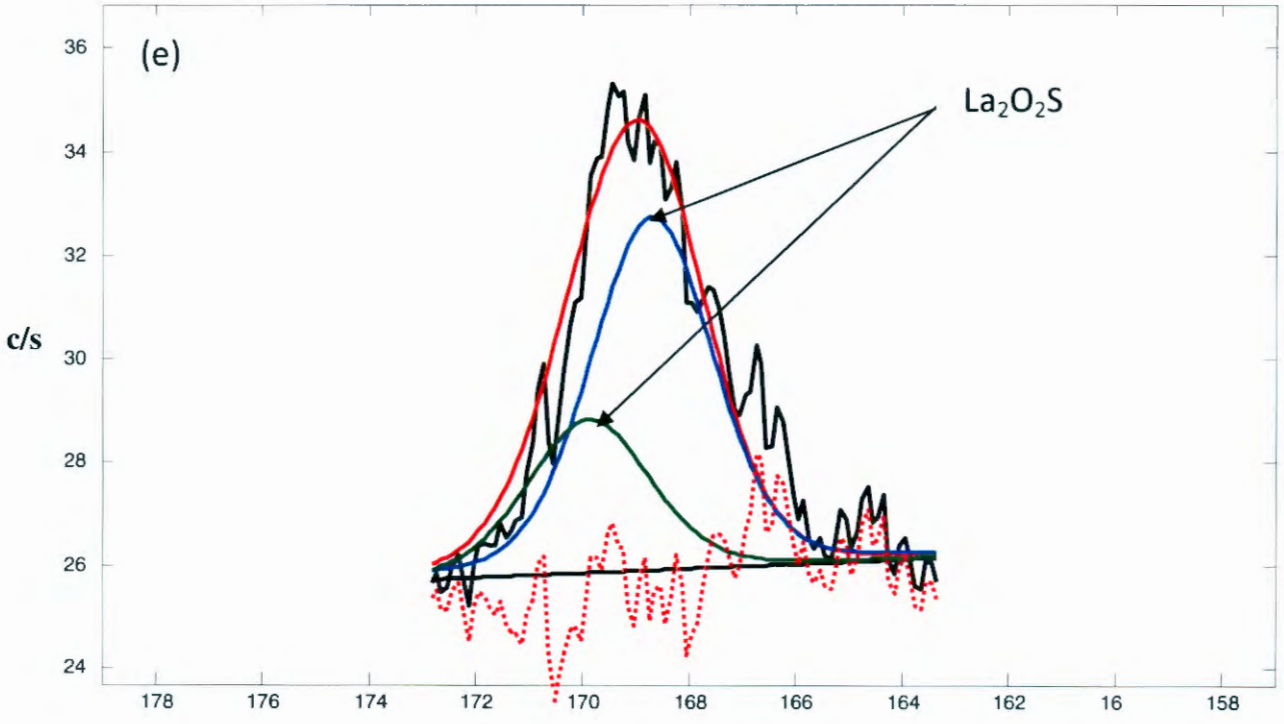

Figure 5.6 (e). XPS S2p peak for La_2O_2S with the peak fitting components for the $S2p_{5/2}$ peak.

5.3.4 Morphology

Figure 5.7 shows the SEM images of the La_2O_2S: Eu^{3+}microcrystalline powders. It is obvious that all the powders yield microparticles and they tend to aggregate together. The images show that the morphology consisted of a foamy agglomeration and a continuous three-dimensional network at lower fuel to oxidizer ratio. At higher La/S molar ratio the morphology appear as regular crystalline lattices.

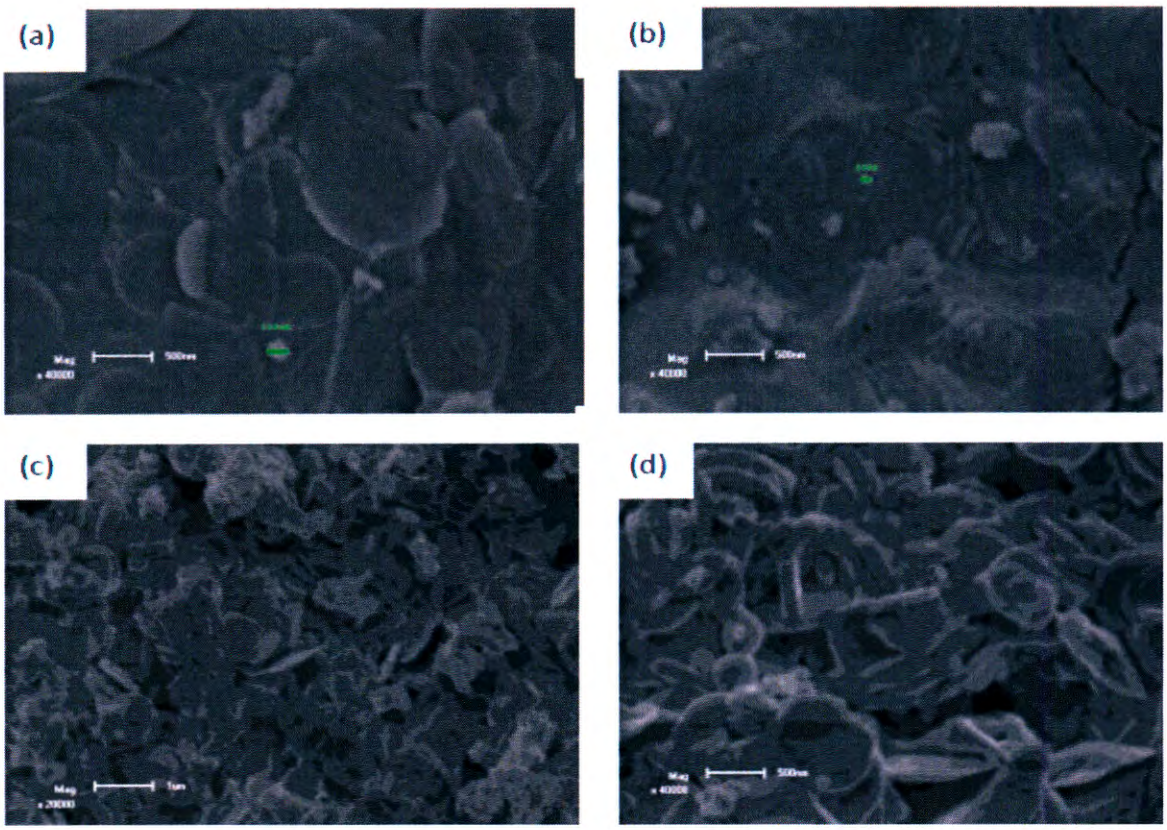

Figure 5.7. SEM micrographs of the as-prepared La_2O_2S: Eu^{3+}powders with La/S molar ratios of (a) 1.0, (b) 1.8, (c)2.0, (d)2.5 with 5000 nm field of view.

5.3.5 Photoluminescence

The excitation spectrum of the phosphor in the spectral region 200- 400 nm is shown in Figure 5.8 (a). The spectra mainly consist of two broad peaks, one located near 242 nm and the other near 328 nm. The band near 242 nm is attributed to the O^{2-} -Eu^{3+} CTB (charge transfer band), while the one near 328 nm is due to the La_2O_2S host absorption.

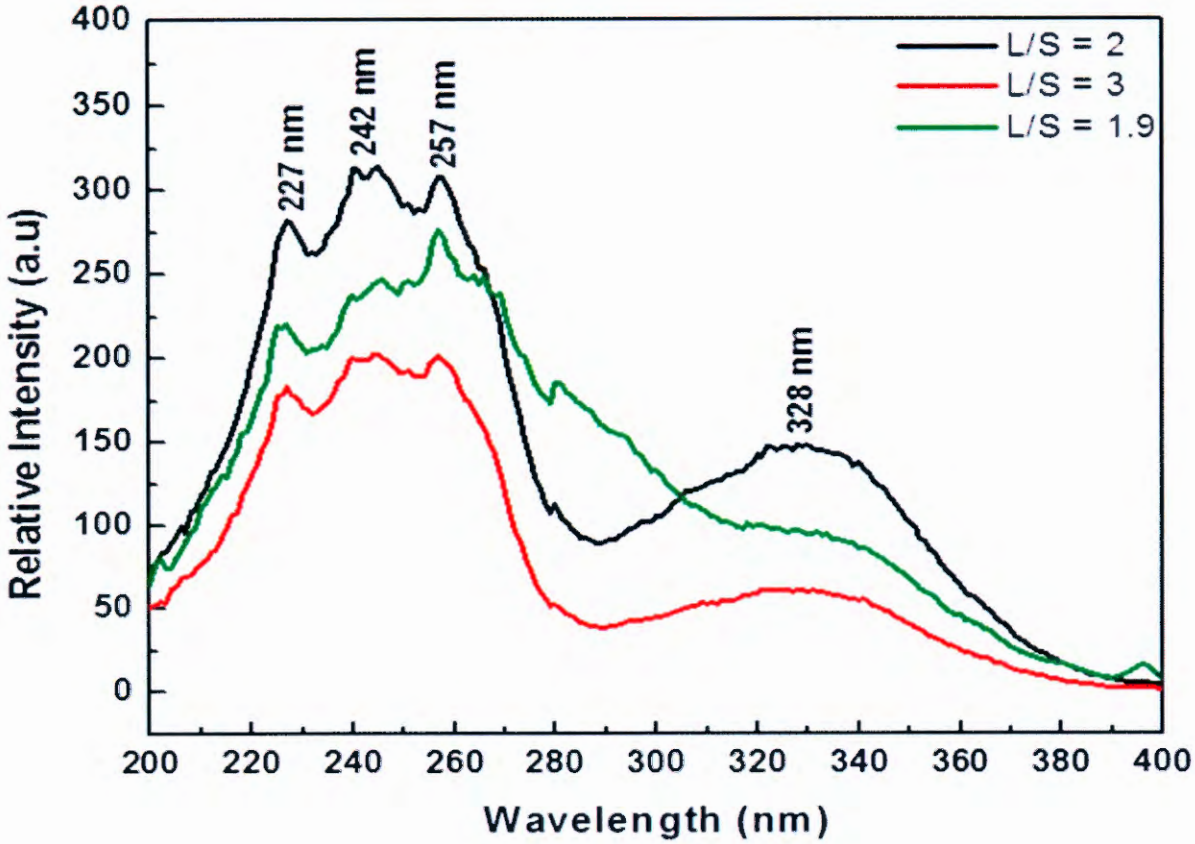

Figure 5.8 (a). Excitation spectra of La_2O_2S with different La/S molar ratios.

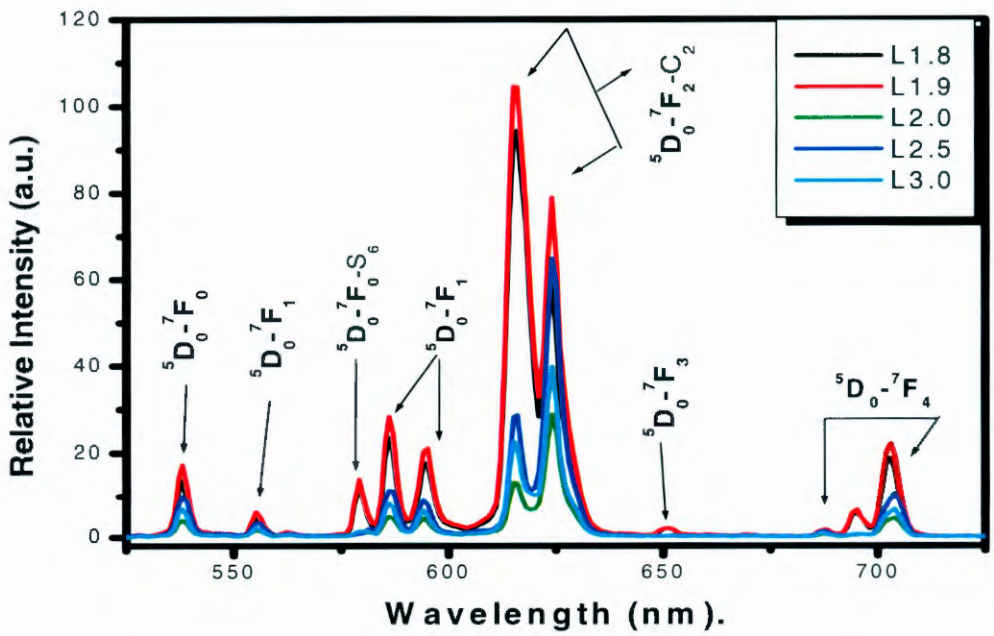

Figure 5.8 (b). PL emission spectra of La_2O_2S with La/S=1.8, 1.9, 2.0, 2.5 and 3.0 molar ratios.

Figure 5.8 (b) shows the emission spectra of Eu^{3+} which are assigned to the $^5D_0 \rightarrow {}^7F_{0,\,1,\,2,\,3,\,4}$ transitions of Eu^{3+}. There are three groups of distinctive emission peaks between 537 and 624nm, which are related to the $^5D_0 \rightarrow {}^7F_J$ (J = 0, 1, 2) transitions of Eu^{3+}, respectively. The strongest emission peak near 615 nm corresponding to forced electron dipole transitions of Eu^{3+} is due to the $^5D_0 \rightarrow {}^7F_2$ transition in the C_2 symmetry of Eu^{3+} incorporated in La_2O_2S, which is hypersensitive to environmental effects [26, 27]. In addition, there are other energy transitions of Eu^{3+} corresponding to $^5D_0 \rightarrow {}^7F_0$ (537- 555 nm), $^5D_0 \rightarrow {}^7F_1$– S_6 in S_6 symmetry (579-595 nm), $^5D_0 \rightarrow {}^7F_3$ (~650 nm) and $^5D_0 \rightarrow {}^7F_4$ (688- 713 nm) in the luminescence spectra [28]. In the hexagonal La_2O_2S there are two crystallographic sites, one with C_2 symmetry and the other with S_6 symmetry. Therefore, it can be concluded that the Eu^{3+} ions replace La^{3+} ions and occupy both the C_2 and S_6 symmetries because the emissions assigned to both symmetries were observed (Figure 5.8 (b)). The La/S molar ratios may be affecting the crystallinity of the system and consequently the neighborhood around the Eu^{3+} ions. Compared with the $^5D_0 \rightarrow {}^7F_2$ transition, the intensity of the $^5D_0 \rightarrow {}^7F_1$ transition corresponding to the orange color is much lower, which makes $La_2O_2S:Eu^{3+}$ a more pure red phosphor. The emissions of the samples doped with Eu^{3+} differ from each other, the peaks for samples La/S=2.0, 2.5 and 3.0 are quenched at emission wavelength of 615 nm but slightly enhanced at 624 nm wavelength. The $^5D_0$–$^7F_2$ transition is an electron dipole transition and thus is very sensitive to the symmetry in which the Eu^{3+} is situated. The peak intensity for samples La/S=1.8 and 1.9 are quenched at a wavelength of 624 nm. Bohus et al. [29] obtained emission spectra of core–shell Y_2O_3 :(Eu^{3+}, La^{3+}) samples and compared the spectra to the spectra of core–shell $Y_2O_3:Eu^{3+}$ samples and found new emission peaks that were visible at 613 and 622 nm. These emission peaks correspond to the $^5D_0$–$^7F_2$ transition of the $La_2O_3:Eu^{3+}$ phosphor. In $La_2O_3:Eu^{3+}$ phosphor Eu^{3+} ions replace La^{3+} ions at the C_2 symmetry sites and that is why new emission peaks appear at 613 and 622 nm in their case. The changes in the relative ratio of the $^5D_0$–$^7F_2$ to $^5D_0$–$^7F_1$ emission and the 615 nm to 624 nm emission may therefore be explained by the fact that there were presence of both electric and magnetic dipoles which favor enhancement of intensities depending on the position of emission wavelengths and also the La/S mole ratios. The relative change in the 615 nm to 624 nm emission ratios is an indication that for the higher La/S ratios the Eu^{3+} occupied the La^{3+} position in La_2O_3.

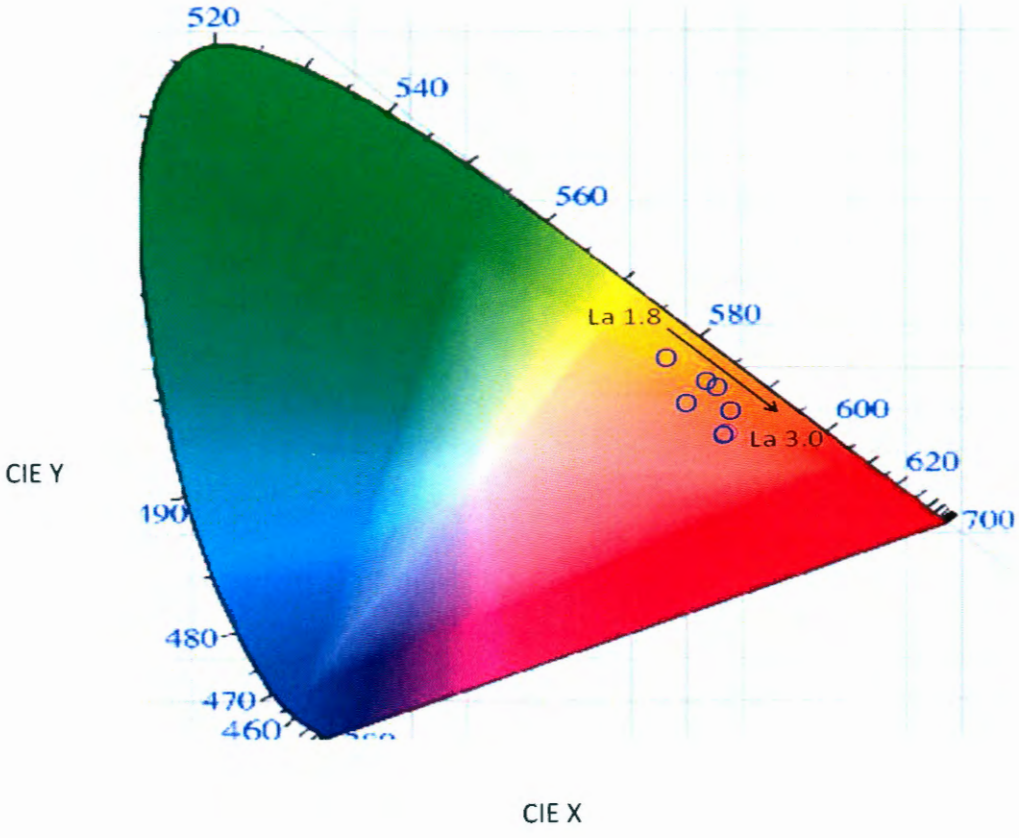

Figure 5.8 (c). CIE coordinate of emission of La_2O_2S phosphor.

Figure 5.8 (c) represents the chromacity co-ordinates of the PL spectra for the sample La/S=1.9, which are determined using the CIE (International Commission on Illumination) Coordinate Calculator software. According to the software the position of the color coordinates (0.49, 0.45) lie well in the red/orange region. The detailed analysis of the phosphor finds its suitability in making the red/orange producing phosphor for display applications and light emitting diode.

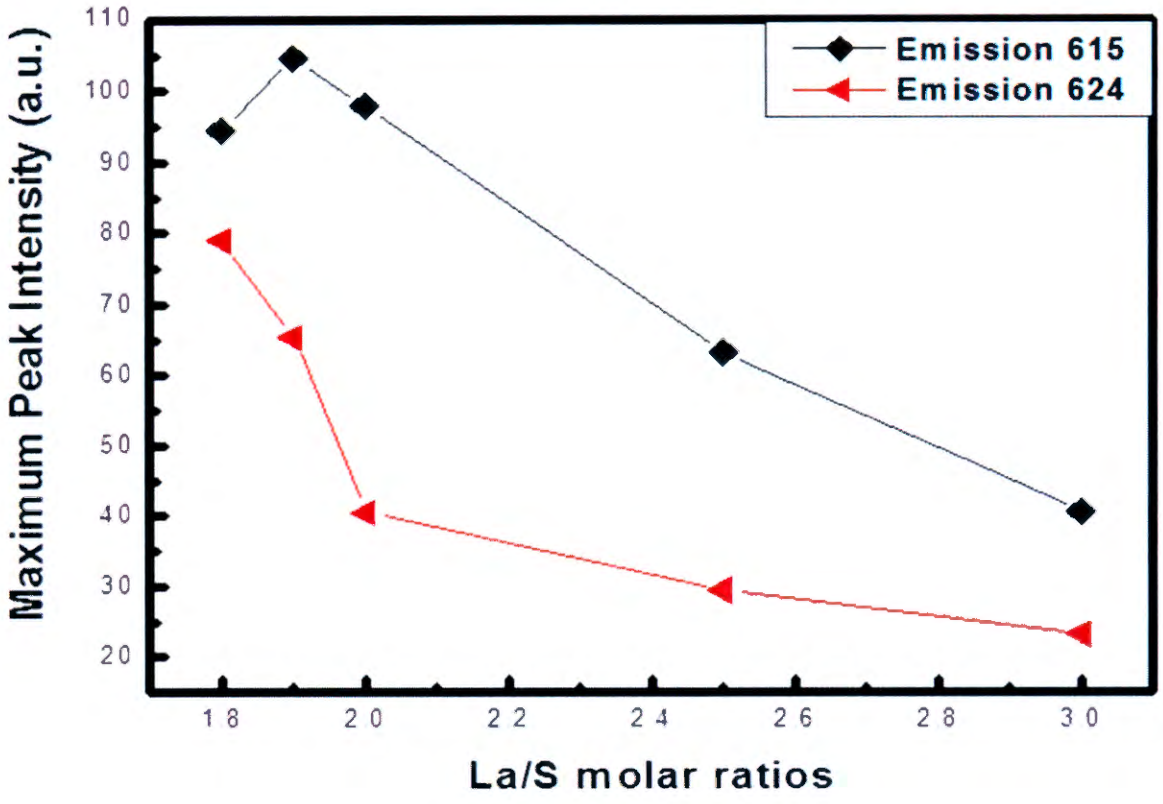

Figure 5.9. Graph of maximum peak intensity versus La/S molar ratios.

The graph of maximum PL intensity of the as-prepared powders as a function of La/S molar ratios are shown in Figure 5.9. The emission peak intensity decreased when the La/S molar ratio increased, and a maximum value was found when La/S=1.9, thereafter the emission intensity quenches gradually. Persistent luminescence spectra of the phosphor powders are shown in Figure 5.8. It can be seen from the spectra that the powders showed differences in initial intensity and medium persistence when the powders were efficiently activated by the UV lamp. The results indicate that the initial luminescence intensity and the decay time of phosphors are enhanced with a decrease in the La/S molar ratios. The Inset of Figure 5.8 indicates the plot of In (natural logarithm) of intensities versus the decay times of the phosphor. The slopes of the graphs decrease gradually and bend to be almost horizontal showing a double exponential function. The decay behavior can be analyzed by curve fitting, relying on the following double exponential equation:

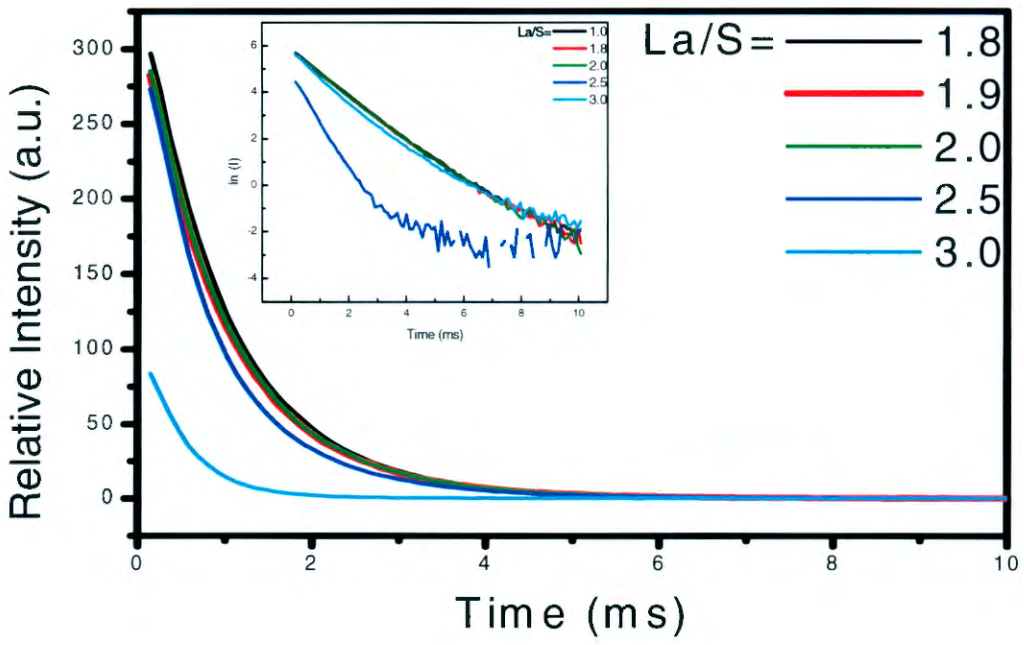

Figure 5.10. Afterglow characteristics of $La_2O_2S$with different La/ S molar ratios.Inset: A graph of ln log of intensity versus decay time showing a double exponential function.

$$I = A_1 \exp(-t/\tau_1) + A_2 \exp(-t/\tau_2) \text{ ---------- (5.5)}$$

WhereI is phosphorescence intensity, A_1, and A_2 are constants, t is time, τ_1 andτ_2 are decay constants, deciding the decay rate for rapid and slow exponentially decay components, respectively. The fitting results of parameters τ_1 and $\tau_2$are listed in Table 5.2 below.

Table 5.2. Results for the fitted decay curves of the phosphor powders with different La/S molar ratios.

La/S	**1.0**	**1.8**	**2.0**	**2.5**	**3.0**
Components(ms)					
Fast (τ_1)	0.97	0.95	0.91	0.88	0.82
Slow (τ_2)	1.08	0.99	0.97	0.95	0.89

Two components namely fast and slow are responsible for the luminescence properties of the as- synthesized phosphor. A trend can be observed (Table 5.2) that the decay constants of the phosphors decrease gradually with the increasing La/S molar ratios

5.3.6 Thermoluminescence

The peaks between 50 and 110^0C in the TL plots have been previously associated with persistent luminescence [30]. Our TL data for all the samples exhibit peaks below this range, which means they have poor afterglow. According to [31], defects introduced by doped ions play a key role in long-lifetime light emission. The doped Eu^{3+} ions can replace La^{3+}, creating traps of electrons and holes. Upon heating in the TL experiment, the trapped electrons and holes escape and recombine, resulting in the emission of light. The characteristic ionization energy of a trap can be estimated from the following equation:

$$E = {2k(T_m)^2}/{T_2} - T_m \text{----------} (5.7)$$

Here k is the Boltzmann constant, T_m is the TL peak temperature and T_2 corresponds to the point on the slope to the right of the TL peak where the intensity is half of the peak value. The related parameters are calculated using equation (5.7) and are listed in Table 5.3.

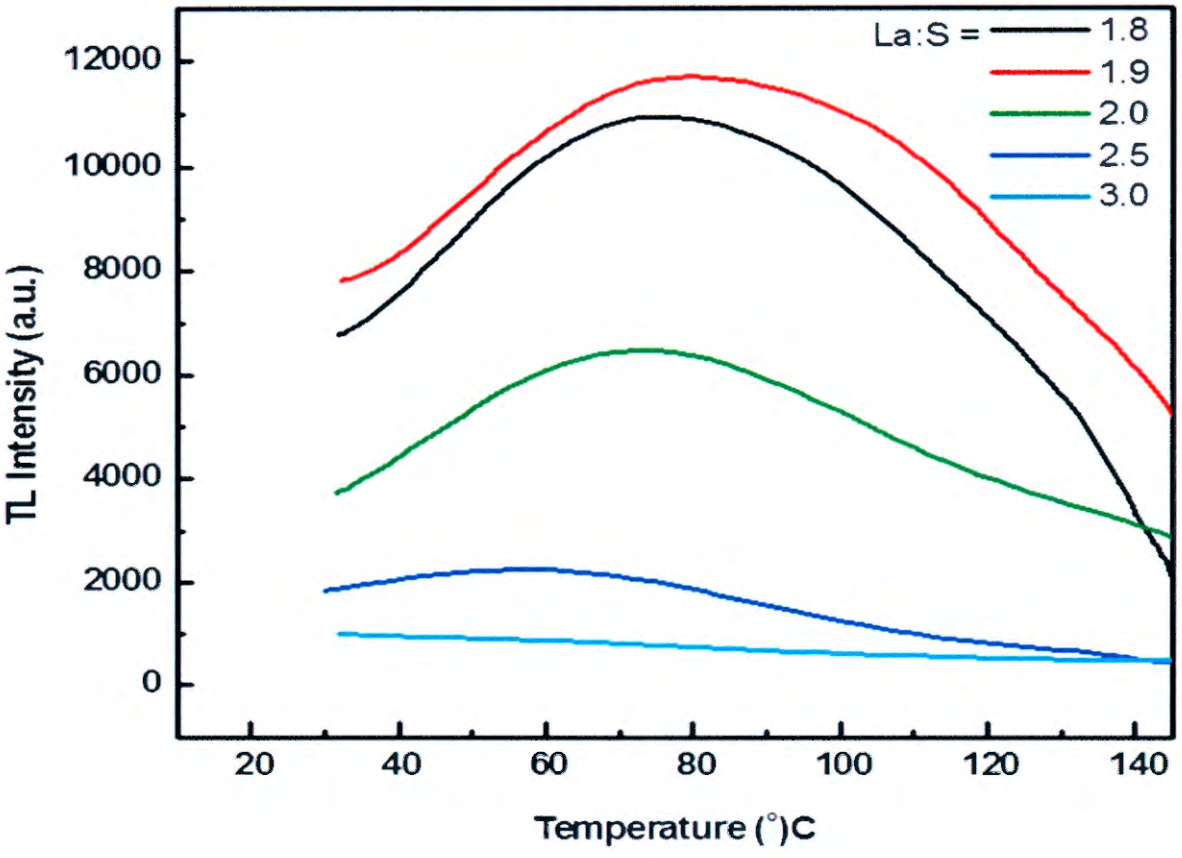

Figure 5.11. Thermoluminescence plots of the La_2O_2S: Eu^{3+} phosphor.

In order to achieve long-lasting phosphorescence, the trapping levels need to be located at suitable depths. If the trap level is too shallow, only a small amount of electrons can be captured by the traps. Under the action of thermal disturbances, electrons are easily released from traps and then recombine with holes in the ground state, which results in a shorter afterglow time. On the other hand, if the traps level is too deep, it would be difficult for the captured electrons to gain enough energy to return to the excited state levels at room temperature, which also results in a poor afterglow property [32, 33]. From Table 3, the sample with a La/S=1.8 and1.9 ratios have the most suitable depth of 0.81 and 0.80eV, respectively which also give the highest peak intensities in the PL spectra as shown in Figure 6(b) [34, 35]. The intensity of the sample with a La/S= 2.0 ratio was low due to a too deep trap level (1.8 eV), while that of the sample with a La/S=2.5 and 3.0 ratio were lower due to shallower trap levels (0.58eV).

Table 5.3. Trap energy levels for different concentration of La_2O_2S.

La/S	T_m(k)	T_2 (k)	E (eV)
1.8	300.4	331.4	0.8
1.9	350.0	376.2	0.8
2.0	350.2	369.1	1.8
2.5	327.3	378.2	0.6
3.0	302.8	346.4	0.6

5.4 Conclusions

In conclusion, trivalent-europium doped La_2O_2S microcrystals were prepared by sol-combustion method and their material properties were studied at room temperature. The phosphors emit bright red phosphorescence originating from the $^5D_0$- $^7F_2$ transition of Eu^{3+}.TheXRD pattern of the as-synthesized powder revealed the presence of the hexagonal La_2O_2S phase with an average crystalline sizes of 178 nm with a space group P3m1[164] and cell constants of (a) 0.4128 nm and (*c*) 0.6985 nm. The lower ratio of fuel to oxidizer favors the formation of the La_2O_2S rather than La_2O_3 phosphor. De-hydration of the reactants was crucial for the successful synthesis of the oxysulfide phase. SEM images of the as-synthesized powders showed that the morphology consisted of a foamy agglomeration and a continuous three-dimensional network. At higher La/S molar ratio the morphology appear as regular crystalline lattices.

References

[1] P. Majewski, M.Rozumek, H. Schluckwerder, F. Aldinger, Int. J. Inorganic Mater. 3 (2001) 1343.

[2] G-Murillo, C. Luyer, C. Garapon, C. Dujardin, E. Bernstein, C. Pedrini, J. Mugnier, Opt. Mater. 19 (2002) 161.

[3] W. Jungowska, J. Thermal Anal. Calorimetry 60 (2000) 193.

[4] T, Feldmann, T. Justel, C. Ronda, P. Schmidt, Adv. Funct. Mater.13 (7) (2003) 511.

[5] Y. Nakanishi, in: Proc. of the III Int. meeting on Information Display, IMID, Daegu, Korea, (2003) 203.

[6] V.L. Levshin, M.A. Konstantinova, E.A. Trapeznikova, on the application of rare-earth elements in the chemistry of phosphors, in: Rare-earth Elements, USSR AN Publishing, Moscow (1959) p. 314.

[7] T. Hisamune, Technical trend of phosphors for plasma display panels, in: Proceedings of the 9th International Display Workshops (2002) p. 685.

[8] T. Justel, H. Nikol and C. Ronda. Angew.Chem. Int. 37 (1998) 3085.

[9] S. Shionoya and W.M. Yen, Editors, Phosphor Handbook, CRC Press, Boca Raton, FL (1998).

[10] C.F. Bacalski, M.A. Cherry, G.A. Hirata, J. Mckittrick, J. Mourant, J. Soc. Inf. Display (Suppl-1) (2000) 93.

[11] G.C. Kim, H.L. Park and T.W. Kim. Mater. Res. Bull. 36 (2001) 1603.

[12] M. Kottaisamy, D. Jeyakumar, R. Jagannathan, M.M. Rao. Mater. Res. Bull.31 (1996), 1013.

[13] M.I. Martnez-Rubio, T.G. Ireland, G.R. Fern, et al. Langmuir 17 (2001) 7145.

[14] Y. Tian, W.H. Cao, X.X.Luo, et al. J. Chin Rare earth Soc, 23(2005) 271.

[15] T. Hirai, T. Orikoshi. J Colloid Interface Sci, 273(2004) 470.

[16] L.E. Shea, J. Mckittrick, O.A. Lopez, E. Sluzky and M.L. Phillips, J.Soc.Inf. Display5 (1997) 117.

[17] K.C. Patil and S. Ekambaram., J.Alloys Compounds248 (1997) 7.

[18] T. Jin, S. Tsutumi, Y. Deguuchi, K. Machida, G. Adaci, J. Alloys Compounds 252 (1997) 59.

[19] B. Tissue, B. Bihari, J. Fluoresc. 8 (4) (1998) 289.

[20] M. Haase, K. Riwotski, H. Meyssama, A. Kornowski, J. Alloys Compounds 303-304 (2000) 191.

[21] G. Bohus, V. Hornok, A. Oszkó, A. Vértes, E. Kuzmann, I. Dékány, Colloids and Surfaces A: Physicochemical and Engineering Aspects, 405(5) (2012) 6-13.

[22] A. Huignard, T. Gacoin, J.P. Boilot, Chem. Mater. 12 (4) (2000) 1090.

[23] N. Murase, R. Jagannathan, Y. Kawasaki, J. Alloys Compounds 303-304 (2000)191.

[24] Y. Volokitin, J. Sinzig, L. Jongh, G. Schmid, M. Vargaftik, I. Moiseev, Nature 384 (1996) 621.

[25] R. Sakai, T. Katsumata, S.Komuro, T. Morikawa, J. Lumin. 85 (1-3) (1999) 149.

[26] G. Liu, G. Hong, X. Donga, J. Wang, J. of Lumin. 126 (2007) 702–706

[27] J. Silver, M.I. Martunez, T.G. Ireland, R.J. Withnall, J. Phys. Chem. B 105 (2001) 7200;

[28] M. Maitric, B. Antic, M. Balanda, D. Rodic, M.L. Napijalo, J. Phys. Condens. Matter 9 (1997) 4103.

[29] Z.X. Yuan, C.K. Chang, D.L. Mao, W.J.J. Ying, J. Alloys Compd. 377(1) (2004) 268-271 77.

[30] M. Ihara, T. Igarashi and T. Kusunoki,J. Electrochem. Soc. (2002)**149**72.

[31] J. Qiu, A.L. Gaeta and K. Hirao, Chem. Phys. Lett. *(2001)***333**236.

[32] J. Geng, Z.P. Wu, W. Chen and L. Luo, J. Inorg. Mater. *(2003)* **175**480.

[33] H.H. Zheng, X.M. Zhou, L. Zhang, X.P. Dong, J. Alloys Compd. 460 (2008) 704- 707.

[34] H. Yamamoto and T. Kano, J. Electrochem. Soc. (1979) 126, 305.

[35] H. Jungk, C. Feldman, J. Mater. Sci. 36 (2001) 297.

Chapter 6

The influence of oxygen partial pressure on material properties of Eu^{3+}-doped Y_2O_2S thin film deposited by Pulsed Laser Deposition

6.1 Introduction

Europium-doped Y_2O_2S exhibits strong UV and cathode ray-excited luminescence, so it is widely used as red phosphors for low-pressure fluorescent lamps, cathode-ray tubes and plasma display panels (PDPs) [1]. Also, the hexagonal Y_2O_2S is a good host material for rare earth ions. A lot of attention has been given to the nanoscale $Y_2O_2S:Eu^{3+}$ for its tremendous potential applications in optical display and lighting materials and basic science research on special luminescent spectra [2-4]. Nanoscale $Y_2O_2S:Eu^{3+}$ has remarkably different luminescent properties from those of bulk samples: such as emission line broadening, lifetime changes and its spectral shift [5]. There are several methods to synthesize nanocrystalline $Y_2O_2S:Eu^{3+}$, such as sol–gel [6], combustion [7], micro emulsion [8], and spray pyrolysis method [9], but these methods are limited in the complexity of the preparation methods. Solid state reaction at room temperature is a good method to synthesize nanoparticles [10-12]. It is generally accepted that thin-film phosphors have several advantages over bulk-type powder phosphors: better thermal stability, reduced outgassing, better adhesion, and improved uniformity over substrate surface. However, the biggest hindrance in the application of thin-film phosphors is their low brightness and efficiency in comparison to those of powder phosphors. Pulsed laser deposition (PLD) technique, which provides a unique process for stoichiometric evaporation of target materials and control of film morphology [13, 14], has been used for the deposition of oxysulfide films [15–17].

In this work, we report on a study of the PLD conditions, the consequent crystalline and surface morphology structures, and photoluminescence (PL) characteristics of $Y_2O_2S:Eu^{3+}$ thin films.

Physica B: Physics of Condensed Matter (2016), pp. DOI information: 10.1016/j.physb.2015.10.005

Our study showed that the oxygen partial pressure positively affected the crystalline phase, the morphology and the PL efficiency of the thin films. The luminescence results show that the PL intensity from $Y_2O_2S:Eu^{3+}$ films under oxygen partial pressure may be as much as 1.4 times higher than that from $Y_2O_2S:Eu^{3+}$ film deposited in vacuum. As far as our knowledge is concerned, no one has so far investigated the influence of oxygen partial pressure of material properties of $Y_2O_2S:Eu^{3+}$ under these conditions and achieved similar results.

6.2 Experimental procedure

6.2.1 Powder synthesis

$Y_2O_2S:Eu^{3+}$ nanocrystals were synthesized using the sol- combustion route. The method of synthesis essentially comprises of mixing the precursors in appropriate stoichemetric ratios, followed by firing in an air tube furnace at a temperature of 500 °C. The white foamy product was then grounded and left to dry in an enclosed oven for 24 hours. A pellet with a 2.4 cm diameter and 6 mm thickness was prepared by pressing the $Y_2O_2S:Eu^{3+}$ powder for 1hour at a pressure of 1.96×10^7 mbar. The pellet was then annealed for 3 hours at 600°C temperature in an open –air furnace to improve its hardness.

6.2.2 Pulsed Laser Deposition (PLD)

The Si (100) wafers used as substrate were first cleaned using ethanol, followed by methanol each for 10 minutes in a ultrasonic bath. This was followed by rinsing the substrate in distilled water also for 10 minutes in a ultrasonic bath. The cleaned substrate was then dried in an oven for 2 hours. The deposition chamber was evacuated to a base pressure of 8×10^{-6} mtorr. The Lambda Physic 248 nm KrF excimer laser was used to ablate the phosphor pellet in vacuum and various O_2 partial pressure atmospheres. A Baratron Direct (Gas Independent) PressureVacuum capacitance Manometer (1.33×10^{-2} mtorr) was used for the high pressure measurements. The laser energy density, number of pulses and laser frequency were set to 0.74 J/cm^2, 12000 and 10 Hz respectively. The substrate temperature was fixed at 300 °C, and the target to substrate distance was 5 cm. The ablated area was 1 cm^2. The Shimadzu

Superscan SSX-550 system was used to collect the Scanning Electron Microscopy (SEM) micrographs. Atomic Force Microscopy (AFM) micrographs were obtained from the Shimadzu SPM - 9600 model. X-ray diffraction (XRD) data was collected by using a SIEMENS D5000 diffractometer using CuKα radiation of $\lambda = 1.5405$ nm. PL excitation and emission spectra were recorded using a Cary Eclipse fluorescence spectrophotometer (Model: LS 55) with a built-in xenon lamp and a grating to select a suitable wavelength for excitation. The excitation wavelength was 230 nm and the slit width was 10 nm. The afterglow curves for the films were also obtained with the Cary Eclipse spectrophotometer.

6.3 Results and discussion

6.3.1 X-ray diffraction

Figure 6.1 shows the XRD patterns of $Y_2O_2S:Eu^{3+}$ thin films grown at 300 °C in vacuum atmosphere as well as in various oxygen partial pressures. The patterns show mixed phases of cubic and hexagonal crystal structures. The films grown at low and high oxygen partial pressure are predominantly cubic, while that grown at moderate pressure (100 mtorr) is predominantly hexagonal. The average lattice parameters for hexagonal phase a=3.785nm and c=6.589nm, are very close to the standard values provided in the powder diffraction file PDF #24–1424. The intensities of the XRD peak from the (100) and (113) crystal planes were found to increase with the oxygen partial pressure in the range from 20 to 140 mtorr O_2. This may be attributed to the enhanced oxidation kinetics and improvement in crystalline nature of the films. As the oxygen partial pressure increase, the crystallinity of the films improved. It is also clear that the 300 °C thin film consist of nanoparticles as seen from the broad XRD peaks. The estimated crystallite size of the films with hexagonal and cubic phase ranging between 50 and 70 nm and is shown in figure 2.

It is observed that for the $Y_2O_2S:Eu^{3+}$ nanostructures, there is a marginal decrease (-0.26%) in crystallographic unit-cell that tends to contract due to the increase in surface area of the deposited film as compared to that of the substrate itself. This may have been caused by stress between the two surfaces and may lead to a decrease in the lattice constant. Eu_2O_3 diffraction peaks from XRD patterns were not detected indicating that the Eu^{3+} was incorporated into the Y_2O_2S host lattice homogeneously [18].

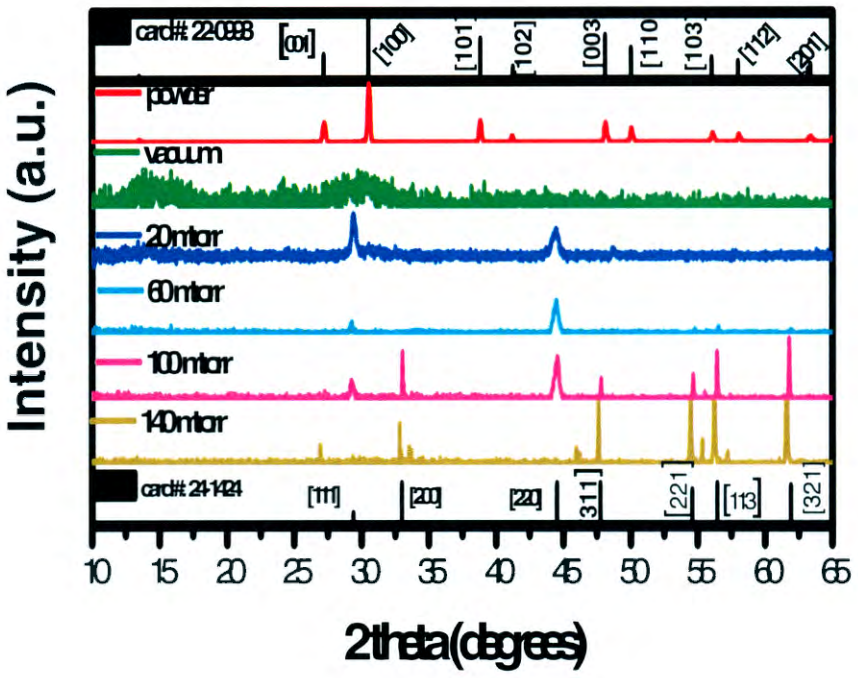

Figure 6.1. X-ray diffraction patterns of films deposited in vacuum and various O_2 partial pressures and the standards JCPDS card Nos: 24-1424 and 22-0993.

Figure 6.2 shows the role of oxygen partial pressure on crystallite sizes and axial ratio. A monotonous increase of the axial ratio (c/a) and decreasing particle size is established by means of X-ray analysis for a series of thin films deposited at vacuum as well as various oxygen ambient. It is shown that the effect cannot be explained by impurity or intrinsic defects in the thin films. The relations obtained are based on the size dependence of the internal stress and the intra-crystalline pressure stipulated by the interaction of the elements of the crystal charge lattice. Calculations made for the ion charge lattice of quartz agrees with the monotonous increase of the lattice parameters with decreasing particle size.

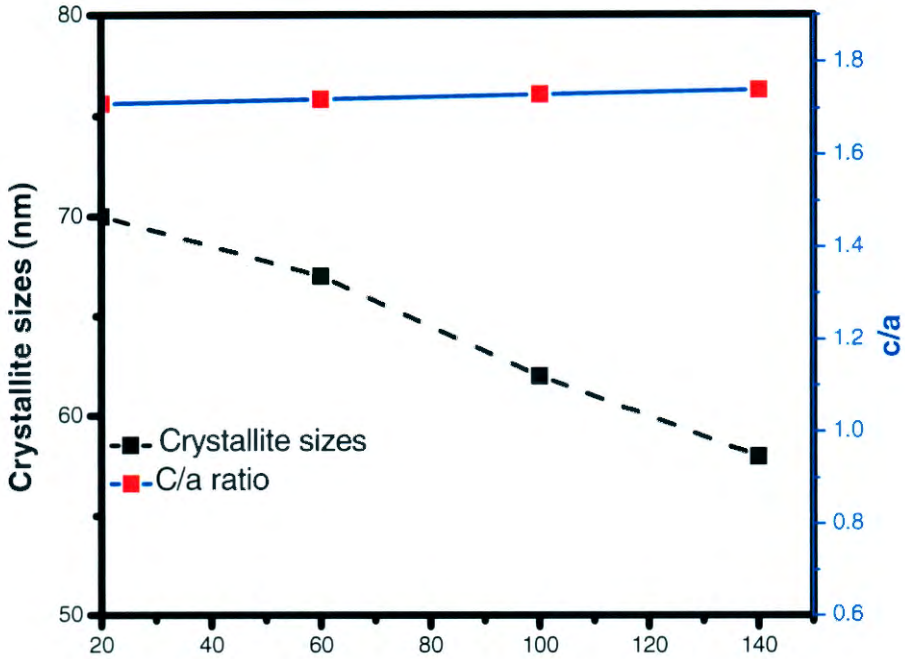

Figure 6.2. Crystallite sizes and axial ratio as functions of oxygen partial pressure

Table 6.1: Showing how oxygen partial pressures affect lattice parameters and particle size of the films.

O_2 partial pressure (mtorr)	Lattice parameters			Particle size (nm)
	Hexagonal		Cubic	
	a	c	a	
Vacuum	-	-	-	-
20	3.805	6.650	3.789	70 ± 0.5
60	3.798	6.642	3.785	67 ± 0.5
100	3.786	6.633	3.781	62 ± 0.5
140	3.745	6.596	3.776	58 ± 0.5

6.3.2 Morphology

Figure 6.3 shows the SEM images for $Y_2O_2S:Eu^{3+}$ thin films ablated in a) vacuum, b) 20 mtorr, c) 100 mtorr and d) 140 mtorr oxygen ambient, at 300 °C and fluence of 1.6 ± 0.1 J cm^{-2}. The thin film ablated in vacuum and 20 mtorr O_2 show rougher layers. A smoother surface is however visible from the films ablated in 60 mtorr O_2 and it appears as a layer consisting of spherically shaped nano - particle layer in all the images. The film deposited in 140 mtorr ambient show some layer on the substrate which is even smoother than that in figure c) as shown in figure d). The size distribution was broad and the average diameter was about 60± 0.5 nm. The existence of bigger micron size particles also occur on all the thin films. These bigger micron particles can severely degrade the performance of electronic and optical devices and elimination can be done by optimization of the process parameters [19]. These SEM images give a rough indication of the surface morphology but better imaging was obtained with AFM analysis.

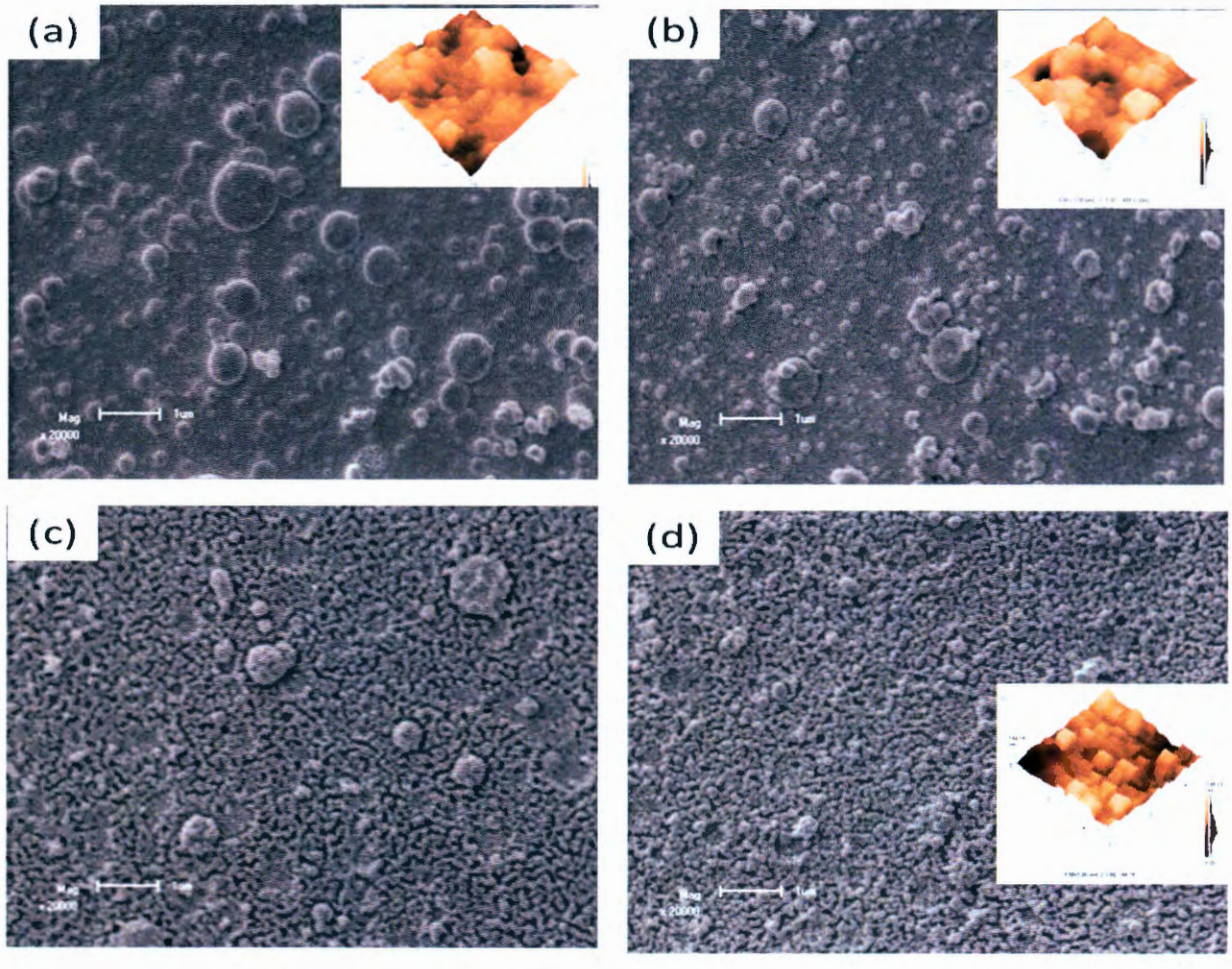

Figure 6.3: SEM images of the thin films ablated in a) vacuum, b) 20 mtorr, c) 60 mtorr and c)140 mtorr O_2 ambient at 300 °C with a fluence of 0.767 ± 0.1 Jcm-2 (5 kV beam energy, magnification of x 20 000 and a scale of 1 μm (FOV: 2 x 1μ m). As insets: 3D Height AFM images done in contact mode for the thin films ablated in a) Vacuum, b) 20 mtorr and c) 140 mtorr oxygen ambient.

6.3.3 Atomic Force Microscopy (AFM)

Figures 6.3 also shows AFM images of the samples deposited in (a) vacuum, (b) 20 mtorr and (c) 140 mtorr as insets. It is clear that almost hexagonally-shaped nanoparticles were deposited during the deposition process. The particle sizes of the different films varied from 60 to 70 nm depending on the oxygen partial pressure. An average particle size of 70 nm was calculated for the film grown at 20 mtorr, 300 °C, and the particle size of 58 nm was calculated for the film grown at 140 mtorr, 300 °C. The particles were also less agglomerated at the higher oxygen partial pressures. The mean free path of the particles in a low ambient pressure is longer compared to the mean free path at higher ambient pressures.

More collisions between the ultrafine particles (vaporised particles close to the target) at a higher ambient pressure lead to nucleation and growth of smaller nanoparticles when arriving at the substrate. In vacuum there are virtually no collisions between the particles before reaching the substrate. Longer residence time of the particles in the plume, as is the case at higher ambient pressures, lead to more evenly distributed particles. Light emission from the spherical shaped phosphor particles as excited by the electron beam is more intense due to the fact that much less photons encounter total internal reflection [20]. The increase in the deposition pressure is reported to have caused an increase in the connectivity (agglomeration) between particles due to sintering of small particles [21]. This would eventually lead to grain growth at high enough pressure. In this case, we also found that more agglomeration occurred at higher oxygen partial pressure.

6.3.4. Photoluminescence spectra

Figure 6.4 indicates the excitation spectra of $Y_2O_2S:Eu^{3+}$ thin films as well as Y_2O_2S; Eu^{3+} powder (inset). Excitation spectra were recorded keeping the emission wavelength at 619 nm. These spectra consist of several excitation bands of the f-f transitions, which are ascribed to

different transitions from ground state $^5D_0$ to the various excitation states of ^5D_J (J= 1,2,3,4,.....) electronic configuration of the Eu^{3+} ions.

Figure 5 shows the emission spectra of Y_2O_2S: Eu^{3+} thin films and Y_2O_2S:Eu^{3+} powder (inset) red-emitting phosphor. Films deposited in vacuum and those deposited at different oxygen partial pressures as well as the powder Y_2O_2S:Eu^{3+} were used for the PL spectrum measurements. All the samples were excited at a wavelength of 230 nm. For the powder sample, the PL emission spectra consist of several peaks corresponding to different energy transitions of the Y_2O_2S:Eu^{3+} phosphor. Totally, there are three groups of distinctive emission peaks between 590 and 629 nm, which are related to the $^5D_0$-^7F_J (J= 1, 2, 3) transitions of Eu^{3+}, respectively. In the case of the thin films the PL reveals three peaks only which are assigned to $^5D_0$-$^7F_1$, $^5D_0$-$^7F_2$ and $^5D_0$-$^7F_3$ transitions of Eu^{3+} ions. The strongest emission peak for all these samples both thin films and powder Y_2O_2S:Eu^{3+} is from the $^5D_0$–$^7F_2$ transition of Eu^{3+}. The fact that the dominant emission is from the parity forbidden electric dipole transition rather than from the magnetic dipole transition ($^5D_0$–$^7F_1$) indicates that Eu^{3+} is located at the site with no inversion symmetry in the Y_2O_2S lattice (C_2 site) [22]. Compared with the $^5D_0$–$^7F_2$ transition, the intensity of the $^5D_0$–$^7F_1$ transition corresponding to the orange colour is much lower, which makes the deposited Y_2O_2S:Eu^{3+} a purer red phosphor. This is also confirmed by the inset of Fig.5, which shows that the PL emission intensity of the powder is more than 6 times higher than the intensity of Y_2O_2S:Eu^{3+} thin films.

The reason behind observing the intense red emission from Y_2O_2S:Eu^{3+} in the case of hexagonal and also cubic phase can be understood by considering the structure of Y_2O_2S. The coordinate number of Y_2O_2S is twelve and forms hexagonal structure with two different sites (C_2 and C_{3i}) for rare-earth (RE) ions substitution. The C_2 is a low symmetry site without an inversion centre whereas C_{3i} is a high symmetry site having an inversion centre. When Eu^{3+} is located at a low symmetry (C_2), the red emission is dominant whereas the orange emission is dominant when Eu^{3+} is located at high symmetry (C_{3i}). In the present case, red emission is dominant suggesting that the location of Eu^{3+} is more favorable at C_2 site. As the C_2 site does not have an inversion centre, electric dipole transition from Eu^{3+} ions attached to this site are more favorable than the magnetic dipole transitions. The similarity of the ionic radii of Eu^{3+} and Y^{3+} ions for both hexagonal as well as cubic phase allows the easy substitution of Y^{3+} ions with Eu^{3+} ions at C_2 sites giving rise to intense red emission in all the samples. The emission peaked at 590 nm due to $^5D_0$-$^7F_1$ transition of Eu^{3+} is quenched at higher O_2 partial pressure. The most intense peak at 619 nm due to $^5D_0$-$^7F_2$ transition is totally quenched at

higher O_2 partial greater than 20 mtorr. Similarly, the peaks at 630 nm due to $^5D_0$-$^7F_3$ transition are quenched at higher O_2 pressure. In the case of vacuum atmosphere as well as 60 mtorr O_2 partial pressure, the peaks are not visible in all the three transitions, while 20 mtorr O_2 partial pressure provides the highest intensity at all the transitions. This can be explained by visiting the oxidation states or kinetics of the Eu^{3+} ions. The most intense peak at 619 nm is assigned to the $^5D_0$-$^7F_2$ transition for 20 mtorr O_2 partial pressure confirms the presence of Eu^{3+}, making 20 mtorr to have highest intensity in all three transitions.

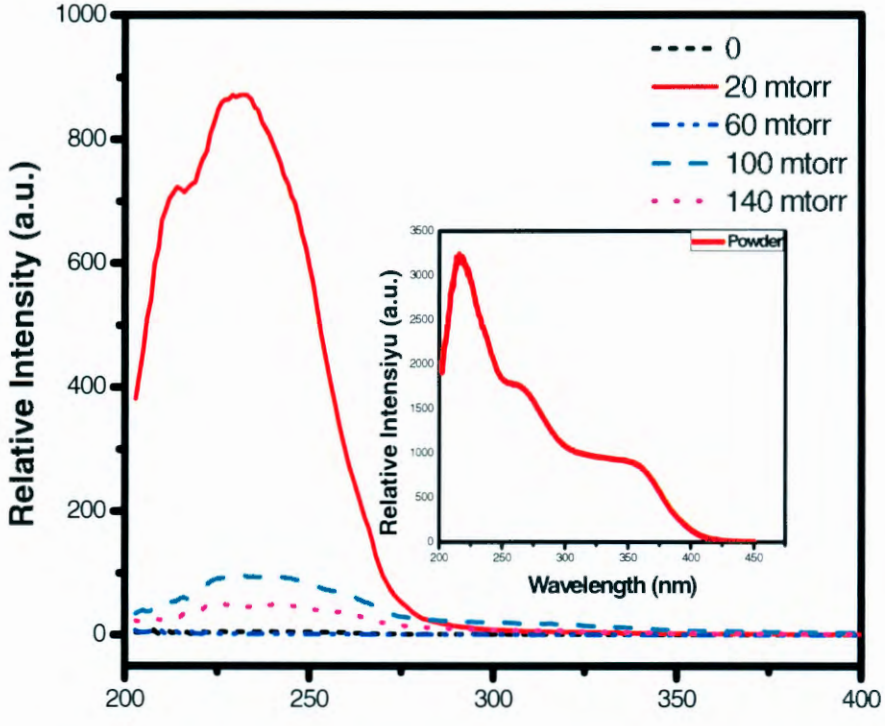

Figure 6.4. Excitation spectra for films deposited in vacuum and at different oxygen partial pressure. The inset show excitation spectrum of $Y_2O_2S:Eu^{3+}$ powder phosphor.

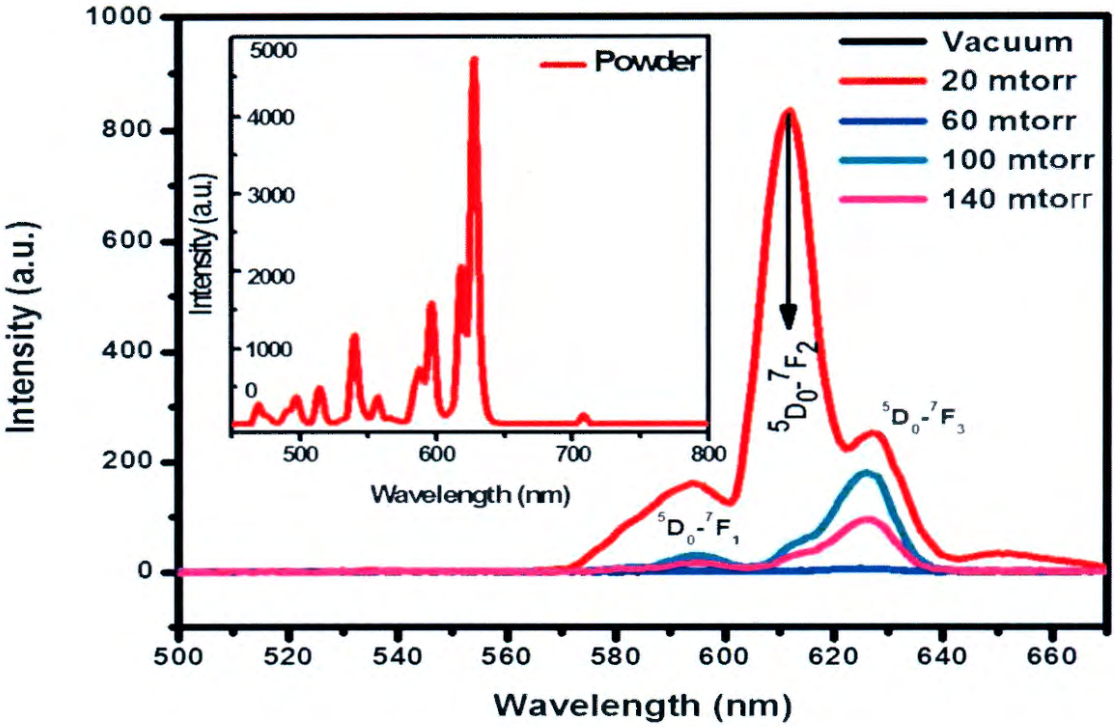

Figure 6.5. Emission spectra for films deposited in vacuum and at different oxygen partial pressure. The inset show emission spectrum of $Y_2O_2S:Eu^{3+}$ powder phosphor.

Figure 6.6 shows a plot of maximum peak intensity as a function of oxygen partial pressure. The figure indicates that the maximum peak intensity initially increases monotonously between 0 mtorr and 20 mtorr, then decreased at higher oxygen partial pressure. The optimum luminescence intensity was achieved at 20 mtorr due to the fact that posible oxidation of Eu^{3+} to Eu^{2+} did not take place at this particular O_2 partial pressure. This optimum value of 20 mtorr O_2 partial pressure can be utilized in future research but under different deposition conditions.

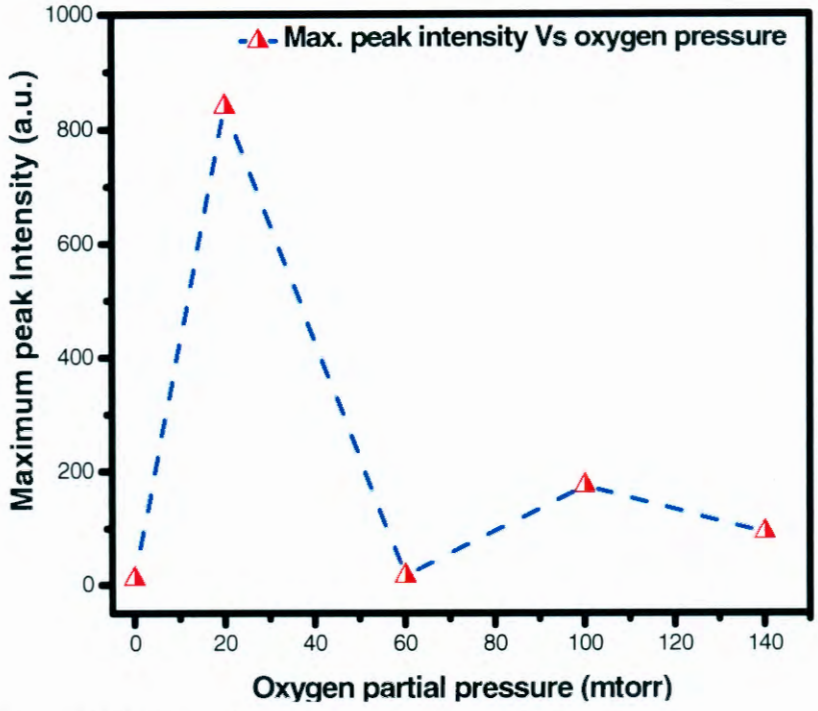

Figure 6.6. The plot of maximum peak intensity versus oxygen partial pressure.

3.5 Afterglow decay curves of the red phosphors

The afterglow properties of thin films ablated at vacuum and various oxygen pressures are compared, as shown in Fig. 7. It can be seen that the decay curve of the film ablated at 20 mtorr has highest afterglow and brightness, while the film ablated in vacuum and 60 mtorr has the lowest afterglow and brightness. This indicates that vacuum and lower oxygen pressure favors long afterglow and higher intensities and vice versa. The decay times of the phosphor can be estimated by using the following double exponential equation;

$$I = A_1 \exp(-t/\tau_1) + A_2 \exp(-t/\tau_2)$$

where I is the phosphorescence intensity, A_1, and A_2, are constants, t is time, τ_1 and τ_2, are decay times for exponential components, respectively. The fitting results of parameters t_1 and t_2 are listed in Table 6.3 below and the expected experimental error is ± 0.0017 m/s.

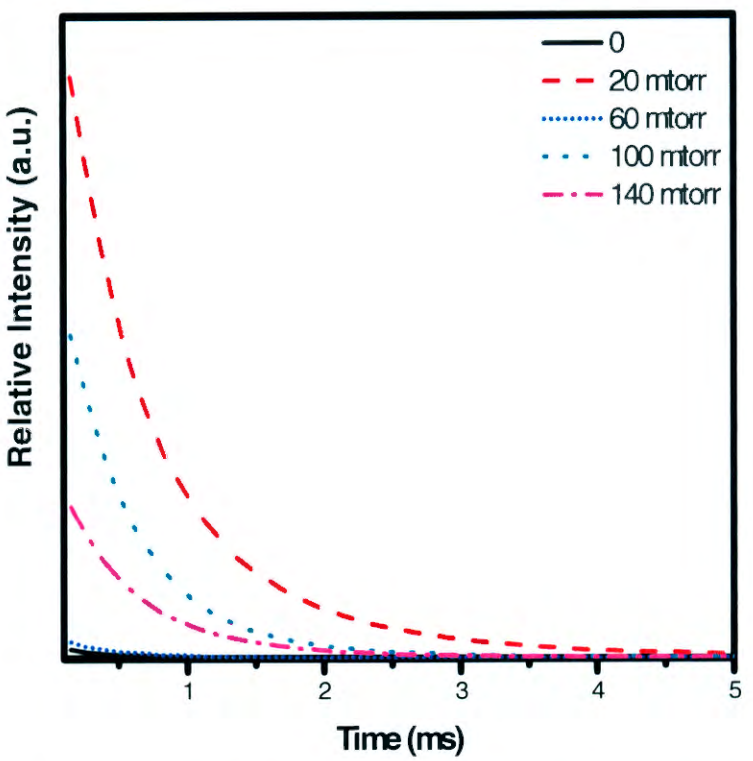

Figure 6.7: Decay curves for the thin films deposited in vacuum atmosphere and at different oxygen ambient.

Table 6.2: Decay constants for the fitted decay curves of the thin films ablated in vacuum and various oxygen partial ambient.

O_2 pressure (mtorr)	Vacuum	20	60	100	140
Components (ms)	Decay constants(τ, s)				
Fast (τ_1)	0.346	0.400	0.352	0.388	0.372
Medium (τ_2)	0.542	0.600	0.558	0.597	0.582

6.3.6 Optical properties

6.3.6.1 Absorbance spectra

The UV–vis reflectance spectra of the samples are given in Fig. 8. The spectra of all the samples show good optical quality in the visible range due to reflectance in the 200– 500 nm range. The sharp absorption edge is characteristic of a homogeneous structure [23]. The figure shows that the absorption edge shifted to higher wavelength for lower O_2 partial pressure and then reduced to lower wavelength for higher O_2 partial pressure. Furthermore,

absorption bands corresponding to the forbidden Eu^{3+} 4f–4f transitions were detected for higher O_2 partial pressure. The band at around 344 nm is attributed to the exciton absorption, which is red-shift compared with powder $Y_2O_2S:Eu^{3+}$ [24]. The absorption peaks at around 290 and 340 nm are assigned to ^5Do-$^7F_1$and $^5D_0$-$^7F_2$ transitions of Eu^{3+} ions, respectively [25].

6.3.6.2 Determination of band gap from reflectance spectra

The Kubelka- Munk equation was used to calculate the band gap of the as- deposited thin film using a diffuse reflectance spectrum. On the other hand, the band gap (Eg) and absorption coefficient α of the indirect band gap semiconductor is related through the well-known Tauc relation. The average Eg value for the thin films was found to be 4.03 eV, which is almost in agreement with the literature values by other researchers [26-27]. The observed optical band gap for Y_2O_2S: Eu^{3+} thin films has increased to 4.24 eV as the O_2 partial pressure increased to 100 mtorr as shown in Fig. 9 (a). The change in optical band gap values may also be due to the change of crystal structure of the Y_2O_2S thin films. This is also confirmed by the fact that the PL emission intensity of the powder is more than 6 times greater than the intensity of $Y_2O_2S:Eu^{3+}$ thin films

The dependence of the band gap energy of the Y_2O_2S on the O_2 partial pressure is shown in Fig. 6.9 (b). It can be seen from this graph that the band gap of the Y_2O_2S; Eu^{3+} thin films increased with the amount of O_2 partial pressure except for film deposited in 60 mtorr ambient. The decrease in the band gap energy and the shift of the absorption edges to higher wavelengths might be due to the presence of defect states and disorder due to the O_2 partial pressure [28-30]. The O_2 partial pressure might have introduced new states close to the conduction band of the $Y_2O_2S:Eu^{3+}$. A new defect band is therefore formed below the conductions which lead to reduction in the effective band gap [31-32]. It is clear that at 20 mtorr O_2 partial pressure the estimated band gap increased to 4.40 eV.

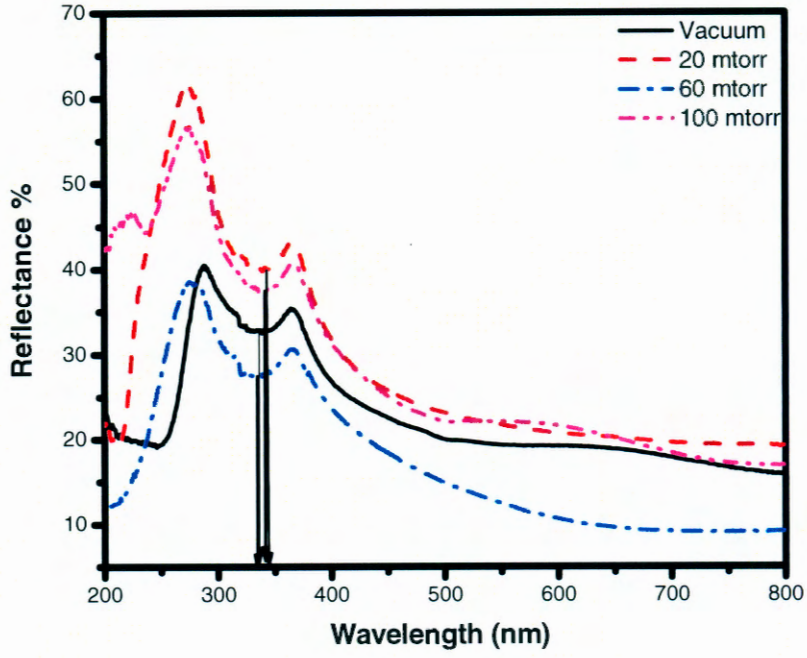

Figure 6.8. UV-vis diffuse reflectance spectra of nanocrystalline $Y_2O_2S:Eu^{3+}$ thin film deposited in vacuum and different oxygen pressure.

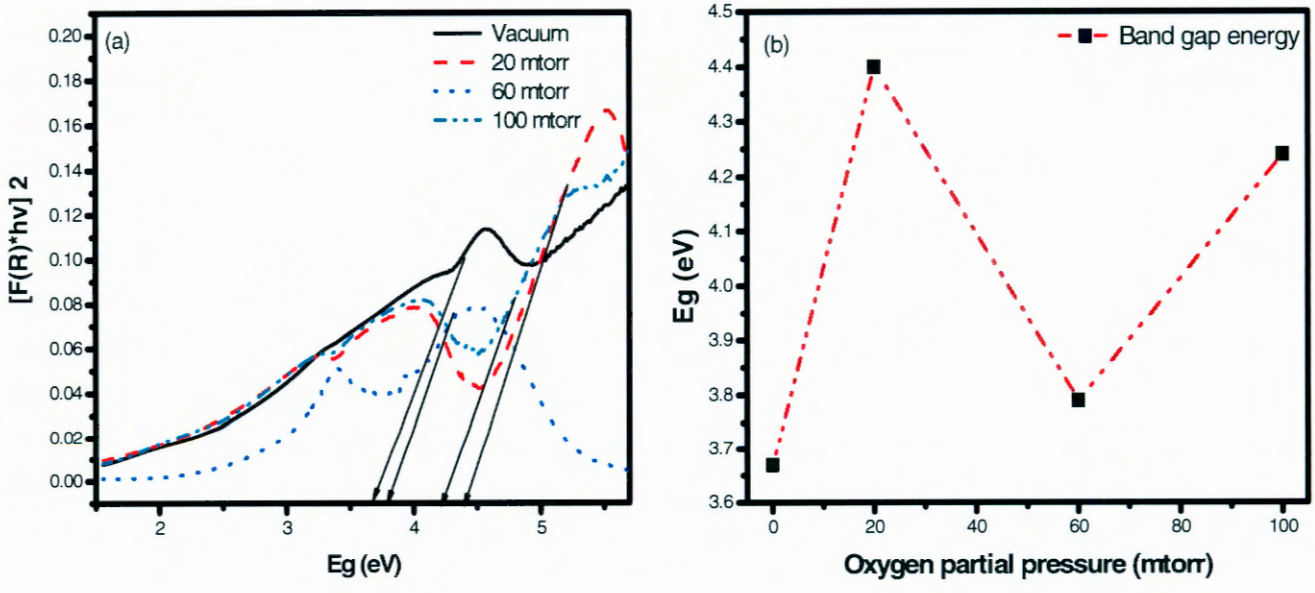

Figure 6.9. (a) Graph of $F[(R)*hv]^2$ as a function of band gap energy, (b) Dependance of band gap energy on partial oxygen pressure

6.4 Conclusion

$Y_2O_2S:Eu^{3+}$ thin films were successfully grown onto the Si (100) substrates at different oxygen ambient. XRD show mixed phases of cubic and hexagonal crystal structures. The films grown at low and high oxygen partial pressure are predominantly cubic, while that grown at moderate pressure (100 mtorr) is predominantly hexagonal. The thin films were composed of nanoparticles. The size of the particles depended on the oxygen partial pressure. The decrease in the oxygen partial pressure resulted into big particles which are actually piling up of smaller particles and therefore a rougher surface. The PL measurements showed red emission of $Y_2O_2S:Eu^{3+}$ thin films as well as the powder $Y_2O_2S: Eu^{3+}$ with the most intense peak appearing at 619 nm, which is assigned to the $^5D_0$-$^7F_2$ transition of Eu^{3+}. This intense peak is quenched at higher O_2 partial pressure greater than 20 mtorr. The emission peak at 590 nm due to $^5D_0$-$^7F_1$ transition of Eu^3+ is also quenched at higher O_2 partial pressure. Uv-vis measurement revealed an average band gap of 4.03 eV.

References

[1] C.R. Ronda, J. Lumin. 49 (1997) 72.

[2] R. Schmechel, M. Kennedy, H. Von Seggern, J. Appl. Phys. 89 (3) (2001) 1679.

[3] A. Konrad, U. Herr, R. Tidecks, F. Kummer, K. Samwer, J. Appl. Phys. 90 (7) (2001) 3516.

[4] H.S. Peng, H.W. Song, B.J. Chen, S.Z. Lu, S.H. Huang, Chem. Phys. Lett. 370 (2003) 485.

[5] W.W. Zhang, W.P. Zhang, P.B. Xie, M. Yin, J. Colloid Interface Sci. 262 (2003) 588.

[6] Y.Q. Zhai, Z.H. Yao, S.W. Ding, M.D. Qiu, J. Zhai, Mater. Lett. 57 (2003) 2901.

[7] H.S. Peng, H.W. Song, B.J. Chen, S.Z. Lu, S.H. Huang, Chem. Phys. Lett. 370 (2003) 485.

[8] T. Hirai, Y. Asada, I. Komasawa, J. Colloid Interface Sci. 276 (2004) 339.

[9] J. Hao, S.A. Studenikin, M. Cocivera, J. Lumin. 93 (2001) 313.

[10] L.P. Wang, G.Y. Hong, Mater. Res. Bull. 35 (2000) 695.

[11] J.P. Lang, X.Q. Xin, J. Solid State Chem. 108 (1994) 118.

[12] H.T. Cui, G.Y. Hong, H.P. You, J. Colloid Interface Sci. 252 (2002) 184.

[13] R. K. Singh and J. Narayan, Phys. Rev. B 41, 8843 (1991).

[14] A. Gupta, in Pulsed Laser Deposition of Thin Films, edited by D. B. Chrisey and G. K. Hubbler (Wiley, New York, 1994), p. 265.

[15] A. Greer and M. Tahal, Mater. Res. Soc. Symp. Proc. 341, 87 (1994).

[16] S. S. Yi, J. Korean Phys. Soc. 45, 1625 (2004).

[17] J. Seon, B. Kyoo, S. Shim, B. K. Moon, S. B. Kim, J. H. Jeong, S. S. Yi and J. H. Kim, J. Korean Phys. Soc. 46, 1193 (2005).

[18] W. Kang, J. Park, D.-K. Kim, K.S. Suh, Bull. Korean Chem. Soc. 22

(2001) 921.

[19] L. Chen, Particles generated by pulsed laser ablation, in D. B. Chrisey, G. K Hulber (Eds), Pulsed Laser Deposition of Thin Films, John Wiley & Sons, Inc, New York, (1994) 184.

[20] S. Yi, J.S. Bae, B.C. Choi, K.S. Shim, H.K. Yang, B.K. Moon, J.H. Jeong,

J.H. Kim, Opt. Mater. 28 (2006) 703.

[21] S. Erdei, B. Jin, F.W. Ainger, A.S. Bhalla, B. Keszei, J. Vandlik, A.

Suveges, J. Appl. Phys. 79 (1996) 2834.

[22] H. Zhang, J. Liu, J. Wang, C. Wang, L. Zhu, Z. Shao, X. Meng, X. Hu, Opt.

Lasers Eng. 38 (2002) 527.

[23] V. Buissette, A. Huignard, T. Gacoin, J.-P. Boilot, P. Aschehoug, B. Viana,

Surf. Sci. 532–535 (2003) 444.

[24] R.W.G. Wyckoff, Crystal Structures, Vol. 3, Interscience, New York,

1963, p. 17.

[25] L.D. Sun, C. Qian, C.S. Liao, X.L. Wang, C.H. Yan, Solid State Commun.

119 (393) (2001).

[26] J.C. Park, H.K. Moon, D.K. Kim, S.H. Byeon, B.C. Kim, K.S. Suh, Appl.

Phys. Lett. 77 (2162) (2000).

[27] O.A. Lopez, J. McKittrick, L.E. Shea, J. Lumin. 71 (1) (1997).

[28] S.H. Byeon, K.G. Ko, J.C. Park, D.K. Kim, Chem. Mater. 14 (2002) 603.

[29] G. James, J. Vac. Sci. Technol., A, Vac. Surf. Films 13 (1995) 1175.

[30] C. Misbra, J.K. Berkowitz, K.H. Johnson, P.C. Schmidt, Phys. Rev., B 45

(1992) 10902.

[31] O.A. Lopez, J. Mckittrick, L.E. Shea, J. Lumin. 71 (1997) 1.

[32] D. Hommel, H. Hartmann, J. Cryst. Growth 72 (1985) 346.

Chapter 7

Energy transfer and material properties of Y_2O_3: Eu^{3+}:Ho^{3+}nanophosphors synthesized by sol- combustion method

7.1 Introduction

Europium-activated Y_2O_3 (Y_2O_3:Eu^{3+}) has attracted much attention as a red-emitting phosphor for commercial use in fluorescent lighting and screen due to its high luminescence emission around 626nm. Because of the fast development of nano technology, the optical properties of nanocrystalline Y_2O_3:Eu^{3+} have also been extensively investigated for its potential application in high resolution imaging for flat plasma displays and in fundamental research [1, 2]. Therefore, many researchers have already performed investigations related to this nanophosphor, such as the study of the influence of particle size on the intense luminescence of nanocrystalline Y_2O_3:Eu^{3+} [3–5]. In recent years, luminescent nanocrystals (NCs) doped with rare earth ions were paid more attentions because of their interesting luminescent properties. They can be as components in displays [6], light emitting diodes [7], biological assays [8], and optoelectronic devices [9]. Cubic Y_2O_3:Eu^{3+} is one of the most important commercial red phosphors, which can be used in fluorescent lights, cathode ray tubes (CRTS), plasma display panel (PDP), and field emission display (FED) [10]. Yttrium oxide (Y_2O_3) has been investigated widely as a host material for rare-earth ion doping in optical applications [11] on account of its excellent chemical stability, broad transparency range (0.2 to 8μm) with a band gap of 5.6eV, high refractive index, and low phonon energy [12-14]. Furthermore, the similarities in the chemical properties and ionic radius of RE ions and Y_2O_3 make it an attractive choice as a host material [15, 16]. Many methods for synthesis of Y_2O_3:Eu^{3+}:Ho^{3+} phosphor has been reported, including sol-gel method [17], spray pyrolysis method [18], hydrothermal method [19], and precipitation method [20]. Wet chemical methods have been widely developed to prepare the luminescent materials [21], since these processes have advantages of good homogeneity through mixing the starting materials at the molecular level in solution, a lower calcination temperature and a shorter heating time. However, sol-gel process often requires expensive (and environmentally unfriendly) organic precursors and solvents. Then a simple technique, sol- combustion synthesis, is beginning to attract a great deal of interest. Sol- combustion is one of the simplest and most versatile approaches available to obtain single-phase powders at low temperatures with shorter reaction times and little residual impurities as compared with conventional solid-state reactions [22].

In the present study, a series of red –emitting phosphors Y_2O_3:Eu^{3+}: Ho^{3+} was prepared by sol- combustion method. The luminescence, excitation, and optical absorption, structural and morphological properties of Y_2O_3:Eu^{3+}: Ho^{3+} has been studied. To investigate the effect of

Ho^{3+} on the morphology and luminescence properties of the phosphor, the percentage concentration of Ho^{3+} ions were varied while Eu^{3+} ions were kept constant. To the best of our knowledge, there is no publication on the synthesis of Y_2O_3: Eu^{3+}: Ho^{3+} by sol-combustion method and got similar results.

7.2 Experimental

7.2.1 Nanocrystal synthesis

All the chemicals used for the preparation of the powders were of analytical grade. In the present study Y $(NO_3).6HO_2$ is used as an oxidizer, thiourea employed as a fuel and Eu^{3+} and Ho^{3+} as activators. Stoichiometric compositions of metal nitrates and fuel are mixed. Precursors were dissolved in a very minimum amount of distilled water and ethanol to obtain homogeneous solution. The solution was then introduced into a muffle furnace preheated to 500^0c. After about 7 minutes the solution boiled and was ignited to a self-propagating flame. The fluffy masses obtained were crushed into a fine powder and was ready for characterization.

7.2.2 Characterization

To determine the average crystallite diameter and the phase of the samples, X-ray powder diffraction (XRD) spectra were measured with a D8 Bruker Advanced AXS GmbH X-ray diffractometer using Cu *Ka* radiation at a wavelength of 0.154056 nm. The measurement conditions were as follows: the wavelength was 0.15419 nm (pure Cu Kα radiation), tube voltage/tube current was 40 kV/50 mA, and machine scanning range was $2\theta = 10^0$- 90^0. The size and morphology of the as-prepared particles were carried out by using a scanning electron microscope (SEM), Tescan VEGA 3 SEM. The photoluminescence (PL) spectrum as well as decay curves for all the samples were investigated by Cary Eclipse fluorescent spectrophotometer equipped with a 150 W xenon lamp at an excitation source with the slit of 1.0 nm and scan speed of 240 nm min^{-1}.

7.3 Results and discussions

7.3.1 X-ray diffraction study

Fig. 7.1 illustrates the X-ray diffraction patterns of Y_2O_3:Eu^{3+}: Ho^{3+} powder samples, synthesized by the sol–combustion method. Six main peaks are observed, which can be assigned to (211), (222), (400), (440), and (622) of cubic Y_2O_3. All diffraction peaks are attributed to the pure body-centered cubic (bcc) structure for Y_2O_3 phase and match well with JCPDS (25-1200) card with space group Ia3. All samples present (222) as the preferential orientation. At 0.1% Ho3+, the product is already crystallized and presents some three peaks. At higher concentrations more peaks are detected. This difference in crystallization is due probably to the difference in the Ho^{3+} ions concentrations. Increasing Ho^{3+}% ions leads to the increase of the main peaks intensity with a sharpening, indicating the improvement of the crystallinity quality of the powders. This phenomenon can be explained by the fact that the Y^{3+} ions are accommodated in two different symmetries, i.e., the C_2 without inversion center and the S_6 with inversion center [23]. The Eu^{3+} ion might be replacing the Y^{3+} ions in theY_2O_3 host lattice because no diffraction pattern characteristic of Eu_2O_3 phase is detected. The radii of Y^{3+}, Eu^{3+} and Ho^{3+} ions are 0.89 A° , 0.947 A° and 0.9 A° respectively,[24]. According to the ion radius approximation principle in the crystal field theory, Eu^{3+} and Ho^{3+} ions enter into crystal lattices by replacing Y^{3+} ions other than by occupying the slot between crystal lattices. Compared with Y^{3+} ionic radius (0.89 Å), Eu^{3+} and HO^{3+} have larger ionic radii of 0.947 Å and 0.9 Å respectively. Therefore, the lattice constant would increase with increasing atomic content of Ho^{3+} ions in the powder.

The crystallite size of these materials has been estimated from the same XRD patterns. As a first approximation, it is suggested that the appearance of broad XRD peaks is due to the nano-sized particles formation. The average crystallite size 'D' of Y_2O_3:Eu^{3+}: Ho^{3+} powders can be estimated using Scherrer's formula [25],

$$D = \frac{0.9\lambda}{\beta cos\theta}$$

where λ=1.5406 Å is the wavelength of the X-ray radiation used, β is the full width at half maximum (FWHM) of the (222) diffraction peak in the XRD patterns in radians, θ is the Bragg diffraction angle.

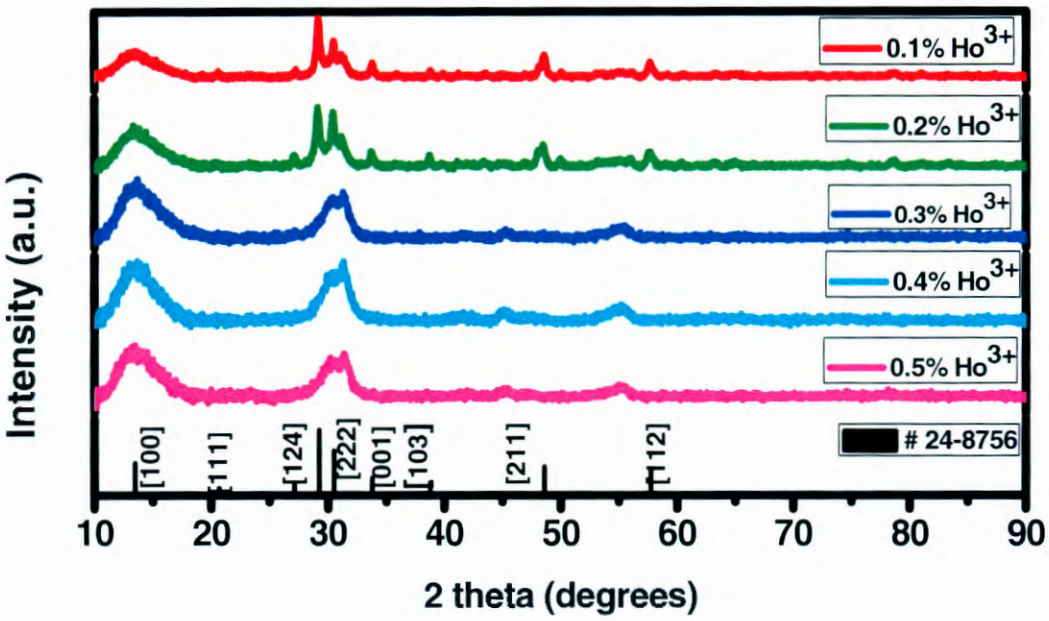

Fig.7.1. X-ray diffraction pattern of Y_2O_3: Eu^{3+}: Ho^{3+} phosphor

The average crystallite size and crystallographic unit cell parameters are calculated and listed in Table 1. It is found that the diffraction peaks shift to longer angles with increasing Ho%, indicating a decrease of the lattice constant and a development of internal tensile strain. In addition, the crystallite size of synthesized Y_2O_3: Eu^{3+}: Ho^{3+} powder increased with increasing Ho^{3+} ions. It is known that FWHM (β in the Scherrer formula) can be interpreted in terms of lattice strain and crystalline size. The crystal lattice strain generated by the Ho^{3+} ions is determined from the Williamson–Hall relationship [26]:

$$\beta \frac{cos\theta}{\lambda} = \frac{1}{D} + \eta sin\theta$$

where β is the full width at half maximum, λ is the X-ray wavelength, θ is the diffraction angle, D is the effective crystallite size and η is the effective strain. The strain is calculated from the slope of the plot of β ($(\cos\theta)/\lambda$) against $\sin\theta/\lambda$ and the effective crystallite size is calculated from the intercept to β ($(\cos\theta)/\lambda$) axis. They show a difference in angular dependence of the line width for Ho^{3+} ions. Indeed, the best fit is obtained when the Ho^{3+} ion percent is increased from 0.1 to 0.5% and when the slope becomes negative. In the same table, we also present the effective crystallite size and the effective strain η against the Ho^{3+} ions percent. The effective crystallite size values are very close to those extracted from the Scherrer formula and increase when the Ho^{3+} ions percent increases. The tensile strain decreases from 0.1% to the negative value corresponding to 0.5%. It has been reported that a negative value indicates the presence of compressive lattice strain [27]. This strain behaviour

as a function of Ho^{3+} ions is in a good agreement with that of the lattice parameters. The reduction of the lattice parameter and the increase of crystallite size with increasing of the Ho^{3+} ions signify the closeness of lattice plane which can lead to an increase of the density and a decrease in the dislocation density. The average nanocrystallite sizes for Y_2O_3: Eu^{3+} with different concentration of HO^{3+} is compared as shown in the table 1 below;

Table 7. 1. The crystallite sizes as a function of % concentration of HO^{3+} ions ions.

% of Ho^{3+}	0.1	0.2	0.3	0.4	0.5
Crystal sizes (nm)	6.5	7.5	8.9	9.2	9.8

Table 1 lists the crystallite sizes of synthesized particles estimated from the well-known Scherrer's equation. The diffraction data of the strongest peak [222] plane was used to calculate the mean crystallite sizes. The crystallite sizes showed a slightly increasing tendency, which can be attributed to the effect of the increased dopant concentration [28].

Figure 2 shows the role of Ho^{3+} mole concentration on crystallite sizes and lattice parameter. A monotonous decrease of the lattice constant and increasing crystallite size is established by means of X-ray analysis for a series of Y_2O_3: Eu^{3+}: Ho^{3+} powders. It is shown that the effect cannot be explained by impurity or intrinsic defects in the powders. The expressions derived are based on the size dependence of the internal stress and the intracrystalline pressure stipulated by the interaction of the elements of the crystal charge lattice. Calculations made for the ion charge lattice of quartz evidence the monotonous increase of the lattice parameters with decreasing particle size and agree with the results of the X-ray experiment.

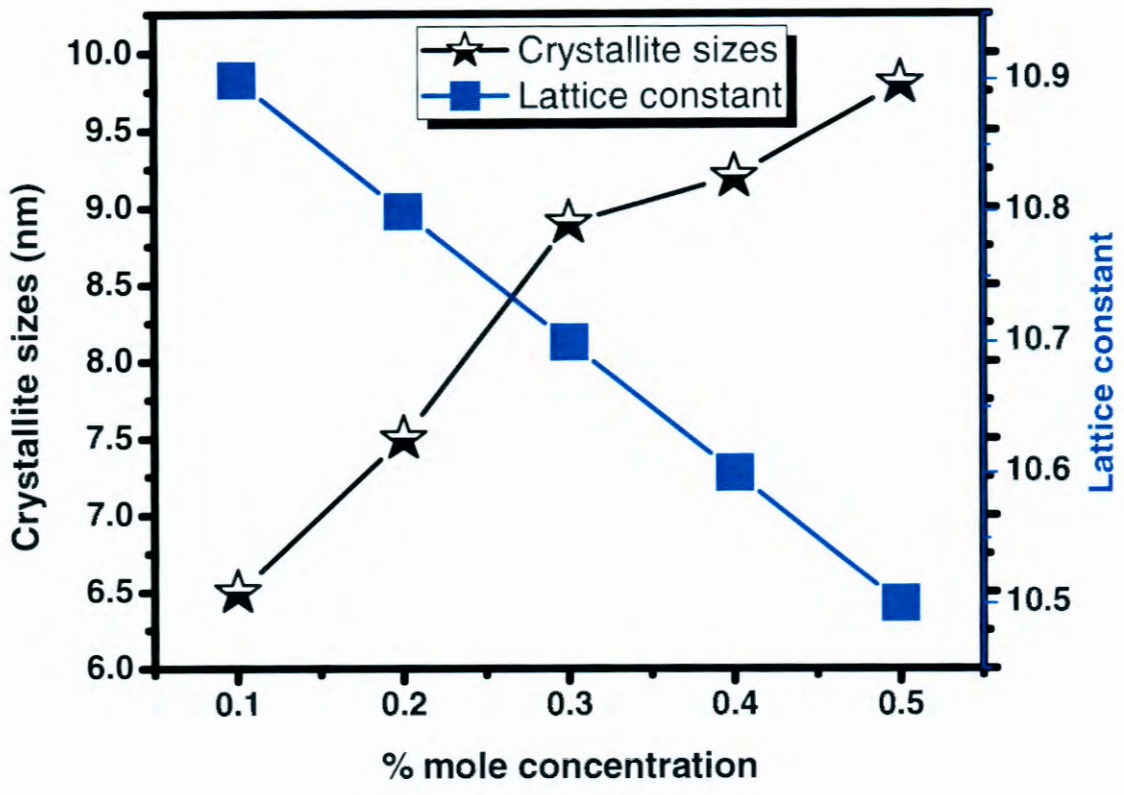

Fig. 7.2. Crystallite sizes and Lattice constant as functions of Ho^{3+} concentration

7.3.2 Scanning electron microscopy

SEM was carried out using Tescan VEGA 3 SEM. Fig. 3 shows the SEM image of the Y_2O_3:Eu^{3+}: Ho^{3+} co-doped phosphor. The image shows the characteristics surface morphology of combustion product. Particles are highly agglomerated and form a connected network type with some vacant space among them, which is expected due to the evolution of different gases during combustion of the gel. It also reveals inhomogeneous distribution of the particles (a variation and shape of the particles). The shape of some of the particles are spherical and the size lie between 5 – 10 nm (fig.2a) which is well in agreement with the crystalline size calculated using XRD. However some particles are of sub-micron size due to agglomeration of many crystallites and lack of separate boundary (fig.2b-2e). The shapes of the particles are irregular and seem to be polygonal.

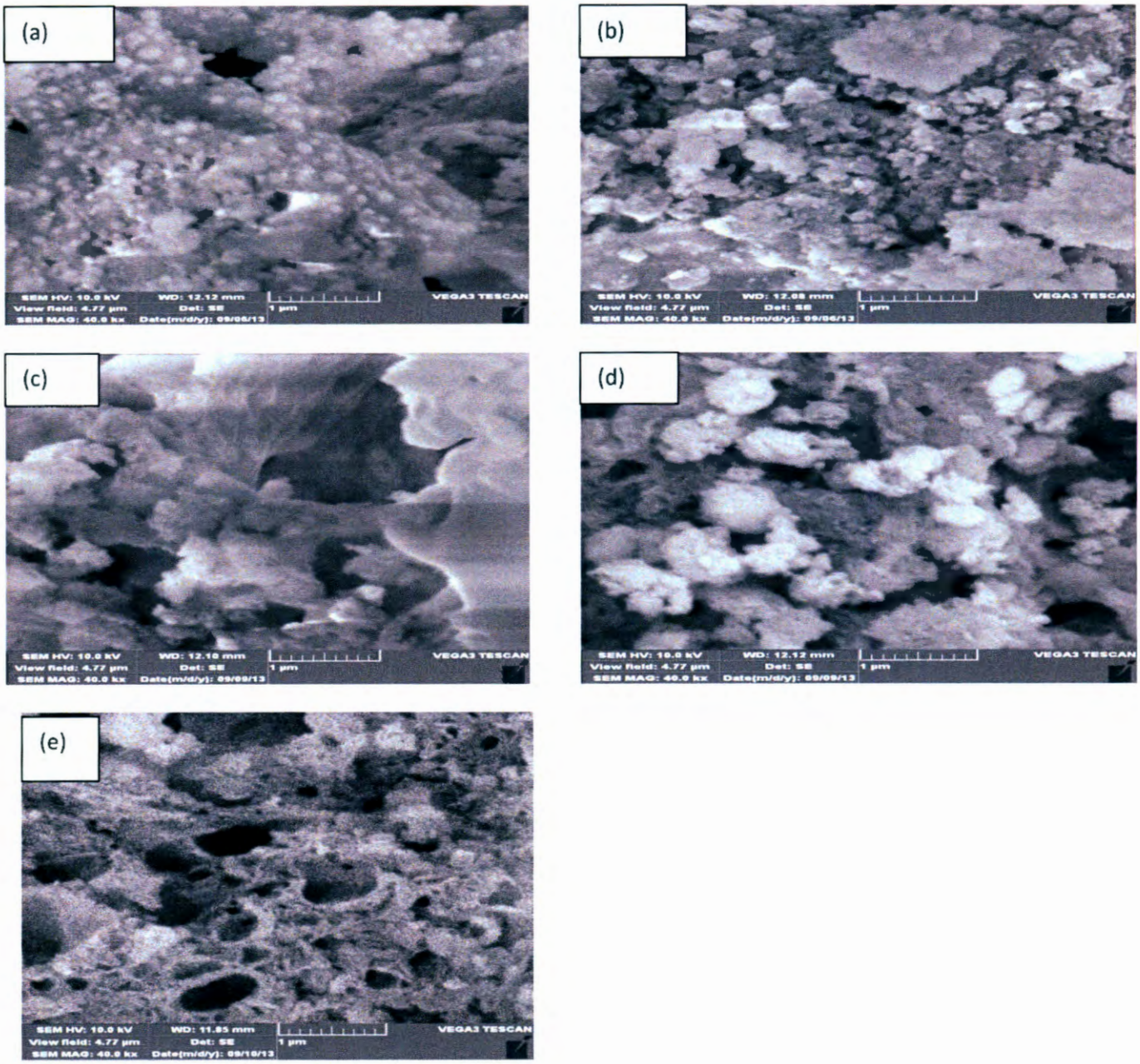

Fig.7.3. SEM micrographs of Y_2O_3: Eu^{3+}: Ho^{3+} samples with (a) 0.1 (b) 0.2 (c) 0.3 (d) 0.4 (e) 0.5 % of Ho^{3+} ions. 4.77μm field of view.

7.3 Photoluminescence

7.3.1 Excitation

Fig. 7.4 shows room-temperature optical absorption spectra of Y_2O_3:Eu^{3+}:Ho^{3+} phosphor. Ho^{3+} absorption bands of $^3H_6$, $^5G^5$, $^5G^6$, $^5F_3$, $^5F_4$ ($^5S_2$) and $^5F_5$ were present in Y_2O_3: Eu^{3+}:Ho^{3+}. The Ho^{3+} doped Y_2O_3:Eu^{3+} showed green (544 nm) and red (626 nm) emission peaks, which are assigned to $^5F_4$ ($^5S_2$) - $^5I_8$ and $^5F_5$-$^5I_8$ transitions of Ho^{3+} ions respectively.

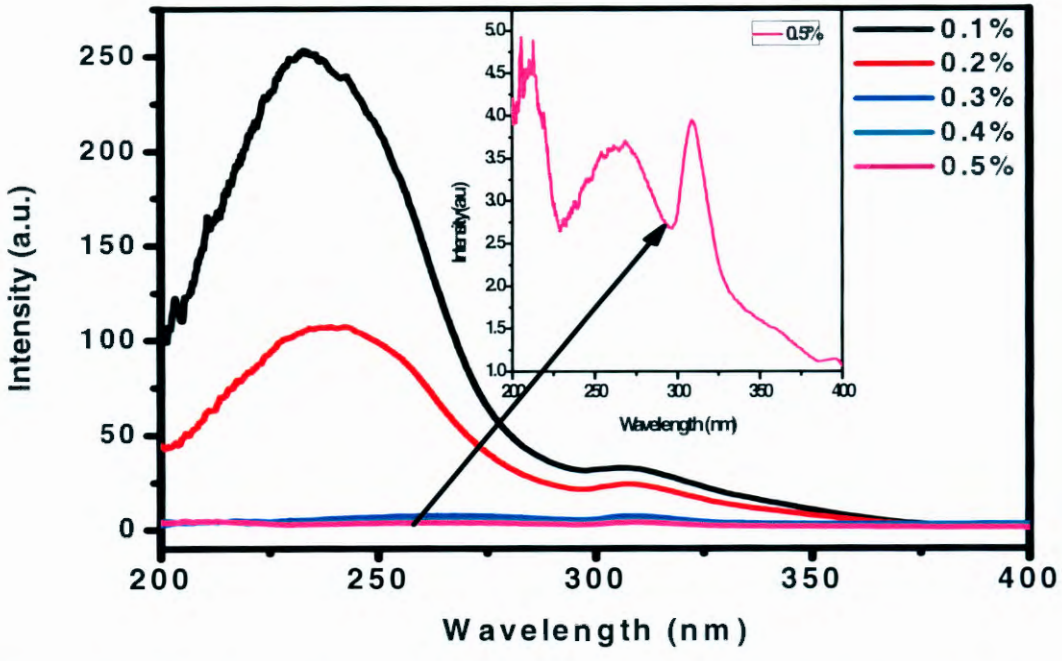

Fig.7.4 Excitation spectra of Ho^{3+} co-doped Y_2O_3: Eu^{3+} phosphor when Ho^{3+} ion concentration was varied from 0.1 to 0.5%

7.3.2 Emission

Fig. 7.5 shows the emission spectra of Y_2O_3: Eu^{3+}:Ho^{3+} powder when the percentage concentration of Ho^{3+} ions was varied. Three main emission spectra appear at 540, 588 and 626 nm for the samples with lower mole concentrations (0.1 and 0.2%) of Ho^{3+} assigned to $^5D_0$-$^7F_1$, $^5D_0$-$^7F_2$ and $^5D_0$-$^7F_3$ transitions of Eu^{3+}. These emission spectra due to Eu^{3+} ions are also confirmed by the inset of Fig. 3. Other minor peaks also appear around 440 and 500 nm

speculated to be from Ho^{3+}. At higher mole concentration of Ho^{3+}, the three main peaks are totally quenched. Y_2O_3:Eu^{3+}:Ho^{3+} phosphor shows a red-emitting afterglow phenomenon, and the Eu^{3+} ions are the luminescent center during the decay process. The bright red emission near 626 nm has been noticeable due to the $^5D_0$-$^7F_2$ transition of Eu^{3+}. The Intensity of the luminescence has decreased with an increase of concentration of Ho^{3+}. In sufficient quantities of Eu^{3+} to Ho^{3+}, the bright red emission near 626 nm has been predominant due to $^5D_0$-$^7F_2$ transition of Eu^{3+}. From the figure, the intensities of spectra are quenched as the % concentration of Ho^{3+} ions are increased. Since Eu^{3+} ions are kept constant, it is speculated that Ho^{3+} ions are the ones which caused the quenching of the intensities of the spectra.

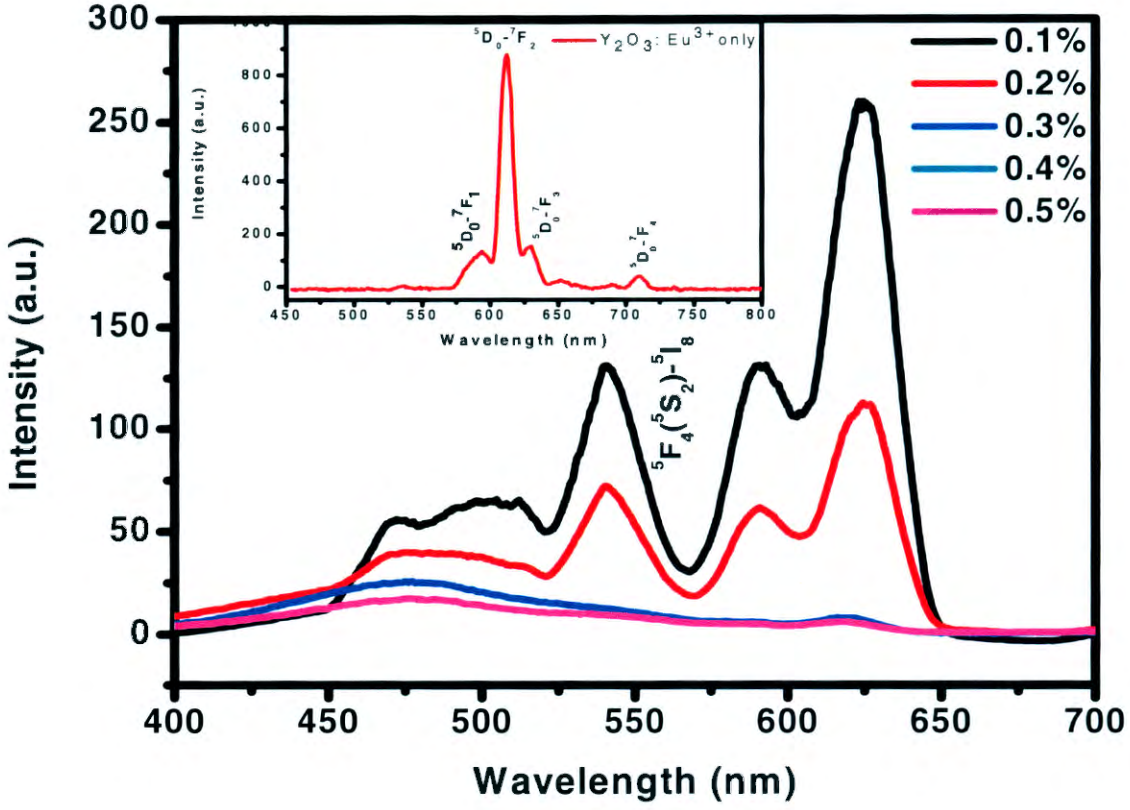

Fig.7.5. Photoluminescence emission spectra of Ho^{3+} co-doped Y_2O_3: Eu^{3+} phosphor when Ho^{3+} ion concentration was varied from 0.1 to 0.5%

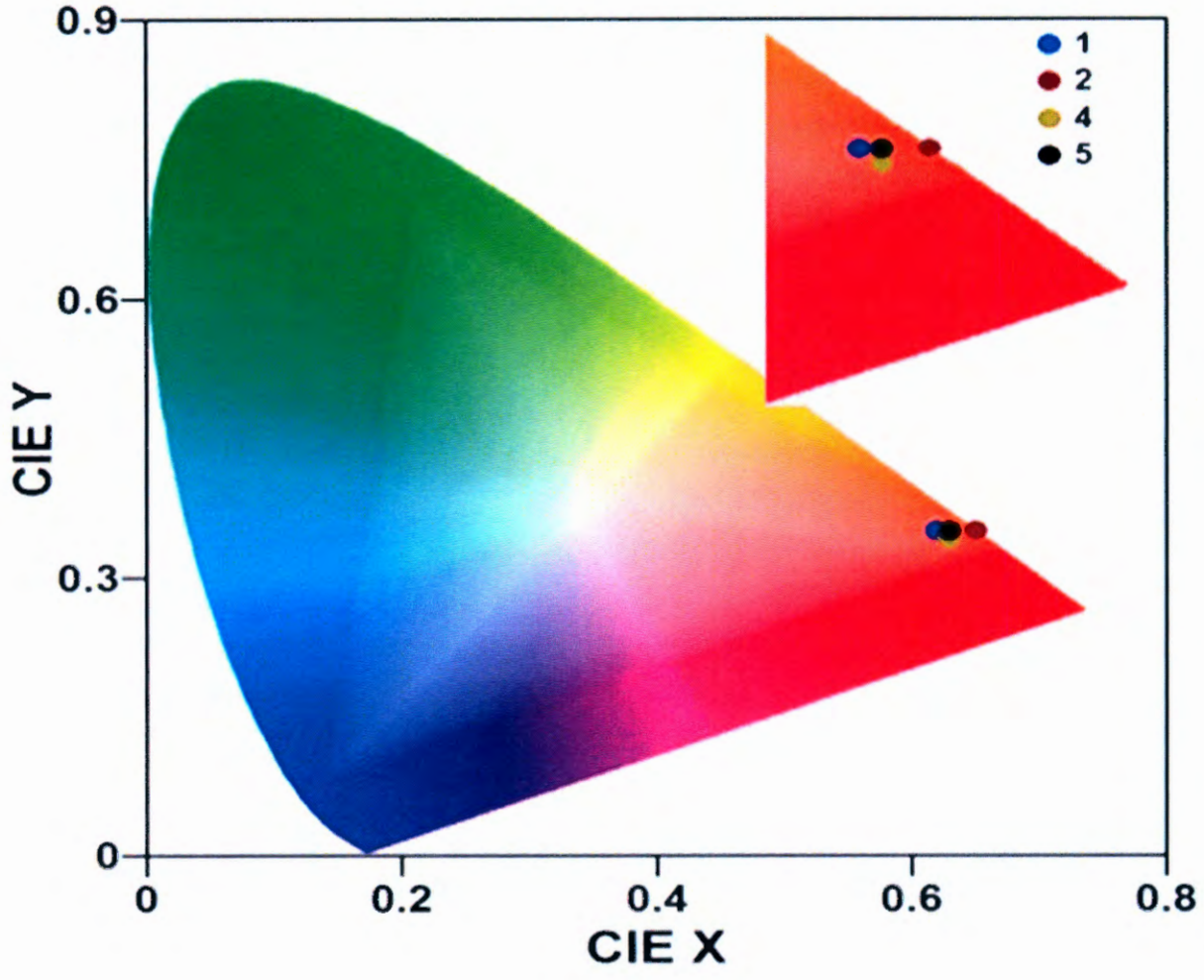

Fig.7.6. Chromaticity colour coordinates of the Y_2O_3:Eu^{3+}:Ho^{3+} powder under 325 nm UV excitation.

7.3.3 Decay characteristics

The afterglow properties of Y_2O_3: Eu^{3+}: Ho^{3+} powder with different mole concentration of Ho^{3+} ions are shown in Fig. 7. It can be seen that decay curve of the powders with lowest concentrations has highest intensities and afterglow, while those with higher mole concentration of Ho^{3+} ions has the lowest intensities and . This indicates that lower mole concentration of Ho^{3+} favors long afterglow and higher intensities and vice versa. The decay times of the phosphor can be estimated by using the following double exponential equation;

$$I = A_1 \exp(-t/\tau_1) + A_2 \exp(-t/\tau_2)$$

where I is the phosphorescence intensity, A_1, and A_2, are constants, t is time, τ_1 and τ_2, are decay times for exponential components, respectively. The fitting results of parameters t_1 and t_2 are listed in Table 2 below.

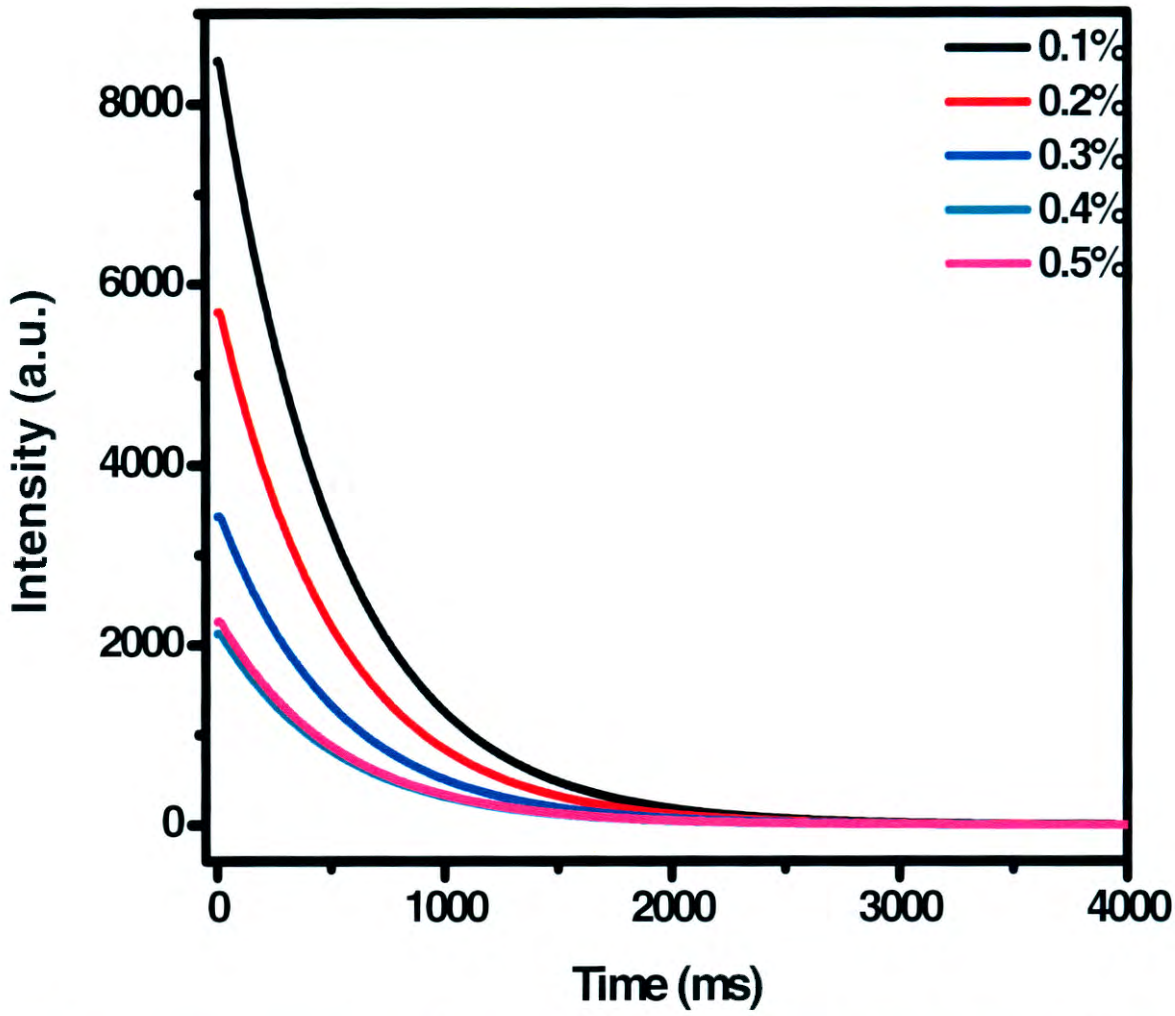

Fig.7.7. Decay curves of Ho^{3+} co-doped Y_2O_3: Eu^{3+} phosphor when Ho^{3+} ion concentration was varied from 0.1 to 0.5%

Table 7.2: Decay constants for the fitted decay curves of the Y_2O_3: Eu^{3+}:Ho^{3+} powder

% concentration	0.1	0.2	0.3	0.4	0.5
Components	Decay constants(τ, s)				
Fast (τ_1)	0.368	0.352	0.345	0.339	0.326
Medium (τ_2)	0.680	0.668	0.641	0.625	0.599

The graph of maximum peak intensity of the as-prepared powders as a function of % Ho^{3+} concentration is shown in Fig.8. The emission peak intensity quenched gradually with increase in the % concentration of Ho^{3+} ions. It can be seen from the curve that the powders showed differences in initial intensity and medium persistence when the powders were efficiently activated by UV lamp. The results indicate that the initial luminescence intensity and the decay time of phosphors are enhanced with a decrease in the % concentration.

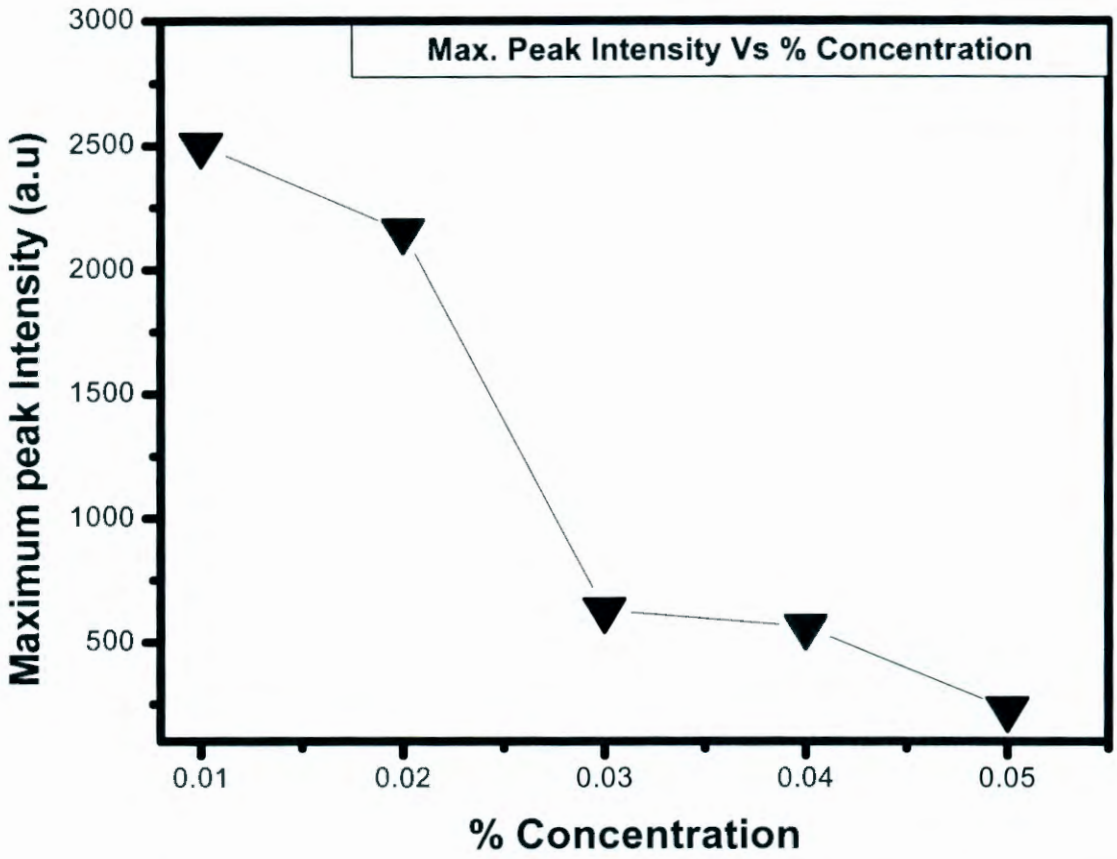

Fig.7.8. Concentration of Ho^{3+} ions vs. maximum peak intensity graph of $Y_2O_3:Eu^{3+}:Ho^{3+}$ phosphor

7.3.4 Optical properties

7.3.4.1 Absorbance spectra

The UV–vis absorbance spectra of the samples are given in Fig. 9. The spectra of all the powder samples show good optical quality in the visible range due to the complete

absorbance in the 200– 700 nm range. The sharp absorption edge is characteristic of a homogeneous structure [29]. The figure shows that the absorption edge shifted to higher wavelength for higher mole concentration and then reduced to lower wavelength for lower mole concentration. Furthermore, absorption bands corresponding to the forbidden Eu^{3+} f–f transitions were detected for higher mole concentration. The band at around 220 and330 nm is attributed to the exciton absorption, which is red-shift compared with powder Y_2O_3:Eu^{3+}:Ho^{3+} [30]. The absorption peaks at around 290 and 340 nm are assigned to ^{5}Do-$^7F_1$and $^5D_0$-$^7F_2$ transitions of Eu^{3+} ions, respectively [31].

7.4.2 Determination of Eg. from reflectance spectra

The Kubelka- Munk equation was used to calculate the band gap of the as- prepared powder as follows;

$$F(R\infty) = \frac{(1-R\%)^2}{2R\%} = k/s \text{----------} (1)$$

Where $R_\infty = R_{sample}/R_{references}$, K is absorption coefficient and S is scattering coefficient.

On the other hand the bang gap Eg, and absorption coefficient α of indirect band gap semiconductor are related through the well- known Tauc relation;

$$\alpha h\nu = C_1(h\nu - E_g)^2 \text{----------} (2)$$

Where hν is the photo energy and C_1 is proportionality constant, n=2 for indirect transition. When the material scatters in a perfectly manner, the absorption coefficient K becomes equal to 2α (K=2α). Considering the scattering coefficient S as constant with respect to wavelength, and using equations (1) and (2), the following expression can be written:

$$[F(R\infty) * h\nu]^2 = C_2(h\nu - E_g) \text{----------} (3)$$

By plotting $[F(R)*h\nu]^2$ against hv and fit the linear region with a line and extend it to the energy axis, then one can easily obtain E_g by extrapolating the linear regions to $[F(R*) h\nu]^2=0$. The average Eg. value for the powders was found to be 4.43 eV, which is in a good agreement with the literature values by other researchers [26-27]. The observed optical bang gap for Y_2O_3: Eu^{3+}:Ho^{3+} samples have decreased to 4.0 eV at lower mole concentration of

Ho^{3+} shown in Fig. 10. The change in optical band gap values may also be due to the change of crystal structure of the Y_2O_3 powders. This change in the optical band gap materials can be explained on the basis of quantum size effect.

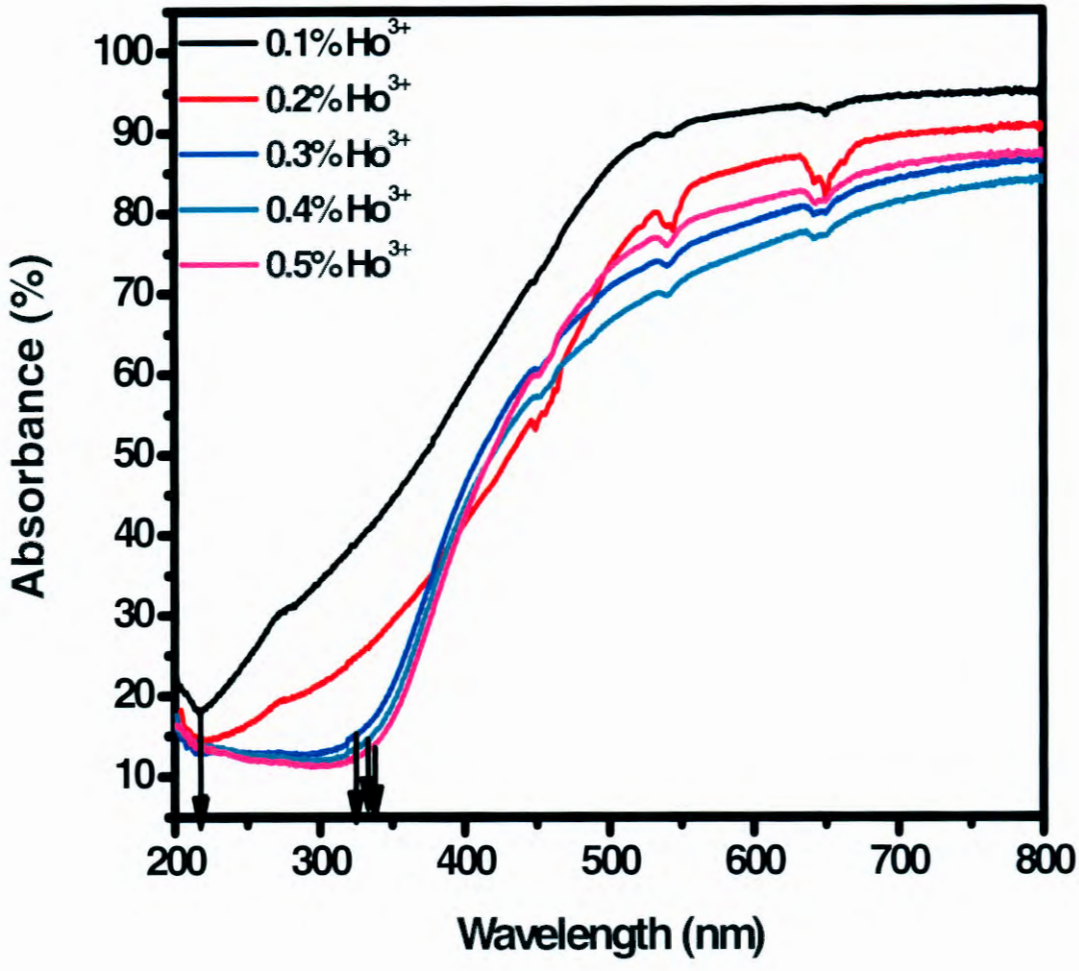

Fig.7.9. Uv-vis absorbance spectra of Y_2O_3: Eu^{3+}: Ho^{3+} red- emitting phosphor with % mole concentration of Ho^{3+} from 0.1 to 0.5%.

The dependence of the band gap energy of the Y_2O_3:Eu :Ho on the percent mole concentration of Ho3+ ions is shown in Fig. 11. It can be seen from the graph that the band gap of the Y_2O_3; Eu^{3+}: Ho^3+ powders increased with the percent mole concentration of Ho^{3+}. The decrease in band gap energy and the shift of the absorption edges to higher wavelengths might be due to the presence of defect states and disorder due to the percent mole concentration. The mole concentration of Ho^{3+} might have introduced new states close to the conduction band of the Y_2O_3:Eu^{3+}: Ho^{3+}. A new defect band is therefore formed below the

conduction which lead to reduction in the effective band gap [32]. It is clear that at 0.5% mole concentration of Ho^{3+} the estimated band gap increased upto 4.7 eV.

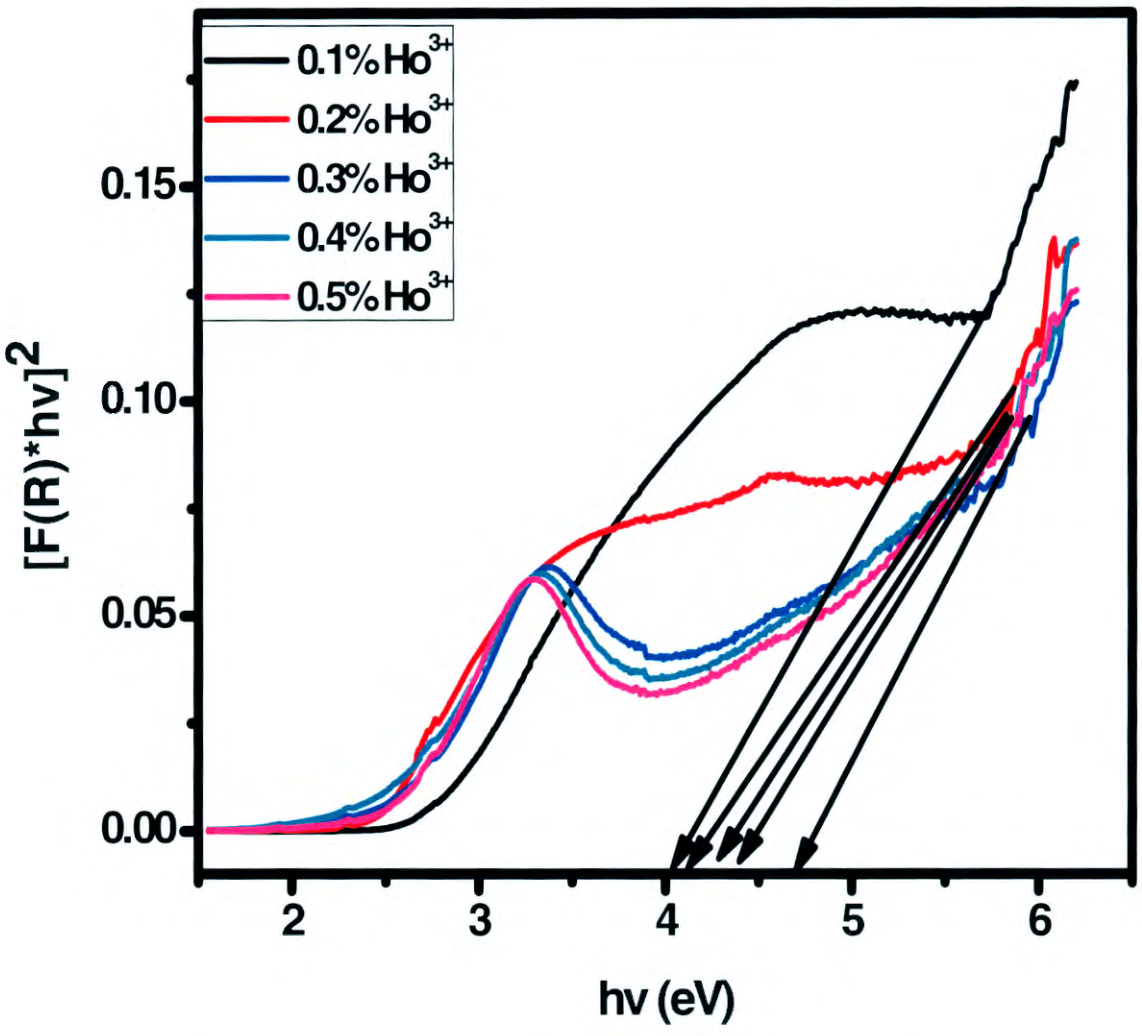

Fig.7.10. Graph of F $[(R)*hv]^2$ as a function of band gap energy

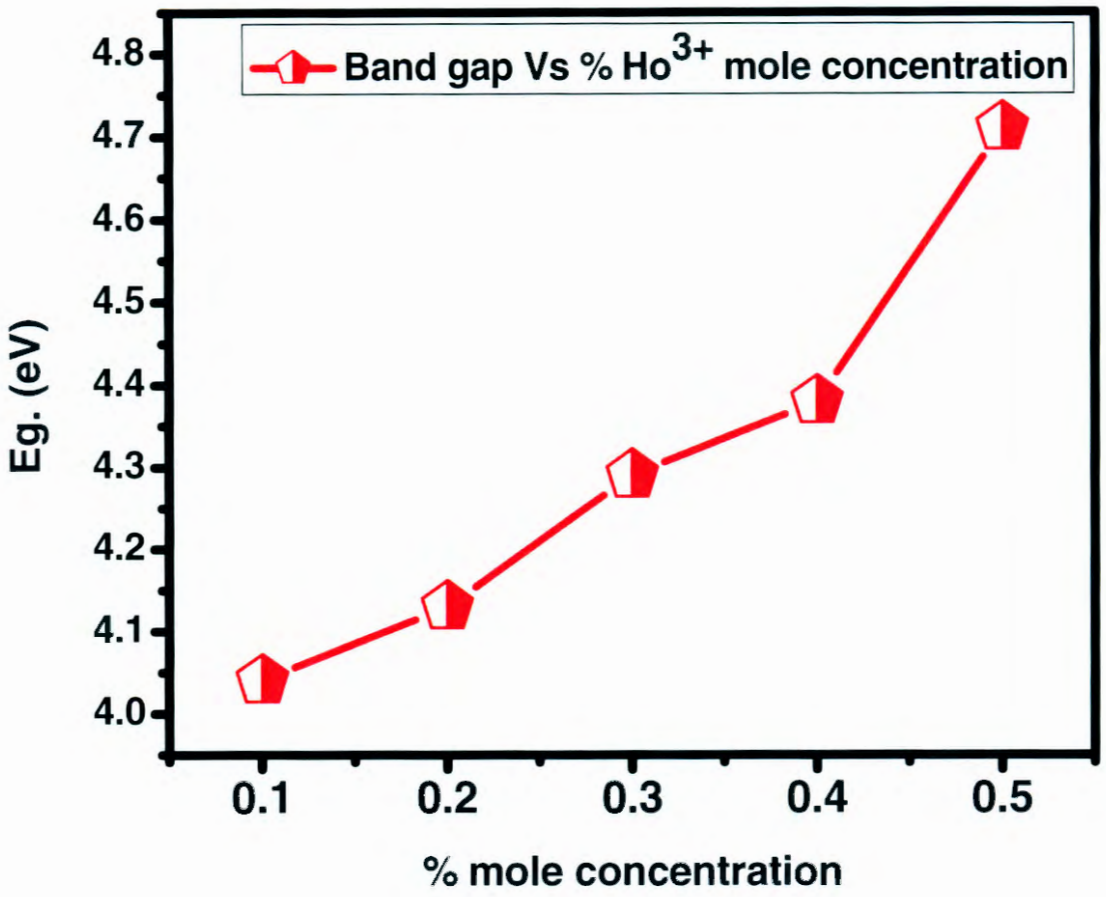

Fig. 7.11. Band gap energy as a function of Ho^{3+} mole concentration

7.4 Conclusion

$Y_2O_3:Eu^{3+}:Ho^{3+}$ red-emitting phosphor was successfully synthesized and the influence of mole percent of Ho^{3+} ions has been investigated. The powders composed of nanoparticles. The size of the particles depended on the Ho^{3+} mole concentration. An increase in the Ho^{3+} percent resulted in smaller crystallite sizes. SEM show particles are highly agglomerated and form a connected network type with some vacant space among them, which is expected due to the evolution of different gases during combustion of the gel. At lower mole of Ho^{3+} all the peaks for both Eu^{3+} and Ho^{3+} were observed. The PL measurements showed red emission of $Y_2O_3:Eu^{3+}:Ho^{3+}$ powder with the most intense peak appearing at 626 nm, which is assigned to the $^5D_0$-$^7F_2$ transition of Eu^{3+}. At higher mole concentration of Ho^{3+}, energy transfer

occurred from Eu^{3+} to Ho^{3+}. The band gap energy increased with increase of Ho^{3+} mole concentration.

References

[1] G. Blasse, B.C. Grabmaier, in: Luminescent Materials, Springer, Berlin, Germany, 1994.

[2] M. Jia, J. Zhang, S. Lu, S. Sun, Y. Luo, X. Ren, H. Song, X. Wang, Chem. Phys. Lett. 384 (2004) 193.

[3] S. Ray, P. Pramanik, A. Singha, A. Roy, J. Appl. Phys. 97 (2005) 094312-1.

[4] J.W.Wang, Y.M. Chang, H.C. Chang, S.H. Lin, L.C. Huang, X.L. Kong, M.W. Kang, Chem. Phys. Lett. 405 (2005) 314.

[5] J. Wan, Z. Wang, X. Chen, L. Mu, Y. Qian, J. Cryst. Growth 284 (2005) 538.

[6] R. Schmechel, M. Kennedy, H. Von Seggern, H. Winkler, M. Kolbe, R.A. Fischer, L. Xaomao, A. Benker, M. Winterer, H. Hahn, J. Appl. Phys. 89 (2001) 1679.

[7] H.W. Song, B.J. Chen, H.S. Peng, J.S. Zhang, Appl. Phys. Lett. 81 (2002) 1776.

[8] X.M. Li, A. Benker, M. Winterer, H. Hahn, J. Appl. Phys. 89 (2001) 1679.

[9] G.Y. Hong, K. Yoo, S.J. Moon, J.S. Yoo, J. Electrochem. Soc. 150 (2003) H67.

[10] G. Wakefield, E. Holland, P.J. Dobson, J.L. Hutchison, Adv. Mater. 20 (2001) 1557.

[11] H. Peng, H . Song, B Chen, S . Lu, S. Huang, Chem. Phys. Lett. 370 (2003) 485.

[12] K .Y. Jung, C. H. Lee, Y. C. Kang, Mater. Lett. 59 (2005) 2451. [13] R. Debnath, A. Nayak, A. Ghosh, Chem. Phys. Lett. 444 (2007) 324.

[13] T. Jüstel, H. Nikol, and C. Ronda, "New developments in the field of luminescent materials for lighting and displays," Angewandte Chemie, vol. 110, pp. 3250–3271, 1998.

[14] A. L. Rogach, N. Gaponik, J. M. Lupton et al, "Light-emitting diodes with semiconductor nanocrystals," Angewandte Chemie, vol. 47, no. 35, pp. 6538–6549, 2008.

[15] M . Dahan, T. Laurence, F. Pinaud et al, "Time-gated biological imaging by use of colloidal quantum dots," Optics Letters, vol. 26, no. 11, pp. 825–827, 2001.

[16] K. E. Gonsalves, G. Carlson, S .P. Rangarajan, M. Benaissa, and M. José-Yacamán, "Synthesis and characterization of a nanostructured gallium nitride-PMMA composite," Journal of Materials Chemistry, vol. 6, no. 8, pp. 1451–1453, 1996.

[17] R. G. Pappalardo and R. B. Hunt, "Dye-laser spectroscopy of commercial Y_2O_3:Eu^{3+} phosphors," Journal of the Electrochemical Society, vol. 132, pp. 721–730, 1985.

[18] C. R. Ronda, "Phosphors for lamps and displays: an applicational view," Journal of Alloys and Compounds, vol. 225, no. 1-2, pp. 534–538, 1995. [19]T. Justel, H. Nikol, and C. Ronda, "New development in the field of luminescent materials for lighting and displays," Angewandte Chemie, vol. 37, pp. 3084–3103, 1998.

[20] X . Jing, T. Ireland, C . Gibbons et al, "Control of Y_2O_3:Eu spherical particle phosphor size, assembly properties, and performance for FED and HDTV," Journal of the Electrochemical Society, vol. 146, no. 12, pp. 4654–4658, 1999.

[21] C. H Kim, I .E. Kwon, C .H. Park et al, "Phosphors for plasma display panels," Journal of Alloys and Compounds, vol. 311, no. 1, pp. 33–39, 2000.

[22] W. W. Zhang, M. Xu, W. P, Zhang et al, "Site-selective spectra and time-resolved spectra of nanocrystalline Y_2O_3:Eu^{+3}," Chemical Physics Letters, vol. 376, no. 3-4, pp. 318–323, 2003.

[23] X. Qin, T. Yokomori, Y. Ju. Flame synthesis and characterization of rare-earth (Er^{3+}, Ho^{3+}, and Tm^{3+}) doped upconversion phosphors. Appl Phys Lett. 2007; 90:073104. Doi: 10.1063/1.2561079.

[24] D. Tu, Y. Liang, R. Liu, D. Li. Eu/Tb ions co-doped white lightluminescence Y_2O_3 phosphors. J Lumin. 2011; 131:2569-2573. Doi: 10.1016/j.jlumin.2011.05.036.

[25] H. Wang, J. Yang, C.M. Zhang, J. Lin, Synthesis and characterization of monodisperse spherical Sio_2@RE_2O_3 (RE=rare earth elements) and SiO_2@Gd_2O_3:Ln^{3+} (Ln=Eu, Tb, Dy, Sm Er,Ho) particles with core shell structure. J solid Stae Chem. 2009; 182:2716-2724. doi: 10.1016/j.jssc.2009.07.033.

[26] T.S Atabaev, H-HT Vu, Z. Piao, H-K Kim, Y-H Hwang, Tailoring the luminescent properties of codoped Gd_2O_3:Tb^{3+} phosphor particles by codoping with Al^{3+} ions. J Alloys Compd 2012, 541:263-268.

[27] M. A. Flores-Gonzales, G . Ledoux, S. Roux, K. Lebbou, P. Perriat, O. Tillement, Preparing nanometer scaled Tb-doped Y_2O_3 luminescent powders by the polyol method. J Solid State Chem 2005, 178:989-997.

[28] T.S Atabaev, J.H Lee, D.W Han, Y-H Hwang, H-K Kim, Cytotoxicity and cell imaging potentials of submicron color-tunable yttria particles. J Biomed Mat Res A 2012, 100(9):2287-2294

[29] Q. Pang, J. Shi, Y. Liu, D. Xing, M. Gong, N. Xu, Mater. Sci. Eng. B 103 (2003) 57.

[30] J.C. Park, H.K. Moon, D.K. Kim, S.H. Byeon, B.C. Kim, K.S. Suh, Appl. Phys. Lett. 77 (2000) 2162.

[31] J.L. Ferrari, A.M. Pires, M.R. Davolos, Mater. Chem. Phys. 113 (2009) 587.[32] J.A.

Huhhey, E.A. Keiter, R.L. Keiter, in: Inorganic Chemistry, HarperCollins, New York, 1993.

Chapter 8

Temperature dependence of structural and luminescence properties of Eu^{3+} -doped Y_2O_3 red- emitting phosphor thin films by Pulsed Laser Deposition

8.1 Introduction

In an early development of low-voltage cathodoluminescent (CL) phosphors for applications in field emission display (FED) devices, the cathode-ray tube (CRT) phosphors have readily been tested as candidates. In the case of the red phosphor materials, unfortunately, $Y_2O_2S:Eu^{3+}$ which is used as the red primary color in the CRT has known to be degraded under electron bombardments with high current densities and the sulphur containing volatile gases escaping from the surface under electron bombardment contaminate the cold cathodes, resulting in a fatal damage to FED devices [1]. The oxide based thin-film phosphors are highly attractive in the use of the FED devices because of the advantages such as higher lateral resolution from smaller grains, better thermal and mechanical stability, and reduced outgassing over conventional powder phosphors [2]. Among the oxide phosphors, $Y_2O_3:Eu^{3+}$ is currently one of the leading red phosphor materials for FEDs [3]. $Y_2O_3:Eu^{3+}$ films have been grown using various deposition techniques [4-6]. However, because of its high melting point of about 2400 °C, $Y_2O_3:Eu^{3+}$ thin films require a post-annealing process at high temperatures above 1000 °C to crystallize the deposits [7-10]. Therefore, the high temperature process is inevitable in order to obtain high efficient and bright $Y_2O_3:Eu^{3+}$ thin film phosphors and $Y_2O_3:Eu^{3+}$ films had been grown only on the heat-resistant substrates such as Si wafers [11, 12], Ni based alloys [9] and sapphire plates [13-15]. However, annealing at high temperature is definitely a concern for the fabrication of the current FED devices which adapt low temperature glass substrates.

Journal of Applied Physics A, APYA-D-15-01792.1, DOI: 10.1007/s00339-016-9946-5

By replacing the rastered electron beams in the CRT with an array of cathodes, FEDs promise to be significantly thinner and lighter, have higher brightness, better power efficiency, and viewing angle, and operate over a large temperature range as compared to liquid crystal displays (LCDs) [16-18]. While the cathode array enables FEDs, the light from this emissive display comes from the phosphor anode. Phosphor anodes are currently powders screened onto glass plates using a variety of techniques including electrophoretic, dusting, and slurry methods [19]. The slurry method is the most common method, in which phosphor powder is mixed with photosensitive chemicals and is patterned using photolithography techniques. For operating voltages greater than 2 kV, the screen is back coated with a thin layer of aluminium which acts as an optical reflector as well as a charge dissipater [20-22]. At operating voltage below 2 kV, the electron penetration depth is so small that the screens are left un-coated [23-25]. Even though powder phosphors are very efficient, the particle size may limit resolution of the display. Thin films are an alternative to powder phosphors, and have both advantages and disadvantages as compared to powders [26-29].

The intention of the present research is to investigate whether modifying the surface of deposited thin film phosphors by annealing at different temperatures would result in increased efficiency. We therefore report on the study of the annealing temperature on pulsed laser deposited thin films, the consequent crystalline and surface morphology structures, and photoluminescence (PL) characteristics of $Y_2O_3:Eu^{3+}$ thin films.

8.2 Experimental details

8.2.1 Powder synthesis

$Y_2O_3:Eu^{3+}$ nanocrystals were synthesized using the sol- combustion route. The method of synthesis essentially comprises of mixing the precursors in appropriate stoichemetric ratios, followed by firing in an air tube furnace at a temperature of 400 ^{0}C. The white foamy product was then grounded and left to dry in an enclosed oven for 24 hours.

8.2.2 Pulsed Laser Deposition (PLD)

The Si (100) wafers used as substrate were first chemically cleaned. The phosphor was pressed with binders to prepare a pellet that was used as an ablation target. The deposition chamber was evacuated to a base pressure of 8×10^{-6} mtorr. The Lambda Physic 248 nm KrF excimer laser was used to ablate the phosphor pellet in a constant 20 mtorr O_2 atmospheres. A Baratron Direct (Gas Independent) Pressure/Vacuum capacitance Manometer (1.33×10^{-2} mtorr) was used for the high pressure measurements. The laser energy density, number of pulses and laser frequency were set to 0.74 J/cm^2, 12000 and 10 Hz respectively. The substrate temperature was fixed at 300 ^{0}C, and the target to substrate distance was 6 cm. The ablated area was 1 cm^2. The films were then annealed at the temperatures of 600, 700, 800 and 900 ^{0}C.

8.2.3 Characterization

The Shimadzu Superscan SSX-550 system was used to collect the Scanning Electron Microscopy (SEM) micrographs. Atomic Force Microscopy (AFM) micrographs were obtained from the Shimadzu SPM - 9600 model. X-ray diffraction (XRD) data was collected by using a SIEMENS D5000 diffractometer using CuKα radiation of λ = 1.5405 nm. PL excitation and emission spectra were recorded using a Cary Eclipse fluorescence spectrophotometer (Model: LS 55) with a built-in xenon lamp and a grating to select a suitable wavelength for excitation. The excitation wavelength was 209 nm and the slit width was 10 nm. The afterglow curves for the films were also obtained with the Cary Eclipse spectrophotometer.

8.3 Results and discussions

8.3.1 Structural and morphological analysis

8.3.1.1 X-ray diffraction analysis (XRD)

XRD data were analyzed for the identification of phase and crystallite size. Figure 1 shows the X-ray diffraction patterns of the un-annealed and thin films annealed at the temperature of 600 to 900 ^{0}C for 2 hours. The un-annealed thin film was amorphous, while those annealed were crystalline. Two different phases were obtained at low and high annealing temperatures.

The thin film annealed at lower temperatures were indexed to cubic bixbyte phase [space group Ia-3(206)] with average lattice constant a=10.60Å which is in good agreement with the standard value for bulk cubic Y_2O_3 (JCPDS No. 72-0927). At low annealing temperature (600 to 700 ^{0}C), there are mainly two diffraction peaks at 2 theta values of 29.4 and 44.3. It can be clearly seen that by increasing the annealing temperature to 800 ^{0}C more peaks emerged at 2 theta values of 29.4, 33.0, 44.5, 47.8, 54.6, 56.3 and 62.0. This seven diffraction peaks indexed to hexagonal structure of Y_2O_3 are in agreement with data from JCPDS card No. 24-1424 with average lattice constants a=3.779 and c=6.590. The thin film annealed at 900 ^{0}C also revealed two peaks at 2 theta values of 29.4 and 44.5 similar to the peaks annealed at 600 and 700 ^{0}C, indicating same phase of cubic. This change in the structure when the annealing temperature is increased to 800 ^{0}C could be due to reduction in the lattice stress. The films annealed at 600, 700 and 900 ^{0}C have large lattice stress; while the stress of film at 800 ^{0}C is small. The role of crystal field change in the formation of a new phase should not be neglected as well. The broadening of the peaks in both the phases suggests small particle size. No other impurities peaks have been found which means that dopant ion completely occupies the Y_2O_3 host lattice. Also, the ionic radii of Y^{3+} (0.90Å) and Eu^{3+} (0.89 Å) are very close, and hence it is possible to substitute Y^{3+} with Eu^{3+} ions.

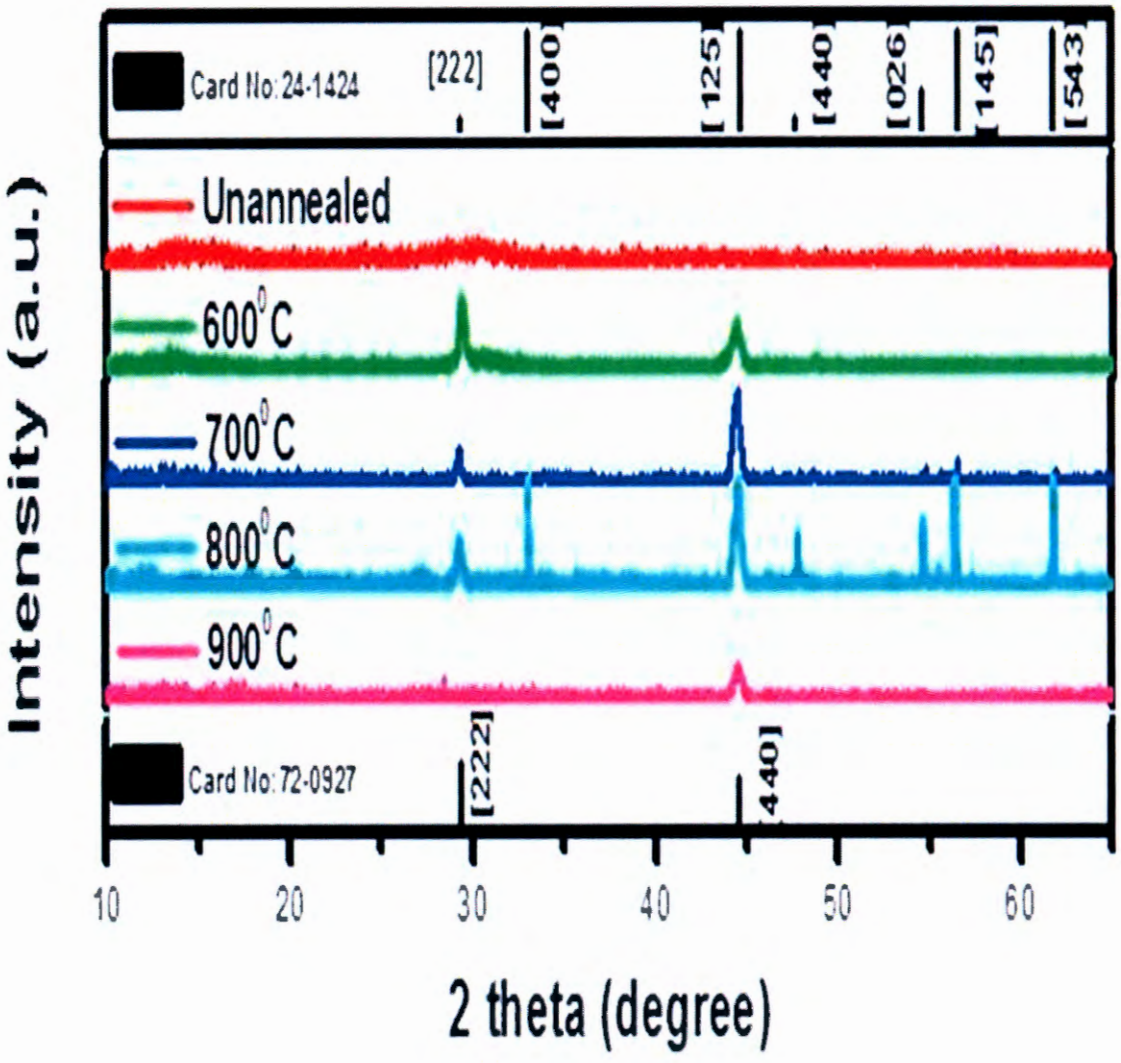

Figure 8.1. X-ray diffraction pattern of un-annealed and annealed Y_2O_3: Eu^{3+} thin film deposited on a (100) Si substrate after firing at temperatures between 600 and 900 ^{0}C in air for 2 hours.

Figure 8.2 shows the role of annealing temperature on crystallite sizes and lattice parameters. A slight increase in the crystallite size and a decrease in lattice parameters are established by means of X-ray diffraction analysis for a series of thin films annealed at temperatures between 600 and 900 ^{0}C.

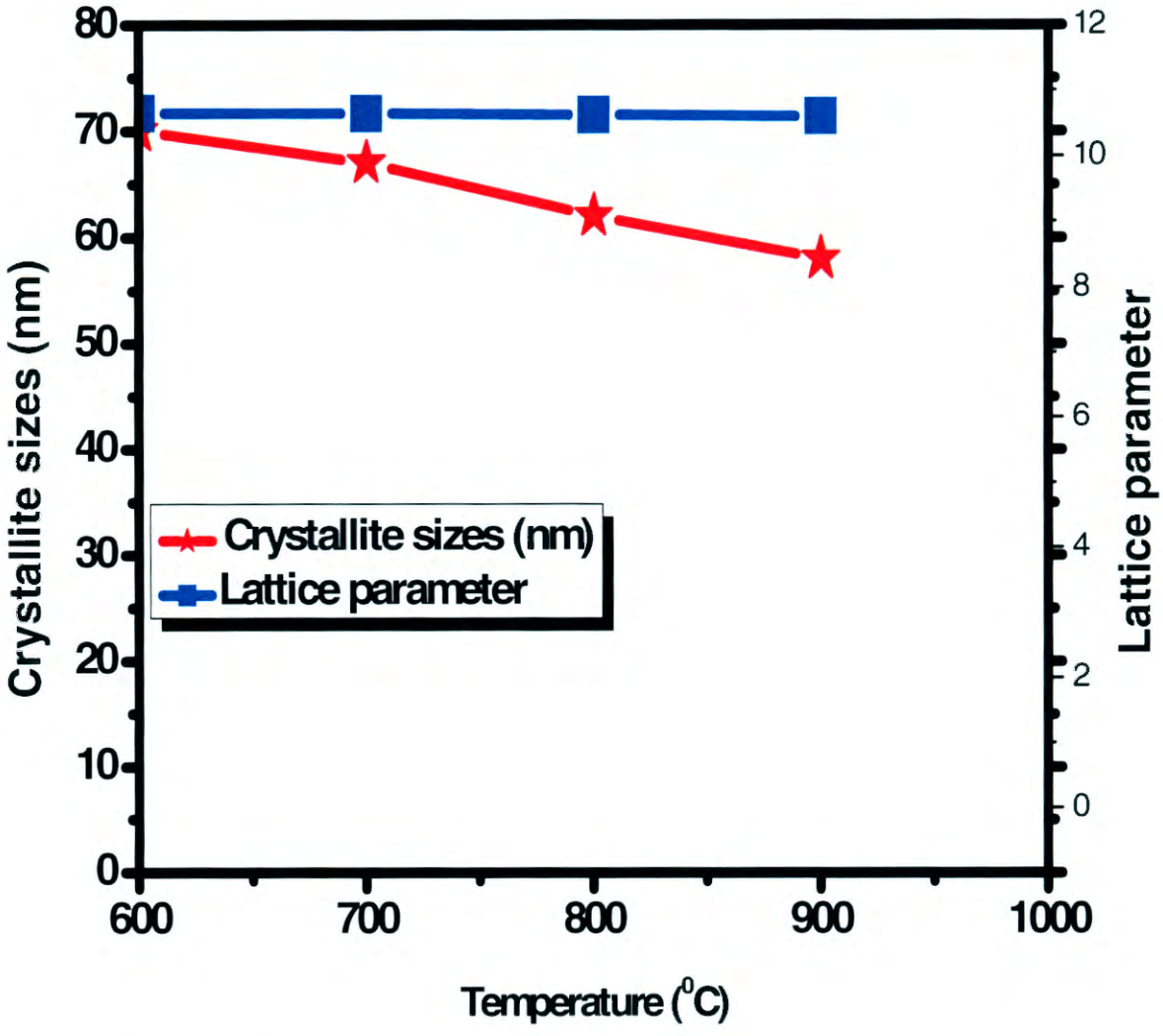

Figure 8.2. The crystallite sizes and lattice parameters as a function of temperature.

Further, it is marked that as the sample is annealed at higher temperatures the FWHM (full width at half maximum) of the diffraction peaks decreased and peaks became sharper. This suggest for an increase in the crystalline size of the annealed sample. To confirm this, crystalline size of both samples was calculated using the Scherrer formula [30-31].

$$D = \frac{0.9\lambda}{\beta cos\theta} \text{---------- (8.1)}$$

Where, D is crystallite size, λ is the wavelength of incident x-ray [Cuk (1.54056)], β is the FWHM and θ is the diffraction angle for (hkl) plane. To calculate crystallite size, three most intense peaks (29.24^0, 32.91^0 and 44.51^0) were selected. The FWHM of these peaks were taken by their Gaussian peak fitting. The average crystallite size for the annealed films

calculated through aforementioned procedure comes out to be 64 nm. The lattice parameters and crystallite sizes are shown in table 8.1.

Table 8.1. Showing lattice parameters and crystalline sizes of Y_2O_3: Eu^{3+} thin films.

Annealing temp. (^{0}C)	Lattice parameters			Crystallite size (nm)
	Hexagonal phase		Cubic phase	
	a	c	a	
Unannealed	-	-	-	-
600	3.712	6.575	10.603	70
700	3.790	6.630	10.625	67
800	3.796	6.645	10.647	62
900	3.815	6.649	10.654	58

8.3.1.2 Scanning Electron Microscopy (SEM)

The morphologies of the nanostructures of the Y_2O_3: Eu^{3+} thin films annealed at different temperatures were studied by the SEM patterns and presented in Figure 8.3. It shows that the obtained films are composed of particles which are nearly spherical in shape. SEM micrograph shows the aggregated nature of the secondary particles which were made up of the agglomeration of many primary particles. The films which were un-annealed and those annealed at lower temperatures appeared with the same morphology and crystalline sizes. At higher annealing temperature, the morphology of the film changed drastically to finer one probably due to change in the structure as also revealed by XRD.

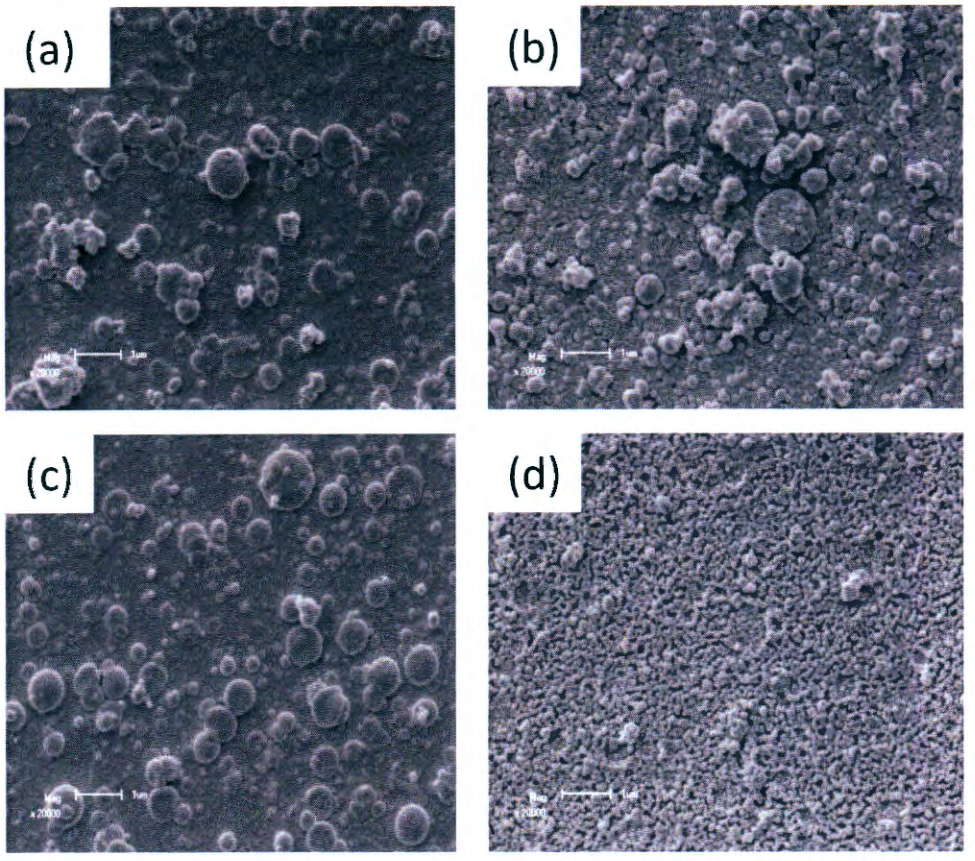

Figure 8.3. SEM micrographs of (a) un-annealed and annealed samples (b) 600 (c) 800 and (d) 900 ^{0}C.

8.3.1.3 Atomic Force Microscopy

Figure 8.4 show the AFM images of the Y_2O_3: Eu^{3+} thin films (a) unannealed, (b) annealed at 600 °C and (c) annealed at 900 ^{0}C in an open-air furnace. The images were obtained in contacting mode taken over a scale of 5×5 μm^2. Better crystal gain can be obtained by annealing at different temperatures, and the surface with different features can also be observed. The crystal grains of Y_2O_3:Eu^{3+} film annealed at higher temperature is more even and the grain size is lesser than that of un-annealed sample. The uneven grains are distributed on the surface of Y_2O_3:Eu^{3+} un-annealed film, large 72 nm and small 40 nm.

(a)

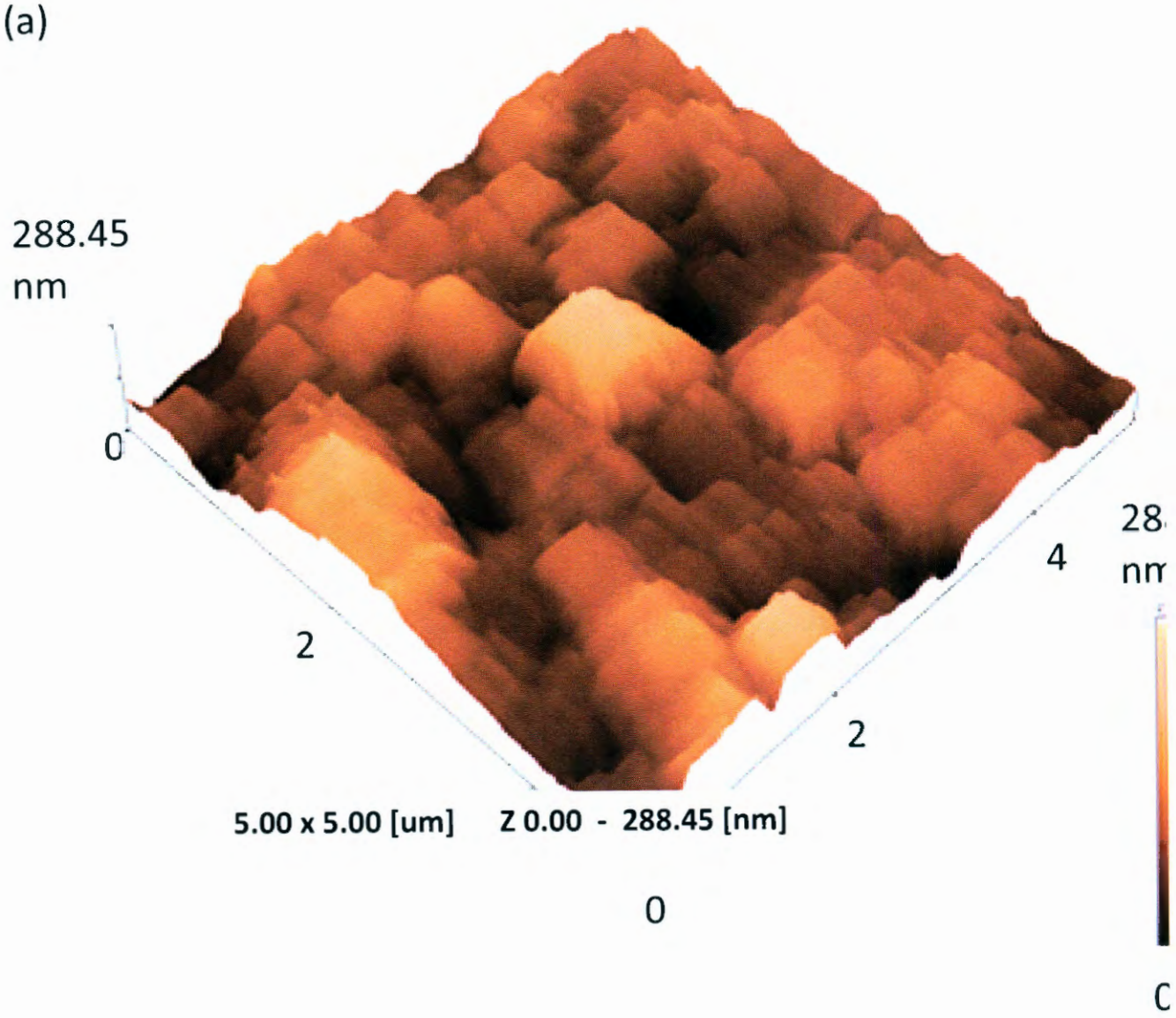

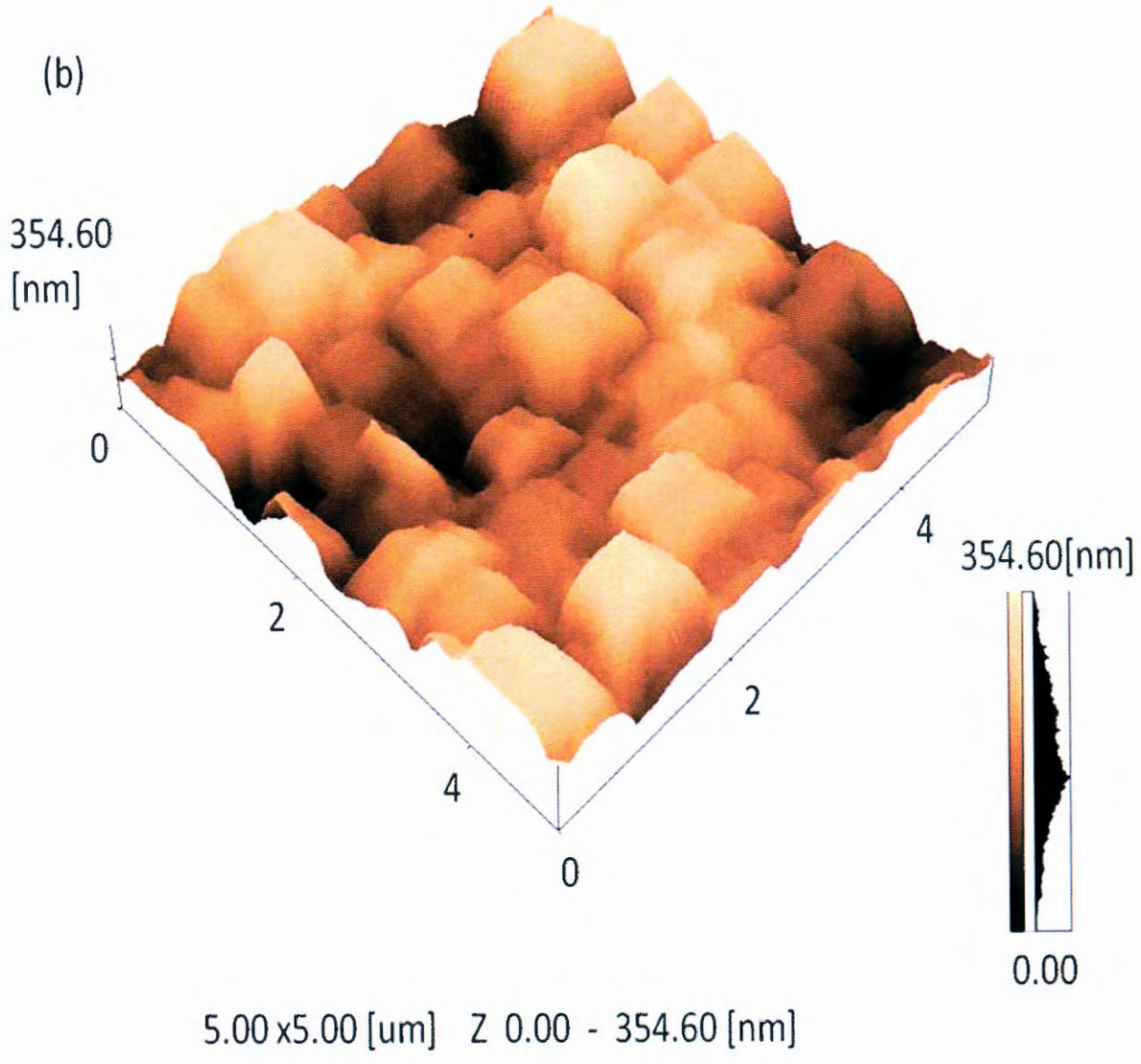
(b)
354.60
[nm]
0
2
4
0
2
4
354.60[nm]
0.00
5.00 x5.00 [um] Z 0.00 - 354.60 [nm]

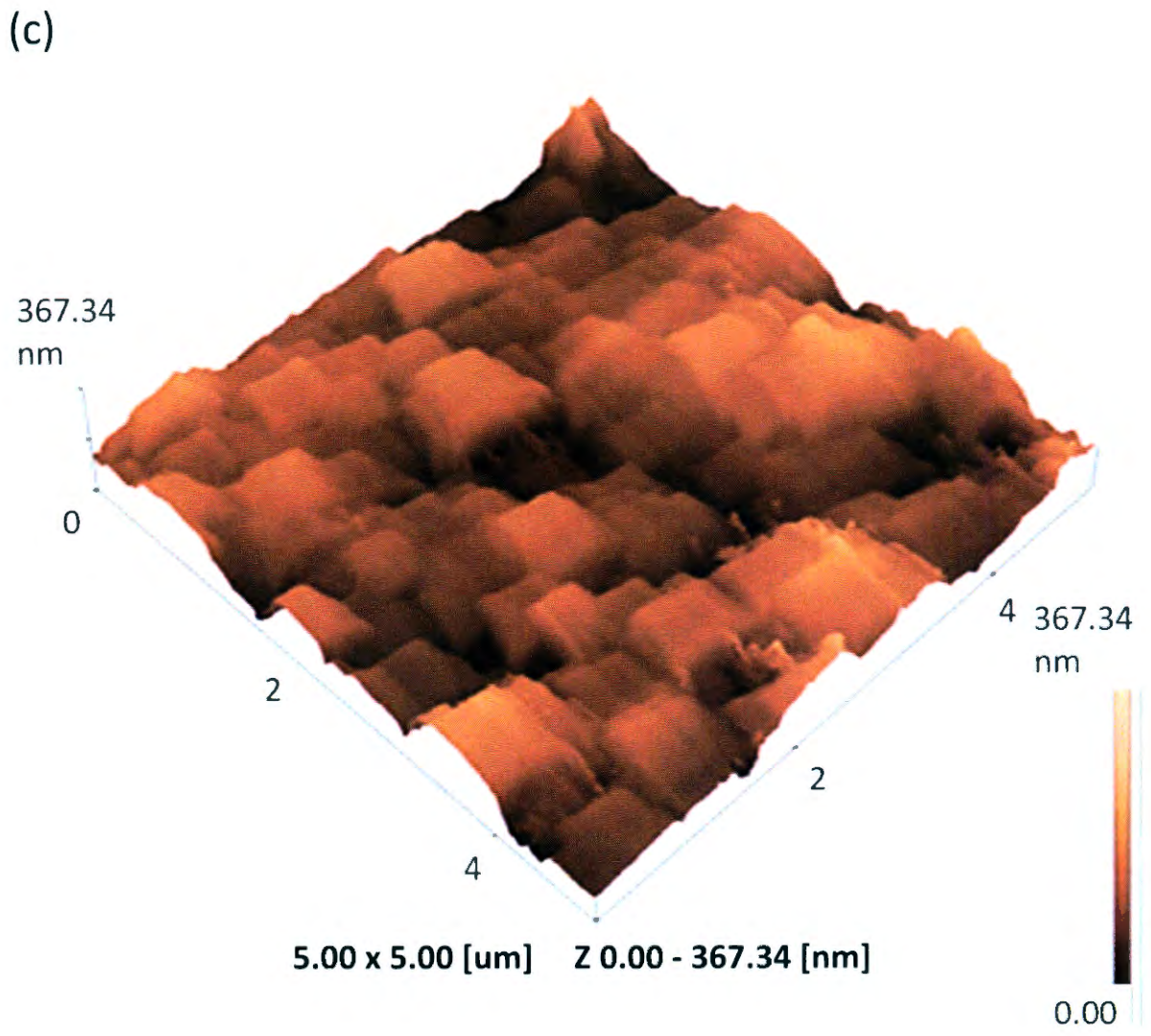

Figure 8.4. 3D Height AFM images done in contact mode for the thin films a) un-annealed, b) annealed at 600 and c) annealed at 900 ^{0}C

8.3.2 Optical properties

8.3.2.1 Absorption band

The UV–visible reflectance spectra of the as prepared samples are illustrated in Figure 8.5. The spectra of all the samples show good optical quality in the visible range due to the complete reflectance in the 200–400 nm range. It clearly indicates that, firstly as the annealing temperature increased the optical absorption edge shift to a higher wavelength while the reflectance intensity decreased [32]. Furthermore, absorption bands corresponding to the forbidden 4f–4f transitions are usually weak and therefore not detected. From the

graph, Figure 8.5, (indicated by arrows) the material absorbs between 320 and 350 nm depending on the annealing temperatures. Except for the thin film annealed 900 ^{0}C, the absorption wavelength of the films increased with increasing annealing temperature.

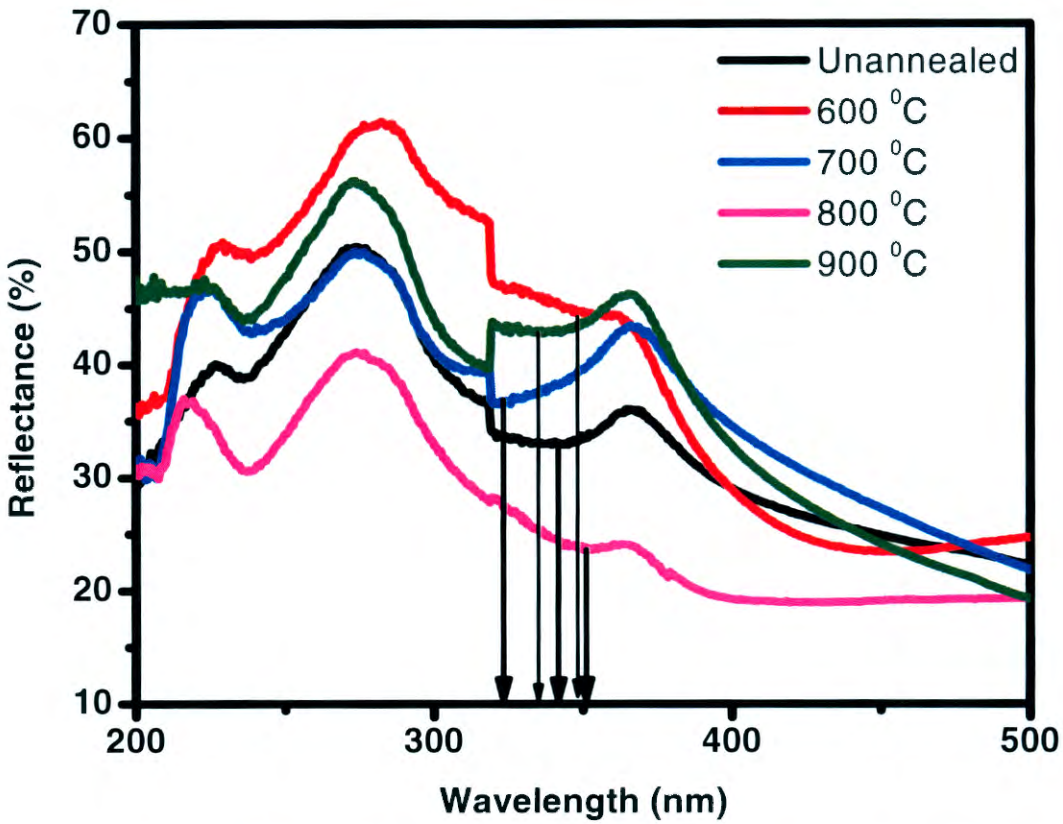

Figure 8.5. Diffuse reflectance measurements for unannealed and those annealed at different temperatures for Y_2O_3:Eu^{3+}thin films.

8.3.2.1.1 Determination of Eg. from reflectance spectra

Figure 8.6 shows graph of $[F(R)*hv]^2$ versus hv for the un-annealed and thin films annealed at various temperatures. In order to calculate the band gap of the films, the following Kubelka- Munk equation was used;

$$F(R_\infty) = (1-R_\infty)^2/2R_\infty = K/S \quad (8.2)$$

Where $R_\infty = R_{sample}/R_{references}$, K is absorption coefficient and S is scattering coefficient.

On the other hand the bang gap Eg, and absorption coefficient α of direct band gap semiconductor are related through the well- known Tauc relation:

$$\alpha hv = C_1 (hv-E_g)^{1/2} \text{----------(8.3)}$$

Where hv is the photo energy and C_1 is proportionality constant. When the material scatters in a perfectly manner, the absorption coefficient K becomes equal to 2α (K=2α). Considering the scattering coefficient S as constant with respect to wavelength, and using equations (8.1) and (2), the following expression can be written:

$$[F(R_\infty)* hv]^2 = C_2(hv-Eg) \text{----------(8.4)}$$

By plotting $[F(R)*hv]^2$ against hv and fit the linear region with a line and extend it to the energy axis, then one can easily obtain Eg by extrapolating the linear regions to $[F(R_\infty)hv]^2=0$. The arrows in the figure indicate these extrapolations for the unannealed and the thin films annealed at different temperatures. Eg is the band gap at n=2 for direct transitions. From the figure, the band gap of Y_2O_3: Eu^{3+} was found to be in the range of 4.6-4.8 eV. It can be seen clearly that the band gap energy of the Y_2O_3 decreases linearly with increasing temperature.

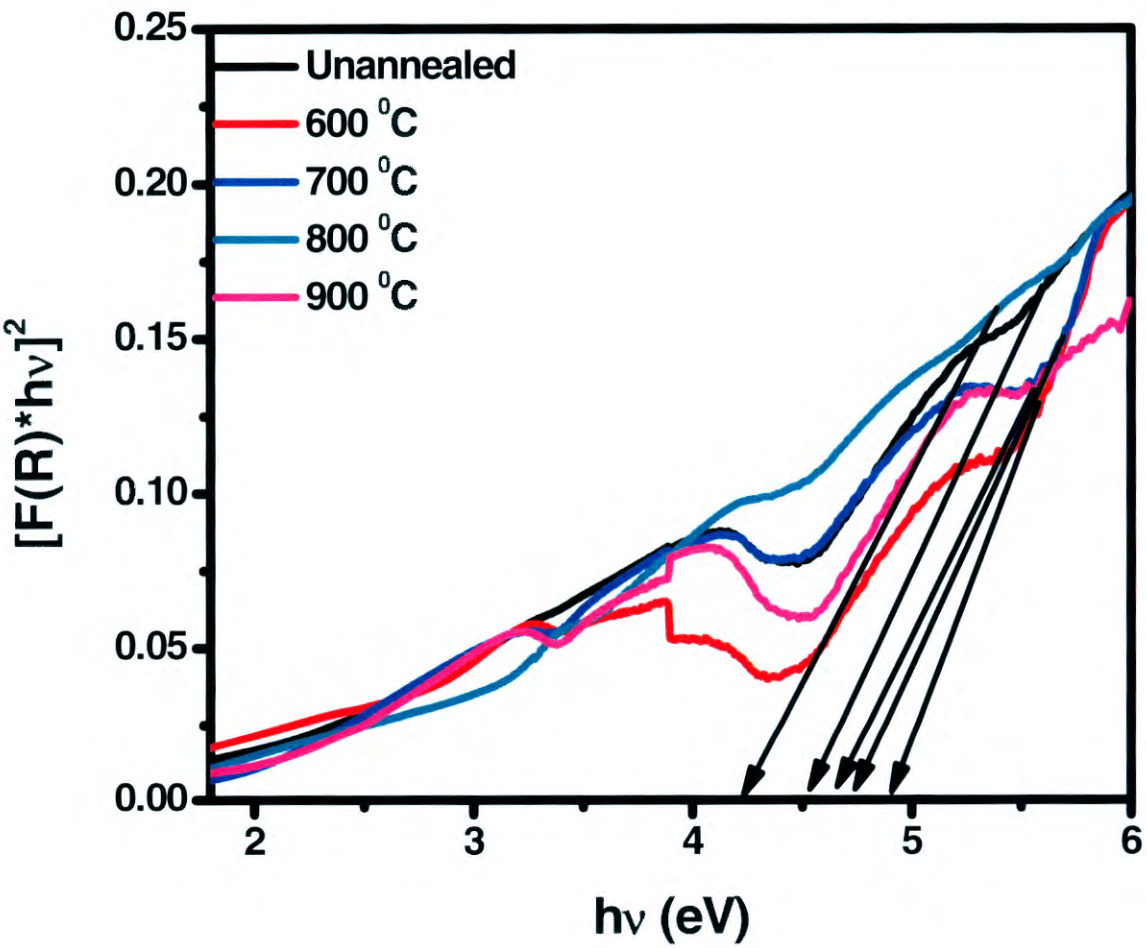

Figure 8.6. Graph of $F[(R)*hv]^2$ as a function of band gap

8.3.4 Photoluminescence

8.3.4 .1 Excitation spectra

Figure 8.7 gives the PL excitation spectra of the $Y_2O_3:Eu^{3+}$ thin films for un-annealed and those films annealed at temperatures between 600 and 900 ^{0}C. These spectra consist of several excitation bands which are ascribed to different transition. In the excitation spectrum monitored by $^5D_0$ - $^7F_2$ transition of Eu^{3+} at 612 nm for $Y_2O_3:Eu^{3+}$ thin films, the broad band with a maximum at 209 nm originates from the excitation of the oxygen-to-europium ($O^{2-} \rightarrow Eu^{3+}$) charge transfer band (CTB) and some very weak peaks in the longer-wavelength region of 300 nm are ascribed to the f → f transitions of the Eu^{3+} ions. The band located at 234 nm is due to host absorption band.

8.3.4.2 Emission spectra

Figure 8.8 shows the emission spectra of un-annealed and films annealed between 600 and 900 ^{0}C. The emission spectra were recorded at excitation wavelength of 209 nm. The most intense peaks appearing at 612 nm are recorded for the un-annealed and films annealed at lower temperatures of 600 and 700 ^{0}C. At higher annealing temperature of 800 ^{0}C, this peak is tremendously quenched possibly due to structural change. At annealing temperature of 900 ^{0}C, all these peaks are quenched but the peak appearing at 612 nm is red-shifted and enhanced which is a confirmation of formation of a new phase. Also, this peak is predominant at 588 and 715 nm wavelengths. This phenomenon can be explained by the fact that the 209 nm radiation excites the Eu^{3+} ions from ground state to the higher excited state $^5D_0$-$^7F_2$ and quickly relaxes to $^5D_0$-$^7F_4$ level by emitting non-radiative transition. The strong red emission band centred at 612 nm corresponds to the hypersensitive transition $^5D_0$-$^7F_2$. Another feeble yellow emission band at 588 nm corresponds to $^5D_0$-$^7F_1$ transition, which is less sensitive to the host. The reason behind observing the intense red emission from $Y_2O_3:Eu^{3+}$ can be understood by considering the structure of Y_2O_3. The coordinate number of Y_2O_3 is six and forms cubic bixbyite structure with two different sites (C_2 and S_6) for RE ions substitution. The C_2 is a low symmetry site without an inversion centre whereas C_2 is a high symmetry site having an inversion centre.

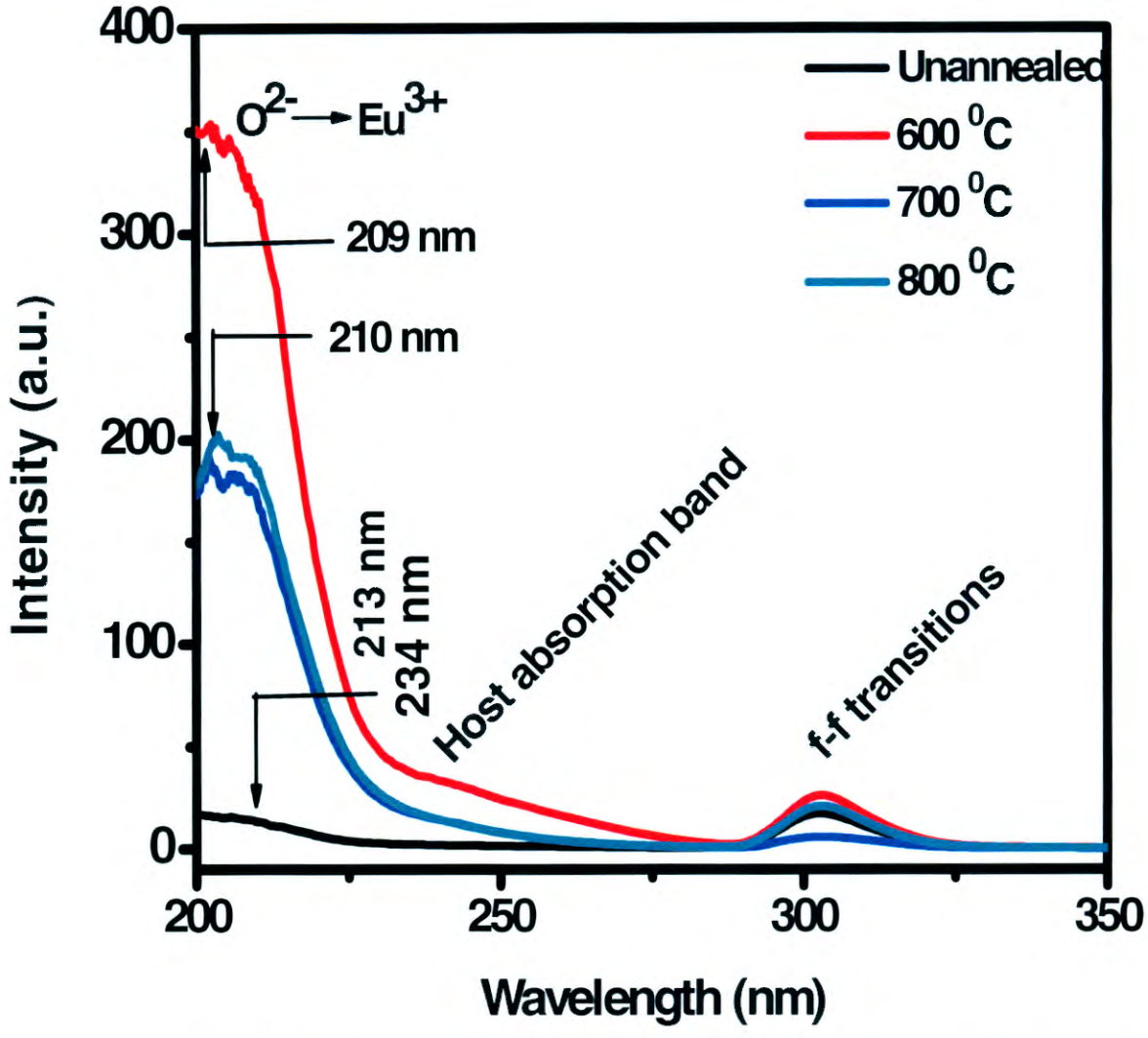

Fig. 8.7. The excitation spectrum of Y_2O_3: Eu^{3+} thin films for un-annealed and those annealed at 600, 700, 800 and 900 ^{0}C.

When Eu^{3+} is located at a low symmetry (C_2), the red emission is dominant whereas the yellow emission is dominant when Eu^{3+} is located at high symmetry (S_6) [34]. In the present case, red emission is dominant suggesting that the location of Eu^{3+} is more favourable at C_2 site. As the C_2 site does not have an inversion centre, electric dipole transition from Eu^{3+} ions attached to this site are more favourable than the magnetic dipole transitions. The similarity of the ionic radii of Eu^{3+} and Y^{3+} ions allows the easy substitution of Y^{3+} ions with Eu^{3+} ions at C_2 sites giving rise to intense red emission in the un-annealed and films annealed at lower temperatures [35].

Figure 8.9 represents the chromacity co-ordinates of the PL spectra for the samples (a) Un-annealed and those annealed at (b) 600, (c) 700, (d) 800 and (e) 900 ^{0}C, which are determined using the CIE (International Commission on Illumination) Coordinate Calculator software. According to the software the position of the color coordinates lie well in the red and orange region. The detailed analysis of the phosphor finds its suitability in making the red/orange producing phosphor for display applications and light emitting diodes.

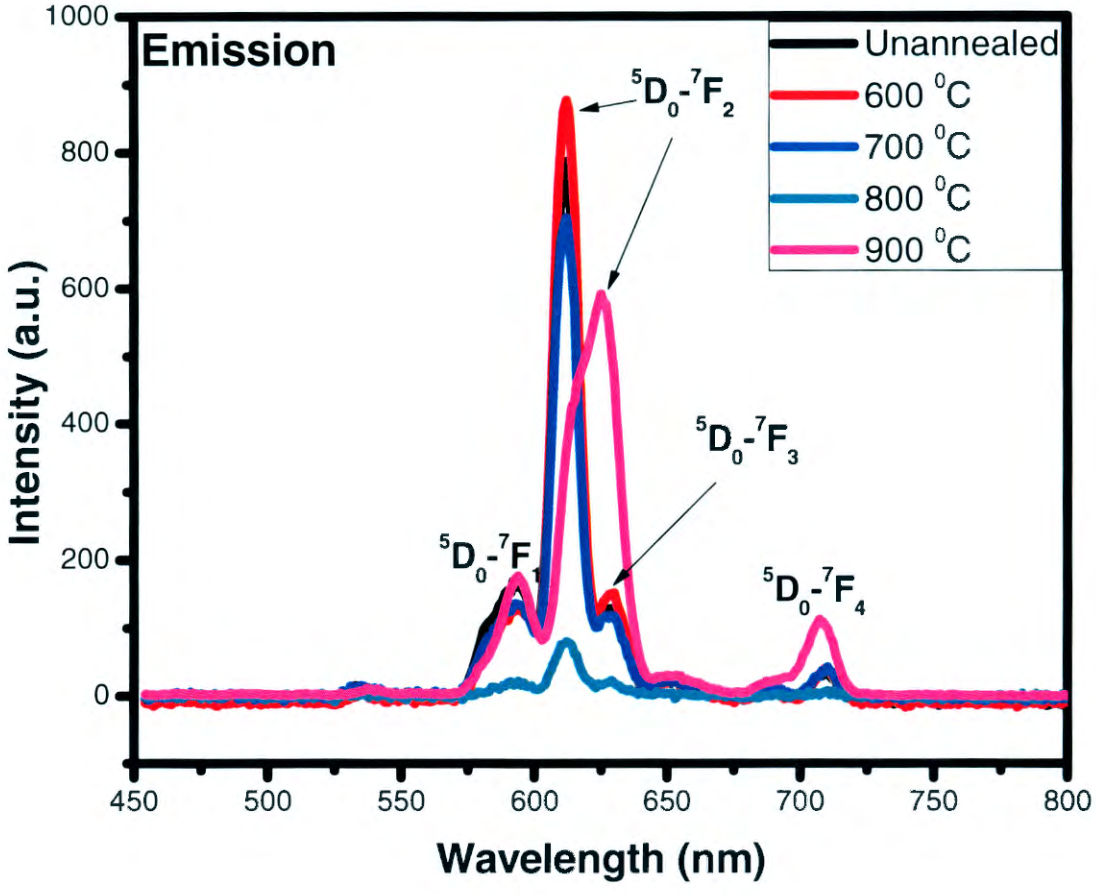

Figure 8.8. The emission spectrum of Y_2O_3: Eu^{3+} thin films for un-annealed and those annealed at 600, 700, 800 and 900 ^{0}C.

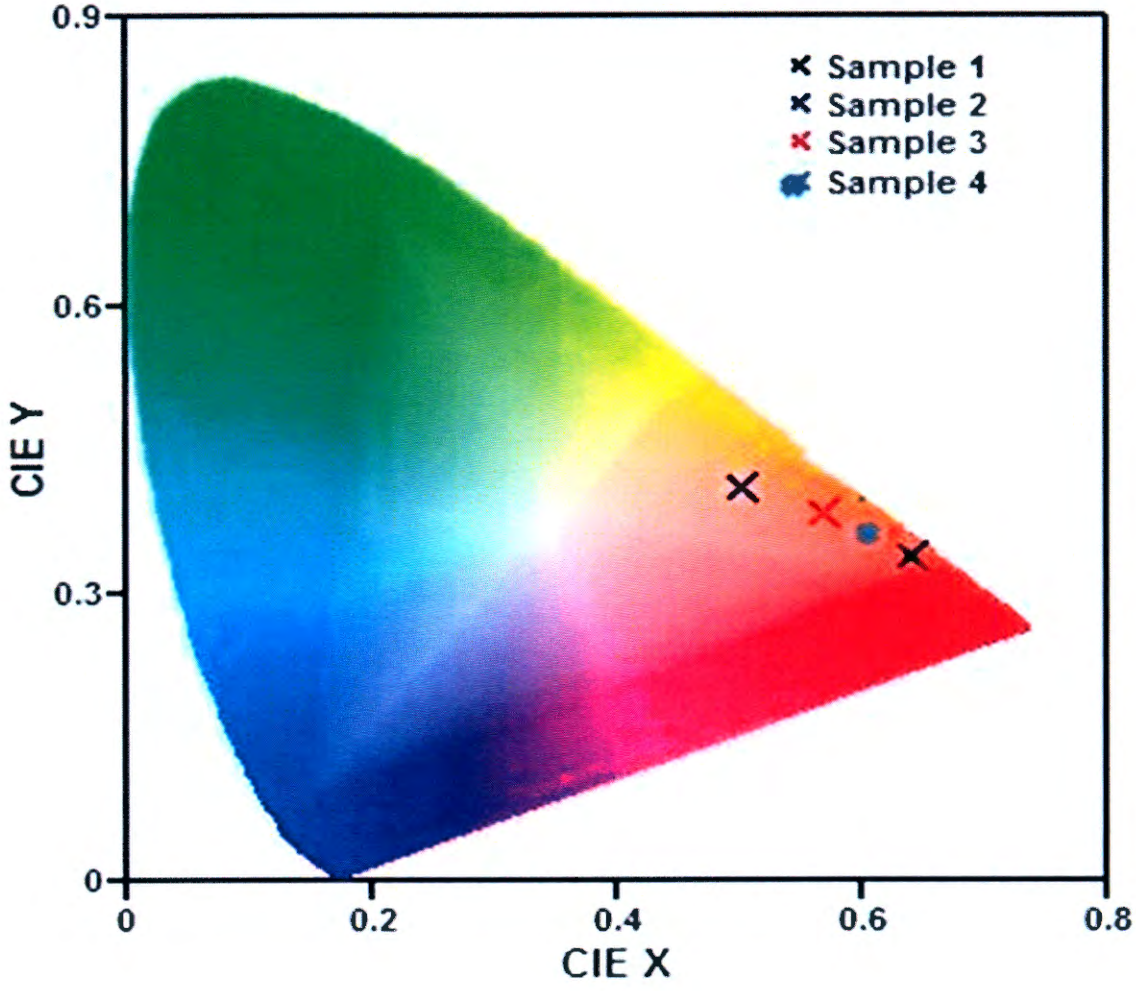

Figure 8.9. The CIE co-ordinates for samples that were un-annealed and those annealed at various temperatures

8.3.4.3 Decay curve

Figure 8.10 shows the decay characteristics of the thin films un-annealed and those annealed at temperatures between 600 and 900 ^{0}C. The films which are un-annealed and those annealed at lower temperatures has the highest initial intensities. This is also consistent with the PL spectra shown in Figure 8. The films were characterized by the fast and medium decays characteristics, since they are indicative of the different rates of decay for the films. The decay curves were fitted according to the equation (3) and gave the decay constants listed in Table 2.

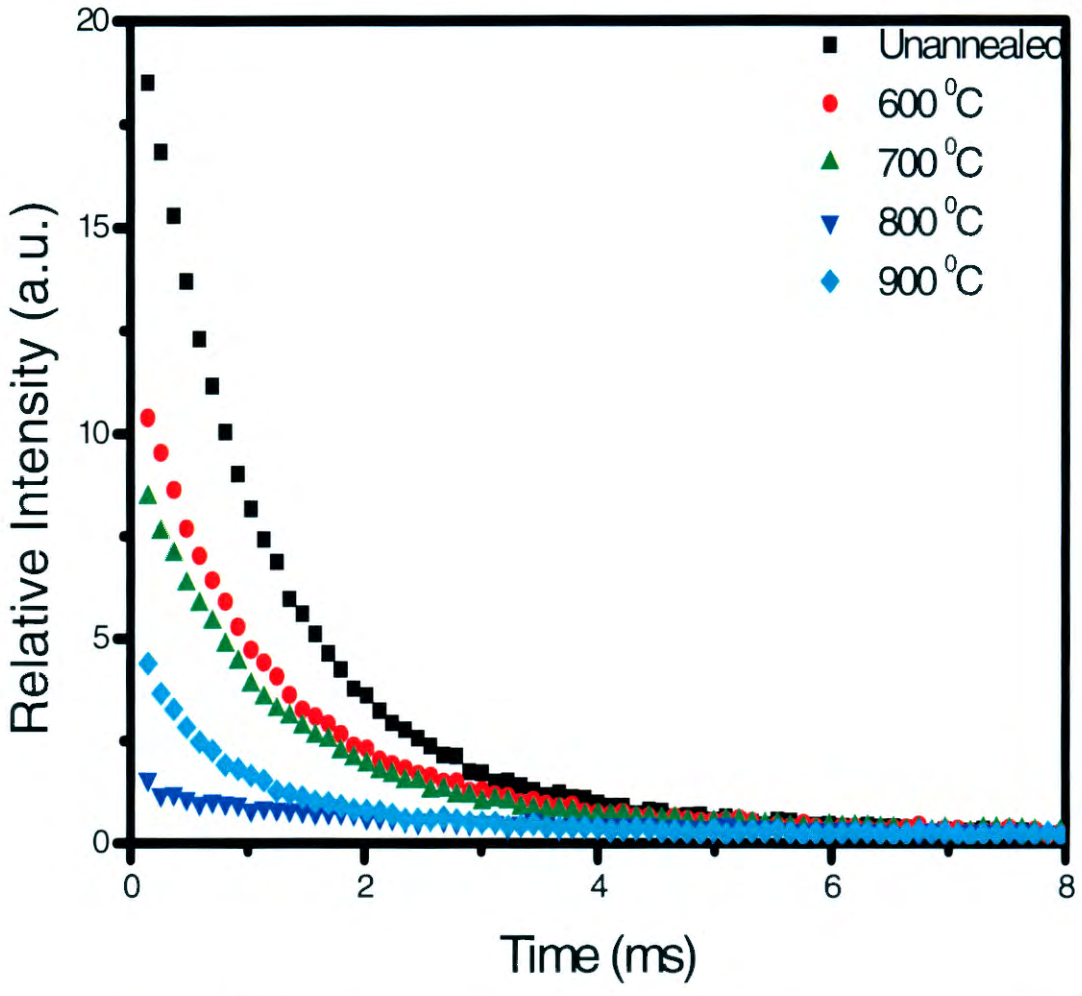

Figure 8.10. Showing decay characteristics of Y_2O_3: Eu^{3+} phosphor thin films for un-annealed and films annealed at 600, 700, 800 and 900 ^{0}C.

$$I = A_1 \exp(-t/\tau_1) + A_2 \exp(-t/\tau_2) \text{ ---------- (3)}$$

Where I is phosphorescence intensity, A_1, and A_2 are constants, t is time, τ_1 and τ_2 are decay constants, deciding the decay rate for rapid and slow exponentially decay components, respectively. The fitting results of parameters τ_1 and τ_2 are listed in Table 2 below.

Table 8.2. Results for the fitted decay curves of the un-annealed and films annealed at different temperatures.

Temperature (^{0}C)	Unannealed	600	700	800	900
Components					
Fast (τ_1)	0.5896	0.5524	0.5275	0.5165	0.4962
Medium (τ_2)	0.8564	0.8124	0.7856	0.7522	0.7050

Two components namely fast and slow are responsible for the luminescence properties of the as- synthesized phosphor. A trend can be observed (Table 2) that the decay constants of the phosphors decrease gradually with the increasing annealing temperature.

8.4 Conclusion

Y_2O_3: Eu^{3+} thin films have been successfully deposited using PLD. The average crystallite size of the films after annealing was 64 nm. The study showed that the annealing temperature positively affected the crystalline phase, the morphology and the PL efficiency of the thin films. The un-annealed thin films were amorphous, while the annealed films consist of cubic and hexagonal phases depending on the annealing temperatures. SEM show similar morphology for the un-annealed and films annealed at lower temperatures which changed at higher temperature. The luminescence results show that the PL intensities were quenched and red-shifted at higher annealing temperatures showing formation of a new phase. UV-vis measurement indicated a band gap in the range of 4.6 to 4.8 eV.

References

[1] H. C. Swart, J. C. Sebastian, T. A. Trottier, S. R. Jones, P. H. Holloway, *J. Vac. Sci. Technol. A 13*, 1697 (1996).

[2] G. A. Hirata, J. Mckittrick, M. Avalos-Borja, J. M. Siqueiros, D. Devlin, Appl. *Surf. Sci. 113*, 509 (1997).

[3] S. L. Jones, D. Kumar, K. G. Cho, R. Singh, P. H. Holloway, *Displays 19*, 151 (1999).

[4] R. N. Sharma, S. T. Lakshami, A. C. Rastogi, Thin *Solid Films 199*, 1 (1991).

[5] K. Onisawa, M. Fuyama, K. Tamura, K. Taguchi, T. Nakayama, Y. Ono, *J. Appl. Phys. 66*, 719 (1990).

[6] R. Rao, Solid *State Commun. 99*, 439 (1996).

[7] K. L. Choy, J. P. Feistand, A. L. Heys, B. Su, *J. Mat. Res.* (1999), *14*, 3111 (1999).

[8] S. L. Jones, O. Kumar, R. K. Singh, P. H. Holloway, *Appl. Phys. Lett*, *71*, 404 (1997).

[9] K. G. Cho, D. Kumar, D. G. Lee, S. L. Jones, P. H. Hollway, R. K. Singh, Appl. *Phys. Lett. 71*, 3335 (**1997**).

[10] K. G. Cho, D. Kumar, P. H. Holloway, R. K. Singh, Appl. *Phys. Lett. 73*, 3058 (1998).

[11] H. Leverenz, An Introduction to Luminescence of Solids, Dover Publications Inc, New York, (1968).

[12] P. H. Holloway, S. L. Jones, P. Rack, J. Sebastian, T. Trottier, Proc. Of Tenth Intl. Sym. Applications of Ferroelectrics, in: B. Kulwicki (Ed.), East Brunswick, NJ, (IEEE, NY,) p.127 (1996).

[13] T. Hase, T. Kano, E. Nakazawa, Yamamoto, E. Advances in Electronics and Electron Physics. 79 (1990).

[14] H. Bechtel, W. Czarnojan, M. Haase, W. Mayr, H. Nikol, Philips Journal of Research 50 433 (1996).

[15] C. M. Feldman, Journal of the Optical Society of America 47 790 (1957).

[16] M. R. Royce, US Patent no. 3418, vol.246, (1968).

[17] S. H. Cho, Y. S. Yoo, J. D. Lee, J. Electrochem. Soc. 145 1017 (1998).

[18] T. Matsuzawa, Y. Aoki, N. Takeuchi, et al. A new long phosphorescent phosphor SrA1204: Eu^{2+}", Dy^{3+} with high brightness [J]. *J. Electrochem.* Soc., 143: 2670 (1996).

[19] J. Qiu, M. Kawasak, K. Tanaki, et al. Phenomenon and mechanism of long lasting phosphor escence in Ed^{i2+}- doped aluminosilicate glasses [J]. J. *Phys. Chem . Solids, 59:* 1521 (1998).

[20] T. Katsumata, T. Nabae, K. Sasajima, Growth and characteristics of long persistent SrA1204 and CaA1204 based phosphor crystals by a floating zone technique [J 1. *J, Cryst. Growth,* 83: 361 (1998).

[21] T. Kinoshita, M. Yamazaki, H. Kawazoe, et al. Long phosphorescence and photostimulated luminescence in Tb ion activated reduced calcium aluminate glasses [J 1. J. *Appl . Phys.*, 86: 3729 (1999),.

[22] **N.** Kodama, T. Takahashi, M. Yamaga, et a1. Long lasting phosphorescence in Ce3 + doped CaZAlzSiO7 and CaYA130 crystals [J]. *Appl . Phys. Ltt .* , 75: 1715 (1999),.

[23] R. Sakai, T. Katsumata, S. Komuro, et a1. Effect of composition on the phosphorescence from BaAlzOI: Eu", Dy3' crystals [J]. J.Lumin. 85: 149 (1999).

[24] Y. L. Chang, H. I. Hsiang, M. T. Liang, J. of Alloys and Comp. 461 598 (2008)

[25] T. Peng, L. Huajun, H. J. Yang, Mater. Chem. & Phys 85 68 (2004).

[26] P. D. Sarkisov, N. V. Popovich, A. G. Zhelnin, Glass and Ceramics 60 9 (2003).

[27] T. Peng, H. Yang, X. Pu, B. Hu, Z. Jian, C. Yan, Mater. Lett. 58 352 (2004).

[28] X. Li, Y. Qu, X. Xie, Z. Wang, R. Li, Mater. Lett. **60** 3673 (2006).

[31] J. S. Bae, K. S. Shim, S. B. Kim, J. H. Jeong, S. S. Yi, J. C. Park, J. Cryst. Growth **264** 290 (2004).

[32] D. P. Norton, Materials Science and Engineering R 43 139 (2004).

[33] D. R. Baer, A. S. Lea, J. D. Geller, J. S. Hammond, L. Koyer, C. J. Powell, M. P. Seah, M. Suzuki, J. F. Watts, J. J. Wolstenholme, Electron Spectros. & Relat. Phenom. 176 80 (2010).

[34] F. Adams, L. Van Vaeck, R. Barrett, Spectrochimica Acta Part B **60** 13 (2005).

[35] S. Choopun, H. Tabata, T. Kawai, J. of Cryst. Growth 274 167 (2005).

Chapter 9

The influence of different species of gases on the luminescent and structural properties of pulsed laser ablated $Y_2O_2S:Eu^{3+}$ thin films

9.1 Introduction

Nanostructure materials are being actively explored nowadays because of their size induced novel characteristics and applications ranging from micro tips to optoelectronics. To exploit the optical properties of these materials and to meet the ever–increasing demands of energy, tremendous emphasis is being placed on alternate sources of energy conservation and low power driven display devices. Afterglow phosphors are materials that are readily excited by ambient lights and continuously radiate visible light for many hours at high brightness levels [1]. Nanoscale $Y_2O_2S:Eu^{3+}$ has remarkably different luminescent properties from those of bulk samples: such as emission line broadening, lifetime changes and its spectral shift [2]. There are several methods to synthesize nanocrystalline $Y_2O_2S:Eu^{3+}$, such as sol–gel [3], combustion [4], micro emulsion [5], and spray pyrolysis method [6], but these methods are limited in the complexity of the preparation methods. Solid state reaction at room temperature is a good method to synthesize nanoparticles [7-9]. Recently, the pulsed laser deposition (PLD) technique, which provides a unique process for stoichiometric evaporation of target materials and control of film morphology [10, 11], has been used for the deposition of oxysulfide films [12–14]. In most of the reported works [15-17], the $Y_2O_2S: Eu^{3+}$ phosphors have been prepared and investigated in the form of powders.

Journal of Applied Physics A. •DOI: 10.1007/s00339-016-0062-3

However, for various industrial applications such as device fabrication and surface coatings it is also important to investigate the performance of these phosphors in the form of thin films. Moreover, it is well documented that thin film phosphors have several advantages over powders, such as higher lateral resolution from smaller grains, better thermal stability, reduced out gassing, and better adhesion to solid substrates [18]. Amongst the techniques used to prepare luminescent thin films, PLD has several attractive features, including stoichiometric transfer of the target material, generation of quality plume of energetic species, hyper thermal reaction between the ablated cations and molecular gas in the ablation plasma and compatibility with background pressures ranging from UHV to 100 Pa [19]. The plasma fabricated during pulsed laser ablation is very energetic, and its mobility can be easily controlled by changing processing parameters [20]. The presence of a background gas in the chamber has a strong influence on the quality of the plasma produced by the laser. The gas can modify the kinetic energy and the spatial distribution of the ejected species present in the plasma, and it may also induce compositional changes in the deposited films [21]. Plume collisions may also provide an increase in the vibrational energy of molecular species [22]. Thus, the gas affects the spatial distribution, the deposition rate, the energy and distribution of ablated particles thereby controlling the cluster formation, cluster size, cluster energy and particle distribution [23]. Dauscher et al. [24] investigated the influence of argon atmosphere on the microstructural properties of $Ca_xCO_4Sb_{12}$ films prepared by pulsed laser deposition and found that the films deposited in argon atmosphere were more delaminated than those prepared in vacuum. The report from Supab et al. [25] on laser ablated ZnO nanorods showed that the growth rate of nanostructures in oxygen atmosphere was slower than in argon atmosphere.

In the current work, we report on the influence of vacuum, argon and oxygen atmospheres on the morphology, structural and photoluminescence (PL) properties of pulsed laser deposited (PLD) Y_2O_2S: Eu^{3+} thin films. A detailed report on the influence of working atmosphere on the properties of the pulsed laser deposited Y_2O_2S: Eu^{3+} thin films are presented.

9.2 Experimental procedures

9.2.1 Powder preparation

Eu^{3+}-doped yttrium oxysufide nanocrystals were synthesized using the sol- combustion route. The method of synthesis essentially comprises of mixing the precursors in appropriate

stoichemetric ratios, followed by firing in an air tube furnace at a temperature of 400 ^{0}C. The stoichemetric ratio between the fuel (thiourea) and the flux (ethanol) is very important otherwise ylttrium oxide formation is inevitable. The white formy product was then grounded and left to dry in an enclosed oven for 24 hours.

9.2.2 Pulsed laser deposition (PLD)

The Si (100) wafers used as substrate were first chemical cleaned. The powder was pressed without binders to prepare a pellet that was used as an ablation target. The target was annealed at 700°C for 12 hours in air to remove water vapour and other volatile compounds that might be trapped in the pellet before placing it on the target holder of the PLD system. The deposition chamber was evacuated to a base pressure of 8.2 x 10^{-6} mtorr. The Lambda Physic 248 nm KrF excimer laser was used to ablate the phosphor pellet in vacuum, argon and oxygen atmospheres. A Baratron Direct (Gas Independent) Pressure/Vacuum capacitance Manometer (1.33 x 10^{-2} mtorr) was used for the 50 mtorr pressure measurements. The laser energy density, number of pulses and laser frequency were set to 0.74 J/cm^2, 12000 and 10 Hz respectively. The substrate temperature was fixed at 300 °C, and the target to substrate distance was 5 cm. The ablated area was 1 cm^2.

9.2.3 Characterization

The Shimadzu Superscan SSX-550 system was used to collect the Scanning Electron Microscopy (SEM) micrographs. Atomic Force Microscopy (AFM) micrographs were obtained from the Shimadzu SPM - 9600 model. X-ray diffraction (XRD) data was collected by using a SIEMENS D5000 diffractometer using CuKα radiation of λ = 1.5405 nm. PL excitation and emission spectra were recorded using a Cary Eclipse fluorescence spectrophotometer (Model: LS 55) with a built-in xenon lamp and a grating to select a suitable wavelength for excitation. The excitation wavelength was 230 nm and the slit width was 10 nm. The afterglow curves for the films were also obtained with the Cary Eclipse spectrophotometer.

9.3 Results and discussion

9.3.1 X-ray diffraction analysis

Figure 9.1 shows the XRD patterns of $Y_2O_2S:Eu^{3+}$ thin films grown at 300 °C in vacuum, argon and oxygen atmospheres. The patterns show mixed phases of cubic and hexagonal crystal structures. The film grown in O_2 atmosphere has a cubic phase, while that grown in vacuum and argon atmospheres are hexagonal. The average lattice parameters for the hexagonal phase a=3.785 nm and c=6.589 nm, are very close to the standard values provided in the powder diffraction file PDF #24–1424. The average lattice parameters for the cubic phase a=6.026 nm according to card # 72-0927. The intensities of the XRD peaks were found to increase in the order argon, vacuum and oxygen. This may be attributed to the enhanced oxidation kinetics and improvement in crystalline nature of the films. It is also clear that the thin film consist of both nanoparticles and microparticles as seen from the narrow and broad XRD peaks. The crystallite size of the films with hexagonal and cubic phase ranging between 80 and 480 nm were estimated by using equations (1) and (2) respectively;

$$\frac{1}{d^2} = \frac{4(h^2 + k^2 + hk)}{3a^2} + \frac{l^2}{c^2} \text{---------- (9.1)}$$

$$\frac{1}{d^2} = \frac{h^2+k^2+l^2}{a^2} \text{---------- (9.2)}$$

There is a marginal decrease (-0.17%) in crystallographic unit-cell that tends to contract due to the increase in surface area of the layers for the $Y_2O_2S:Eu^{3+}$ nanostructures. This may lead to a decrease in the lattice constant. Eu_2O_3 diffraction peaks from XRD patterns were not detected indicating that the Eu^{3+} was incorporated into the Y_2O_2S host lattice homogeneously [26].

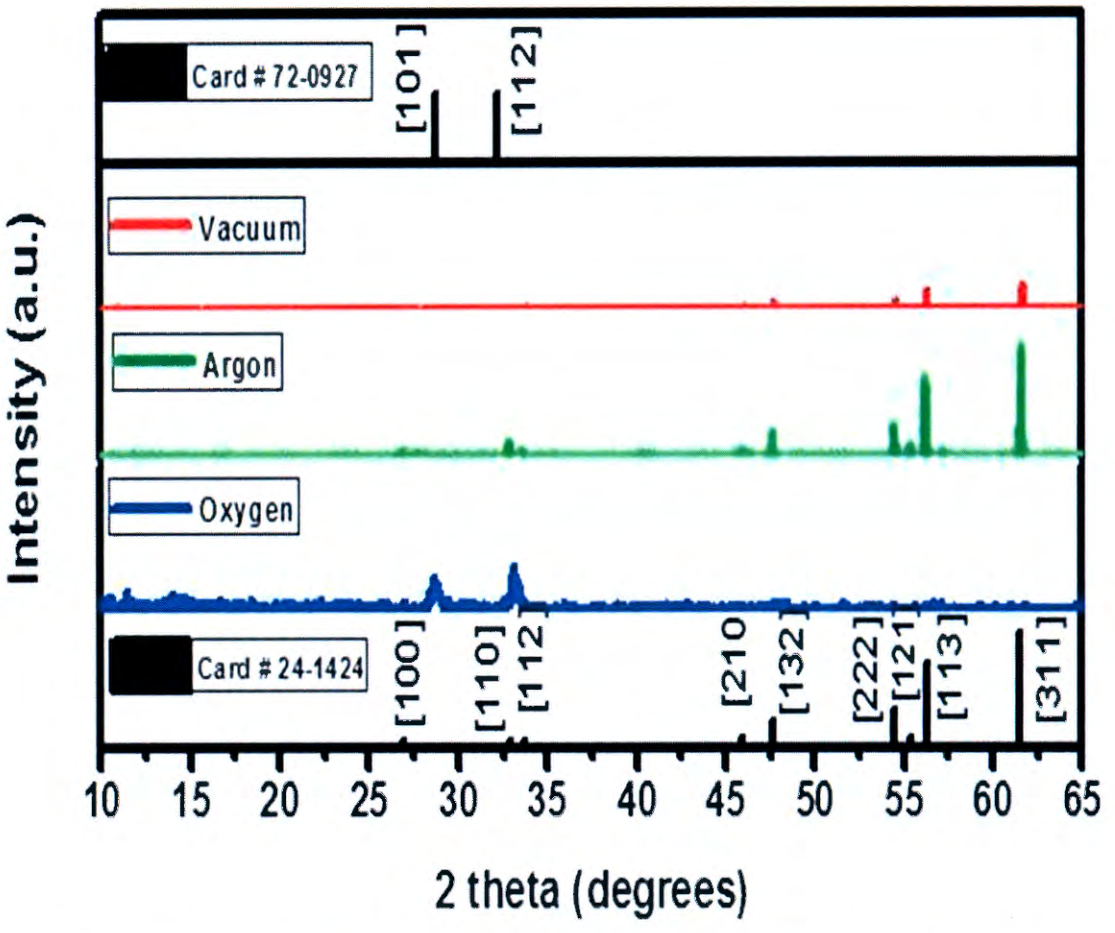

Figure 9.1. The XRD spectra of the Y_2O_2S: Eu^{3+} thin films deposited in vacuum and different gas atmospheres.

9.3.2 Scanning electron microscopy (SEM)

Figure 9.2 shows the SEM pictures of the films prepared in different working atmospheres. The film deposited in vacuum, shown in Figure 9.2 (a), had a smooth surface with numerous bigger spherical particles. The film deposited in Ar atmosphere (Figure 9.3(b)) had a much rougher surface packed with larger number of spherical particles than that of the film deposited in the O_2 atmosphere. The film that was deposited in the O_2 atmosphere, in Figure 9.3(c), had a rougher surface with small cracks on the surface. The crystallite sizes as shown by SEM micrographs consist of both nano and micro particles. The SEM micrographs show that the surfaces of the films prepared in the gas atmosphere are much rougher than that deposited in vacuum. The increase in surface roughness in the O_2 and Ar atmospheres is due to the enhanced particulate formation in the plume, which is a typical characteristic of high-pressure laser ablation [27].

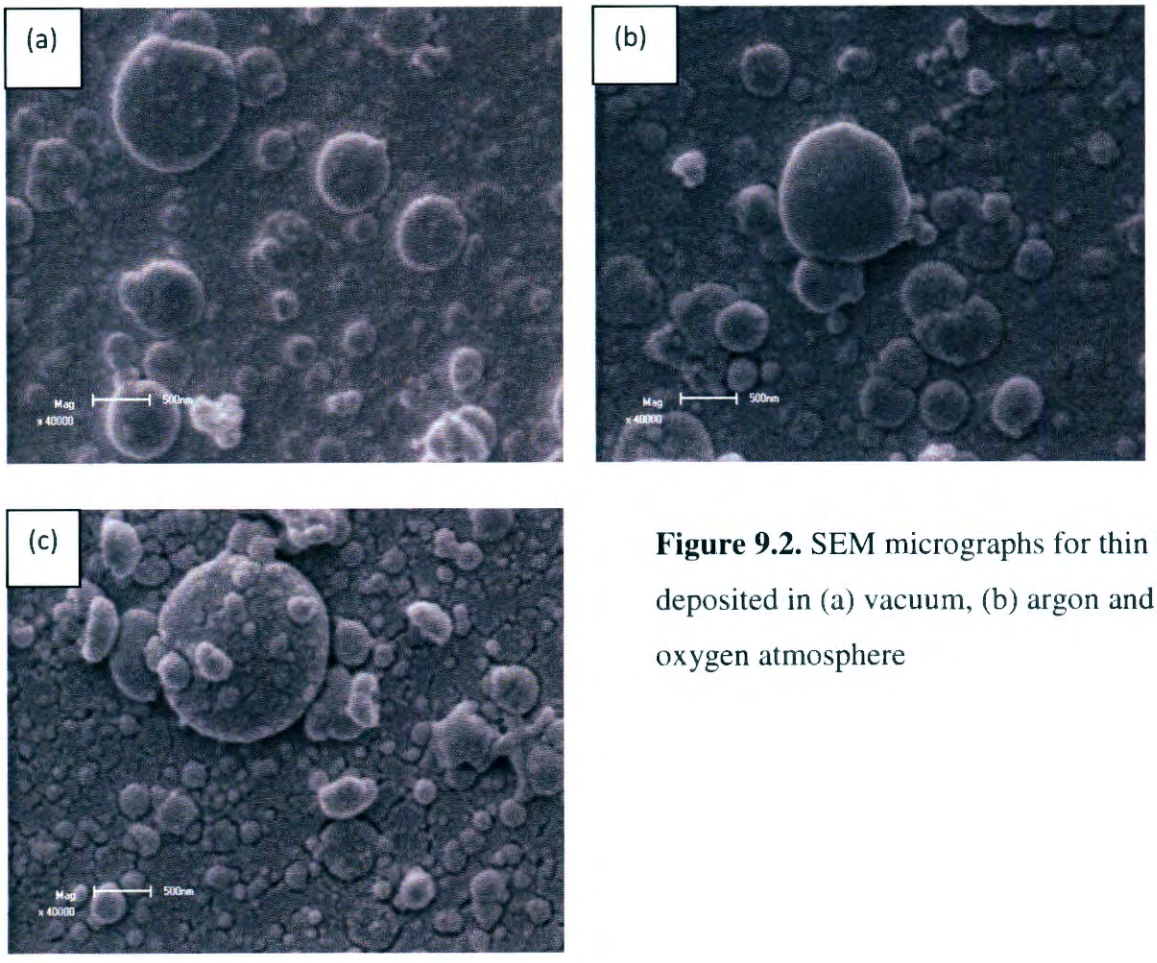

Figure 9.2. SEM micrographs for thin films deposited in (a) vacuum, (b) argon and (c) oxygen atmosphere

9.3.3 Atomic force microscopy (AFM)

Figures 9.3 shows AFM images of the samples deposited in (a) vacuum, (b) argon and (c) oxygen atmosphere. It is clear that almost hexagonally-shaped nanoparticles were deposited during the deposition process. The particles were also less agglomerated for films grown in gas atmospheres (Fig. 9.3 (b) versus Fig. 9.4 (c)). In vacuum, the plume does not undergo scattering (collisions) due to gas particles hence the arrival of the particle is more compared to case of argon and oxygen and thus higher PL intensity. Argon being a heavier gas scatters more particles as compared to oxygen; however the speed of argon particles is less than those of oxygen. The arrival of the particles is higher in case of oxygen, hence intensity.

(a)

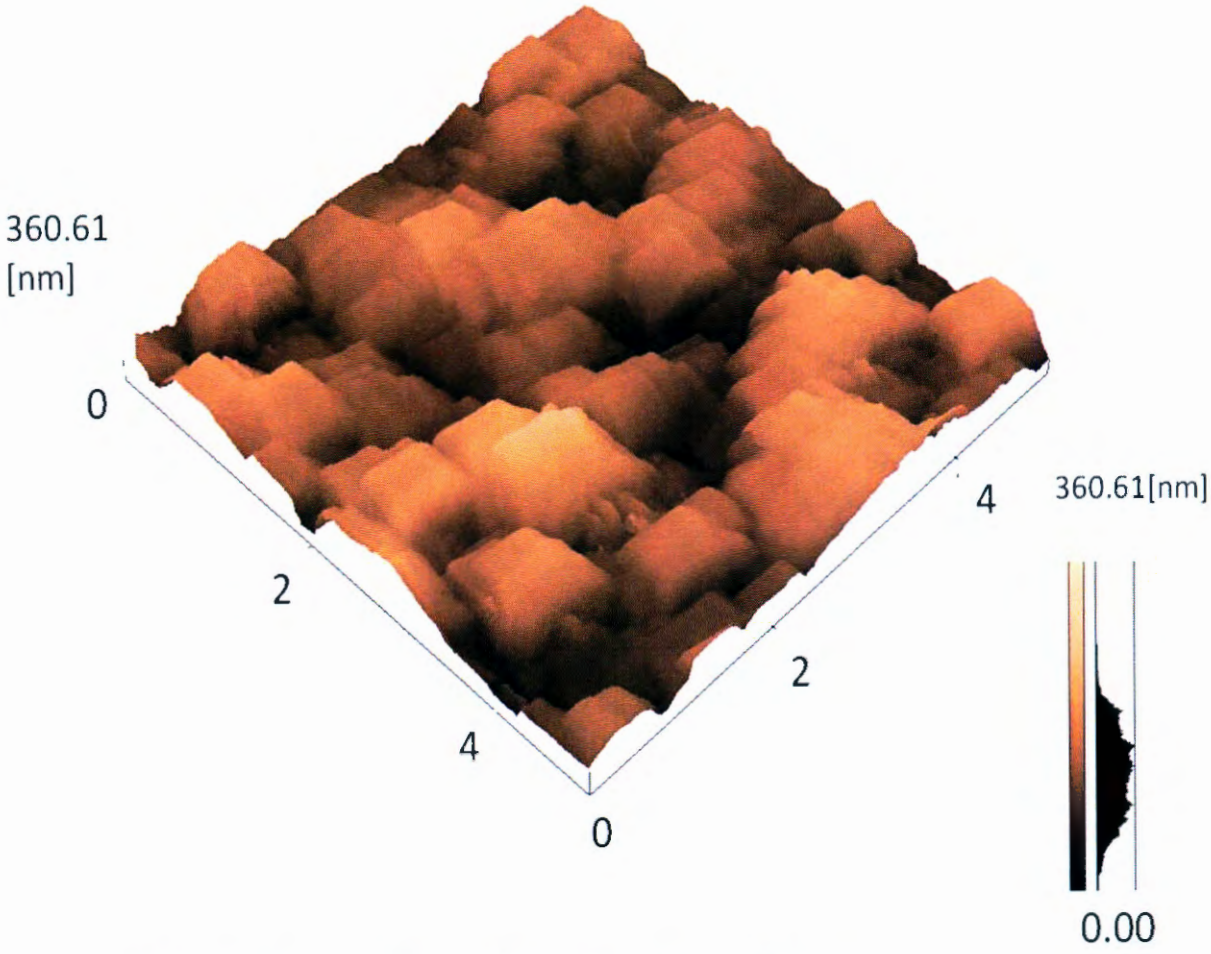

5.00 x 5.00 [um] Z 0.00 – 306.61 [nm]

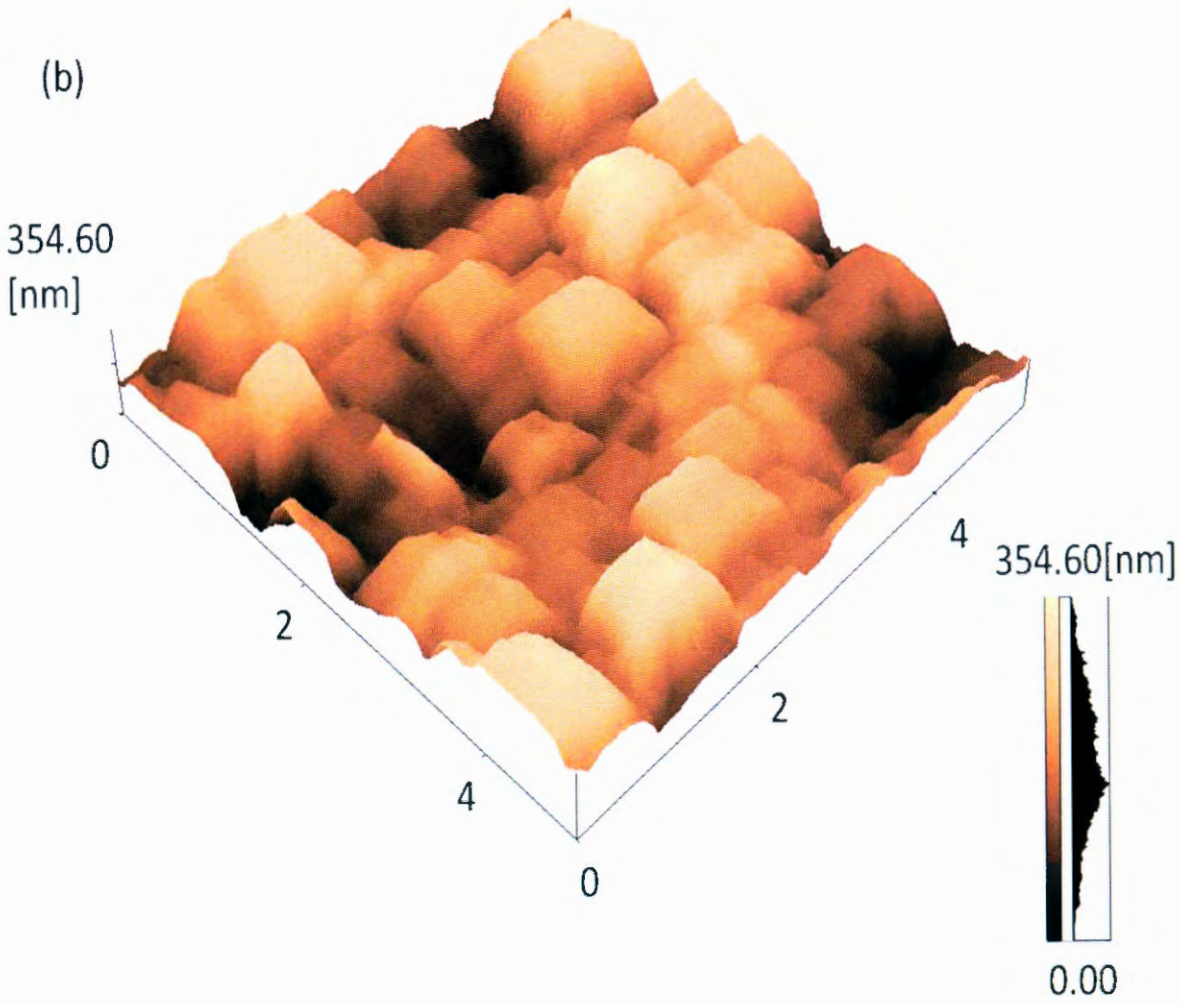
(b)
354.60
[nm]
0
2
4
0
2
4
354.60[nm]
0.00
5.00 x5.00 [um] Z 0.00 - 354.60 [nm]

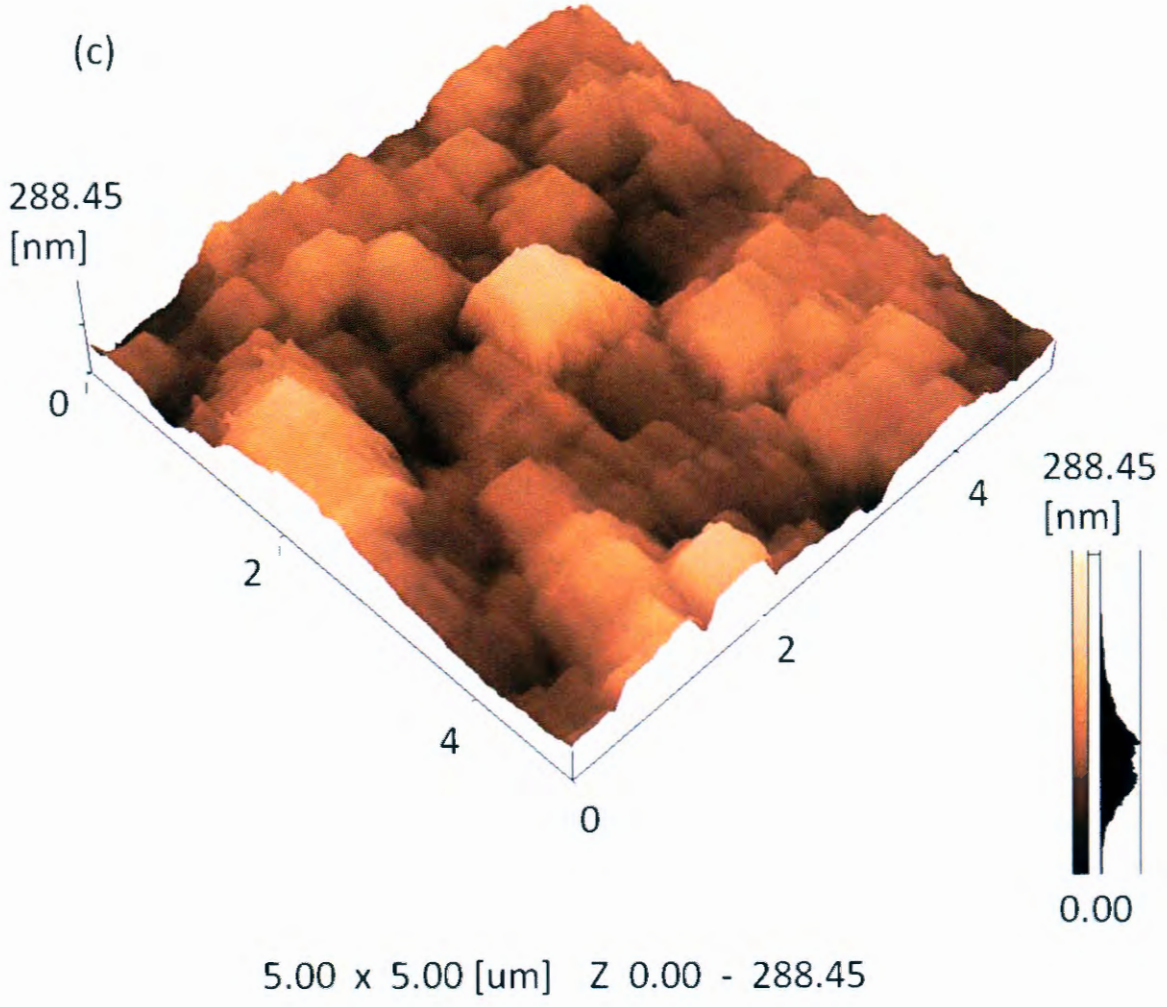

Figure 9.3. AFM images of thin films deposited in (a) vacuum, (b) argon and (c) oxygen atmospheres

Collisions between the vaporised particles close to the target in the case of films deposited in gas atmosphere lead to nucleation and growth of smaller nanoparticles when arriving at the substrate. In vacuum there are virtually no collisions between the particles before reaching the substrate. Longer residence time of the particles in the plume, as is the case of films deposited in gas atmosphere, lead to more evenly distributed particles (Fig. 9.3 (c)). Light emission from the spherical shaped phosphor particles as excited by the electron beam is more intense due to the fact that much less photons encounter total internal reflection [28-30]. The increase in the deposition pressure is reported to have caused an increase in the connectivity (agglomeration) between particles due to sintering of small particles [31-32].

This would eventually lead to grain growth at high enough pressure. In this case, we also found that more agglomeration occurred during deposition in gas atmosphere than in vacuum.

9.3.4 Photoluminescence results

Figure 9.4(a) indicates the excitation spectra of Y_2O_2S: Eu^{3+} thin films grown under vacuum, argon and oxygen atmosphere. The inset indicates the magnified spectrum for sample deposited in oxygen atmosphere. Excitation spectra were recorded keeping the emission wavelength at 612 nm. These spectra consist of two charge transfer bands (CTB). The band located at 237 nm is due to $O^{2-} \rightarrow Eu^{3+}$ CTB, while that at 312 nm is due to $Eu^{3+} \rightarrow S^{2-}$ CTB. Figure 9.4(b) show the deconvulated excitation spectra of Y_2O_2S:Eu^{3+} thin films deposited in vacuum, argon and oxygen. The figure indicates two transitions at 237 and 312 nm wavelengths. The transition located at 237 nm is due to charge transfer band between O^{2-} and Eu^{3+} ions, while that located at 312 and 315 nm is associated with $Eu^{3+} \rightarrow S2^{-}$ charge transfer band.

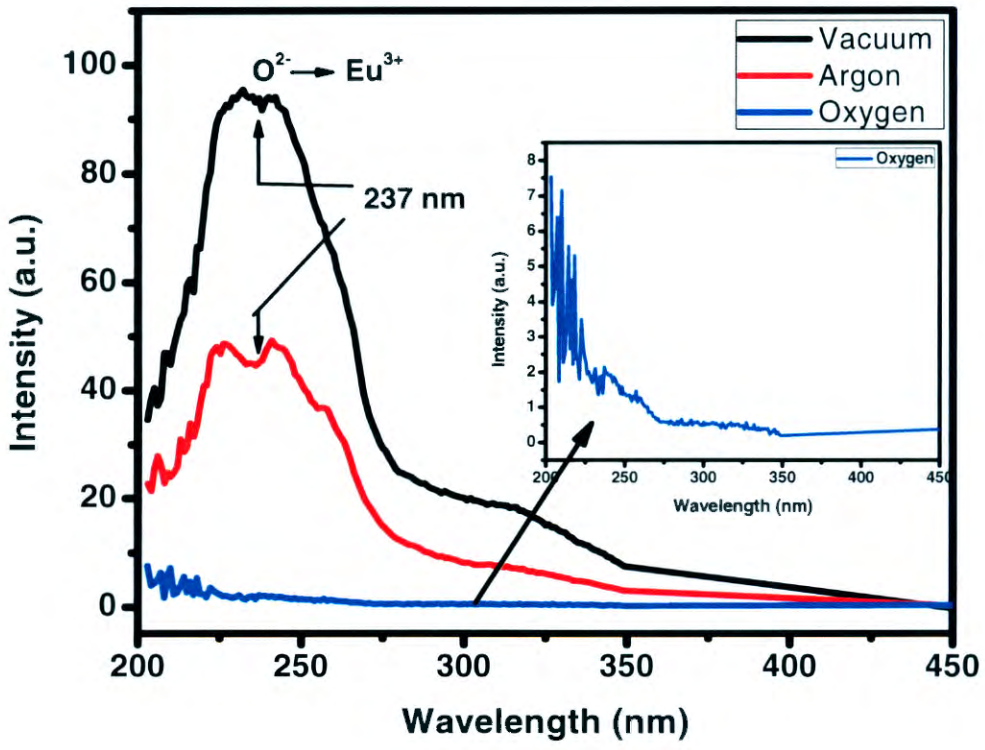

Figure 9.4(a). Excitation spectra for Y_2O_2S: Eu^{3+} thin films deposited in vacuum, argon and oxygen atmosphere. **Inset:** Excitation spectrum for sample deposited in oxygen atmosphere

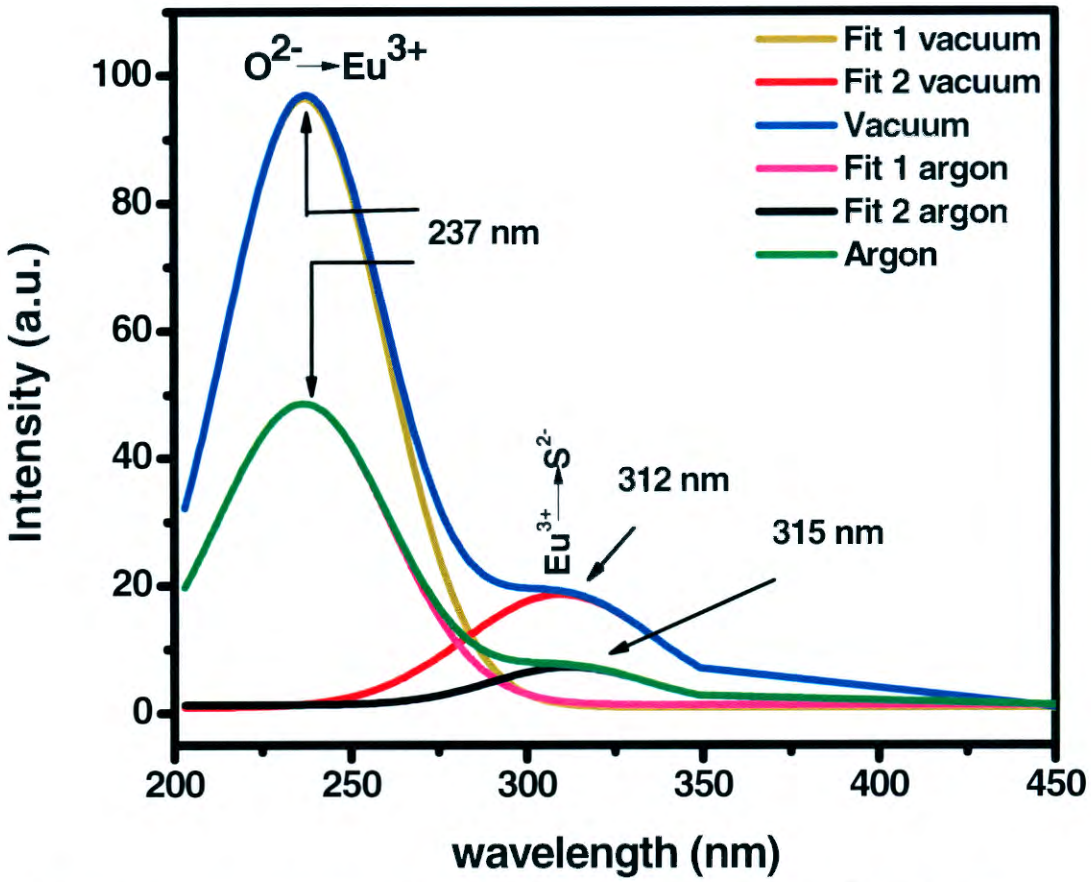

Figure 9.4(b). Deconvoluted excitation spectra for Y_2O_2S: Eu^{3+} thin films deposited in vacuum, argon and oxygen atmosphere

Figures 9.4(c) to 4(e) show excitation wavelengths for each film deposited in different atmospheres. In each case, the excitation wavelengths were found at different emissions wavelengths in order to find the best excitation for each film. Figure 9.4(c) indicate the excitation wavelength for the film deposited in vacuum. At all the emission wavelengths of 590, 612, 625 and 655 nm, no reasonable excitation wavelength have been achieved indicating this situation does not favour vacuum atmosphere. Figure 9.4(d) indicate excitation wavelengths for the film deposited in argon atmosphere. The best excitation wavelength was achieved when the emission wavelength was at 612 nm, followed by 625 and 590 nm respectively. The excitation wavelength with the least intensity is achieved at 655 nm emission wavelength. Similar results are obtained for film deposited in oxygen atmosphere as shown in Figure 9.4(e).

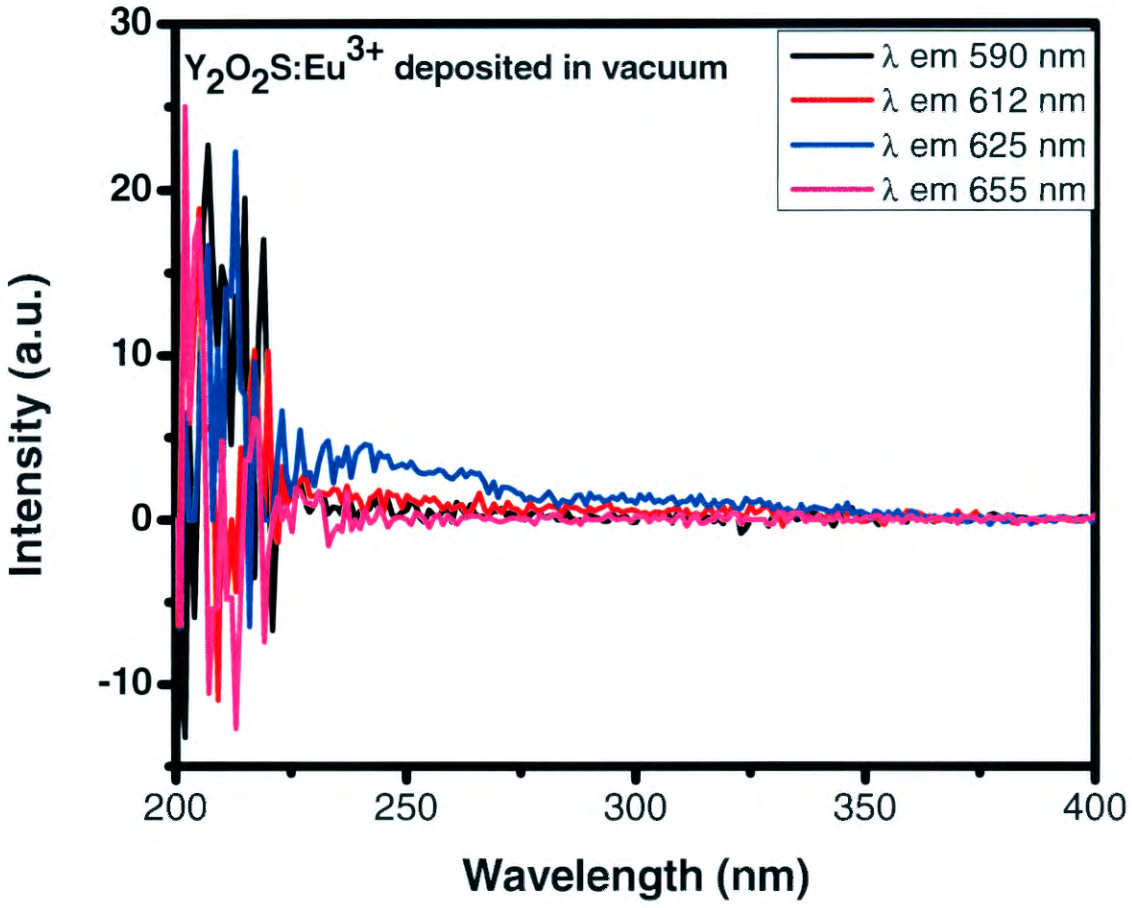

Figure 9.4(c). Excitation spectra of $Y_2O_2S:Eu^{3+}$ thin film deposited in vacuum recorded at 590, 612, 625 and 655 nm emission wavelengths

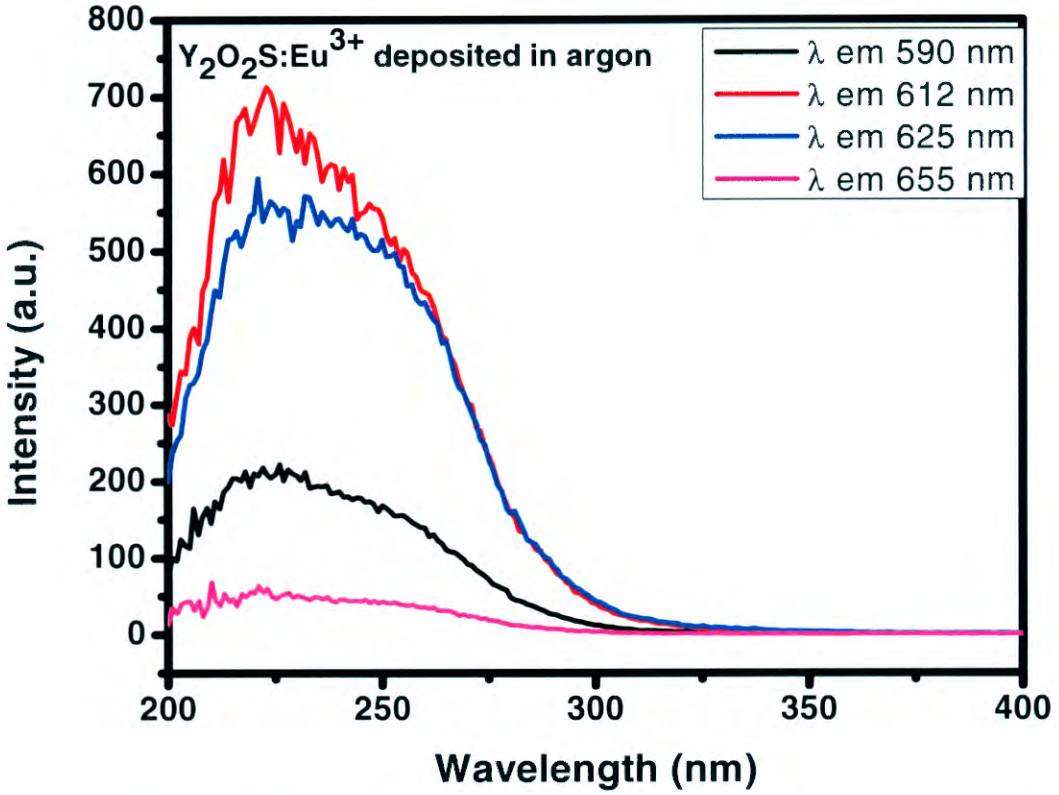

Figure 9.4(d). Excitation spectra of $Y_2O_2S:Eu^{3+}$ thin film deposited in argon recorded at 590, 612, 625 and 655 nm emission wavelengths

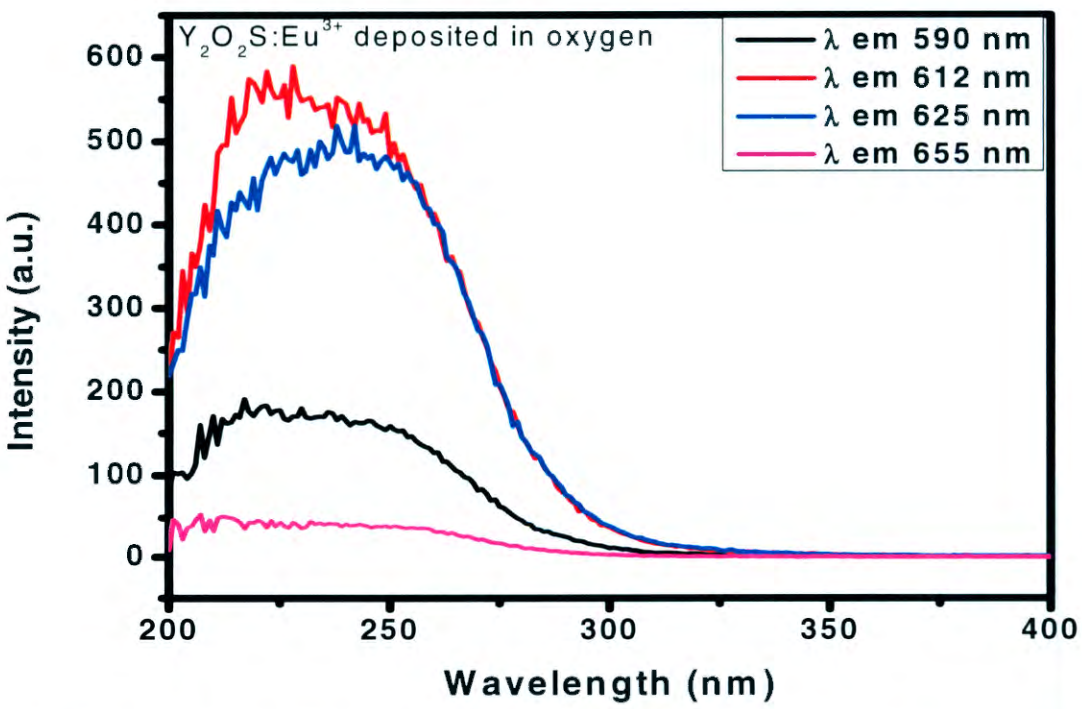

Figure 9.4(e). Excitation spectra of $Y_2O_2S:Eu^{3+}$ thin film deposited in oxygen recorded at 590, 612, 625 and 655 nm emission wavelengths

Figure 9.5 (a) and (b) show the room temperature PL emission spectra for the Y_2O_2S: Eu^{3+} films deposited in vacuum, argon and oxygen. All the samples were excited at 245 nm using a monochromatized xenon lamp. The intense red emission peak that is observed at 612 nm from the film deposited in vacuum is ascribed to the $^5D_0 \rightarrow {}^7F_2$ transition of Eu^{3+} [33]. A shoulder at 595 nm for the vacuum sample is also visible, which is ascribed to Eu^{2+} transitions. Minor emission peaks associated with residual Eu^{3+} [34, 35] was also observed at 402, 469, 496, 514 and 540 nm for the films deposited in the vacuum atmosphere. The relative ratios of the 595 nm to 613 nm peaks (Eu^{2+} to Eu^{3+} ratio) clearly support this observation. It should be mentioned that O_2 atmosphere should favour the stabilization of Eu^{3+} cations (oxidation), while vacuum should play the opposite role and favour Eu^{2+} (reduction). The intensity of the film deposited in the vacuum atmosphere was the highest followed by the one prepared in the argon atmosphere, though greatly quenched. All the peaks for the sample deposited in O_2 are totally quenched due to the smallest intensity as compared to that of vacuum and argon, hence not visible. But when PL emission spectra for sample deposited in O_2 is drawn alone, the peaks are clearly visible as shown in the inset of Figure 9.5 (a). The most intense peak for this sample also appears exactly at 612 nm just as that of vacuum. In the case of film deposited in argon atmosphere, the peak at 612 nm is quenched while that at 315 nm is enhanced. In all the three cases, the peak at 612 nm is associated with $O^{2-} \rightarrow Eu^{3+}$ charge transfer band (CTB) between O^{2-} and Eu^{3+} ions, while the peak at 315 nm is due to $Eu^{3+} \rightarrow S^{2-}$ charge transfer band. These peaks are clearly shown by Figure 9.5 (b) inset. A shift of the Y_2O_2S: Eu^{3+} main peak toward shorter wavelengths was measured for sample deposited in argon atmosphere. This is due to the quantum size effect of the nano-sized particles, compared with those deposited in vacuum and oxygen as confirmed by XRD results.

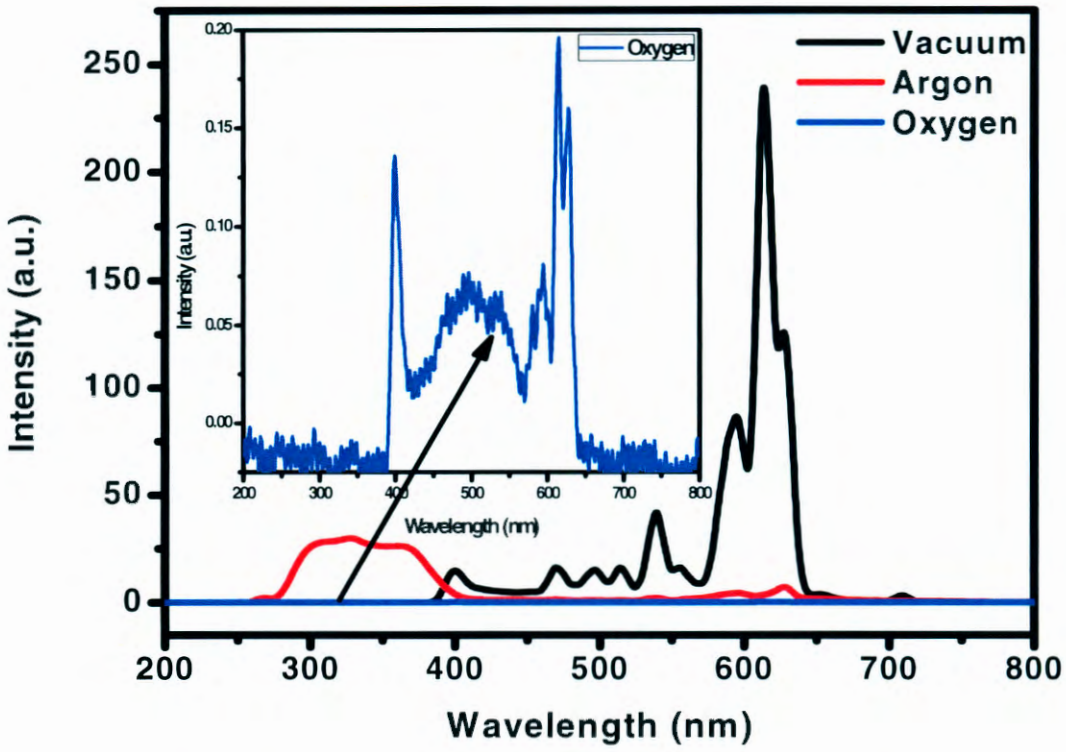

Figure 9.5 (a). Emission spectra for Y_2O_2S: Eu^{3+} thin films deposited in vacuum, argon and oxygen atmosphere. **Inset**. Emission spectrum for thin film deposited in oxygen.

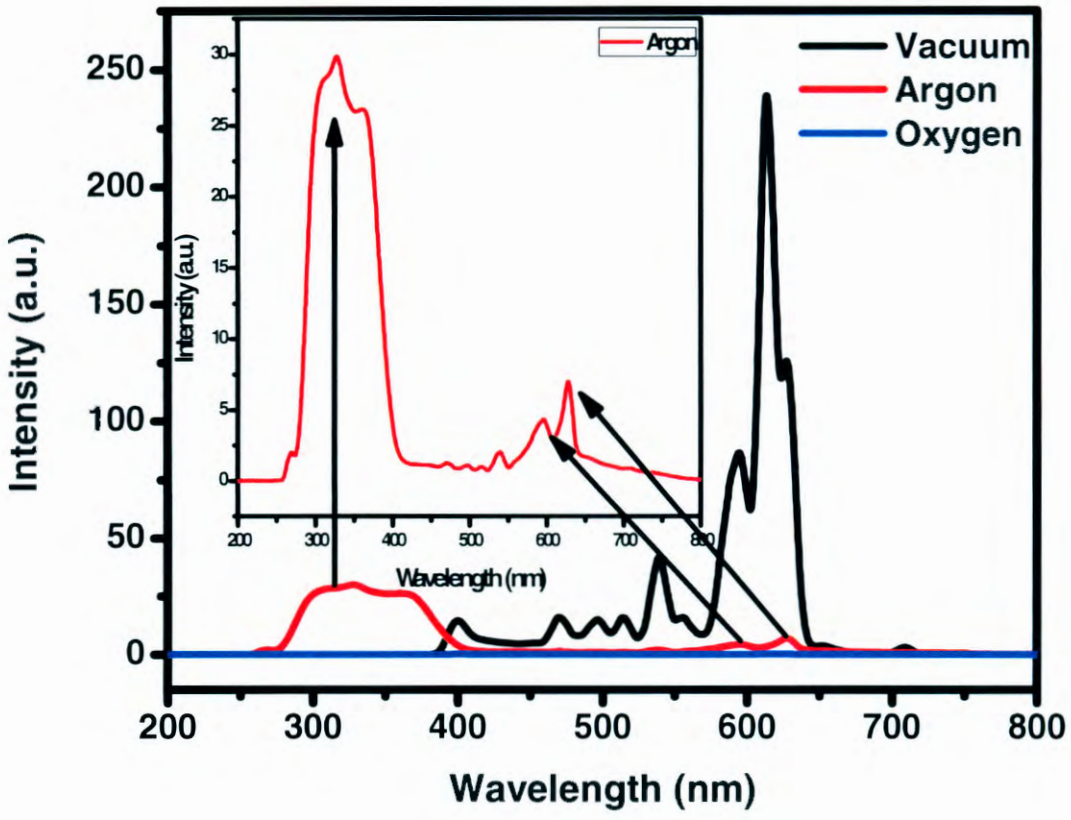

Figure 9.5(b). Emission spectra for Y_2O_2S: Eu^{3+} thin films deposited in vacuum, argon and oxygen atmosphere. **Inset**. Emission spectrum for thin film deposited in argon.

Figures 9.5(c) to 9.5(d) show emission wavelengths for each film deposited in different gas atmospheres. In each case, the emission wavelengths were found at different excitation wavelengths in order to optimize emission for each film. Figures 9.5(c) indicate the emission wavelength for the film deposited in vacuum. At all the excitation wavelengths of 237, 245, 260 and 290 nm, high quality emission wavelength with high intensities have been achieved with 245 and 260 nm excitation providing the highest intensity. Figure 9.5(d) indicate emission wavelengths for the film deposited in oxygen atmosphere. Similarly, the best emission wavelength was achieved when the excitation wavelength was at 245 and 260 nm, followed by 290 nm respectively. The excitation wavelength with the least intensity is achieved at 237 nm excitation wavelength. The film deposited in oxygen atmosphere indicates the lowest intensity as shown in Figure 9.5(d) at all excitations.

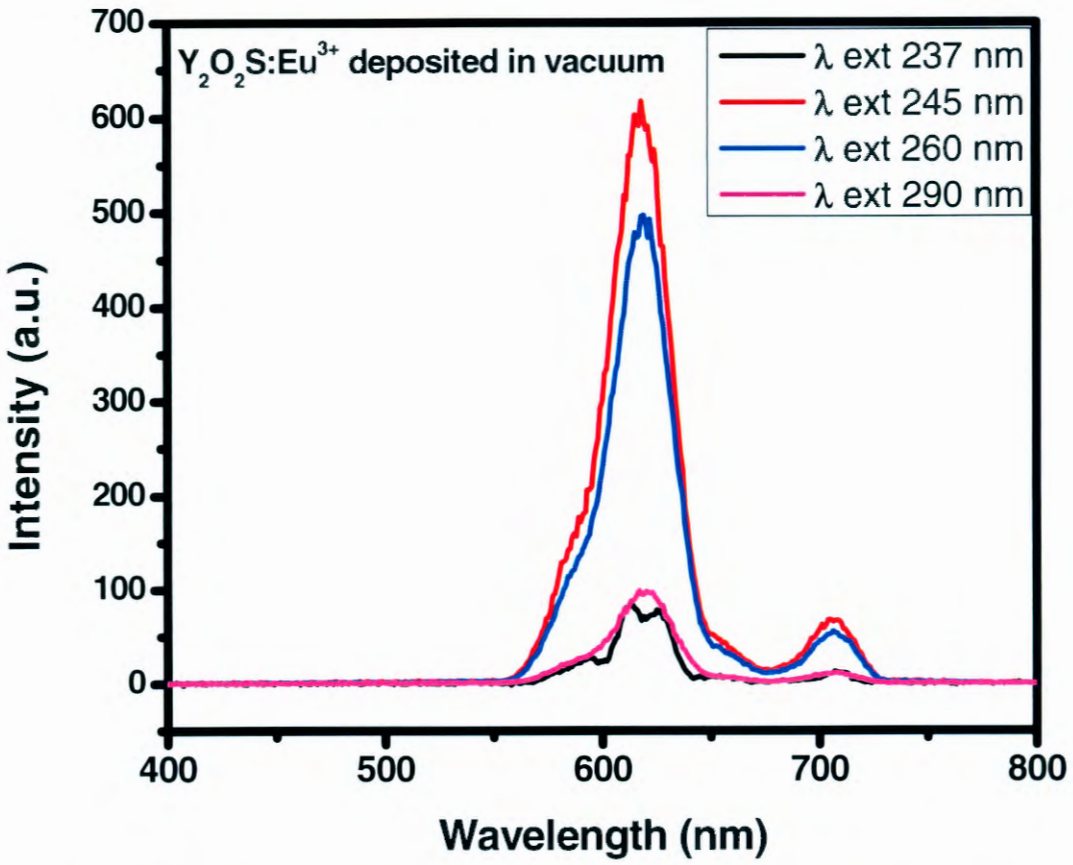

Figure 9.5(c). Emission spectra of $Y_2O_2S:Eu^{3+}$ thin film deposited in vacuum atmosphere recorded at 237, 245, 260 and 290 nm excitation wavelengths

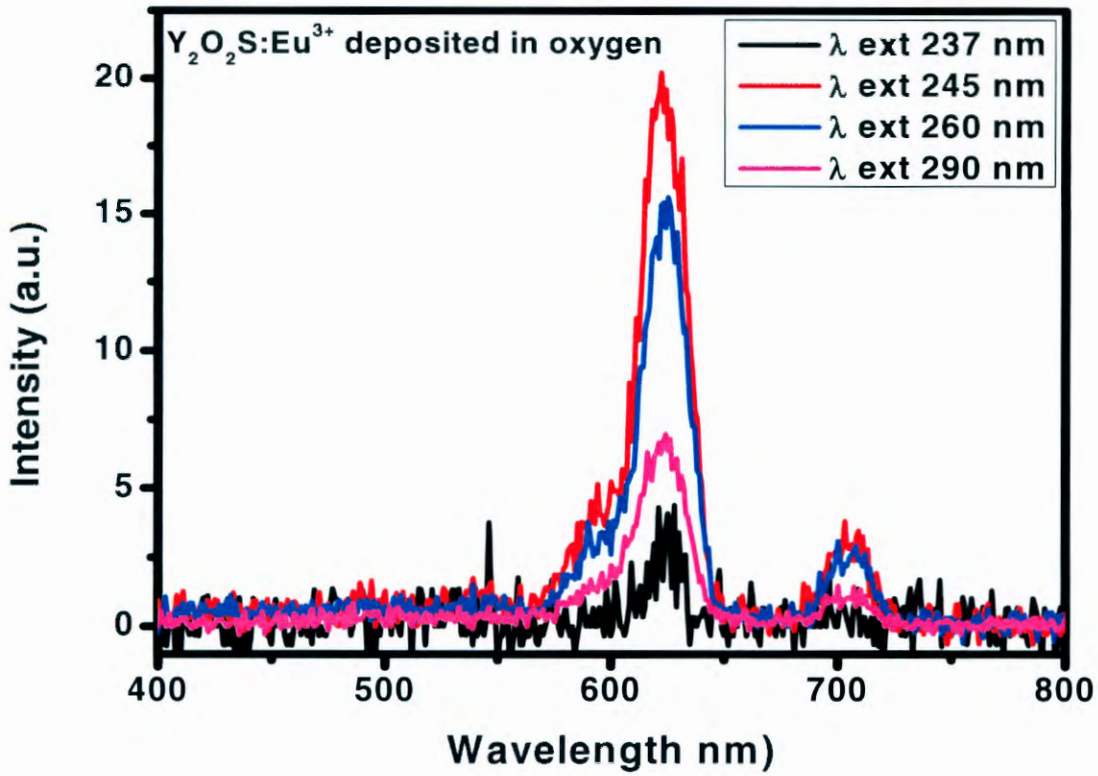

Figure 9.5(d). Emission spectra of $Y_2O_2S:Eu^{3+}$ thin film deposited in oxygen atmosphere recorded at 237, 245, 260 and 290 nm excitation wavelengths

It is well known that the 613 nm peak due to the Eu^{3+} is much more pronounced than the 402-595 nm peak for thinner films (less laser pulses) [33]. With all these in mind it might be speculated at this stage that the shift in the emission wavelength of the Eu^{3+} emission in argon atmosphere might also be due to reduction of Eu^{3+} to Eu^{2+}. The crystal field due to different structures of cubic and hexagonal must also be kept in mind. The nano size of the particles formed during deposition also can play a role. The higher PL intensities from the films deposited in the vacuum atmospheres can be ascribed to the films' relatively rougher surface as observed from the AFM pictures in Figure 3. It is well known that rough surfaces increases the probability of light emission from the surface by limiting the chances of total internal reflection at the film-substrate interface [34-37].

9.3.5 Decay curves

Figure 9.6 shows the decay characteristics of the thin films deposited in vacuum, O_2 and Ar atmospheres. Consistent with the PL data in Figure 5, the film prepared in vacuum

atmosphere has the highest initial intensity followed by the film prepared in the argon atmosphere. The fluorescence of Y_2O_2S: Eu^{3+} is believed to originate from the photo-oxidation of Eu^{2+} cation under UV-irradiation [38]. According to this model, an electron from the $^4f_7$ ground state is excited to the $^4f_6$-$^5d_1$ level of Eu^{2+} followed by an electron capture from the valence band reducing Eu^{2+} to Eu^+.

The films were further characterized by the fast and slow decays characteristics [38], since they are indicative of the different rates of decay for the films. The decay curves were fitted according to the equation (3) and gave decay constants listed in Table 9.1.

$$I = A_1 \exp(-t/\tau_1) + A_2 \exp(-t/\tau_2) \text{ ---------- (9.3)}$$

where I is the phosphorescence intensity, A_1, and A_2, are constants, t is time, τ_1 and τ_2, are decay times for exponential components, respectively. The fitting results of parameters t_1 and t_2 are listed in Table 9.1 below.

Table 9.1: Decay constants for the fitted decay curves of the thin films ablated in vacuum, argon and oxygen atmospheres.

Atmosphere	Vacuum	Argon	Oxygen
Components	Decay constants(τ, s)		
Fast (τ_1)	0.48±0.002	0.47±0.007	0.47±0.001
Medium (τ_2)	0.66±0.006	0.62±0.006	0.59±0.005

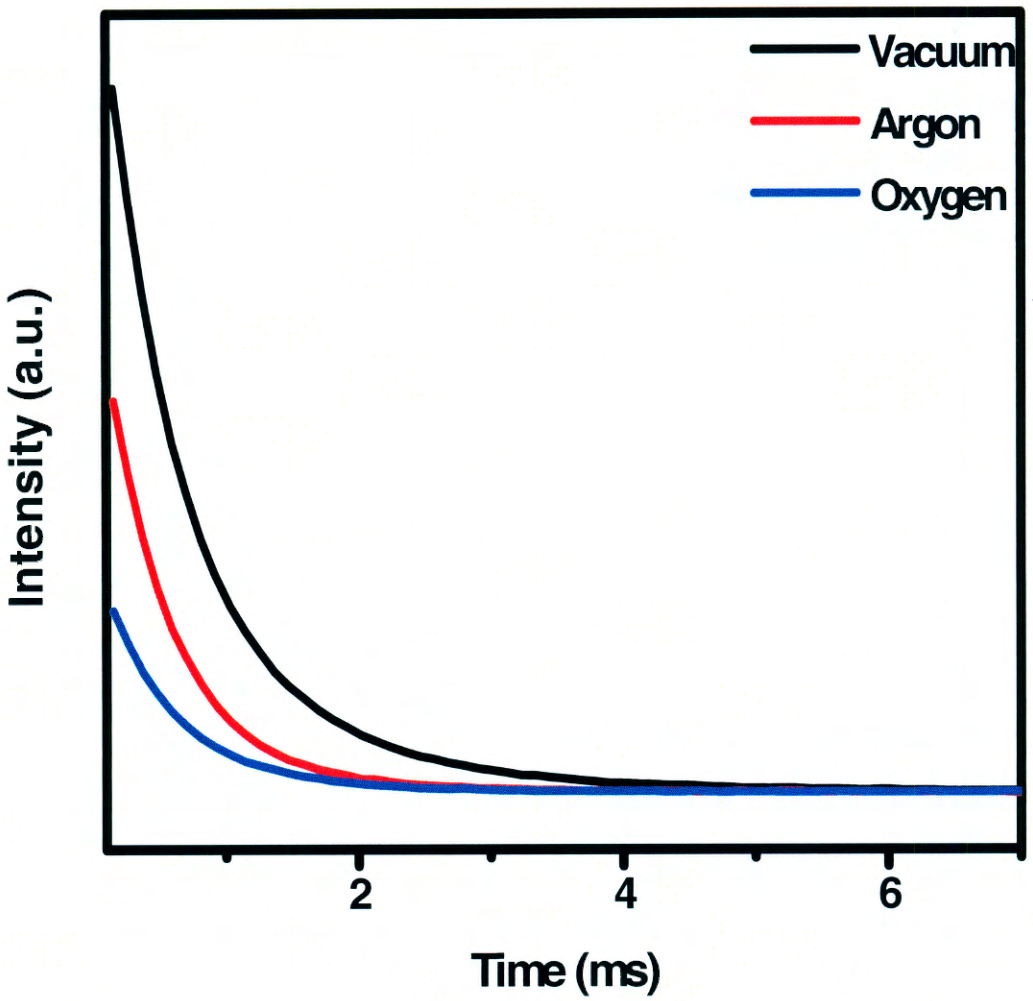

Figure 9.6. The decay curves for PLD Y_2O_2S: Eu^{3+} thin films deposited in vacuum and different gas atmospheres.

It is clear from Table 9.1 that the decay constants for the vacuum and argon samples are longer than that of the oxygen sample. According to these results the gas atmospheres did not play any role in the trap level concentration and also in the possible trap types.

9.3.6 Optical properties

9.3.6.1 Reflectance spectra

The UV–vis reflectance spectra of the samples are given in Figure 9.7. The spectra of all the samples show good optical quality in the visible range due to the complete reflectance in the 200– 500 nm range. The sharp absorption edge is characteristic of a homogeneous structure [39]. The figure shows that the absorption edge shifted to higher wavelength in the order vacuum, argon and oxygen. Absorption bands corresponding to the forbidden Eu^{3+} 4f–4f transitions were also detected for film deposited in O_2. The band at around 343 nm is

attributed to the exciton absorption, which is red-shift compared with powder $Y_2O_2S:Eu^{3+}$ [40]. The absorption peaks at around 290 and 340 nm are assigned to ^5Do-$^7F_1$and $^5D_0$-$^7F_2$ transitions of Eu^{3+} ions, respectively [41].

9.3.6.2 Determination of band gap from reflectance spectra

The Kubelka- Munk equation was used to calculate the band gap of the as- deposited thin film using a diffuse reflectance spectrum. The bang gap (Eg), and absorption coefficient α of direct band gap semiconductor are related through the Tauc relation. By plotting $[F(R)*h\nu]^2$ against hv and fit the linear region with a line and extending it to the energy axis, then one can easily obtain Eg by extrapolating the linear regions to $[F(R)*h\nu]^2=0$.

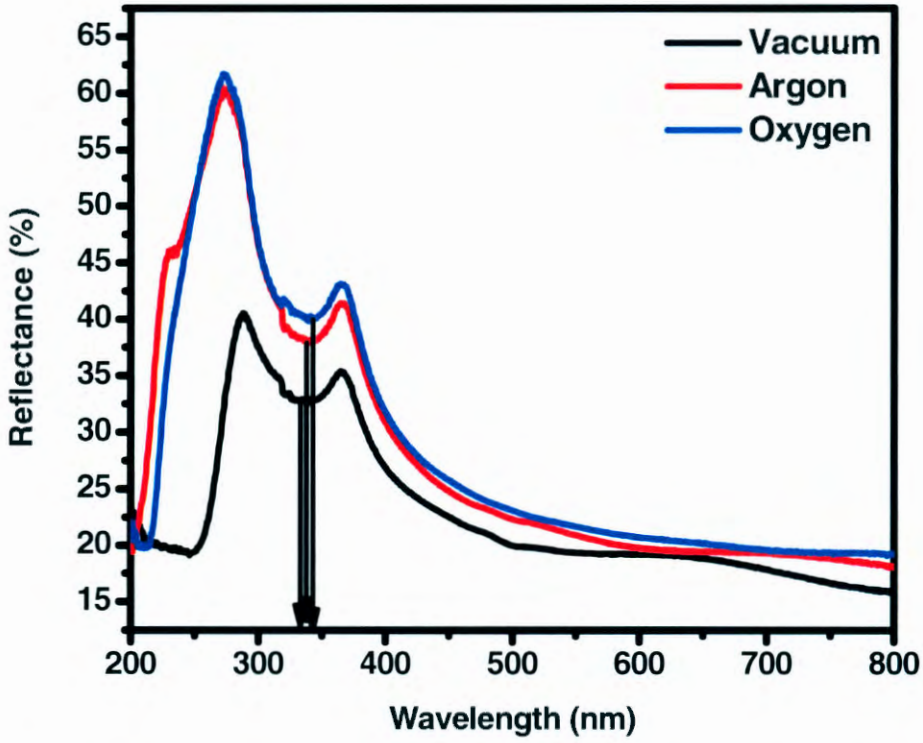

Figure 9.7. UV-vis diffuse reflectance spectra of nanocrystalline $Y_2O_2S:Eu^{3+}$ thin film deposited in vacuum, argon and oxygen atmospheres

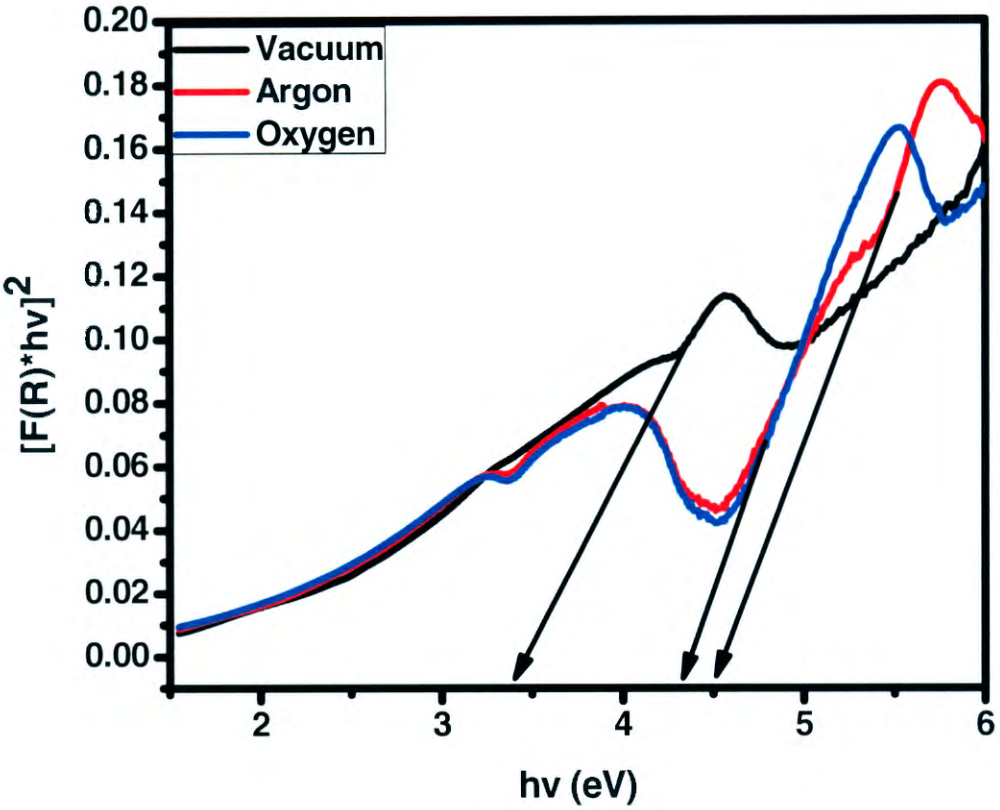

Figure 9.8. Graph of $F[(R)*hv]^{1/2}$ as a function of band gap energy

The dependence of the band gap energy of the Y_2O_2S on the vacuum and different gas species is shown in Figure 9.8. The observed optical band gap for Y_2O_2S: Eu^{3+} thin films increased in the order vacuum (3.4 eV), argon (4.3 eV) and oxygen (4.4 eV) as shown in Figure 8. The average Eg. value for the thin films was found to be 4.07 eV, which is in a good agreement with the literature values by other researchers [42]. The change in optical band gap values may also be due to the change of crystal structure of the Y_2O_2S thin films (Hexagonal verse Cubic). This is also confirmed by the fact that the PL emission intensity of the films deposited in vacuum is more than 5 times greater than the intensity of Y_2O_2S:Eu^{3+} thin films deposited in gas atmosphere.

The increase in band gap energy and the shift of the absorption edges to higher wavelengths in the case of film deposited in gas atmosphere might be due to the presence of defect states and disorder due to the different deposition atmospheres [43-44]. The gas atmospheres might have introduced new states close to the conduction band of the Y_2O_2S:Eu^{3+}. A new defect

band is therefore formed below the conductions which lead to reduction in the effective band gap [44].

9.4 Conclusion

Red- emitting Y_2O_2S: Eu^{3+} thin film phosphors were successfully ablated on Si (100) substrates by the pulsed laser deposition technique. The X-ray diffraction patterns showed mixed phases of cubic and hexagonal crystal structures. The SEM micrographs show that the surfaces of the films prepared in the gas atmosphere are much rougher than that deposited in vacuum. Intense red emission, with a maximum peak at 612 nm associated with the $^5D_0$-$^7F_2$ transitions of Eu^{3+} was detected from the films deposited in vacuum and argon atmosphere. The working atmosphere has a severe influence on the PL properties of the films. The films deposited in the vacuum atmospheres gave better PL and afterglow properties than the film prepared in gas atmospheres. The crystallinity and PL properties of the sample ablated in vacuum gave the best bright red emission. UV-vis measurement gave an average band gap of 4.69 eV.

Reference

[1] P. Sharma, D. Haranath, Harish Chander, Sukhivir Singh, Appl. Surf. Sci. 254 4052 (2008).

[2] W.W. Zhang, W.P. Zhang, P.B. Xie, M. Yin, J. Colloid Interface Sci. 262 (2003) 588 (2003).

[3] Y.Q. Zhai, Z.H. Yao, S.W. Ding, M.D. Qiu, J. Zhai, Mater. Lett. 57 2901 (2003).

[4] H.S. Peng, H.W. Song, B.J. Chen, S.Z. Lu, S.H. Huang, Chem. Phys. Lett. 370 485 (2003).

[5] T. Hirai, Y. Asada, I. Komasawa, J. Colloid Interface Sci. 276 339 (2004).

[6] J. Hao, S.A. Studenikin, M. Cocivera, J. Lumin. 93 313 (2001).

[7] L.P. Wang, G.Y. Hong, Mater. Res. Bull. 35 695 (2000).

[8] J.P. Lang, X.Q. Xin, J. Solid State Chem. 108 118 (1994).

[9] H.T. Cui, G.Y. Hong, H.P. You, et al., J. Colloid Interface Sci. 252 184 (2002).

[10] R. K. Singh and J. Narayan, Phys. Rev. B 41, 8843 (1991).

[11] A. Gupta, in Pulsed Laser Deposition of Thin Films, edited by D. B. Chrisey and G. K. Hubbler (Wiley, New York), p. 265(1994).

[12] A. Greer and M. Tahal, Mater. Res. Soc. Symp. Proc. 341, 87 (1994).

[13] S. S. Yi, J. Korean Phys. Soc. 45, 1625 (2004).

[14] Jong Seong Bae, Kyoo Sung Shim, Byung Kee Moon, Sung Boo Kim, Jung Hyun Jeong, Soung Soo Yi and Jung Hwan Kim, J. Korean Phys. Soc. 46, 1193 (2005).

[15] S-D. Han, Krishan C. Singh, T-Y. Cho, H-S. Lee, D. Jakhar, J. P. Hulme, C-H. Han, J-D. Kim, II-S. Chun, J. Gwak, Journal of Luminescence 128 301 (2008).

[16] Y-L. Chang, H-I. Hsiang, M-T. Liang, Journal of Alloys and Compounds 461 598 (2008).

[17] P.D. Sarkisov, N.V. Popovich, A.G. Zhelnin, Glass and Ceramics 60 9 (2003).

[18] T. Peng, L. Huajun, H. Yang, J. Mater. Chem. & Phys 85 68 (2004).

[19] T. Peng, H. Yang, X. Pu, B. Hu, Z. Jian, C. Yan, Mater. Lett. 58 352 (2004).

[20] X. Li, Y. Qu, X. Xie, Z. Wang, R. Li, Mater. Lett. 60 3673 (2006).

[21] D.P. Norton, Materials Science and Engineering R 43 139 (2004).

[22] J. Gonzalo R. G mez San Rom n J. Erri re C.N. AFonso R. P rez Casero, Appl. Phys. A 66, 487 (1998).

[23] A. Bailini, P.M. Ossi, A. Rivolta, Appl. Surf. Sci. 253 7682 (2007).

[24] A. Dauscher, M. Puyet, B. Lenoir, D. Colceag, M. Dinescu, Appl. Phys. A 79 1465 (2004).

[25] S. Choopun, H.Tabata, T. Kawai, J. Cryst. Growth 274 167 (2005).

[26] E. Coetsee, H.C. Swart, J.J. Terblans, O.M. Ntwaeaborwa, K.T. Hillie, W.A. Jordaan, U. Buttnerk, Opt. Mater. 29 1338 (2007).

[27] S.S. Kim, B-T. Lee, Thin Solid Films 446 307 (2004).

[28] L. Chen, Particles generated by pulsed laser ablation, in D. B. Chrisey, G. K Hulber (Eds), Pulsed Laser Deposition of Thin Films, John Wiley & Sons, Inc, New York, chap. no. 6, p. 167 and 184 (1994).

[29] K. Sato, S. Komuroa, T. Morikawa, H. Aizawa, T. Katsumata, S. Harako, X. Zhao, J. Cryst. Growth 275 1137 (2005).

[30] P.D. Nsimama, O.M. Ntwaeaborwa, E. Coetsee and H.C. Swart, Phys. B, Condens. Matter 404 4489 (2009).

[31] O.M. Ntwaeaborwa, P.D. Nsimama, S. Pitale, I. Nagpure, V. Kumar, E. Coetsee, J.J. Terblans, H.C. Swart, P.T. Sechogela, J. Vac. Sci. Technol. A 28 901 (2010).

[32] O.M. Ntwaeaborwa, P.D. Nsimama, J.T. Abiade, E. Coetsee, H.C. Swart, Phys. B: Phys. Condens. Matter 404 4436 (2009).

[33] D. Jia, Optical Materials 22 65 (2003).

[34] H. K. Yang, K.S. Shim, B.K. Moon, B.C. Choi, J.H. Jeong, S.S. Yi, J.H. Kim, Thin Solid Films 516 5577 (2008).

[35] F. Clabau, X Rocquefelte, S. Jobic, P. Denieard, M-H. Whangbo, A. Garcia, T Mercier, Sol. State Sci. 9 608 (2007).

[36] D. Zang, Y. Zhinong, W. Xue, T. Zhang, Z. Ding, W. Wang, J. Rare Earths 28 185 (2010).

[37] J.S. Kim, J. of Ceram. Proc. Res. 10 443 (2009).

[38] L. Luan, C.F. Guio, D.X. Huang, J. Inorg. Mater. 24 53 (2009).

[39] Y. Q. Li, N. Hirosaki, R-J. Xie, M. Mitomo, Sci. Technol. Adv. Mater. 8 607 (2007).

[40] C. Chang, Z. Yuan, D. Mao, J. Alloys Compds. 415 220 (2006).

[41] S.L. Jones, D Kumar, K-G Cho, R Singh, P.H. Holloway, Displays 19 151 (1999).

[42] J.M.Ngaruiya, S.Nieuwoudt, O.M.Ntwaeaborwa, J.J.Terblans, H.C.Swart, Mater.Lett. 62 3192 (2008).

[43] F. Clara, X. Rocquefelte, S. Jobic, P. Deniard, M.H. Whangbo, A. Garcia, T.L. Merciesr, Chem. Mater. 17 3909 (2005).

[44] B.M. Mothudi, O.M. Ntwaeaborwa, J.R. Botha, H.C. Swart, Phys. B:Condens. Matter 404 4440 (2009).

Chapter 10

Summary and suggestions for future work

10.1 Thesis summary

A simple and efficient chemical route to prepare a promising red- emitting phosphors by sol-combustion synthesis is presented. Ethanol has the effect of decreasing the water needed, hence simplifying the experimental procedure by dissolving rare earth nitrate and sulfur-contained organic fuel into an even solution. This prompts the formation of rare earth oxide by igniting first during heating that leads to a combustion decomposition reaction. Y_2O_3: Eu^{3+} microcrystalline structures were obtained using thiourea as organic fuel. The increase in the ratios of fuel to the host decreased the grain size and the maximum PL intensity of the phosphors. Also, trivalent-europium doped La_2O_2S microcrystals powders were prepared by sol- combustion method and their material properties were studied at room temperature. The phosphors emit bright red phosphorescence originating from the $^5D_0$- $^7F_2$ transition of Eu^{3+}. The XRD pattern of the as-synthesized powder revealed the presence of the hexagonal La_2O_2S phase with an average crystalline sizes of 178 nm with a space group P3m1 [164] and cell constants of (a) 0.4128 nm and (*c*) 0.6985 nm. The lower ratio of fuel to oxidizer favors the formation of the La_2O_2S rather than La_2O_3 phosphor. De-hydration of the reactants was crucial for the successful synthesis of the oxysulfide phase. SEM images of the as-synthesized powders showed that the morphology consisted of a foamy agglomeration and a continuous three-dimensional network. At higher La/S molar ratio the morphology appears as regular crystalline lattices. In order to study the effect of co-dopant, Y_2O_3:Eu^{3+}:Ho^{3+} red-emitting phosphor was synthesized and the influence of mole percent of Ho^{3+} ions has been investigated. The powders composed of nanoparticles. The size of the particles depended on the Ho^{3+} mole concentration. An increase in the Ho^{3+} percent resulted in smaller crystallite sizes. SEM show particles are highly agglomerated and form a connected network type with some vacant space among them, which is expected due to the evolution of different gases during combustion of the gel. At lower mole of Ho^{3+} all the peaks for both Eu^{3+} and Ho^{3+} were observed. The PL measurements showed red emission of Y_2O_3:Eu^{3+}:Ho^{3+} powder with the most intense peak appearing at 626 nm, which is assigned to the $^5D_0$-$^7F_2$ transition of

Eu^{3+}. At higher mole concentration of Ho^{3+}, energy transfer occurred from Eu^{3+} to Ho^{3+}. The band gap energy increased with increase of Ho^{3+} mole concentration.

To compare the material properties of the phosphors, the as- prepared powder samples were deposited on Si (100) substrates by PLD under various conditions. In the initial sample, $Y_2O_2S:Eu^{3+}$ thin films were successfully grown onto the Si (100) substrates at different oxygen ambient. XRD show mixed phases of cubic and hexagonal crystal structures. The films grown at low and high oxygen partial pressure are predominantly cubic, while that grown at moderate pressure (100 mtorr) is predominantly hexagonal. The thin films were composed of nanoparticles. The size of the particles depended on the oxygen partial pressure. The decrease in the oxygen partial pressure resulted into big particles which are actually piling up of smaller particles and therefore a rougher surface. The PL measurements showed red emission of $Y_2O_2S:Eu^{3+}$ thin films as well as the powder Y_2O_2S: Eu^{3+} with the most intense peak appearing at 619 nm, which is assigned to the $^5D_0$-$^7F_2$ transition of Eu^{3+}. This intense peak is quenched at higher O_2 partial pressure greater than 20 mtorr. The emission peak at 590 nm due to $^5D_0$-$^7F_1$ transition of Eu^{3}+ is also quenched at higher O_2 partial pressure. Uv-vis measurement revealed an average band gap of 4.03 eV. To investigate effect of annealing temperature, the next sample, Y_2O_3: Eu^{3+} thin films have been successfully deposited using PLD. The average crystallite size of the films after annealing was 64 nm. The study showed that the annealing temperature positively affected the crystalline phase, the morphology and the PL efficiency of the thin films. The un-annealed thin films were amorphous, while the annealed films consist of cubic and hexagonal phases depending on the annealing temperatures. SEM show similar morphology for the un-annealed and films annealed at lower temperatures which changed at higher temperature. The luminescence results show that the PL intensities were quenched and red-shifted at higher annealing temperatures showing formation of a new phase. UV-vis measurement indicated a band gap in the range of 4.6 to 4.8 eV. Finally, a Red- emitting Y_2O_2S: Eu^{3+} thin film phosphors were successfully ablated on Si (100) substrates by the pulsed laser deposition technique and effect of different species of gases were studied. The X-ray diffraction patterns showed mixed phases of cubic and hexagonal crystal structures. The SEM micrographs show that the surfaces of the films prepared in the gas atmosphere are much rougher than that deposited in vacuum. Intense red emission, with a maximum peak at 612 nm associated with the $^5D_0$-$^7F_2$ transitions of Eu^{3+} was detected from the films deposited in vacuum and argon atmosphere. The working atmosphere has a severe influence on the PL properties of the films. The films

deposited in the vacuum atmospheres gave better PL and afterglow properties than the film prepared in gas atmospheres. The crystallinity and PL properties of the sample ablated in vacuum gave the best bright red emission. UV-vis measurement gave an average band gap of 4.69 eV.

10.2 Suggestions for future work

The work presented in this thesis is very valuable to the literature of powder synthesis as well as laser ablated $Y_2O_2S:Eu^{3+}$ thin films. Other methods of synthesising powder Y_2O_2S: Eu^{3+}, Y_2O_3: Eu^{3+} and La_2O_2S: Eu^{3+} should be investigated. However, there are some investigations which need more attention to get more light on some of the findings. With regards to the deposition conditions, it is important to investigate more on the changes of oxygen, argon and nitrogen with the PL properties of Y_2O_2S: Eu^{3+} thin film phosphors. A wider range of the gas pressures (0.1-2 Torr) is needed for better optimizations. Other deposition parameters which are of interest are the target-substrate, the laser-target distance and the substrate type. It is important to do some more investigations on the in-situ post deposition analysis on the films and compare with the ex-situ annealing to determine the better annealing process for better PL and afterglow properties of Y_2O_2S: $^{3+}$ films. Annealing in different atmospheres such as argon, nitrogen can also be interesting. In the current work, all the depositions were done by using a 248 nm KrF laser source. It will be interesting to use another source of laser with higher energy such as 193 nm ArF in the course of seeing how the properties of Y_2O_2S: Eu^{3+} thin films will change.

Publications

(1) Abdub G. Ali, Francis B. Dejene, Hendrik C. Swart, Reinhardt J. Botha, Kittesa Roro, Liza Coetsee and Mart M. Biggs, Optical properties of ZnO nanoparticles synthesized by varying the sodium hydroxide to Zinc acetate molar ratios using a sol- gel process, ***Cent. Eur. J. Phys. 9(2).2011.1321-1326. DOI: 10.2478/S11534-011-0050-3***

(2) A.G. Ali, B.F. Dejene, H.C. Swart, Effect of Mn^{3+} doping on structural and optical properties of Sol-gel derived ZnO nanoparticles, ***Cent. Eur. J. Phys.10 (2).2012.478-484.DOI: 10.2478/S11534-011-0106-4***

(3) A.G. Ali, B.F. Dejene, H.C. Swart, Synthesis and Characterization of $Y_2O_3S:Eu^{3+}$ phosphors Using Sol-combustion Method, ***Physica B: Physics of Condensed Matter, Volume 439, pp. 181-184. DOI: 10.1016/j.physb.2013.11.051***

(4) A.G. Ali, B.F. Dejene, H.C. Swart, The influence of oxygen partial pressure on material properties of Eu^{3+}- doped Y_2O_2S thin film deposited by Pulsed Laser Deposition, ***Physica B: Physics of Condensed Matter (2016), pp. DOI information: 10.1016/j.physb.2015.10.005***

(5) A.G. Ali, B.F. Dejene, H.C. Swart, Temperature dependence of structural and luminescence properties of Eu^{3+}-doped Y_2O_3 red-emitting phosphor thin films by pulsed laser deposition, ***Journal of Applied Physics A, APYA-D-15-01792.1, DOI: 10.1007/s00339-016-9946-5***

(6) A.G. Ali, B.F. Dejene, H.C. Swart, The influence of different species of gases on the luminescent and structural properties of pulsed laser ablated $Y_2O_2S:Eu^{3+}$ thin films, ***Journal of Applied Physics A. •DOI: 10.1007/s00339-016-0062-3***

(7) A.G. Ali, B.F. Dejene, H.C, Swart, Energy transfer and material properties of Y_2O_3: Eu^{3+}:Ho^{3+} nanophosphors synthesized by sol- combustion method, ***This paper has been accepted by Journal of Chemistry and Engineering***

(8) A.G. Ali, B.F. Dejene, H.C, Swart, Structural, thermal and optical properties of ZnO, SiO_2 and ZnO: SiO_2:Ce^{3+} nanoparticles by sol-gel process. ***This paper was submitted to the Journal of Rare- earths***

(9) A.G. Ali, B.F. Dejene, H.C, Swart, Structural and Luminescent Properties of Y_2O_3:Eu^{3+}:Ho^{3+} Nanocrystals Prepared by Sol- Combustion Synthesis" at the South African Institute of Physics (SAIP) conference July 2015. ***This paper is under review***

(10) A.G. Ali, B.F. Dejene, H.C, Swart, Synthesis and characterization of europium activated yttrium oxysulphide by sol- combustion method. ***This paper was submitted to the Journal of Rare- earths***

(11) A.G. Ali, B.F. Dejene, H.C, Swart, Synthesis and characterization of europium activated lanthanum oxysulphide by sol- combustion method, ***This paper was submitted to the Journal of Luminescence***

(12) A.G. Ali, B.F. Dejene, H.C, Swart, Synthesis and characterization of europium activated lanthanum oxide by sol- combustion method, ***This paper was submitted to the Journal of Luminescence***

Papers presented at conferences

(1) A paper entitled "Optical properties of ZnO nanoparticles synthesized by varying the sodium hydroxide to Zinc acetate molar ratios using a sol- gel process" at the South African Institute of Physics(SAIP) conference in Durban in July 2009. This paper was published in Cent. Eur. J. Phys. 9(2).2011.1321-1326. DOI: 10.2478/S11534-011-0050-3.

(2) A paper entitled "Effect of Mn^{3+} doping on structural and optical properties of Sol-gel derived ZnO nanoparticles"at the South African Institute of Physics (SAIP) conference in Johannesburg in July 2010.This paper was published in Cent. Eur. J. Phys.10(2).2012.478-484.DOI: 10.2478/S11534-011-0106-4

(3) A paper entitled "Synthesis and Characterization of $Y_2O_3S:Eu^{3+}$ phosphors Using Sol-combustion Method" at the South African Institute of Physics conference in Kariega in July 2011. This paper is in press at the Journal of Condensed Matter Physics- Physica B.

(4) A paper entitled "Structural, thermal and optical properties of ZnO, SiO_2 and ZnO: $SiO_2:Ce^{3+}$ nanoparticles by sol-gel process" at the African Material Society (AMRS) conference in Victoria Falls Zimbabwe December 2011. This paper was submitted to the Journal of Rare- earths.

(5) A paper entitled "Synthesis and characterization of europium activated yttrium oxysulphide by sol- combustion method" at the African Material Society conference(AMRS) in Victoria Falls Zimbabwe December 2011. This paper was submitted to the Journal of Rare- earths.

(6) A paper entitled "Synthesis and characterization of europium activated lanthanum oxysulphide by sol- combustion method" at the South African Institute of Physics conference in University of Pretoria in July 2012. This paper was submitted to the Journal of Luminescence.

(7) A paper entitled "Synthesis and characterization of europium activated lanthanum oxide by sol- combustion method" at the African Laser Center(ALC) conference in University of Namibia in Windhoek in November 2012. This paper was submitted to the Journal of Luminescence.

(8) A paper entitled "Synthesis and Characterization of $Y_2O_3:Eu^{3+}$ phosphors Using Sol-combustion Method" at the South African Institute of Physics conference in Kariega in May 2013. This paper is in Press in the Journal of Condensed Matter Physics- Physica B.

(9) A paper entitled "Structural and Luminescent Properties of $Y_2O_3:Eu^{3+}:Ho^{3+}$ Nanocrystals Prepared by Sol- Combustion Synthesis" at the South African Institute of Physics (SAIP) conference in Richards Bay in July 2013. This paper is under review.

(10) The influence of different species of gases on the luminescent and structural properties of pulsed laser ablated $Y_2O_2S:Eu^{3+}$ thin films at the conference of laser ablation (COLA) at Cairns, Australia. This paper was submitted to the Journal of Applied Physics A.

(11)Temperature dependence of structural and luminescence properties of Eu^{3+} -doped Y_2O_3 red- emitting phosphor thin films by Pulsed Laser Deposition at the conference of laser ablation (COLA) at Cairns, Australia. This paper was submitted to the Journal of Applied Physics A.

Appendix: Emission spectra for films deposited in vacuum and at different oxygen partial pressure. The inset show emission spectrum of $Y_2O_2S:Eu^{3+}$ powder phosphor.